



Etude des phénomènes nucléaires collectifs à travers des mesures de masse de précision d'isotopes riches en neutron d'argon et de chrome

Maxime Mougeot

► To cite this version:

Maxime Mougeot. Etude des phénomènes nucléaires collectifs à travers des mesures de masse de précision d'isotopes riches en neutron d'argon et de chrome. Physique Nucléaire Expérimentale [nucl-ex]. Université Paris Saclay (COMUE), 2018. Français. NNT : 2018SACLS455 . tel-02017986

HAL Id: tel-02017986

<https://theses.hal.science/tel-02017986>

Submitted on 13 Feb 2019

HAL is a multi-disciplinary open access archive for the deposit and dissemination of scientific research documents, whether they are published or not. The documents may come from teaching and research institutions in France or abroad, or from public or private research centers.

L'archive ouverte pluridisciplinaire **HAL**, est destinée au dépôt et à la diffusion de documents scientifiques de niveau recherche, publiés ou non, émanant des établissements d'enseignement et de recherche français ou étrangers, des laboratoires publics ou privés.

Nuclear Collectivity Studied through High-precision Mass Measurements of Neutron-rich Argon and Chromium Isotopes

Thèse de doctorat de l'Université Paris-Saclay
préparée à Université Paris-Sud

Ecole doctorale n°576 particules hadrons énergie et noyau : instrumentation, image,
cosmos et simulation (PHENIICS)
Spécialité de doctorat : Structure et réactions nucléaires

Thèse présentée et soutenue à Orsay, le 30 Novembre 2018, par

M. MAXIME MOUGEOT

Composition du Jury :

Mme. Araceli LOPEZ-MARTENS Directrice de recherche, Université Paris-Sud, CSNSM (UMR8609)	Président
Mme Kamila SIEJA Chargée de recherche, IPHC (UMR7178)	Rapporteur
M. Iain MOORE Professeur, Université de Jyväskylä	Rapporteur
M. Laurent GAUDEFROY Chargé de recherche, CEA/DAM	Examineur
Mme Beyhan BASTIN Chargée de recherche, GANIL	Examineur
M. David LUNNEY Directeur de recherche, Université Paris-Sud, CSNSM (UMR8609)	Directeur de thèse

Contents

Acknowledgements	xi
1 Introduction	1
1.1 The field of mass spectrometry	1
1.2 The nuclear binding energy and shell structure	2
1.3 This thesis	7
2 Experimental methods and measurements	9
2.1 Radioactive ion beam production	9
2.2 Experimental cycle	12
2.3 Charged-particle traps	15
2.3.1 The Penning trap	15
2.3.2 The Time-of-Flight Ion Cyclotron Resonance (ToF-ICR) technique	18
2.3.3 The Multi-Reflection Time-of-Flight device	24
2.3.4 Ion traps for beam accumulation and cooling	26
2.4 Measurements	28
2.4.1 Neutron-rich chromium isotopes	29
2.4.2 Neutron-rich argon isotopes	31
3 Analysis of the data and mass determination	37
3.1 Generalities	37
3.1.1 ToF-ICR analysis	37
3.1.2 MRToF-MS analysis	41
3.2 Neutron-rich argon isotopes	47
3.2.1 Analysis of the $^{46-47}\text{Ar}$ ToF-ICR resonances	47
3.2.2 Analysis of ^{48}Ar MRToF spectra	49
3.2.3 Results	52
3.3 Neutron-rich chromium isotopes	53
3.3.1 Analysis of the $^{58-62}\text{Cr}^+$ ToF-ICR resonances	53
3.3.2 Analysis of the $^{59-63}\text{Cr}^+$ MRToF-MS spectra	54
3.3.3 Results	56
4 Theoretical approaches to the nuclear many-body problem	59
4.1 The nuclear many-body problem	59
4.1.1 Formulation of the problem	59
4.1.2 Nuclear forces	61
4.2 The nuclear shell-model	63

4.2.1	The independent particle model	63
4.2.2	The interacting shell model	63
4.2.3	The ANTOINE shell-model code	66
4.3	Self-consistent mean-field calculations	66
4.3.1	The Hartree-Fock-Bogolibov method	66
4.3.2	Nuclear energy-density functionals	70
4.3.3	The HFBTHO code	71
4.4	The In-Medium Similarity Renormalization Group	75
5	Interpretation	77
5.1	The $N = 28$ and $N = 40$ "Islands of Inversion"	77
5.2	Development of ground-state collectivity towards $N=40$ in the chromium chain	80
5.2.1	Phenomenological discussion of the S_{2n} trend	80
5.2.2	Development of quadrupole collectivity : the mean-field point of view	81
5.2.3	Large-scale shell-model calculations and VS-IMSRG	82
5.3	Strength of the $N=28$ shell closure in neutron-rich Argon isotopes	85
5.3.1	Phenomenological discussion of the binding energy trends	85
5.3.2	Comparison to various theoretical approaches	87
6	Conclusion and Outlook	91
A	Publications related to this thesis work	97
B	Precision Mass Measurements of $^{58-63}\text{Cr}$: Nuclear Collectivity Towards the $N = 40$ Island of Inversions	99
C	High-precision measurement of the ^{18}Ne superallowed β-decay Q-value	107
D	Résumé en langue française	117

List of Figures

1.1	Various mass filters for the calcium ($Z = 20$) isotopic chain as a function of the neutron number N . The error bars are smaller than the size of the point.	4
2.1	Simulated production yield of a typical ISOLDE uranium carbide target. The argon and chromium isotopes measured in this work are highlighted with red squares. <i>Credit: Frank Wienholtz</i>	11
2.2	3D view of an ISOLDE target and ion source assembly. The depicted ion source is similar to a VD7 VADIS plasma ion source (see [K ⁺ 76, P ⁺ 10]). The primary 1.4 GeV proton beam induces nuclear reaction in the material contained in the tantalum container (red arrow). The neutral radioactive atoms thus created diffuse out of the target material (green arrow). The latter effuse through the transfer line into the ionisation region (yellow arrow). Finally, the species are ionised and extracted as an ion beam (blue arrow). In the present case, the primary electrons produced by heating the cathode are accelerated through the potential difference created between the anode grid and the cathode. Electron impact ionisation inside the anode volume simply follows.	12
2.3	Schematic representation of the ISOLTRAP mass spectrometer as it stands today.	13
2.4	a) 3D rendering of ISOLTRAP's hyperbolic Penning trap. The ring electrode is 4-fold segmented in order to allow for the application of azimuthal dipole and quadrupolar RF driving fields. Annotations indicate the different electrodes constituting ISOLTRAP Penning trap. b) Idealized potential distribution inside ISOLTRAP hyperbolic Penning trap (red indicates higher values while blue lower values). The potential distribution being axially symmetric, an arbitrary 2D plane of view containing the trap axis is chosen. The corresponding electric field lines are represented as black arrows the width of which is proportional to the field strength. The intersection of the trap's electrodes with the plane of representation is indicated with dashed lines.	17

- 2.5 Computed trajectory of a singly charged ^{133}Cs ion inside ISOLTRAP's Penning trap. The full trajectory is represented in black. This trajectory is decomposed into three eigenmotions : an axial harmonic motion at the frequency ω_z (blue), the slow drift motion at the magnetron frequency ω_- (green), the circular cyclotron motion at the reduced cyclotron frequency ω_+ (red). 18
- 2.6 a) Idealized potential distribution corresponding to a dipole excitation. The corresponding idealized electric field lines are also represented. For the sake of illustration the 4-fold segmented ring electrode is sketched as well. b) Schematic representation of the trajectory of an ion subjected to an RF dipole pulse. The radius of the ion's motion (chosen to be pure magnetron in this case) continuously increases with time. The final radius is marked with a dashed circle and depends on the amplitude and duration of the excitation. 20
- 2.7 a) Same as Figure 2.6a but for a quadrupole excitation. b) Schematic representation of the trajectory of an ^{133}Cs ion subjected to a quadrupole excitation at the true cyclotron frequency ν_c . A pure magnetron motion (initial radius marked with dashed circle) is progressively converted into a pure cyclotron motion. 21
- 2.8 Scan of the quadrupole excitation frequency around the free cyclotron frequency of an $^{85}\text{Rb}^+$ ion ensemble. The excitation time is 1200 ms. Approximately 1000 ions were used to produce this resonance. The color map represents the individual ion events recorded in each (frequency, tof) bin. For each frequency bin, the mean time-of-flight and the associated standard deviation is represented as open circles. The red line is a fit to the theoretical line shape [K⁺95]. 22
- 2.9 Simulated potential distribution along ISOLTRAP's MRToF-MS axis (*top*). The corresponding 2D rendered cut view of the MRToF is shown (*bottom*). The schematic separation of an ion bunch into two distinct species is also represented. 24
- 2.10 *Top*: A typical ToF-ICR resonance of $^{62}\text{Cr}^+$ ions using a Ramsey-type excitation scheme with 10 ms-80 ms-10 ms ($\tau_{on}^{RF}-\tau_{off}^{RF}-\tau_{on}^{RF}$) [G⁺07b]. The solid line represents a fit to the data points. *Bottom*: Number of events as a function of flight time after 1000 revolutions of the $A=63$ ISOLDE beam inside the MR-ToF MS. 29
- 2.11 Typical two-pulse Ramsey TOF-ICR resonance obtained for $^{47}\text{Ar}^+$ with 10 ms-80 ms-10 ms ($\tau_{on}^{RF}-\tau_{off}^{RF}-\tau_{on}^{RF}$) [G⁺07b, G⁺07a]. The color-map represents the individual ion events recorded in each (frequency; tof) bin while the red line represents the least-squares adjustment of the theoretical line shape to the data points. 33
- 2.12 Typical one-pulse TOF-ICR resonance obtained for $^{46}\text{Ar}^+$. A quadrupole excitation time of 200 ms was used. The color-map represents the number of individual-ion time-of-flight events recorded in each (frequency; tof) bin while the red line represents the least-squares adjustment of the theoretical line shape to the data points [K⁺95]. The dashed red vertical line indicates the expected cyclotron frequency of the $^{34}\text{S}^{12}\text{C}^+$ contaminant. 34

2.13	$A=48$ time-of-flight spectrum after 1000 revolutions inside the MRToF-MS. The spectrum recorded with protons on target results from the sum of 13 consecutive files and is represented in yellow. The spectrum in red represents a background measurement performed while the protons were off and is the sum of 21 consecutive files. Each spectrum is thus normalised to the total number of counts in the spectrum and stacked on top of each other to ease comparison. . . .	35
2.14	Intensity of the $^{48}\text{Ar}^+$ signal as a function of the buncher cooling time for a buncher RF amplitude of 16 mV and 20 mV. All other experimental parameters were kept constant. Each point was extracted from a spectrum resulting from the sum of 3 to 4 consecutive files. Hence, the intensity of the $^{48}\text{Ar}^+$ signal was normalised to the total number of ions obtained after summing.	36
3.1	Time-of-flight deviation from the nominal value as function of the mirror-electrode voltages extracted from simulations (solid lines) and from experimental data (square points). Figure taken from [W ⁺ 12b].	44
3.2	Relative change in the CToF coefficient as a function of the time-of-flight shift. The slopes of these curves are given by the coefficients A, B and C (see text for details).	45
3.3	Histogram representing the number of detected ion for different total number of ions detected in one ejection. See text for details. . . .	48
3.4	A $^{46}\text{Ar}^+$ resonance when only events where 1 detected ion per ejection are selected. The solid red line represents the result of the least-squares adjustement to the theoretical line-shape.	48
3.5	The model pdf used to extract the time of flight of $^{48}\text{Ar}^+$. The full pdf is represented using the solid green line while the solid blue and red lines represent respectively the background (two Gaussians) and signal (one Gaussian). The background component is used to constrain the width of the signal component. The reference $^{48}\text{SO}^+$ peak is outside the represented time of flight window.	50
3.6	Scattering of the individual C_{ToF} coefficients around the average C_{ToF} value for $^{48}\text{Ar}^+$. The light-grey band represents the statistical 1σ band of the average C_{ToF} . The reduced χ^2 value is 1.05. . . .	50
3.7	Typical time-of-flight distribution of the $^{85}\text{Rb}^+$ offline reference. The peak distributions obtained after a fit to the data using a Gaussian pdf and the Exponentially Modified Gaussian pdf of [L ⁺ 01] are represented in red and black respectively.	51
3.8	Same as Figure 3.7 but for the online reference $^{32}\text{S}^{16}\text{O}^+$	52
3.9	Deviation of the atomic mass excess of $^{46-47}\text{Ar}$ obtained in this work with respect to the AME2012 values. For ^{48}Ar our result is compared with that of [M ⁺ 15a]. The grey shaded area represent the $1\text{-}\sigma$ uncertainty band. The filled red circles represent the values obtained from the Penning trap measurement while the green diamonds represent the MRToF-MS measurements.	54
3.10	Typical MRToF spectrum for $A = 59$ at 1000 revolutions. The time of flight distribution corresponding to $^{59}\text{Cr}^+$ is represented in red. .	56

3.11	Deviation of the atomic mass excess of $^{58-63}\text{Cr}$ obtained in this work with respect to the AME2012 values. The grey shaded area represent the AME2012 uncertainty band. The filled red circles represent the values obtained from the Penning trap measurement while the green diamonds represent the MRToF-MS measurements.	58
4.1	Evolution of several phenomenological N - N -interactions in the $^1\text{S}_0$ channel as a function of the inter-nucleon distance r . The picture was taken from ref. [AHI08]. I, II, III correspond to the long, intermediate and short range of the interaction (see text for details).	62
4.2	The structure of the "naive" shell model. Picture taken from ref. [PN01].	64
4.3	Difference between the HFB+Lipkin Nogami corrections energy computed using $N_{\text{shells}}=12$ (plain lines) and $N_{\text{shells}}=16$ (dashed lines) compared to that computed using $N_{\text{shells}}=20$. The difference is plotted against neutron number in the range $N=32-42$ for even-even nickel (red-diamonds), iron (green-squares) and chromium isotopes (blue-circles).	73
4.4	Difference between S_{2n} values computed using $N_{\text{shells}}=12$ (plain lines) and $N_{\text{shells}}=16$ (dashed lines) compared to that computed using $N_{\text{shells}}=20$. The difference is plotted against neutron number in the range $N=32-42$ for even-even nickel (red-diamonds), iron (green-squares) and chromium isotopes (blue-circles).	74
5.1	Evolution of the energy of the first excited 2^+ state in even-even isotopes for isotopic chains from $Z = 14$ to 28 . Source ENSDF database 2017 [ens17].	78
5.2	S_{2n} trends for the isotopic chains ranging from $Z = 16$ to 28 [W ⁺ 17a]. The trends for the argon and chromium isotopic chains are decomposed into the contribution from the AME2012 [A ⁺ 12] and recent time-of-flight measurements performed with the S800 spectrometer at the NSCL [M ⁺ 15a, M ⁺ 16].	79
5.3	<i>Top</i> : S_{2n} trend obtained from the newly measured chromium masses. <i>Bottom</i> : δ_{2n}^* for the ground and excited 2_1^+ state in the chromium and iron isotopic chains [G ⁺ 10, S ⁺ 15].	81
5.4	Potential energy curves as a function of the quadrupole deformation-parameter β_2 for the $Z = 24$ isotopes. For each the absolute minimum value of the potential energy curve is taken as the energy reference. In addition, each curve is arbitrarily shifted by 3 MeV in order to ease comparison. Dashed and dash-dotted vertical lines indicate β_2 values of 0 and 0.2 respectively.	82
5.5	Proton and neutron single-particle energies for ^{64}Cr calculated for the UNDEF0 functional. The thick red line indicates the position of the fermi level.	83
5.6	Schematic representation of the valence spaces used for the LNPS', GXPF1A and VS-IMSRG calculations.	84
5.7	<i>Top</i> : Two-neutron separation energy of the Mg chain [W ⁺ 17a]. <i>Bottom</i> : Comparison between the experimental S_{2n} trends predicted by various theoretical approaches.	84
5.8	Trends of S_{2n} in the $N=28$ region for isotopic chains ranging from sulfur to calcium.	86

5.9	Three points estimator of the odd-staggering for the calcium, argon and sulfur isotopic chains.	86
5.10	Comparison between the S_{2n} trend obtained from this work and the ones predicted from various theoretical approaches. See text for details.	87
5.11	Comparison between the pairing gap trend obtained from this work and the ones predicted from various theoretical approaches. See text for details.	88
5.12	Comparison between the empirically determined pairing-gap trend and the one obtained by the valence-space IMSRG calculations. See text for details.	89
D.1	Gap empirique d'appariement neutron pour les chaines isotopiques du calcium, de l'argon et du soufre. La courbe bleue est tirée des mesures expérimentales obtenues dans cette thèse. La courbe orange quant à elle est tirée de [M ⁺ 15a].	120
D.2	<i>Top</i> : Energie de séparation à deux neutrons, S_{2n} , obtenue lors de cette thèse (courbe bleue). La courbe orange est obtenue d'après [M ⁺ 16]. <i>Bottom</i> : δ_{2n}^* pour l'état fondamental et le premier état excité 2_1^+ pour les chaines isotopiques de chrome (courbe bleue) et de fer (en vert) [G ⁺ 10, S ⁺ 15].	120
D.3	Comparaison entre le gap empirique d'appariement neutron expérimental et diverses approches théoriques. Voir texte pour plus de détails. La courbe bleue est obtenue d'après les mesures rapportées dans cette thèse.	121
D.4	<i>Top</i> : Energie de séparation à deux neutrons de la chaine du magnésium Mg [W ⁺ 17a]. <i>Bottom</i> : Comparaison entre l'énergie de séparation à deux neutrons expérimentale et diverses approches théoriques. La courbe bleue est obtenue d'après nos mesures expérimentales. . .	122

List of Tables

2.1	Summary of the production, preparation and measurement conditions of $^{58-63}\text{Cr}$. In all cases, the MRToF trapping and the total preparation trap periods are rounded. For the ToF-ICR data, the exact quadrupole excitation time applied in the measurement Penning trap is given. For the Ramsey type ToF-ICR resonances, the total quadrupole excitation time is decomposed as $\tau_{on}^{RF}-\tau_{off}^{RF}-\tau_{on}^{RF}$. See text for details.	31
2.2	Summary of the production, preparation and measurement conditions for the isotopes $^{46-48}\text{Ar}$. In all cases, the MRToF trapping and the total preparation trap cycle are rounded. For the ToF-ICR data, the exact quadrupole excitation time applied in the measurement Penning trap is given. For the Ramsey type ToF-ICR resonances, the total quadrupole excitation time is decomposed as $\tau_{on}^{RF}-\tau_{off}^{RF}-\tau_{on}^{RF}$. See text for details.	36
3.1	Frequency ratios ($r = \nu_{c,ref}/\nu_c$), time of flight ratios (C_{ToF}) and mass excesses of the argon isotopes measured in this work. Values of the mass excesses from the Atomic-Mass Evaluation 2016 (AME2016) [W ⁺ 17a] are given for comparison. Values from AME2012 are also given [A ⁺ 12] (# designates AME2012 extrapolated value). The masses of the reference ions were also taken from AME2016. Experimental half-lives are taken from the NUBASE2016 evaluation [A ⁺ 17c].	53
3.2	Frequency ratios ($r = \nu_{c,ref}/\nu_c$), time of flight ratios (C_{ToF}) and mass excesses of the chromium isotopes measured in this work. Values of the mass excesses from the Atomic Mass Evaluation 2016 (AME2016) [W ⁺ 17a] are given for comparison. Values from AME2012 are also given [A ⁺ 12]. The masses of the reference ions were also taken from AME2016. Experimental half-lives are taken from the NUBASE2016 evaluation [A ⁺ 17c]. The yields correspond to the number of chromium ions per second delivered by the ISOLDE facility. The total transport efficiency of the experiment was estimated to be 0.5% behind the MR-ToF MS. The average proton current on target was $1.8\mu\text{A}$	57

D.1	Rapport de fréquences ($r = \nu_{c,ref}/\nu_c$), rapports de temps de vol (C_{ToF}) et excès de masse atomique pour les isotopes d'argon mesurés dans le cadre cette thèse. Les excès de masse atomique extrait de l'AME 2016 [W ⁺ 17a] et de l'AME 2012 [A ⁺ 12] sont donnés pour comparaison (# désigne des valeurs extrapolées dans l'AME2012). Les masses des ions de références sont extraites de l'AME 2016. Les demi-vie expérimentales proviennent de l'évaluation NUBASE2016 [A ⁺ 17c].	118
D.2	Rapport de fréquences ($r = \nu_{c,ref}/\nu_c$), rapports de temps de vol (C_{ToF}) et excès de masse atomique pour les isotopes de chrome mesurés dans le cadre cette thèse. Les excès de masse atomique extrait de l'AME 2016 [W ⁺ 17a] et de l'AME 2012 [A ⁺ 12] sont donnés pour comparaison (# désigne des valeurs extrapolées de l'AME2012). Les masses des ions de références sont extraits de l'AME 2016. Les demi-vie expérimentales proviennent de l'évaluation NUBASE2016 [A ⁺ 17c]. Les taux de productions correspondent au nombre d'ions de chrome par seconde produit lors de cette expérience. Au total, l'efficacité du transport des ions jusqu'au MRToF-MS était de 0.5 %. En moyenne, la cible a été irradiée avec un courant de protons de 1.8 μ A.	119

Acknowledgements

First and foremost, I would like to express all my gratitude to Hannah Bennett with whom I have been sharing my life for the last ten years. She has been supporting me through thick and thin from the time we first met to the final stage of the writing of the present manuscript as well as the defense of my PhD work. I know how hard it has been for her to see me leave our shared life in Paris to come work at CERN for the whole three years of my PhD. I doubt that the present manuscript could ever live up to the sacrifice she has made for this work to be possible. Nonetheless, I hope she finds that the time spent away from her was not in vain and I dedicate this manuscript to her.

I was fortunate enough to start my work at ISOLTRAP at a time when the team possessed a great deal of skills. The complementarity and dedication of the team was what made it undoubtedly strong but it also made it very easy for a newcomer to jump in. In particular, I would like to thank Dinko Atanasov for teaching me most of what I know regarding the ISOLTRAP control system. Dinko's apparent quietness should not overshadow how reliable and consistent a colleague he is. On the another side of the spectrum we have Frank Wienholtz. Frank can from time to time be as loud a person as his dedication to the experimental setup was strong. He is once more the perfect example of a person one can always count on and his technical feats were such that we never had to worry even in the most crucial of times. Last but not least, I would like to express all my gratitude to maybe the person I learned the most from: Vladimir Manea. Through countless discussions over the last three years he has helped shape and more importantly refine this PhD work. As I am writing these words, all three of them have left for other projects and I very sincerely wish them the best of success in the future. I also wish the best of success to the ISOLTRAP newcomers Jonas Kartheim and Ivan Kulikov.

I would like to thank my PhD supervisor, David Lunney, for giving me the opportunity to spend the last three years at CERN. Even though we were a few hundred kilometers apart, he has always been there in the key moments of this PhD and helped shape the content and form of the present manuscript.

Experiments such as the one reported in the present manuscript involve a lot more people than the members of the ISOLTRAP local team alone. From the people in charge of the target design and ion beam production to the ones in charge of the setting up of the ISOLDE RILIS; from the ISOLDE operators to the colleagues of other ISOLDE experiments; all had a different part to play to make this PhD work successful and my stay at CERN more pleasant. To you all, thank you.

Finally, I would like to thank the members of the jury for their comments and corrections which helped improve the quality of the present manuscript.

Introduction

1.1 The field of mass spectrometry

Retrospectively, the founding moment for the field of mass spectrometry goes back to 1897 and the identification of cathodic rays as beams of negatively charged particles, the electrons, by J.J. Thomson [Tho97, Tho99]. This breakthrough relied on the determination of an intrinsic property of a charged particle, namely its charge-over-mass ratio. Since then, the history of the field of mass spectrometry has been that of a constant refinement of the experimental resolution allowing to probe matter at an ever finer scale. Of particular relevance for the field of nuclear physics were the discoveries that closely followed. After negatively charged cathodic rays, Thomson turned his attention to the "rays of positive electricity". The construction of a new mass spectrograph [Tho07] in 1907 led to the first breakthrough in the field of mass spectrometry with the first direct observation of the isotopes 20 and 22 of neon [Tho12].

The confirmation of the "whole-number" rule whereby all masses are whole numbers was later established by W.F. Aston [Ast19a]. This rule was verified down to the 10^{-3} level which is the precision reached at the time by Aston's mass spectrograph [Ast19b]. Only hydrogen did not respect this rule (with a mass of 1.008) [Ast20]. This result had remarkable implications, since with the realization that the mass of helium is less than the mass of four hydrogen atoms also came an explanation for the source of the sun's energy by Eddington [Edd20]. Aston's second spectrograph reached an accuracy of 1 in 10 000 which "was just enough" to firmly established that the mass of an atom is less than the mass of its constituents [Ast27]. This so-called "mass defect" was immediately identified as being related to the energy of the force binding the atom together according to Einstein's famous relation $E = mc^2$.

Some of the early fundamental concepts of nuclear physics found empirical groundings in the work of Aston who, after studying over 200 nuclides, observed the near consistency of the binding energy per nucleon at about 8 MeV. The apparent saturable nature of nuclear forces lead to the development of the early liquid-drop model of the nucleus as proposed by Gamow [Gam30], Bethe [B+36] and Weizsäcker [Wei35]. Each decade that followed was accompanied with a 10-fold increase in resolving power [Bla06]. In the mid-twentieth century the record of measured atomic masses was key in the establishment of the cornerstone of our understanding of nuclear structure : the independent particle model by Mayer, Haxel, Jensen and Suess [May49, H+49]. Indeed, the in-depth study of the binding

energy trends and their departure from that predicted by the liquid-drop model was key to the identification of such remarkable features as the enhanced stability observed for certain "magic" numbers of neutrons and protons (i.e 2, 8, 20, 28, 50, 82, 126). Mass spectrometry results did not only participate in the establishment of the independent-particle picture of the nucleus. They also significantly contributed to its demise 25 years later when high-accuracy mass measurements performed by Thibault and collaborators [T⁺75] (along with other experimental evidence) suggested that the magic shell structure can be weakened or even broken [S⁺08].

The remarkable impact of the field of mass spectrometry in nuclear physics must not overshadow the ingenious technical developments that always allowed it. The never-ending quest for higher resolving power and accuracy seemed to have culminated three decades ago with the introduction of Penning traps in the field of mass spectrometry [G⁺80]. The measurement of masses of radio-nuclides continues at modern radioactive-ion-beam facilities around the world, where new mass-measurement techniques continue to push the boundaries of what is currently achievable in terms of relative precision and accuracy [E⁺14]. The practical challenges inherent to working with radioactive species (short half-lives, low production yield, high level of contamination) find innovative technical solutions with the development of purification tools, the working principles of which are inherited from mass spectrometry (i.e separation according to the quantity m/q). The recently introduced, Multi-Reflection Time-of-Flight mass separator (MRToF-MS, see details in Chapter 2) is a perfect example of such a device [W⁺12b].

The advancement of Penning traps as the tool of choice in the field also opened it to a wider range of addressable fundamental questions such as the search for candidates for neutrinoless double- β decay or the study of the weak interactions by the high-precision determination of the Q -value of the transitions in question [Bla06]. For such studies, Q -values have to be determined with a relative precision of 10^{-4} or equivalently 10^{-10} relative precision on the individual masses involved. No other technique can currently provide this. Remarkably, combining what the field of nuclear physics has best to offer in terms of precision and accuracy has put the most stringent constraints on the unitary nature of the Cabibbo-Kobayashi-Maskawa quark-mixing matrix [H⁺15a]. Nearly a century after Eddington, the field of astrophysics also continues to greatly benefit from the growing wealth of highly accurate mass values. Such an open fundamental question as the origin of the element heavier than iron has found the beginning of an answer with the dawning of the multi-messenger era in astrophysics [A⁺17b, A⁺17a] and the first direct identification of neutron-star mergers as r-process sites [K⁺17]. Mass measurements performed at the extreme of the nuclear landscape provide direct inputs for the nuclear-astrophysical models used to predict element abundances as well as the electromagnetic signatures of the diverse astrophysical processes thought to play a role in nucleosynthesis.

1.2 The nuclear binding energy and shell structure

As we saw, the wide interest for nuclear masses (and by extension atomic masses) lies in the fact that the mass $M(N, Z)$ of a nucleus with N neutrons and Z protons is less than the sum of its individual constituents. This "mass defect" $\delta_m(N, Z)$ is nothing but the binding energy of the system :

$$M(N, Z) = Nm_n + Zm_p - \delta_m(N, Z) = Nm_n + Zm_p + E(N, Z)/c^2, \quad (1.1)$$

where $m_{n,p}$ are the mass of neutron and proton respectively, c is the velocity of light and $E(N, Z)$ represents the binding energy of a nucleus with N neutrons and Z protons (taken as negative if the system is bound).

The most recent Atomic Mass Evaluation lists 2497 experimentally known ground-state masses [W⁺17a]. The experimental mass information is not given in terms of the atomic mass or even the binding energy but rather in an "ad-hoc" quantity, the so-called atomic mass excess, which allows presenting only the relevant part of the mass information with the least number of digits possible. The mass excess $ME(N, Z)$ is expressed as :

$$ME(N, Z) = M_{at}(N, Z) - (N + Z)u, \quad (1.2)$$

where $M_{at}(N, Z)$ is the atomic mass of the species under consideration and u is unified atomic mass unit, defined as $1/12^{th}$ of the atomic mass of ^{12}C .

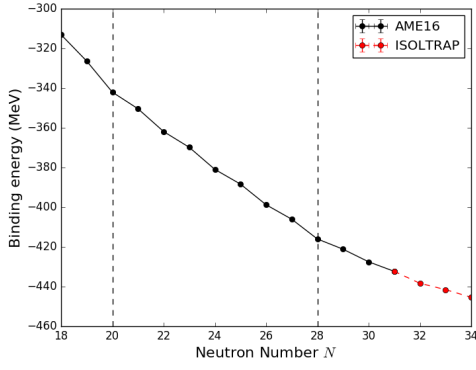
The nuclear binding energy represents the sum of all the interactions acting between all the constituents of the nucleus. As a result, it is a large quantity (e.g ~ 1.6 GeV for ^{208}Pb) when compared to the typical energy scale of nuclear processes (\sim few MeV). Hence, it is difficult to relate the variation of $E(N, Z)$ along an isotopic or isotonic line to a change in the underlying nuclear structure. In order to reveal the structural effects of interest, one typically investigates the variation with N or Z of empirical quantities defined as finite differences of the binding energy. Since the results of applying various finite-difference operators to the binding energy can be more or less sensitive to certain structural effects, these quantities are called mass filters. A comprehensive discussion regarding various mass filters is detailed in Chapter 1 of [Vla16] and will not be repeated here. In the following, we rather illustrate three important mass filters which will be used later in this work. We shall give their definition as a function of the binding energy and atomic mass excess and discuss their trends along the calcium isotopic chain (see Figure 1.1). The following discussion will pertain to the trend of mass filters along isotopic lines, since it is the most relevant for this work. However, all the relations and discussion can be translated to isotonic lines provided the correct substitutions are made.

Figure 1.1a shows the evolution of $E(N, Z)$ along the calcium isotopic chain ($Z = 20$). The choice of the calcium chain is not random as it not only has a so-called "magic" number of protons; i.e a number for which an enhanced binding is observed (similar to the noble gases of chemistry), but also this isotope crosses a line of enhanced neutron stability in two occasions : at $N = 20$ and 28 . As seen from Figure 1.1a the change of slope usually associated with the crossing of such a magic-number of neutrons is barely visible from the trend of the binding energy itself. In addition, one sees an oscillation of the binding-energy trend with even and odd N with the even-even nuclei appearing more bound than the average of their odd-even neighbors. This effect, the so-called "odd-even" staggering of binding energies, is a direct consequence of the nuclear pairing phenomenon. The simplest mass filter clearly revealing the presence of an enhanced binding at $N = 20$ and 28 is the one-neutron separation energy S_n defined as :

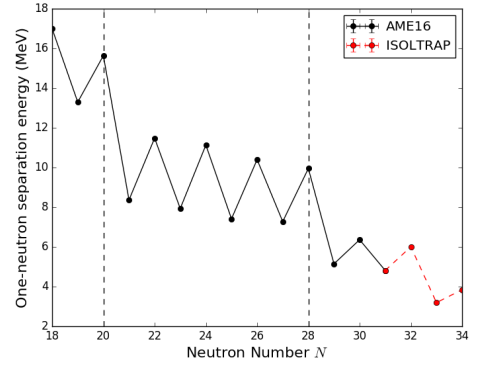
$$\begin{aligned} S_n(N, Z) &= E(Z, N-1) - E(Z, N) \\ &= [ME(N-1, Z) - ME(N, Z) + ME_n] c^2, \end{aligned} \quad (1.3)$$

where ME_n is the neutron mass excess.

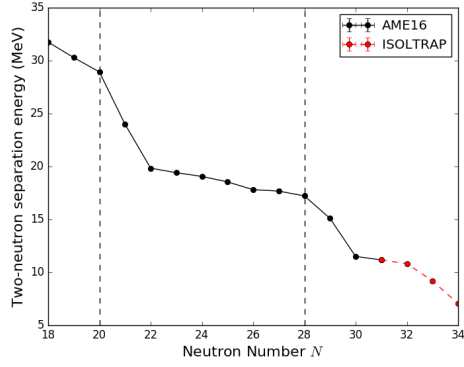
The one-neutron separation energy is nothing but the Q -value of the reaction consisting of removing one neutron from a nucleus with N neutrons and Z protons.



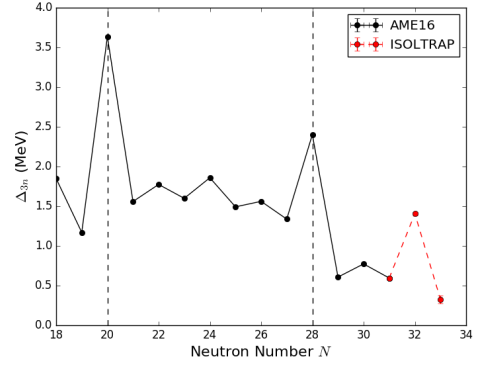
(a) Binding energy.



(b) One-neutron separation energy.



(c) Two-neutron separation energy.



(d) Empirical pairing gap.

Figure 1.1: Various mass filters for the calcium ($Z = 20$) isotopic chain as a function of the neutron number N . The error bars are smaller than the size of the point.

With this in mind, it is easy to understand the two most prominent features of the one-neutron separation energy trend namely, the odd-even staggering and the sharp one-step drops obtained at the magic-numbers $N = 20$ and 28 . Due to nucleon-nucleon pairing effects, an even-even nucleus is on average more bound than the average of its odd-even neighbors. Hence, for even-even nuclei additional energy is required in order to break the nucleon-nucleon pair thus explaining the staggering of S_n . Similar to the noble gases, magic nuclei correspond to closed proton or neutron shells with a large shell gap to the next single particle level [May49, H⁺49]. Hence, it costs significantly less energy to remove a sole neutron outside of a closed shell core than it does to remove one neutron from the closed shell nucleus. This explains the sharp drops observed at $N = 20$ and 28 . The very sharp drop obtained at $N = 20$ is also revealing of the extra binding observed for nuclei with $N \approx Z$, the so-called Wigner effect [Wig37].

The problem of the S_n mass filter is the fact that it reveals both the signatures of shell closures and the odd-even mass staggering. A way to filter out contributions from the odd-even staggering is to use binding differences from nuclei separated by two neutrons. The associated quantity, the two-neutron separation energy is represented on Figure 1.1c for the calcium isotopic chain and is defined as :

$$\begin{aligned} S_{2n}(N, Z) &= E(Z, N-2) - E(Z, N) \\ &= [ME(N-2, Z) - ME(N, Z) + 2ME_n] c^2. \end{aligned} \quad (1.4)$$

The two-neutron separation has similar interpretation as S_n , it represents the energy required to remove two neutrons from the nucleus. From Figure 1.1c, it appears that the contributions from the "odd-even" staggering are greatly reduced while the magic neutron numbers are indicated by two-step drops. The two-step decrease after the crossing of a magic number is understood in a similar fashion as the one-step decrease of S_n . In between magic numbers the two-neutron separation energy follows a steady decrease with increasing N .

The last mass filter we will be addressing is one that aims at isolating contributions from the odd-even staggering of the binding energy. This mass filter is the so-called three-point estimator of the odd-even staggering defined as :

$$\begin{aligned} \Delta_{3n}(N, Z) &= \frac{-1^N}{2} [S_n(N, Z) - S_n(N+1, Z)], \\ &= \frac{-1^N}{2} [E(Z, N+1) - 2E(Z, N) + E(Z, N-1)], \\ &= \frac{-1^N}{2} [ME(Z, N+1) - 2ME(Z, N) + ME(Z, N-1)] c^2. \end{aligned} \quad (1.5)$$

This mass filter corresponds to the absolute value of the magnitude of the drop in S_n between N and $N+1$. One sees in Figure 1.1d that the odd-even staggering is greatly enhanced at the crossing of a magic number. This mass filter is also called the pairing gap and is often used to empirically adjust the strength of the pairing interaction used in the self-consistent HFB calculations (see Chapter 4) [RS80].

The measured mass excesses are used to compute various mass filters. The observed trends of the calculated mass filters are plotted along an isotopic or isotonic line and their systematics are examined and interpreted in terms of the underlying structural changes observed. An illustrative example is given here using the mass values of $^{53-54}\text{Ca}$ (red points of Figure 1.1) which are determined by a measurement performed at ISOLTRAP [W⁺13a]. Examining the trends of mass

filters which have been addressed, all three mass filters point to the existence of an exotic shell closure at $N=32$ in the calcium isotopic chain. Typically, the same mass filters are computed from the binding energies obtained using various models and then compared to the experimental trends [W⁺13a].

Within the independent particle model of Mayer, Haxel, Jensen and Suess [May49, H⁺49], the nuclear "magic" numbers are understood in terms of large gaps arising within the single-particle spectrum of a spherical nuclear mean-field. The advancement of modern radioactive ion beam facilities such as ISOLDE at CERN revealed that far from being immutable, the spherical gaps can erode or even collapse far away from the valley of stability. Interestingly enough, one of the early pieces of evidence for the existence of this phenomenon was revealed in the 1970s from mass measurements performed by a team from CSNSM-Orsay [T⁺75]. The extra binding observed for ^{31}Na and ^{32}Mg was understood in terms of deformed configurations associated with n -particle/ n -hole excitations across a weakened $N = 20$ spherical shell gap.

Normally, the cost of promoting n nucleons across a spherical shell gap, which is n times the shell gap, should yield a configuration at high energy. However, the n -particle/ n -hole configuration can be associated with a huge gain in correlation energy which effectively brings its energy down. The effect of correlations can be such that the high lying, so-called "intruder" configuration, can even become the ground-state of the system. The example of the $N = 20$ shell closure is far from being isolated as most of the regular shell closures have been proven to erode far from stability [S⁺08]. Nuclides having such an inverted configuration are now said to belong to an Island of Inversion (IoI). Similar to how the spherical magic numbers only emerged with the addition of the correct prescription for the form of the nuclear mean-field (addition of a spin-orbit term) the disappearance of the same shell gaps is very sensitive to the details of the nuclear interaction.

On the one hand, the reduction of the spherical shell gaps is a pre-requisite for the existence of such regions since it reduces the energy cost for creating particle-hole excitations across the closed shell. Such variations are dictated by the evolution of the monopole part of the two-body nuclear interaction [S⁺10b, C⁺05], which is itself under the influence of various components of the nuclear interaction. Among these components, the proton-neutron tensor interaction is thought to play a particularly significant role [O⁺01, O⁺05]. However, as demonstrated by [C⁺14b], if the reduction of the spherical shell gap is a necessary condition for the emergence of intruder configurations it is not sufficient. Strong proton-neutron correlations are indeed necessary to the effective lowering of the intruder configuration [H⁺11].

More than four decades after its discovery, the $N=20$ IoI continues to attract significant experimental and theoretical attention. But more importantly, this region is far from being isolated and such regions of enhanced nuclear collectivity have been observed for most magic numbers [S⁺08]. Of particular relevance for the present work is the question of the erosion of $N=28$ shell and $N=40$ sub-shell closures. As evidenced by recent in-beam γ ray spectroscopy measurements [D⁺13] the $N = 20$ IoI seems to further extend towards $N=28$. The merging of these two IoIs has been studied theoretically [C⁺14b]. Similarly, the region of enhanced collectivity seems to persist in the iron and chromium chains past $N=40$ [S⁺15]. The merging of the $N=40$ region of deformation with a fifth IoI in the vicinity of ^{78}Ni has even been proposed in [N⁺16, W⁺17b].

1.3 This thesis

In light of what has been discussed in the previous section, this thesis addresses the question of the development of nuclear collectivity in the neutron-rich argon and chromium isotopic chains by complementing the set of available nuclear observable with high-precision mass measurements of the neutron-rich $^{46-48}\text{Ar}$ and $^{58-63}\text{Cr}$. The measurements were performed using the on-line mass spectrometer ISOLTRAP [M⁺08, K⁺13] located at the ISOLDE facility at CERN.

This thesis is organised as follows. First, experimental techniques related to the production of the radioactive ion beams of interest are discussed. The generic concepts pertaining to Penning-trap and Multi-reflection Time-of-Flight (MRToF) mass spectrometry are then presented. For each dataset, the content and the details of the corresponding mass-measurement campaigns are described.

Secondly, following the analysis procedure, various sources of systematic errors are presented for the Penning-trap mass data evaluation. Because using the MRToF for mass measurements is still in its infancy, special care is taken to present the details of the MRToF data evaluation procedure developed in the course of this thesis. The different sources considered in the systematic error estimation are also presented. A summary of the yielded atomic mass excesses is presented and the comparison between the new mass values and previous results is given.

Before discussing the physics impact of the newly measured masses, concepts pertaining to nuclear structure theory are presented in the fourth chapter. Special focus is made on the interacting shell model and self-consistent mean-field theories. Emphasis is also given to the fast-developing approach of the Valence-Space formulation of the *ab-initio* In-Medium Similarity Renormalisation Group (VS-IMSRG). For the purpose of this work, shell-model calculations for the argon isotopic chain and self-consistent mean-field calculations were performed. Details of the calculation procedure are presented.

Finally, the binding-energy trends extracted from the newly measured masses are discussed. While new insights into the development of ground-state collectivity in the chromium isotopic chain are provided, the confirmation of the presence of a strong $N = 28$ shell closure in the argon chain is presented. For both chains, a comparison between theoretically predicted binding energy trends and the newly obtained trends is presented. The data are compared to the predictions from large-scale shell-model calculations as well state-of-the-art VS-IMSRG. For the chromium chain, the development of ground-state axial deformation is studied within the framework of the self-consistent mean-field calculations.

The work presented in this thesis regarding the chromium isotopic chain already resulted in a peer-reviewed publication, presented in Appendix B [M⁺18b]. A peer-reviewed publication describing the result obtained for the argon chain is currently in preparation as is a publication describing the use of the MRToF as a mass spectrometer. During the course of this thesis, a measurement proposal regarding the high-precision measurement of the ^{18}Ne - ^{18}F superallowed β -decay Q -value was presented in front to the INTC-committee. The text of this proposal is also presented, in Appendix C.

Experimental methods and measurements

2.1 Radioactive ion beam production

The modern approach of experimental nuclear physics has been to track the evolution of nuclear observables (charge radii, electromagnetic moments, nuclear binding energies, electromagnetic transition probabilities...) in nuclear systems farther away from the valley of β -stability. Thus, one needs efficient and reliable ways to produce radioactive ion beams (RIBs) and make them available for experiments. It comes as no surprise that venturing in yet uncharted regions of the chart of nuclides comes with challenges. For instance, dramatic drops in the production cross sections and ever decreasing half-lives. Hence, the radioactive species of interest are produced in only minute quantities while at the same time considerably more unwanted species are being produced. This sets constraints on the production process which should combine *high production rate* (higher primary beam intensities) and *efficiency* (extraction, ionization, transport) while at the same time must also be reasonably *fast* (to avoid decay losses) and selective (to reduce the amount of unwanted species) [B⁺13]. Two radioactive beam production schemes combine all the properties listed in the above, namely the Isotope Separation On Line (ISOL) technique and the so-called In-Flight production mechanism.

In the in-flight RIBs production method, an accelerator (e.g. synchrotron, coupled cyclotrons or a linear accelerator) is used to accelerate a primary heavy-ion beam (e.g. ^{238}U) to energies ranging from a few MeV/u up to ~ 1 GeV/u. This primary beam impinges on a relatively thin production target. A substantial part of the reaction products (fusion-evaporation residues at intermediate energies, fragmentation, spallation at higher energy or even fission fragments) is collected through the optics of a multi-stage dipole $B\rho$ -mass separator allowing for a selection of the reaction products according to their charge to mass ratio. An additional Z -selectivity can be achieved introducing an energy degrader at one of the intermediate focal planes. While primary-beam intensities of up to several pμA are already available at facilities such as GANIL (France), GSI (Germany) or LEGNARO (Italy) or RIKEN (Japan), forthcoming facilities such as FRIB (Michigan/USA) or FAIR (Germany) promise the possible production of even the more rare isotopes. The short transition time through the thin target as well as the fast mass separation time (typically of a few μs) offered by the in-flight production method is such that decay losses are typically negligible and the secondary beam intensity in the focal plane of the mass separator is mostly limited by the transport efficiency through the optics of the separation line. Indeed, the optical

quality of the secondary beam is entirely defined by the kinematics of the production reaction and as such is somewhat limited. Thus, the fragment separators have to be designed to allow for a large angular and momentum acceptance. On the up-side, the in-flight RIBs production method is completely independent of the chemical nature of the species of interest [B⁺13]. This property sets apart the in-flight method from the ISOL technique and explains the current high interest in the development of so-called low energy branches in most forthcoming in-flight facilities as well as existing facilities around the world [F⁺13, S⁺14a, R⁺13a].

The radioactive isotopes studied in this work were produced at the radioactive ion beam facility ISOLDE located at the beginning of the CERN accelerator complex [C⁺17]. There, the radioactive species are produced using the Isotope Separation Online (ISOL) technique. This method of production consists of bombarding a thick target by a primary beam of protons. In the present case the latter were provided by CERN's Proton-Synchrotron Booster (PSB) at an energy of 1.4 GeV and a typical average current of 2 μ A. This proton beam interacts with the target material producing radioactive species through spallation, fragmentation and fission reactions. The target material is tailored so as to optimize the beam intensity and purity [Got16]. For instance, fission reactions are very effective to produce middle-mass neutron-rich nuclei. As Figure 2.1 shows, a Uranium carbide (UC_x) target, the typical thickness of which is 50 g/cm² [U. 02], is very well suited to produce intense beams in such regions of the Segré chart. Hence, the argon and chromium isotopes measured in this work (marked as red squares in Figure 2.1) were produced from this target material. When the success of an experiment relies heavily on the beam purity, the primary proton beam can be used to produce secondary neutrons (in the MeV energy range) through spallation reactions induced in a tungsten rod placed parallel to the target material. The use of these neutrons favors low-energy fission over the spallation-fission reactions which at higher energy are responsible for the production of a neutron-deficient background [L⁺12].

The reaction products are neutralised and stopped in the bulk of the target material. Hence, one has to rely on thermal diffusion in order to extract them. To this end, the target unit is heated to a typical temperature of about 2000°C. A transfer line is installed at the back of the target container. This line is heated to a temperature close to that of the target and is used to allow for the radioactive atoms extracted from the target to effuse into a region where they will be ionised. Hence, the choice of target material is not the only parameter which influences the final intensity of the desired RIBs. Indeed, the diffusion and effusion processes that take place within the target and ion source assembly can be relatively slow when compared to the half life of the species of interest. Contrary to in-flight, these two processes are highly dependant on the chemical nature of the element one tries to extract. The chromium isotopes measured in this work are one such example of a beam usually reserved to in-flight facilities due their refractory nature. Indeed, since chromium has a high melting point (on the order of \sim 1900°C) the diffusion process through the target material is greatly hindered.

Another point to take into account to optimise the production of RIB at an ISOL facility is the efficiency of the ionisation process. Three ionisation methods are routinely available at the ISOLDE facility. Upon desorption from a hot (\sim 2000°C) metallic surface the work function of which is high, e.g tungsten or tantalum, an atom with low ionisation potential, e.g alkali metals, has a high probability to lose one of its valence electrons to the surface. This is the so-called surface ion-

isation method. The temperature of the hot surface is critical to increase the ionisation efficiency. In practice, at ISOLDE, surface ionisation is performed by connecting a hot tantalum cavity at the back of the transfer line. Some degree of element selectivity can be achieved optimising the temperature of the cavity but the latter is usually rather poor. Nonetheless, an advantage of this method is that it exclusively produces singly charged ions.

A method which combines both charge state and element selectivity is the resonance ionisation laser ion source (RILIS) [F⁺17]. First, a valence electron is resonantly excited to a high-lying energy level. This is achieved using laser beams the frequencies of which are carefully selected to bring an electron into the desired level. In practice, one or two subsequent steps are required. Finally, the excited electron can be brought to the continuum through non-resonant photo ionization. Because the level structure of an atom is unique to each element, the RILIS method is highly element selective. In practice the laser pulses are overlapped with the flux of neutral atom effusing out of the transfer line into a hot cavity. The element specific ionisation enhancement brought by the use of the ISOLDE RILIS can be key for the success of an experiment. Hence, in our experiment focusing on neutron-rich chromium isotopes, the purposely developed chromium RILIS scheme [D⁺17] brought an enhancement in excess of 2000 over the surface ionised current thus effectively compensating for the loss in efficiency due to the long diffusion time from the target material.

Elements having high ionisation potential (e.g noble gases) can be ionised at ISOLDE using plasma ion sources. ISOLDE plasma ion sources are of the Forced Electron Beam Ion Arc Discharge (FEBIAD) type [K⁺76]. Electrons are emitted by a cathode which is typically heated to 2000°C. A cylinder forming the anode is held at a potential (~ 100 -150 V) higher than that of the cathode. The presence of a grid directly facing the cathode accelerates the electrons from the cathode into

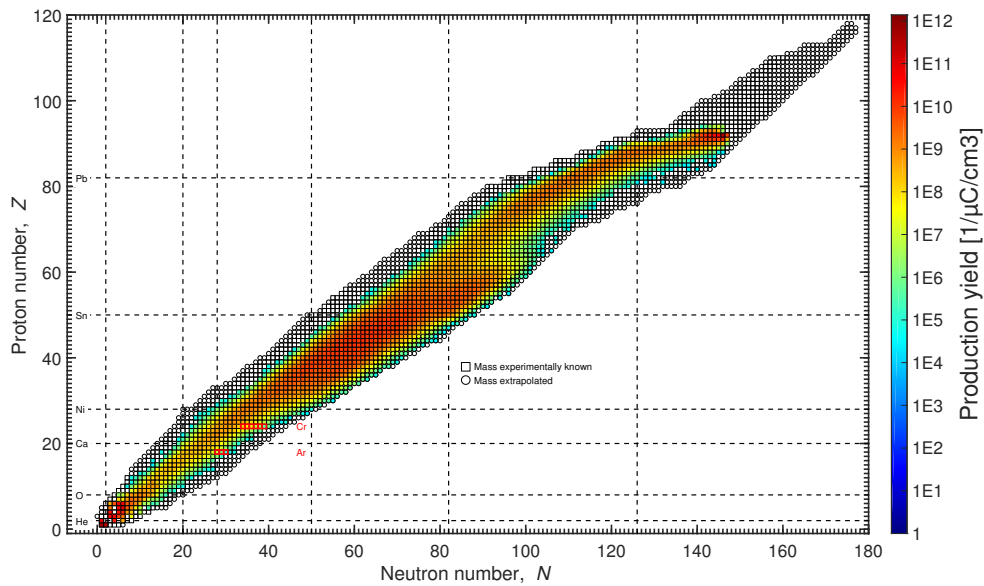


Figure 2.1: Simulated production yield of a typical ISOLDE uranium carbide target. The argon and chromium isotopes measured in this work are highlighted with red squares. *Credit: Frank Wienholtz*

the anode cavity. The flux of the neutral atoms entering the cavity is thus ionised by the arc discharge created by the accelerated electrons. The ions are extracted at the other end of the anode cavity through an aperture as small as 1.5 mm. ISOLDE uses its own variant of the FEBIAD ion source. These so called VADIS (Versatile Arc Discharge Ion Sources) ion sources differ from the standard FEBIAD by an increase of the source's active volume as well as a reduction of graphite from the source materials [P⁺10]. Plasma sources offer high beam current but the ionisation mechanism is in essence element non-selective. Nonetheless, using a water cooled transfer line can help reducing part of the contamination arising from the less volatile of species. This model of VADIS ion source (VD7) is especially useful for the study of exotic noble gases. A typical ISOLDE target/plasma source assembly is depicted in Figure 2.2.

Irrespective of the ionisation method, the target and ion source module is floated to a potential which ranges between 30 to 50 kV. As the ISOLDE beam line is on ground potential, the ions extracted from the ion source are thus accelerated to a kinetic energy equivalent to that of the source floating voltage. Before being guided to an experimental station through several meters of beam line, the radioactive ion beam is sent to one of two dipole magnetic mass separators available at the ISOLDE facility namely the General Purpose Separator (GPS) and the High Resolution Separator (HRS). The nominal resolving power ($\frac{m}{\Delta m}$) of GPS and HRS is on the order of 800 and 6000 respectively [C⁺17].

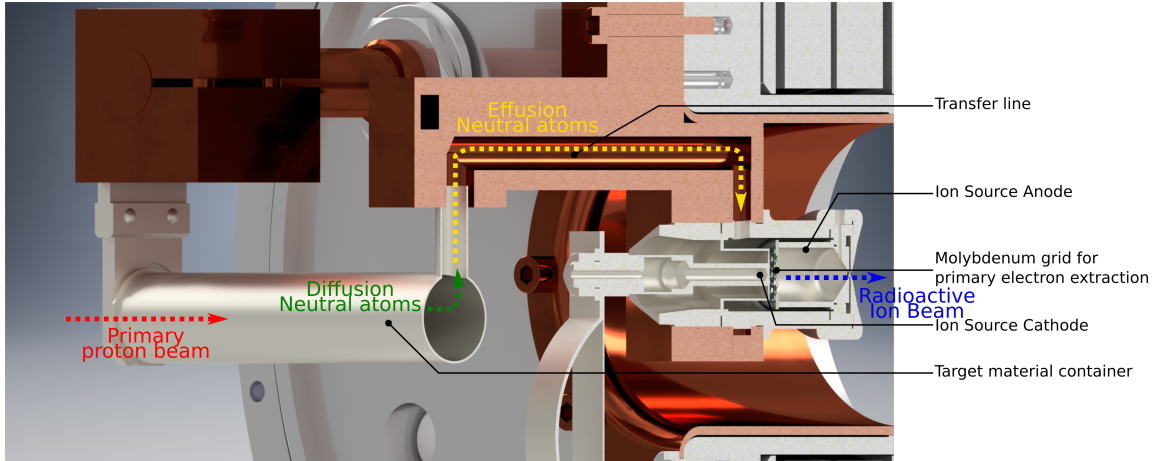


Figure 2.2: 3D view of an ISOLDE target and ion source assembly. The depicted ion source is similar to a VD7 VADIS plasma ion source (see [K⁺76, P⁺10]). The primary 1.4 GeV proton beam induces nuclear reaction in the material contained in the tantalum container (red arrow). The neutral radioactive atoms thus created diffuse out of the target material (green arrow). The latter effuse through the transfer line into the ionisation region (yellow arrow). Finally, the species are ionised and extracted as an ion beam (blue arrow). In the present case, the primary electrons produced by heating the cathode are accelerated through the potential difference created between the anode grid and the cathode. Electron impact ionisation inside the anode volume simply follows.

2.2 Experimental cycle

Before reviewing the principle of operation of the different ion traps which make the current ISOLTRAP mass spectrometer we shall give a brief overview of a

typical experimental cycle. A schematic representation of ISOLTRAP as it stands today is represented on Figure 2.3.

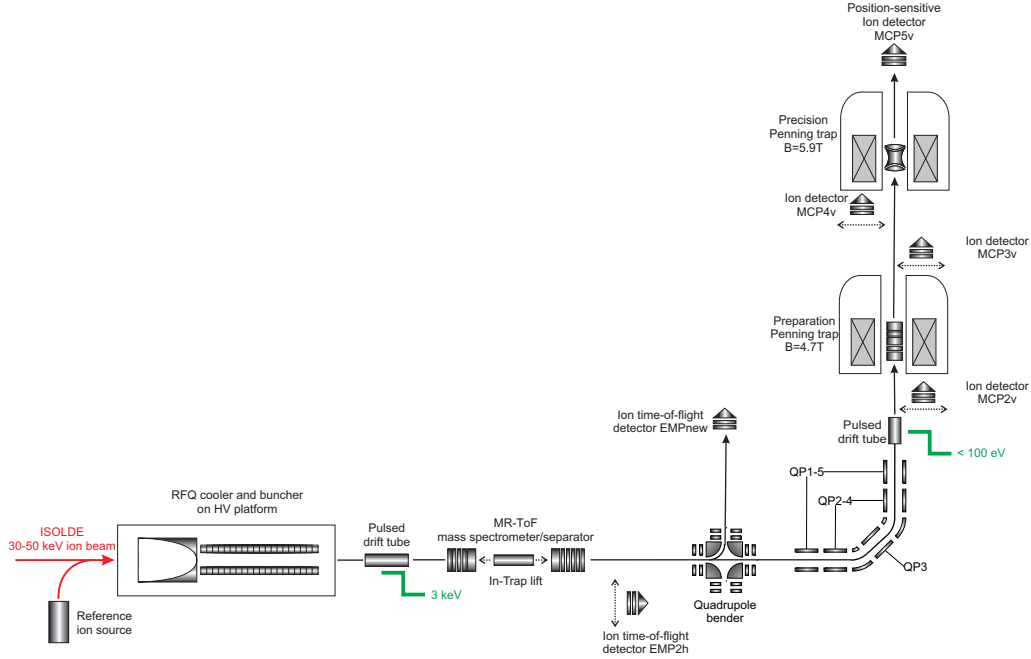


Figure 2.3: Schematic representation of the ISOLTRAP mass spectrometer as it stands today.

The starting signal of an ISOLTRAP cycle is provided by a trigger corresponding to the proton impact on the ISOLDE target. Upon receiving the start trigger, the ISOLDE beam gate is opened for a time T_{bg} . When approaching ISOLTRAP the ISOLDE beam is decelerated and focused through the 6 mm injection aperture of ISOLTRAP Radio Frequency Quadrupole Cooler Buncher (RFQ CB) by an egg-shaped electrode [M⁺08, H⁺01]. The beam is accumulated at the bottom of the RFQ CB's axial potential for as long as the beam gate is opened. After the closing of the beam gate, the ion beam is kept inside the buncher for an additional time $T_{cooling} \sim 10\text{-}20\text{ms}$ to ensure that all ions are properly cooled. To reduce the incoming beam energy to a few eV, the whole buncher trap is sitting on an HV platform. Hence, the ion bunch formed in the axial potential well is re-accelerated to a kinetic energy close to that of the incoming ISOLDE beam upon ejection from the RFQ. A drift tube is placed 90 mm downstream of the RFQ CB. This cavity is placed on a voltage such that $E_{kin} - E_{cavity} = E_{transfer} \approx 3.2\text{ keV}$. When the ion beam is at center of the cavity, the latter is switched to ground potential thus reducing the beam energy to $E_{transfer}$ through ISOLTRAP's horizontal transfer section.

The $\sim 3\text{ keV}$ beam is then captured by ISOLTRAP's MRToF mass separator as explained in section 2.3.3. The typical MRToF-MS trapping time is on the order of 20 ms. If a mass measurement is performed using the MRToF-MS the experimental cycle ends with the ion's detection after the device. If the MRToF-MS is used as a mass separator, the purified ion beam is ejected from the MRToF and it undergoes a 90-degree bend before entering the vertical section of ISOLTRAP where both Penning traps are located. For the ions to be trapped in ISOLTRAP's preparation Penning trap, the energy of the ions must be reduced once more since the lower endcaps of the trap are set to a trapping voltage of 100 V (which is lowered for injection). Hence, a second decelerating drift tube is used to reduce the ions kinetic

energy to below 100 eV. The actual cooling sequence inside the Preparation trap is decomposed into several steps. First, the ions are left to interact with the buffer gas environment for a time $T_{axial} \sim 100$ ms in order to damp their axial motion. In order to start the mass selective recentering in the same fashion for all ion species present in the bunch, a broad band quadrupole RF pulse is applied. This pulse is applied at the cyclotron frequency of the ion of interest but with very high RF amplitude (~ 5 V) which results in the effective recentering of all the ion species present in the bunch at once. A dipole excitation at the preparation trap's magnetron frequency is then applied for a duration corresponding to 3 magnetron periods. The amplitude of this excitation is chosen such that the whole ion cloud is brought on a magnetron radius which is bigger than the aperture of the trap endcaps. The mass selective quadrupole excitation is then applied for a time of ~ 100 ms to recenter the ions of interest while leaving the rest of the ion cloud on a large magnetron radius. Before ejection, the ions are kept for an extra ~ 50 ms in order to ensure the proper damping of ion's motion. All in all, this cycle takes a few 100 ms which is one order of magnitude more than the MRToF processing time to reach similar resolving powers. The times given here are indicative and correspond to cases where the ion's half-life is not a limitation. For short-lived species with half-lives of ~ 100 ms, the whole cycle time is reduced, one consequence being a sacrifice in terms of resolving power. After cooling, the ions are ejected from the trap and are transported towards the hyperbolic measurement Penning trap (confining B-field of 5.9 T).

The capture of the ion in the measurement trap is timed to minimize the initial amplitude of the axial motion. The ring electrodes of both traps are also set to the same voltage to the same end. The measurement of the ions free-cyclotron frequency follows according to the method described in 2.3.2. The cycle ends with the detection of the individual ion events using an MCP placed downstream from the Penning trap in a region of low magnetic field and a new cycle starts. This cycle is repeated until sufficient statistics is collected in the MRToF-MS spectra or the Time-of-Flight Ion-Cyclotron Resonances (ToF-ICR).

The transport settings through ISOLTRAP as well as the working parameters of all four ion traps need to be optimised before and during any experiment with ISOLDE beam. Hence, an offline ion source is attached to the ISOLTRAP setup upstream of the RFQ CB (see Figure 2.3). This surface ion source produces singly charged alkali ions of ^{39}K , $^{85,87}\text{Rb}$ and ^{133}Cs from a pellet heated to $\sim 1000^\circ\text{C}$. The advantage of this source lays in its reliability to produce stable and low ion currents (50 pA - 1 nA). This source also provide the reference ions necessary for the B-field calibration using the ToF-ICR technique. The poor mass range coverage that it offers is a significant limitation. Indeed, as we will discuss in the next chapter it is advisable to use reference ions as close as possible to the ion of interest to minimize the mass dependent systematic effects. Because of the presence of residual magnetic fields the beam transport at ISOLTRAP is strongly mass dependent (this is especially true between the two Penning traps). Hence, the reduced mass range offered by the source also comes as a limitation since tuning the transport towards the final MCP of ions with a large mass difference to the ion of interest usually results in a dramatically low transport efficiency (typically less than 1 % to the measurement Penning trap).

2.3 Charged-particle traps

Charged particle traps are devices which allow for the confinement of sub-atomic particles, atomic or molecular ions within a given volume using static or time varying electromagnetic fields. Since the seminal work (for which they received the Nobel Prize in Physics in 1989) from Wolfgang Paul [Pau90] and Hans Dehmelt [Deh90] the use of ion traps has spread to a wide range of physics application from mass spectrometry to the study of antimatter, from high precision spectroscopy experiments to quantum computing [WGM09]. More specifically, in the field of low-energy nuclear physics ion traps are now routinely used as preparation devices [Bla06]. Trap-based accumulation, bunching, cooling and charge breeding techniques were developed allowing for secondary beams with increased density, well defined time structure, reduced transversal emittance and higher charge states. The motion of ions in a charged-particle traps depends very strongly on its mass-to-charge ratio m/q . Hence, ion traps m/q constitute very adequate beam purifier allowing to separate a beam in its different m/q constituents [Bla06, R⁺16a].

This characteristic also allows ion traps to be used as a high performance mass spectrometer [Bla06]. Since its invention [D⁺68] in the mid-60s, one confinement mechanism has reached unprecedented success in the field of precision measurements for fundamental studies, namely the Penning trap. In a Penning trap, the confinement of charged particles is achieved through the combined effect of a weak static quadrupolar electric potential (axial confinement) and a strong homogeneous magnetic field applied along the trap axis (radial confinement). The field of mass spectrometry also benefited greatly from the advances of the Penning trap since it's introduction in the field and the very first sub-ppm measurement of the proton-electron mass ratio by Gäff *et al.* in 1980 [G⁺80]. A few years later, the mass spectrometer ISOLTRAP at ISOLDE/CERN pioneered the application of Penning trap mass spectrometry to the measurements of short-lived radioactive species with the first mass measurements being performed in the sub-ppm range [B⁺87]. Over the last 30 years, several ion beam preparation and purification techniques were first developed for ISOLTRAP [S⁺91, H⁺01, W⁺12b] before sprawling to other facilities around the world.

A comprehensive treatment of the diverse confinement mechanism of a charged particle can be found in [M⁺05] and is beyond the scope of this thesis. We will present in this section the concepts pertaining to ion trap mass spectrometry and will focus on the aspects most relevant for the online mass spectrometer ISOLTRAP.

2.3.1 The Penning trap

As already mentioned, the confinement of a charged particle in an ideal Penning trap is achieved through the combined action of a strong axial magnetic field and a weak static electric field. The spatial dependence of the electric trapping potential is chosen so as to produce a confining force proportional to the particle's distance to the trap center. In other words, one uses an axially symmetric quadrupole potential which takes the form : $V(z, \rho) = \frac{V_0}{4d^2}(\rho^2 - 2z^2)$. In order to produce such a potential in practice, a potential difference V_0 is applied to a set of three axially hyperboloidal electrodes (one ring electrode and two end caps) which are placed along the equipotential lines of the desired potential distribution. In the (z, ρ) plane, the minimal distance between the trap center and the electrodes are

denoted z_0 and ρ_0 respectively and are such that : $2d^2 = z_0^2 + \rho_0^2/2$, where d is the characteristic trap dimension. In the case of ISOLTRAP's hyperbolic Penning trap, a representation of which is shown in Figure 2.4a, one has $z_0=11.18$ mm and $\rho_0=13$ mm [M⁺08] while the potential depth ϕ_0 is on the order of 8.4 eV. An idealized view of electric potential distribution inside ISOLTRAP's Penning trap is shown on Figure 2.4b. The trap electrodes are represented by black dashed lines and the idealized field lines are depicted by arrows the width of which is proportional to the intensity of the field. As one can readily see from the field line distribution, such a potential allows for the axial confinement of the charged particles but the ions remain radially unbound.

To overcome this radial defocussing, a strong magnetic field is applied along the symmetry axis of the trap electrodes. In the case of ISOLTRAP the magnetic field strength is close to 6 T and is produced by a super conducting magnet. If only the magnetic field was acting upon the charged particle of charge-to-mass ratio q/m , the latter would orbit about the magnetic field lines at the precession frequency (the so-called free cyclotron frequency) : $\nu_c = \frac{qB}{2\pi m}$. The derivation of the equation of motion of an ion in a Penning trap is extensively treated in [BG86] and we will only highlight here the most important results. In the presence of both the B-field (the z-axis following the direction of the magnetic field) and the electric confining potential, the equation of motion for all three Cartesian coordinates read :

$$\ddot{x} - \omega_c \dot{y} - \frac{1}{2}\omega_z^2 x = 0, \quad (2.1)$$

$$\ddot{y} + \omega_c \dot{x} - \frac{1}{2}\omega_z^2 y = 0, \quad (2.2)$$

$$\ddot{z} + \omega_z^2 z = 0, \quad (2.3)$$

where $\omega_z = \sqrt{\frac{qV_0}{md^2}}$ and V_0 and d are the quantities described in the previous paragraph.

From equation 2.3 it appears quite clearly that the ion's motion along the z-axis is a simple harmonic motion about the trap center at the frequency $\nu_z = \frac{\omega_z}{2\pi}$ (~ 45 kHz for an ion of mass ~ 100). Additionally, this motion is fully decoupled from the radial motions. In the radial plane the x-y motions are highly coupled as in this plane the ion describes an epicycloid. The latter motion can be decomposed into two circular motions each with its own characteristic frequency. Hence, the ion follows a slow $\vec{E} \times \vec{B}$ drift about the trap center. This so-called magnetron motion has a characteristic frequency (the so-called magnetron frequency) given by :

$$\nu_- = \frac{1}{4\pi}(\omega_c - \sqrt{\omega_c^2 - 2\omega_z^2}). \quad (2.4)$$

This slow magnetron motion constitutes the "guiding center" for a fast circular motion called the reduced cyclotron motion the characteristic frequency of which is given by :

$$\nu_+ = \frac{1}{4\pi}(\omega_c + \sqrt{\omega_c^2 - 2\omega_z^2}). \quad (2.5)$$

An idealized representation of the trajectory of a singly charged ^{133}Cs ion inside ISOLTRAP's measurement Penning trap is presented in Figure 2.5. In this Figure, the full trajectory (black line) is decomposed into the three eigenmotions namely the axial, magnetron and cyclotron motions (shown in blue, green and red lines respectively).

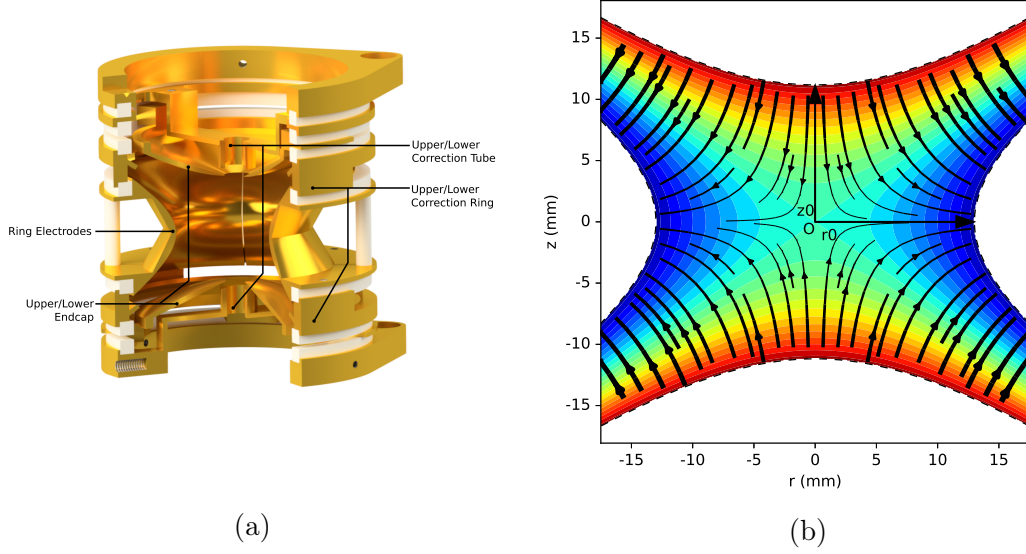


Figure 2.4: a) 3D rendering of ISOLTRAP's hyperbolic Penning trap. The ring electrode is 4-fold segmented in order to allow for the application of azimuthal dipole and quadrupolar RF driving fields. Annotations indicate the different electrodes constituting ISOLTRAP Penning trap. b) Idealized potential distribution inside ISOLTRAP hyperbolic Penning trap (red indicates higher values while blue lower values). The potential distribution being axially symmetric, an arbitrary 2D plane of view containing the trap axis is chosen. The corresponding electric field lines are represented as black arrows the width of which is proportional to the field strength. The intersection of the trap's electrodes with the plane of representation is indicated with dashed lines.

Obviously, the roots in equations 2.4 and 2.5 must be positively defined for the radial ion motion to be bound. This condition translates in turn into a condition for the magnetic field strength and the applied trapping potential which must be such that:

$$\frac{qB^2}{m} \geq \frac{2V_0}{d^2}. \quad (2.6)$$

Requiring a bounded motion along the trap axis, one has the additional condition that the product qV_0 must be strictly positive.

For a singly charged ion of mass $A \approx 100$, the reduced cyclotron frequency in ISOLTRAP's measurement trap is on the order of 900 kHz while the much slower magnetron motion has a frequency which is on the order of 1 kHz. We are thus in a situation such that $\omega_z \ll \omega_c$. Hence, taking the Taylor expansion of ω_+ and ω_- at first order in the quantity $\frac{\omega_z}{\omega_c}$ one can show that both radial frequencies can be approximately expressed as :

$$\nu_- \approx \frac{V_0}{4\pi d^2 B}, \quad (2.7)$$

$$\nu_+ \approx \nu_c \left(1 - \frac{mV_0}{2qd^2 B^2}\right). \quad (2.8)$$

The immediate consequence is that the magnetron frequency appears to be independent of the ion's mass-over-charge ratio while the opposite is true for the cyclotron frequency.

2.3.2 The Time-of-Flight Ion Cyclotron Resonance (ToF-ICR) technique

In this thesis, we are mainly interested in the application of the Penning trap in the field of high precision mass spectrometry. The determination of the mass-over-charge ratio of an ion in a Penning trap relies in the determination of the free cyclotron frequency of the ion in the confining magnetic field. In that regard, a few interesting relations, easily derived from 2.4 and 2.5, are of particular interest:

$$\omega_z^2 + \omega_+^2 + \omega_-^2 = \omega_c^2, \quad (2.9)$$

$$\omega_+ + \omega_- = \omega_c, \quad (2.10)$$

$$2\omega_+\omega_- = \omega_z^2. \quad (2.11)$$

So far, what we touched upon is strictly valid in the case of a single ion confined in an ideal quadrupole field. Reality is more treacherous as frequency shifts can already arise from the very nature of the design of a real Penning trap. Indeed, in practice one can obviously not accommodate infinite hyperboloidal electrodes. In addition, introducing ions inside the trap involves opening injection and ejection apertures in both endcaps. It is thus easy to understand why in the case of a real

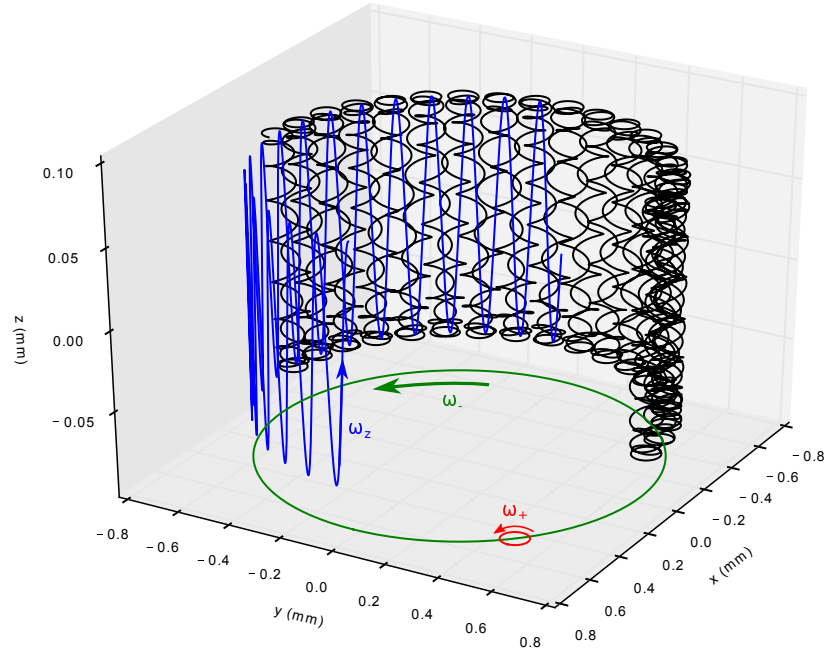


Figure 2.5: Computed trajectory of a singly charged ^{133}Cs ion inside ISOLTRAP's Penning trap. The full trajectory is represented in black. This trajectory is decomposed into three eigenmotions : an axial harmonic motion at the frequency ω_z (blue), the slow drift motion at the magnetron frequency ω_- (green), the circular cyclotron motion at the reduced cyclotron frequency ω_+ (red).

Penning trap design, higher order electric field components come about to spoil the pure quadrupole nature of the confining potential. As described in [B⁺90], such electric field imperfections can have a significant impact on the measured frequencies. Hence, ISOLTRAP's hyperbolic Penning trap design incorporates correction electrodes (the correction rings and tubes visible in Figure 2.4) which allow compensating for these imperfections. More importantly, the use of correction electrodes is essential in the successful realisation of cylindrical Penning traps which offers significant practical advantages over the traditional hyperbolic design such that most modern Penning trap mass spectrometers only make use of the latter. One such example of a cylindrical Penning trap is ISOLTRAP's preparation Penning trap. Other sources of frequency shifts and their impact on mass calibration of the spectrometer are detailed in [B⁺90, Bla06] and will not be further discussed in the present manuscript. The details of the E-field and B-field optimization procedure at ISOLTRAP are given in [B⁺09a].

Hence, with a careful realisation of the Penning trap design, the mass of the stored charged particles could in principle be determined from the individual measurements of the two radial frequencies, according to 2.10 or the measurement of all three characteristics frequencies, using relation 2.9. The latter method is particularly interesting as [BG86] showed that relation 2.9 (the so-called *invariance theorem*) is at first order independent of imperfections. In practice, the frequency measurement can be performed using the non-destructive image-charge detection technique which is once more detailed in [Bla06] (and references therein). With ISOLTRAP, the mass determination rather relies on the direct determination of the ion's free cyclotron frequency using a destructive resonant technique. This workhorse technique is favored over the image charge detection method as it is more readily adaptable to different mass ranges. The Time-of-Flight Ion-Cyclotron-Resonance (ToF-ICR) technique [B⁺90, K⁺95] relies on the identification of the azimuthal excitation frequency for which a minimum time of flight is measured. This technique will be detailed next.

Driving the ion motion

The ToF-ICR mass determination technique first requires the trapped ion to be brought on a well-defined magnetron radius. In order to manipulate one of the radial motions, resonant azimuthal RF pulses at the corresponding frequency can be used [B⁺90]. Because $\nu_+ \ll \nu_-$, it is possible to address each motion separately. The response of the ion to a dipole excitation depends strongly on the relative phase between the ion's motion and that of the excitation. In order to obtain continuous and linear increase of the radius for the whole duration of the excitation the relative phase between the ion motion and the excitation is optimized such that it is equal to $\frac{\pi}{2}$. This is the so-called magnetron phase lock procedure explained in [B⁺03c]. An idealized snapshot of the dipole-field distribution is shown on Figure 2.6a, while the ions motional response is depicted on Figure 2.6b. For the application of the ToF-ICR technique at ISOLTRAP, a dipole excitation at the frequency ν_- is applied for a duration equivalent to three magnetron periods. The amplitude of this excitation (noted U_d in Figure 2.6a) is chosen so that the final magnetron radius is on the order of 0.6-0.7 mm which is still small compared to the trapping volume in which the B-field can be considered as homogeneous. The magnetron frequency being essentially mass independent, such an excitation prepares any ion on the same well-defined magnetron radius. Exploiting the mass dependence of

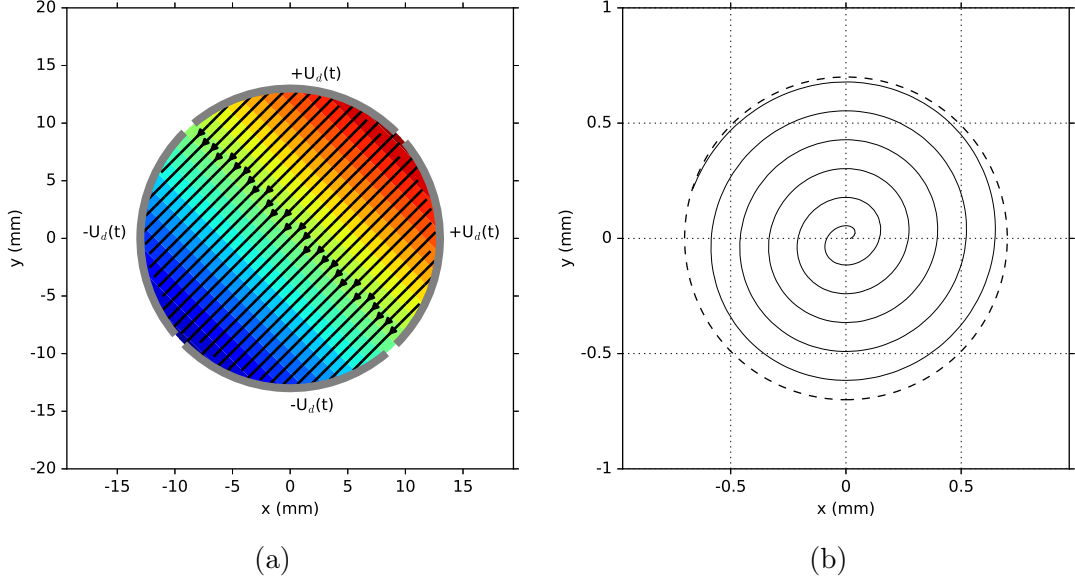


Figure 2.6: a) Idealized potential distribution corresponding to a dipole excitation. The corresponding idealized electric field lines are also represented. For the sake of illustration the 4-fold segmented ring electrode is sketched as well. b) Schematic representation of the trajectory of an ion subjected to an RF dipole pulse. The radius of the ion's motion (chosen to be pure magnetron in this case) continuously increases with time. The final radius is marked with a dashed circle and depends on the amplitude and duration of the excitation.

ν_+ , dipole excitations can also be used to remove contaminating species from the measurement trap; this is the so-called dipole cleaning technique.

Applying a quadrupole sinusoidal excitation at the sum frequency of two eigenmotions results in the coupling of these two motions [K⁺95, B⁺90]. In practice this is achieved by applying azimuthal sinusoidal RF pulses on the 4-fold segmented ring electrode following the configuration depicted on Figure 2.7a. This coupling of the two motions is a resonant process which results in the periodic conversion of one motion into the other. This conversion is maximal when the ion is excited at the sum frequency ($\nu_{RF} = \nu_+ + \nu_-$) of the two radial motions. In the case of an ideal Penning trap, this excitation frequency corresponds to the free-cyclotron frequency ν_c of the trapped charged particle. Hence at resonance, i.e when $\nu_{RF} = \nu_c$, the prepared pure magnetron motion is fully converted into a pure cyclotron motion. The time needed to perform one full conversion between one motion to the other is given by [K⁺95, B⁺90, M⁺08] :

$$T_{magnetron \rightarrow cyclotron} = 2\pi(\omega_+ - \omega_-) \frac{m}{q} \frac{\rho_0}{\alpha U_q}, \quad (2.12)$$

where $\omega_{\pm} = 2\pi\nu_{\pm}$, α is a geometrical factor and U_q is the amplitude of the quadrupole excitation. As $\omega_+ \ll \omega_-$, the quantity $T_{magnetron \rightarrow cyclotron}$ is in first order mass independent. The resonant conversion from pure magnetron motion to pure cyclotron motion is illustrated in Figure 2.7b for a ^{133}Cs ion in ISOLTRAP's measurement Penning trap. During the conversion, the amplitude of the magnetron motion decreases while the amplitude of the cyclotron motion increases. After one full conversion between the two motions, the magnetron motion has disappeared and the amplitude of the cyclotron motion is then equal to the initial

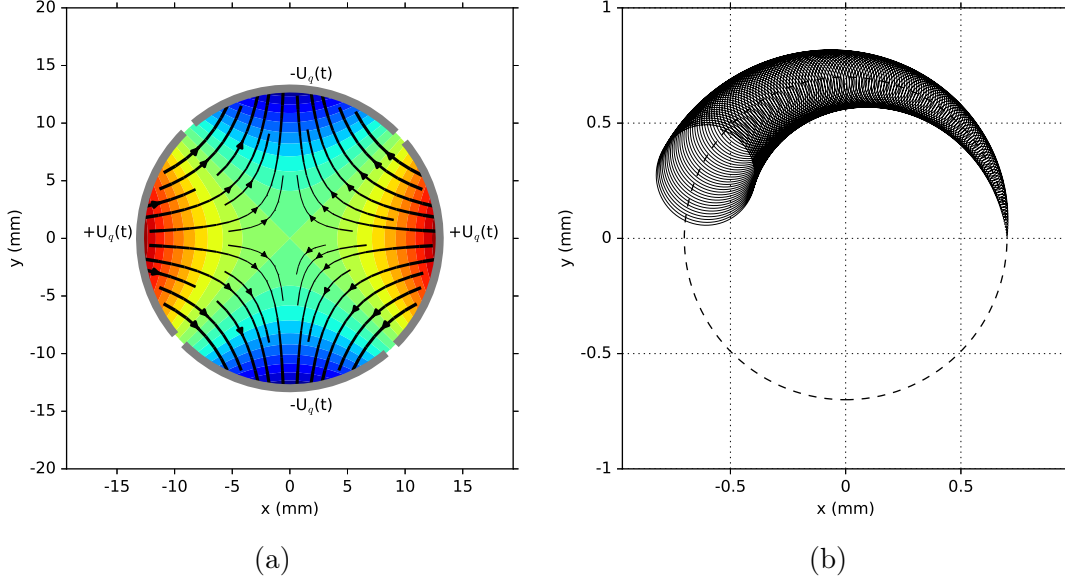


Figure 2.7: a) Same as Figure 2.6a but for a quadrupole excitation. b) Schematic representation of the trajectory of an ^{133}Cs ion subjected to a quadrupole excitation at the true cyclotron frequency ν_c . A pure magnetron motion (initial radius marked with dashed circle) is progressively converted into a pure cyclotron motion.

magnetron amplitude. Because $\omega_+ \ll \omega_-$, the conversion from magnetron to cyclotron motion is accompanied by a dramatic increase in the energy stored in the radial plane since the radial kinetic energy is proportional to the frequencies and amplitude of the two motions ($\rho_+(t)$ and $\rho_-(t)$) [K⁺95]:

$$E_r(t) \propto \omega_+^2 \rho_+(t)^2 - \omega_-^2 \rho_-(t)^2 \approx \omega_+^2 \rho_+(t)^2. \quad (2.13)$$

In the case of a non-resonant excitation ($\nu_{RF} \neq \nu_c$), the magnetron motion is not fully converted into cyclotron motion after T_{RF} resulting in smaller radial kinetic energy gains. At this stage little was said to the concern of the axial motion. It is desirable that the amplitude of the latter motion is kept to a minimum to prevent the recorded time-of-flight of the ion to be strongly dependent on the phase of the axial motion. Hence, the voltage of the ring electrode as well as the time at which the lower endcap is switched to its trapping potential are optimised aiming at keeping the amplitude of the axial motion to a strict minimum.

Time-of-Flight detection technique

The radial motion of the ion orbiting inside the Penning trap bears a magnetic moment given by : $\vec{\mu} = \frac{E_r}{B} \vec{e}_z$. Using equation 2.13, this magnetic moment can be expressed as a function of the frequencies and amplitudes of the two radial motions :

$$|\mu| \propto \frac{\omega_+^2 \rho_+^2 - \omega_-^2 \rho_-^2}{B} \approx \frac{\omega_+^2 \rho_+^2}{B}. \quad (2.14)$$

The ToF-ICR technique is a destructive detection technique which relies on the time-of-flight detection of the ion after manipulation and ejection towards an ion detector (MCP) placed downstream of the Penning trap, outside of the magnetic field. We saw how a quadrupole excitation results in an increase in the radial kinetic energy and, as a result, an increase in the magnitude of the

associated orbital magnetic moment. Along the ion's flight path from the center of the trap towards the detector the magnitude of the B-field decreases from about 6 T to a couple of mT at the position of the detector. The interaction between the orbital magnetic moment $\vec{\mu}$ and the magnetic field gradient $\vec{\nabla}\vec{B}$ results in a force $\vec{F} = \vec{\mu}(\vec{\nabla}\vec{B})$ directed towards the ion detector which will accelerate the ion ejected from the trap. The magnitude of this force depends on the magnitude of the orbital magnetic moment. Hence, an ion bearing little to no magnetic orbital moment, e.g an ion on a pure magnetron motion, will not be accelerated passing through the magnetic field gradient while after a full resonant conversion to a pure cyclotron motion, the ion acceleration will be maximal resulting in a minimum time-of-flight to the detector. The length of the excitation determines the width of the ToF-ICR resonance and consequently the associated resolving power and the uncertainty with which ν_c can be determined [B⁺90]. Thus, the excitation time T_{RF} is set according to the desired precision and the amplitude of the quadrupole driving field is chosen so as to produce exactly one full magnetron to cyclotron conversion in the time T_{RF} .

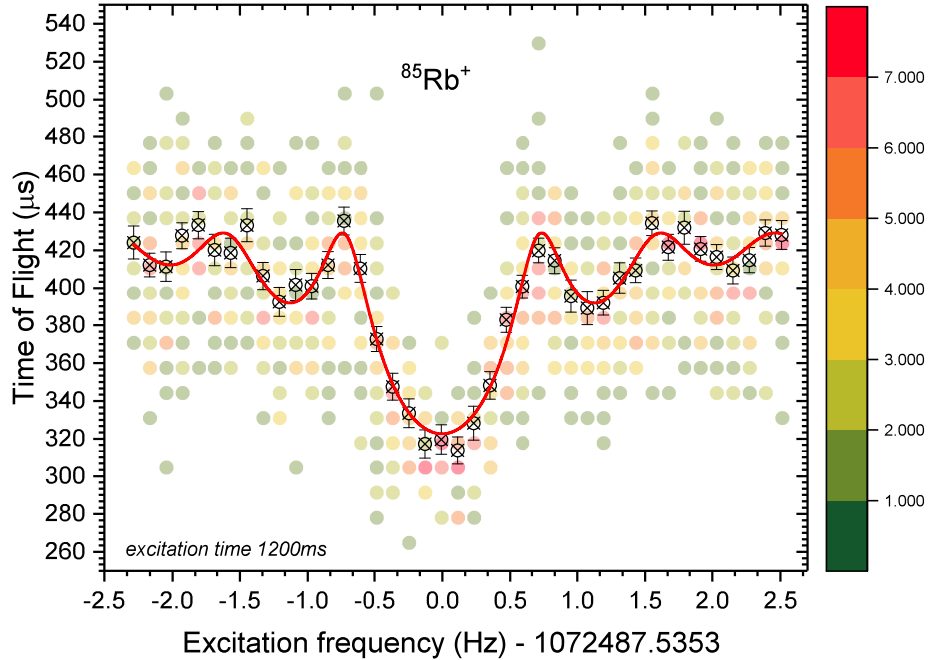


Figure 2.8: Scan of the quadrupole excitation frequency around the free cyclotron frequency of an $^{85}\text{Rb}^+$ ion ensemble. The excitation time is 1200 ms. Approximately 1000 ions were used to produce this resonance. The color map represents the individual ion events recorded in each (frequency, tof) bin. For each frequency bin, the mean time-of-flight and the associated standard deviation is represented as open circles. The red line is a fit to the theoretical line shape [K⁺95].

In practice, a measurement of ν_c consists of a scan of the frequency of the quadrupole driving field around the ion cyclotron frequency. Each experimental cycle corresponds to a new step in the frequency scan and a new ion bunch is injected in the trap. After excitation the ion ensemble is ejected from the trap and the time of flight of the individual ion events is recorded. After several such cycles one obtains a characteristics time-of-flight ion cyclotron resonance an example of which is shown in Figure 2.8 for a $^{85}\text{Rb}^+$ ion. In this figure, the recorded time-of-flight distribution in each of the 41 frequency steps is shown. The number of events in each of the (frequency, tof) bin is represented using a color map. For

each frequency bins, the mean and standard deviation of the corresponding time-of-flight distribution is represented as open circles. According to the discussion of the previous paragraphs, the frequency corresponding to a minimum time-of-flight is thus ν_c , the free-cyclotron frequency of the ion in the confining B-field. Second minima (side bands) are observed off-resonance as a consequence of the shape of the temporal envelope of the excitation. Indeed, the amplitude of the frequency response is given by the Fourier Transform of the excitation amplitude in the time-domain [B⁺90]. As in the present case the temporal envelope of the excitation is given by a square in the time-domain, thus the radial kinetic energy of the ion is modulated by a function of the form $\sin(x)^2/x^2$ [K⁺95]. The red line in Figure 2.8 results from a least-squares fit of the data to a theoretical line shape, the details of which are given in [K⁺95].

The ToF-ICR technique being in essence a scanning technique, substantial statistics in each step of the scan must be collected for the resonance to be exploitable for analysis. As an example, the resonance in Figure 2.8 corresponds to about 1000 single ion events in total which translates into an average of about 25 ion counts per scan step. If statistics poses no problem for stable or long-lived ions, it is obvious that in the case of rare isotopes which are produced in only minute quantities this becomes a limitation. Additionally, since width of the ToF-ICR resonance is Fourier limited the resolving power of the technique can be expressed as $R = \frac{m}{\Delta m} = \frac{\nu_c}{\Delta \nu_c} \approx \nu_c T_{RF}$. There again, in the case of long-lived (or even stable species) T_{RF} can be increased virtually without limitation. However, as ISOLTRAP aims at performing mass measurements on short-lived radioactive species and as such, in most practical cases, one cannot allow for arbitrary long excitation times.

About ten years ago the Ramsey ToF-ICR technique has been introduced in the field of mass spectrometry. This method differs from the regular ToF-ICR in the form of the temporal envelop of the applied quadrupole excitation. It is characterized by the application of two short RF-pulses separated by a waiting time [G⁺07b, G⁺07a]. The obtained resonance pattern is still symmetric about the free cyclotron frequency of the ion. However, it is characterized by a succession of narrow fringes which are not as deep as the central one. Since in practice the excitation frequency is scanned only within a restricted range, the obtained resonance pattern displays fringes the depth of which is of comparable magnitude. Since these fringes are narrower than the central minimum of a regular ToF-ICR resonance, for the same excitation time, the Ramsey ToF-ICR technique is up to a factor three times more precise than the regular ToF-ICR technique.

A more recently introduced technique based on the projection of the ion's motion onto a position sensitive detector (Phase-Imaging ICR) [E⁺14] was successfully commissioned at ISOLTRAP and in principle allows for measurement times reduced by a factor 25, a 40-fold gain in resolving power and considerably increased sensitivity as only a handful of ions are needed to obtain a measurement of the free cyclotron frequency. Bringing significant improvements over the regular ToF-ICR technique, the PI-ICR technique is nonetheless still limited by the time required for the ion beam preparation stages (see 2.3.4) upstream of the measurement Penning trap as well as by the overall transport efficiency to the Penning trap (usually less than 1 %).

2.3.3 The Multi-Reflection Time-of-Flight device

There remains one intrinsic limitation to the destructive ICR techniques that we have not touched upon yet and which is related to the influence of contaminating species in the ion ensemble. In all rigorosity, the several equations which were presented in the previous subsections are all valid for a single ion in an ideal Penning trap. In reality, many ions are confined at once in the measurement trap. Already when considering two ions of the same species confined in a Penning trap, Coulomb interaction, which depends on all three coordinate of space, makes the equation of motion 2.1 no longer exactly solvable [T⁺97]. When more than one ion is present in the Penning trap, space-charge effects cause frequency shifts. Fortunately, for ions of the same kind the latter does not affect the center of mass motion of the cloud. Thus, if it is not so strong as to force a significant fraction of the ion cloud out of the region where imperfections are well kept under control, space-charge should not produce a shift in the measured cyclotron and magnetron frequencies. The presence of different ion species in the trap can be much more detrimental. There, a significant shift in the measured cyclotron frequency can be observed due to the coupling between the different center-of-mass motions of the different species constituting the bunch (see [B⁺90] and references therein).

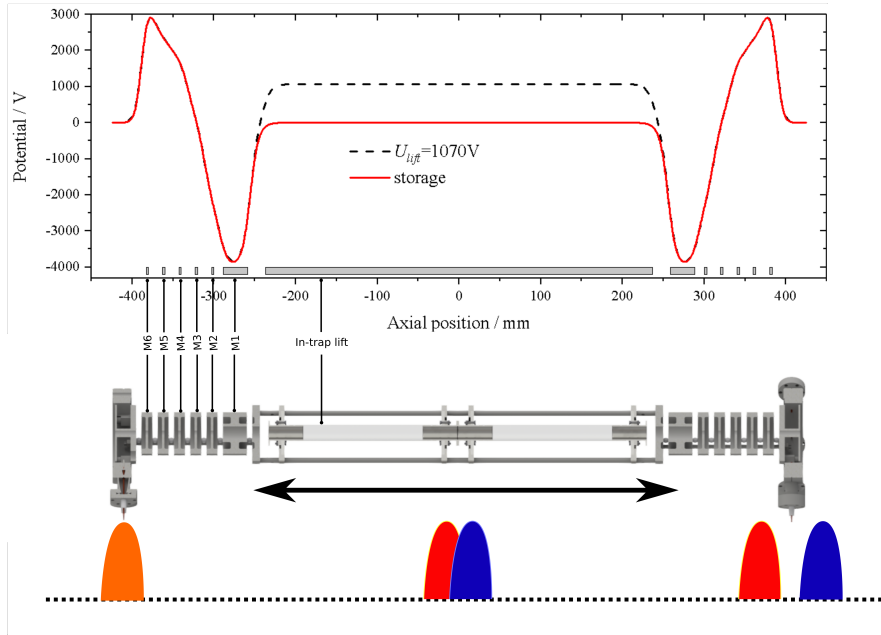


Figure 2.9: Simulated potential distribution along ISOLTRAP’s MRToF-MS axis (*top*). The corresponding 2D rendered cut view of the MRToF is shown (*bottom*). The schematic separation of an ion bunch into two distinct species is also represented.

Keeping contamination under control thus appears as an indispensable prerequisite to high accuracy mass measurements using Penning traps. In the context of mass measurements at ISOL facilities such as ISOLDE, the production of contaminant species is intrinsic to the production mechanism of the ion of interest. If the dipole mass separators available at such facilities usually provide enough resolving power to separate neighbouring isotopes subsequent separation stages are required to isolate the ion species of interest from the contaminants of same mass number. ISOLTRAP has always been at the forefront in the development of innovative separation techniques. A prime example being the development of

the buffer gas mass selective centering technique [S⁺91]. Reaching mass resolving powers in the order of 10^4 - 10^5 , this technique is able to provide isobarically pure ion bunches to ISOLTRAP measurement Penning trap. However, as is the case with most Penning trap based techniques, the buffer gas method is limited due to the relatively long time (several 100 ms) needed to reach the required resolving power. Additionally, venturing into more exotic regions of the chart of nuclides, the dramatic drop in the observed half-life is most often accompanied by an even more dramatic drop in the production cross-section. Hence, one sees the immediate interest for a mass-separation technique which is both fast (a few tens of ms) and able to cope with a contamination ratio well above 1:1000. The use of Multi-Reflection Time-of-Flight (MR-ToF) devices as a viable solution to such problems stemmed from the work reported in [WP90, P⁺01a]. However, it was only at the beginning of this decade that these ideas were successfully applied to the separation of short-lived isotopes at ISOLTRAP [WMRS12, W⁺12b, W⁺13b].

A 2D view of ISOLTRAP's MRToF device is shown in the bottom panel of Figure 2.9. Such a device is constituted by a set of two electrostatic mirrors, each of them made of 6 electrodes. The mirrors are positioned on each side of a 460-mm-long drift cavity. Mirrors 3 to 6 are put on a positive voltage and ensure the axial confinement of the ion bunch, while Mirror 1 and 2 form a negative electrostatic lens which ensures the radial stability by periodically refocusing the ions. In order not to disturb the potential distribution U_z in the mirrors (see top panel of Figure 2.9), the ions are injected into the trap by pulsing the drift cavity. The kinetic energy of the incoming ion bunch is thus reduced such that $E_{transfer} - qU_{lift} = qU_{storage} \leq qU(z)^{max}$. After several revolutions between the mirrors the drift cavity can be switched back to its original voltage for ejection. For ions monitoring a commercial electron multiplier optimised for time-of-flight mass spectrometry (FWHM of the single ion response ~ 1 ns) is used [id18].

Exiting the source (in this case ISOLTRAP's RFQ cooler buncher) with the same kinetic energy the different constituents of the beam will separate according to their mass-over-charge ratio $\frac{m_i}{q_i}$ (i indexes the ion species) after following the same flight path inside the device. The separation mechanism is illustrated in Figure 2.9 where the orange bunch is made of two species which separate into two distinct bunches of the course of several reflections between the mirrors. While being trapped, the ions travel an approximate distance of 1 km over the course of typically 1000 revolutions. At the typical kinetic energies considered, $\sim q_i$ keV, such a distance is travelled in typically ~ 25 ms (for an ion of mass ~ 100). For each species, the mean of the corresponding time-of-flight distribution is given by :

$$t_i = a\sqrt{\frac{m_i}{q_i}} + b, \quad (2.15)$$

where a and b are calibration parameters. The a parameter is intricately dependent on the electric potential experienced by an ion along its trajectory inside the setup while b is a time offset. The corresponding time-of-flight width, Δt consists of several contributions the details of which are discussed in [WMRS12, W⁺17c]. Adjusting the voltage applied on the in-trap lift changes the energy of the ions traveling inside the device. The mirror potential being kept constant this effectively results in a change of the time-energy dispersion relation of the spectrometer. Hence, by carefully adjusting the voltage of the cavity one can compensate for the time-of-flight broadening acquired outside the device and achieve time focus at the position of the time-of-flight detector or another device used for ion selection.

Apart from higher order aberrations picked up outside and inside the MRToF, Δt is essentially reduced to its minimum which is defined by the turn around time of the ions inside the source. Hence, the resolving power, $R = \frac{m}{\Delta m} = \frac{t}{2\Delta t}$, of an MRToF mass separator can therefore be made several orders of magnitude higher than a single path mass time of flight spectrometer. With ISOLTRAP, the mass resolving power thus routinely reaches values well in excess of 10^5 in as short a time as ~ 25 ms. The resolving power can of course be straightforwardly increased by increasing the number laps the ions make inside the MRToF and adjusting the time focus plane according using the in-trap lift cavity. If the resolving power of an MRToF device first scales linearly as a function of the number of revolutions it will ultimately reach a plateau. Indeed, a broadening of the time-of-flight width is observed for trapping times approaching 100 ms and is attributed to higher aberrations which accumulate with at each revolution. An additional effect can be detrimental to the MRToF mass separation capabilities, the so-called "peak-coalescence" phenomenon. Indeed, the number of ions stored inside the MRToF device can be such that the impact of Coulomb interaction between the ions can become significant. For ions of different masses, this results in the counter-intuitive effect that the species do not separate anymore. Through intensive computer simulations and experimental studies, the systematics of this effect are currently being investigated [R⁺13b].

Originally intended to be used in combination with a Bradbury-Nielsen gate (BNG) [W⁺12b, W⁺13b], the mass selection is now performed using the in-trap lift cavity itself and carefully adjusting the ejection timing [W⁺17c]. When the species are sufficiently separated (i.e when $|t_i - t_{i\pm 1}| \geq \frac{t_i}{2R_{FWHM}}$) the time at which the drift cavity is switched for ejection as well as the time for which it stays open (~ 200 ns) are optimised in such way that only the species of interest can exit the MRToF while the others stay trapped in the device. The increased selectivity of this method compared to the BNG solution as well as its straightforward optimisation makes it particularly well suited for online operation.

First designed as a beam purifier, ISOLTRAP's MRToF mass separator quickly became a mass spectrometer in its own right. Indeed, it is easy to understand that using well-known masses to extract parameters a and b from equation 2.15, one can subsequently relate the mean time of flight of the other ion species to their mass. With the resolving power and ion processing speed of MRToF devices this method of mass determination is particularly well suited for cases where the half-life and production yield of the species of interest are very low and a Penning-trap measurement is virtually impossible. One of the most prominent cases in which this method was used successfully is the measurement of neutron-rich $^{53-54}\text{Ca}$ at ISOLTRAP [W⁺13a]. Much like the Penning trap mass spectrometry technique, MRToF devices are appearing at other nuclear research facilities around the world [W⁺15] (and references therein).

2.3.4 Ion traps for beam accumulation and cooling

As already mentioned, the general interest of ion traps in the field of nuclear physics goes far beyond their application to high-precision mass measurements. Traps are intensively used devices for the preparation of the ion beam. The MRToF mass separation briefly discussed in the previous paragraph is only one of many such applications. Charge breeding is another but will not be discussed in this thesis. More specifically we will briefly introduce the use of ion traps for the accumulation,

cooling and bunching of an ion beam. Indeed, achieving better matching between the properties of a RIB (e.g longitudinal, transverse emittance, timing structure ...) and the specifics of a given experimental setup (e.g transverse acceptance, time or energy spread ...) is of general concern in the field of low energy nuclear physics. Several cooling methods have been developed over the years some of them described in [K⁺16]. Some practical considerations have to be taken into account in order to choose the most adequate technique to be used for RIBs. Indeed at facilities like ISOLDE, RIBs come in all sort of chemical species and the available mass range covers the lightest to the heaviest of isotopes. This explains the success of the buffer gas cooling technique in the field of low energy physics.

Buffer gas cooling is conceptually simple. A few ions are stored in a trap (a linear Paul trap or a Penning trap) and they lose part of their kinetic energy to the many atoms of the buffer gas. After a while, the ion cloud thermalises to the temperature of the buffer gas. A detailed treatment of the cooling mechanism (ion loss mechanism, final temperature) would require a microscopic treatment of the cooling process. Nevertheless, for large mass difference between the ions and the gas atoms and low ion energy the overall cooling process can be fairly well approximated considering that the long range interaction between the atoms of the gas and the ion results in an effective viscous damping force [Sch06]:

$$\vec{F} = -\delta m \vec{v}, \quad (2.16)$$

where m and \vec{v} are the mass and velocity vector of the ion. For an ion of charge-over-mass ratio $\frac{q}{m}$, in a buffer gas with pressure p and at temperature T (normalised to the normal pressure and temperature p_N and T_N), the damping coefficient δ can be expressed as :

$$\delta = \frac{q}{m} \frac{1}{\mu} \frac{p/p_N}{T/T_N}. \quad (2.17)$$

Hence, we see that δ is proportional to the gas pressure but inversely proportionally to the gas temperature. The reduced ion mobility μ is a joint property of the ion and the coolant. Additionally, the buffer gas should ideally be inert to prevent a loss of ions due to chemical processes and charge exchange. Hence, most often a noble gas such as helium is used. Typically, the helium pressure in ISOLTRAP RFQ CB reaches 10^{-2} mbar.

At ISOLTRAP, two devices are used for radioactive beam accumulation and buffer gas cooling. The first such device is a radio-frequency quadrupole cooler and buncher (RFQ CB) [H⁺01]. The specifics of ion confinement inside a radio-frequency quadrupole trap (Paul trap) can be found in [M⁺05, WGM09, K⁺16] and will not be further detailed here. ISOLTRAP's RFQ CB is made of a series of 4 parallel rods placed at a distance $r_0 = 6$ mm from the beam axis. Opposite rods are pairwise connected and a fast varying radio-frequency voltage is applied with opposite polarity to each pair. In this configuration, a time-varying quadrupole potential distribution is created in the inner volume of the trap. On average, this fast oscillating quadrupole field has a net confining effect and the radial motion of the ions can be viewed as that of ions trapped in a harmonic quadrupole pseudo-potential. For the typical experimental parameters of ISOLTRAP's RFQ CB the pseudo-potential depth is on the order of 10 eV. In addition, each rod is 26-fold segmented. A constant voltage is applied on each rod so as to create potential distribution which guides the ions as they travel along the ~ 1 m long RFQ. On the last 4 rods, the applied voltages are such that the ions can finally accumulate in an axial potential well which is ~ 50 eV deep. The voltage applied on these

rods is supplied by high stability switch which is used to eject the ions from the device towards the MRToF-MS. In order to reduce the incoming ISOLDE beam's energy, the whole RFQ trap is placed on a high voltage platform the potential of which is placed only a few eV below the beams energy. When the ions enter the buffer gas environment of the trap their motion will be damped until they finally come into equilibrium with the gas temperature. The cooling mechanism reduces the transverse emittance of the beam to $\approx 10 \pi$ mm.mrad while the longitudinal emittance is reduced to about 10 eV. μ s. Hence, after one such cooling, accumulation and ejection cycle (~ 25 ms) the quasi-continuous ISOLDE beam has been turned into a bunched beam with well defined optical properties well adapted to the use of ion traps.

The second trap used for buffer gas cooling at ISOLTRAP is the so-called preparation Penning trap [RH⁺97]. Contrary to the trap used to perform the mass measurements, the preparation Penning trap is of the cylindrical design. The compensated cylindrical trap is placed in a 4.7 T superconducting magnet and operated with helium buffer gas for cooling. This time however, the gas pressure inside the trap is set to a typical pressure of 10^{-6} mbar. Without gas, the dynamics of the ion cloud would follow the description given in the above (see 2.3.1). However, the addition of the damping force 2.16 modifies the ion dynamics quite significantly. A detailed description of the dynamics of an ion stored in a Penning trap in the presence of buffer gas is given in [K⁺95]. It is rather straightforward to understand that the effect of the buffer gas will be to damp the amplitude ρ of ion motion such that :

$$\rho(t)_{\pm} = \rho_0^{\pm} e^{-\alpha_{\pm} t}, \quad (2.18)$$

$$\alpha_{\pm} = \pm \delta \frac{\omega_{\pm}}{\omega_{+} - \omega_{-}}, \quad (2.19)$$

$$\rho(t)_z = \rho_0^z e^{-\delta t}. \quad (2.20)$$

Hence, one can see that if both axial and cyclotron motion are damped by the buffer gas, the magnitude of the magnetron radius increases with time until the ions are lost radially. This effect can be counteracted by the application of an azimuthal quadrupole RF-pulse at the frequency $\nu_{RF} = \nu_c$. As we already saw, such a pulse results in the conversion of magnetron into cyclotron motion. In that way one can cool all three motions at once until the ion cloud thermalises with the buffer gas. In addition, because this resonance frequency of the quadrupole is the free cyclotron frequency, the damping procedure is mass selective. Hence, ISOLTRAP preparation is not only used for beam accumulation and cooling but also as a beam purification tool. In practice, the whole ion cloud containing contaminants and ions of interest is excited to magnetron radius larger than the aperture of the trap. A resonant quadrupole RF-pulse follows resulting in the recentering of the species of interest while the rest of the ion clouds remains at a large radius. At ejection, only the ions at the center of the trap will be transmitted to the measurement Penning trap [S⁺91].

2.4 Measurements

From July 2015 to July 2018 the ISOLTRAP mass spectrometer was used to carry out approximately 15 experiments which made use of the radioactive ion beams produced by the ISOLDE facility at CERN. The original goal of each experiment

could not always be reached in every experiment. Sometimes, only a few isotopes out of the original wish list were measured. Other times, experimental conditions were such that the focus of the experiment had to be redirected towards the measurement of adjacent isotopes or in rarer cases towards on-line commissioning of recently implemented measurement techniques. All in all, about half of the experiments which took place over the course of this PhD work measured nuclear data which were or will be included in peer-reviewed publications. A list of such publications is given in the appendix.

Over the course of the last three experimental campaigns, a wide variety of physics topics were addressed with ISOLTRAP, ranging from mass measurements of interest for nuclear structure studies to nuclear astrophysics and from the high-precision measurement of Q -values for tests of fundamental symmetries to trap-assisted in-source laser spectroscopy. Some of the on-line activities also consisted of employing the ISOLTRAP MRToF-MS as a beam analyser to assist the ISOLDE users, RILIS and TISD (Target and Ion Source Development) teams, by providing them with important information concerning the composition of the ISOLDE beam or production yields of low yield isotopes. In the following, only the measurements constituting the two datasets analysed during this thesis work will be described.

2.4.1 Neutron-rich chromium isotopes

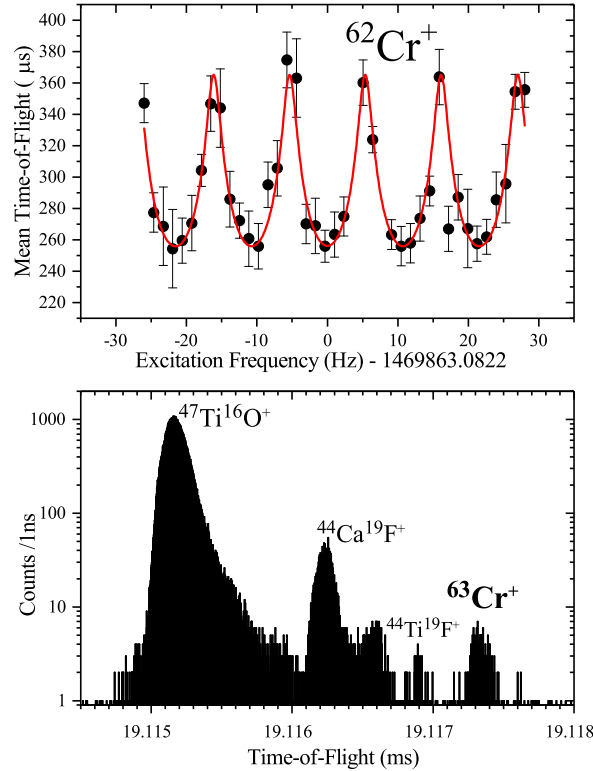


Figure 2.10: *Top*: A typical ToF-ICR resonance of $^{62}\text{Cr}^+$ ions using a Ramsey-type excitation scheme with 10 ms-80 ms-10 ms ($\tau_{on}^{RF}-\tau_{off}^{RF}-\tau_{on}^{RF}$) [G⁺07b]. The solid line represents a fit to the data points. *Bottom*: Number of events as a function of flight time after 1000 revolutions of the $A = 63$ ISOLDE beam inside the MR-ToF MS.

The mass measurement of neutron-rich chromium isotopes with ISOLTRAP began about 10 years ago with the Penning trap measurement of $^{56-57}\text{Cr}$ during

an experiment using a discharge ion source for neutron-rich Ni and Cu [G⁺05b]. As already mentioned, the refractive nature of the chromium element usually reserves these isotopes for in-flight facilities. This explains why chromium mass measurement at ISOLTRAP was not further pursued until 2014 with the first successful tests of a RILIS laser ionisation scheme [D⁺17]. During the first online test (in October 2014) of the new laser scheme, neutron-rich chromium isotopes up to $A = 59$ were observed using the MRToF mass separator. The beam was produced using a UC_x target equipped with a Ta transfer line. The beam was delivered to ISOLTRAP through the HRS mass separator at an energy of 30 keV. During this test the mass of ^{58}Cr could be determined using the Penning trap. The MRToF was used to separate the Cr beam from the more abundant isobaric Fe, Ni and Mn contaminants as well as from a peak identified as $^{42}\text{Ca}^{16}\text{O}$. This online test of the Cr RILIS ionisation scheme stemmed from a run originally intended for the measurement of Sc isotopes. Hence, the preparation Penning trap was set up with a rather short 70 ms cycle. In addition to the regular one RF-pulse ToF-ICR resonance, one Ramsey ToF-ICR was recorded. A summary of the experimental parameters used for the measurement are given in Table 2.1.

After this first successful test of the laser ionisation scheme, ISOLTRAP carried out a dedicated experimental campaign in April 2016. In this experiment, the beam was once more produced using a UC_x target equipped with a tantalum transfer line. The target/line assembly was heated to a temperature close to 1900 °C in order to maximise the diffusion and effusion processes to the ionisation region. The laser ionisation scheme was used. The experiment took place on the HRS target station and the RIB was delivered to ISOLTRAP at an energy of 30 keV. This time, neutron-rich chromium isotopes up $A = 63$ were observed. The beam gate was adjusted depending on the observed yield of the ion of interest and contaminants. It ranged between 10 ms and 200 ms. The ions were kept in the Buncher for an additional 10 ms. For $^{59-62}\text{Cr}$ the MRToF was used to separate the chromium ions from predominant and intense CaF^+ and TiO^+ beams (most likely stemming from chemical reactions within the target) observed over the whole investigated mass range. A 115 ms preparation cycle was used in the preparation Penning trap. Regular and Ramsey-type ToF-ICR resonances were recorded for $^{59-62}\text{Cr}$. Details are summarized in Table 2.1. In addition to the several Penning trap measurements, the MRToF mass separator was used as time of flight mass spectrometer. Hence, MRToF data were also recorded for $^{59-62}\text{Cr}$. The peak corresponding to chromium ions was identified unambiguously by blocking the first step of the RILIS ionisation scheme. The contaminants used as reference for the MRToF mass evaluation were identified by the measurement of their cyclotron frequency in the measurement Penning trap. In the case of ^{63}Cr , the production yield was so low that the mass determination could only be performed with the MRToF. In total, ~ 2000 ^{63}Cr counts were recorded with a typical ratio of 1 ion of interest for a thousand unwanted isobaric species. Table 2.1 also presents the details of the number of recorded MRToF spectra as well as the different number of revolutions used to obtain to spectra. Figure 2.10 presents a typical Ramsey ToF-ICR resonance obtained for ^{62}Cr (top panel) as well as one of the 6 MRToF spectra obtained for ^{63}Cr .

Table 2.1: Summary of the production, preparation and measurement conditions of $^{58-63}\text{Cr}$. In all cases, the MRToF trapping and the total preparation trap periods are rounded. For the ToF-ICR data, the exact quadrupole excitation time applied in the measurement Penning trap is given. For the Ramsey type ToF-ICR resonances, the total quadrupole excitation time is decomposed as $\tau_{on}^{RF} - \tau_{off}^{RF} - \tau_{on}^{RF}$. See text for details.

Production					Preparation/Measurement			
Date	Target/Line	Source	Sep.	Energy	Ion	MRToF-MS	Prep. Trap	Meas. Trap
October 2014	UC_x/Ta	RILIS	HRS	30 kV	$^{58}\text{Cr}^+$	18.3 ms	70 ms	600 ms
								1 \times ToF-ICR
								900 ms
					$^{59}\text{Cr}^+$	18.5 ms	115 ms	100-400-100 ms
								1 \times Ramsey ToF-ICR
April 2016	UC_x/Ta	RILIS	HRS	30 kV	$^{59}\text{Cr}^+$	18.5 ms	115 ms	100 ms
								1 \times ToF-ICR
					$^{60}\text{Cr}^+$	18.5 ms	115 ms	1200 ms
								2 \times ToF-ICR
					$^{60}\text{Cr}^+$	37.2 ms	115 ms	2 \times 1000revs MRToF
								1 \times ToF-ICR
					$^{61}\text{Cr}^+$	18.8 ms	115 ms	100 ms
								1 \times ToF-ICR
					$^{61}\text{Cr}^+$	13.1 ms	115 ms	10-80-10 ms
								2 \times Ramsey ToF-ICR
					$^{62}\text{Cr}^+$	18.8 ms	115 ms	3 \times 700revs MRToF
								2 \times 1000revs MRToF
					$^{62}\text{Cr}^+$	39.8 ms	115 ms	2 \times ToF-ICR
								1 \times Ramsey ToF-ICR
					$^{62}\text{Cr}^+$	18.9 ms	115 ms	10-80-10 ms
								2 \times 1000revs MRToF
					$^{63}\text{Cr}^+$	37.9 ms	115 ms	2 \times 2000revs MRToF
								2 \times 900revs MRToF
					$^{63}\text{Cr}^+$	17.2 ms	115 ms	2 \times 900revs MRToF
								4 \times 1000revs MRToF
					$^{63}\text{Cr}^+$	19.1 ms	115 ms	2 \times 900revs MRToF
								1 \times 1200revs MRToF
					$^{63}\text{Cr}^+$	22.9 ms	115 ms	2 \times 900revs MRToF
								1 \times 1200revs MRToF

2.4.2 Neutron-rich argon isotopes

Beam production and study of the charge-exchange phenomenon

Quantifying the strength of the $N=28$ shell gap in the neutron-rich argon isotopes has been in the focus of the ISOLTRAP mass spectrometer for the past 15 years. Indeed, the Penning trap mass measurement of $^{44-45}\text{Ar}$ by K.Blaum and collaborators [B⁺03b] not only revealed significant deviation from the literature values (e.g $\sim 20\sigma$ for ^{44}Ar) but also brought an overall improvement of an order of magnitude in precision. These early results spawned a mass measurement program dedicated to the study of more exotic argon isotopes a few years later [L⁺09]. However, one of the bottlenecks for noble gas isotopes is the high level of contamination inherent to the use of a plasma ion source. As a result, it is only after the advancement of the MRToF mass separator and lessons learned from a failed attempt in 2010 that the measurement program could be successfully undertaken.

The measurement was done in two separate runs. The first took place in July 2015 while the second was undertaken in August 2017. In both runs, the beam was produced using a uranium carbide target on which the 1.4 GeV proton beam delivered by CERN's PS-Booster impinged. As argon is a noble gas, a VADIS VD7 plasma ion source was used (see schematic view depicted on Figure 2.2). Aiming at reducing the abundance of contaminant species, the VADIS VD7 ion source is mounted with a water-cooled transfer line which inhibits the effusion of the less volatile species towards the active volume of the source [P⁺10]. In 2015, the ion beam was delivered to the ISOLTRAP mass separator at a kinetic energy of 30 keV while in 2017 an energy of 50 keV was used.

Argon, as all noble gases, is characterized by a large first ionization potential. As a result, noble-gas ions are more prone to undergo charge-exchange reactions with the neutral impurities in the buffer gas. The charge exchange mechanism results in a neutralization of the noble gas atoms which are lost during trapping [DAK04]. If not kept under control the charge-exchange phenomenon could become

a true hindrance during the experiment, turning the ISOLTRAP cooler buncher and the preparation Penning trap, both filled with He buffer gas effectively into beam dumps. An obvious workaround was to try clearing the helium buffer gas of its impurity. In practice, both trap's gas injection line was placed inside a bath of liquid nitrogen to freeze impurities on the walls of the gas transfer line. These makeshift cold traps had to be refilled with liquid nitrogen approximately every 8 hours. The charge-exchange half-life was determined by monitoring the evolution of the number of stable $^{38}\text{Ar}^+$ ions detected after ISOLTRAP's MRToF-MS as a function of the Buncher cooling time. Before the installation of the cold traps, the charge exchange half-life was estimated at 23 ± 2 ms while the measurement repeated 6 hours after the installation of the cold traps yields a charge half-life of 50 ± 13 ms, a factor 2 improvement. The preparation Penning-trap charge-exchange half-life was estimated to be 121 ± 19 ms but the tight schedule of the beam time did not allow for further investigations after the installation of the cold traps. In the 2015 experiment, the charge-exchange half-life with the cold traps was estimated, using $^{36}\text{Ar}^+$, to be 33 ± 5 ms (buncher set pressure point at $\sim 2 \times 10^{-3}$ mbar) while for the preparation Penning trap the latter was estimated at 223 ± 38 ms (pressure set point at $\sim 4 \times 10^{-6}$ mbar). These values are significantly smaller than the half-life of the most exotic argon isotope of interest $^{48}\text{Ar}^+$: 415 ± 15 ms. Hence in both runs, even with the use of cold traps, both the buncher and the preparation Penning trap had to be used with short operating cycles (the details of which are given in Table 2.2) which ultimately limited the purification inside the latter trap.

The 2015 experiment

The 2015 mass-measurement campaign started on mass 46. While significant amounts of doubly-charged $^{92}\text{Kr}^{2+}$ were present in the beam, the most detrimental contaminant present on this mass was the molecular ion $^{34}\text{S}^{12}\text{C}^+$ which requires 2×10^5 resolving power to be separated from the $^{46}\text{Ar}^+$ peak. Radioactive species were unambiguously identified by observing the effect of turning on and off the ISOLDE proton request. In particular, the argon isotope of interest was clearly identified by varying the trapping time in the buncher and monitoring the associated count rate decrease with the time-of-flight detector placed downstream the MRToF. The required resolving power was such that the mixture of the two species had to be taken to the precision Penning trap. After lengthy but unsuccessful attempts at performing dipole cleaning, the ratio of 3:1 was in favor of the contaminant $^{34}\text{S}^{12}\text{C}^+$. A double 200 ms excitation time resonance of the pair $^{46}\text{Ar}^+ / ^{34}\text{S}^{12}\text{C}^+$ was recorded and the decision was made to move ahead in the measurement program and attempt measuring $^{47}\text{Ar}^+$.

Contrary to the difficult situation encountered on mass $A = 46$, $^{47}\text{Ar}^+$ was well separated from contaminants. Once more, the peak corresponding to the ion of interest was identified using the proton on/off effect and varying the buncher cooling time. The yields allowed clean bunches to be transported all the way up the measurement Penning trap. Three ToF-ICR of $^{47}\text{Ar}^+$ were recorded using quadrupole excitation of 100 and 200 ms. In addition, two 10-80-10 ms Ramsey type ToF-ICR resonances were also recorded. An example of such resonances is presented in Figure 2.11.

After an initially unfruitful attempt at $A = 48$, where long-lived contamination was observed right in the time-of-flight window where $^{48}\text{Ar}^+$ was expected and

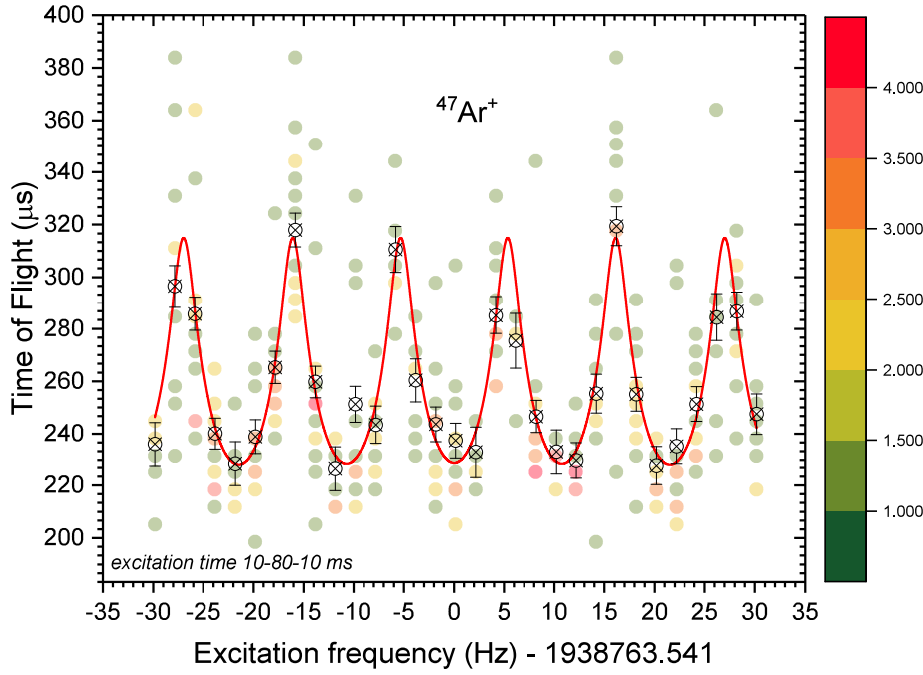


Figure 2.11: Typical two-pulse Ramsey TOF-ICR resonance obtained for $^{47}\text{Ar}^+$ with 10 ms-80 ms-10 ms ($\tau_{on}^{RF}-\tau_{off}^{RF}-\tau_{on}^{RF}$) [G⁺07b, G⁺07a]. The color-map represents the individual ion events recorded in each (frequency;tof) bin while the red line represents the least-squares adjustment of the theoretical line shape to the data points.

no significant proton on/off effect was seen, the last few hours of the run were dedicated to $^{46}\text{Ar}^+$. The few days that had passed since our first attempt permitted an out-gassing of the $^{34}\text{S}^{12}\text{C}^+$ contaminant. A ratio of 3:1 was again observed but this time it was in favor of the species of interest. It was decided to synchronize the start of the ISOLTRAP experimental cycle with the proton impact on target and to add a 50 ms delay to the latter in order to accumulate argon ions at the maximum of their release from the target. The ISOLTRAP buncher cooling was also reduced from 25 ms to 10 ms in order to minimize the loss due to charge exchange. In this configuration, the ratio of contaminants to the argon ions was improved in such a way that a total of two, almost pure, 200 ms ToF-ICR resonances of $^{46}\text{Ar}^+$ could be recorded. An example of such resonances is shown in Figure 2.12. The approximate frequency of the $^{34}\text{S}^{12}\text{C}^+$ contaminant is indicated as a dashed line in Figure 2.12.

The 2017 experiment

The 2017 run aimed at completing the previous dataset with the measurement of the elusive $^{48}\text{Ar}^+$ isotope. Due to the low yield only the MRToF was used. With protons off it appeared that the beam was dominated by a strong $^{38}\text{S}^{16}\text{O}^+$ peak which was unambiguously identified by measuring its cyclotron frequency inside ISOLTRAP's precision Penning trap. In addition, two long-lived species are also observed at later time-of-flight. Due to low count rate and the limited amount of time these two species could not be identified from measuring their respective cyclotron frequencies. Their measured times-of-flight were compared to that expected from a wide variety of singly- and doubly-charged atomic and molecular stable species. This comparison turned out to be inconclusive and the

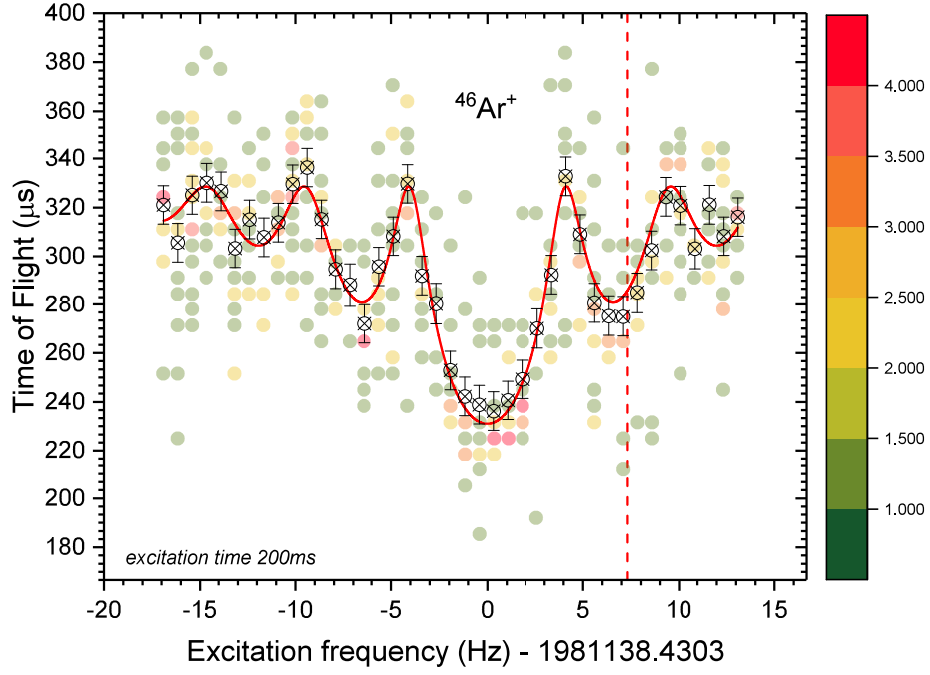


Figure 2.12: Typical one-pulse TOF-ICR resonance obtained for $^{46}\text{Ar}^+$. A quadrupole excitation time of 200 ms was used. The color-map represents the number of individual-ion time-of-flight events recorded in each (frequency;tof) bin while the red line represents the least-squares adjustment of the theoretical line shape to the data points [K⁺95]. The dashed red vertical line indicates the expected cyclotron frequency of the $^{34}\text{S}^{12}\text{C}^+$ contaminant.

latter species still remain unidentified. These contaminants are clearly separated and are located on either side of the time-of-flight window within which $^{48}\text{Ar}^+$ is expected. Shooting protons on target, a peak coinciding with the doubly charged $^{96}\text{Kr}^{2+}$ ion appears clearly in the spectrum. Starting ISOLTRAP in coincidence with the proton impact on target, a minute excess of counts within the $^{48}\text{Ar}^+$ time-of-flight window was observed.

In order to establish the presence of a $^{48}\text{Ar}^+$ peak a series of 20 consecutive files were recorded with protons off. This reference background spectrum (shown in red in Figure 2.13), was compared to a spectrum resulting from the sum of 13 consecutive files recorded with protons on target and while triggering on the protons (shown in yellow in Figure 2.13). In order to compare the two summed histograms, they were normalised to their total number of events. From Figure 2.13 it becomes apparent that a short-lived species appears in the spectrum in between the two long-lived contaminants.

A second test was carried out in order to assess the nature of this signal. Assuming that within a $1\ \mu\text{s}$ time-of-flight window, the candidate $^{48}\text{Ar}^+$ peak is described by a Gaussian peak and the background component is described by two Gaussians sitting on top of a constant background (see 3.2.2), the absolute strength of the signal component was extracted for buncher cooling times ranging from 20 to 150 ms and for two values of the amplitude of the radio-frequency signal. Due to the low production rate of the candidate $^{48}\text{Ar}^+$ species, only 3 data points for each buncher cooling time were recorded. Each point results from the sum of 3 to 4 consecutive files. Hence, the extracted "signal" strength was normalised to the total number of counts present in the summed spectra. The result is presented on Figure 2.14 and clearly shows that the number of counts is

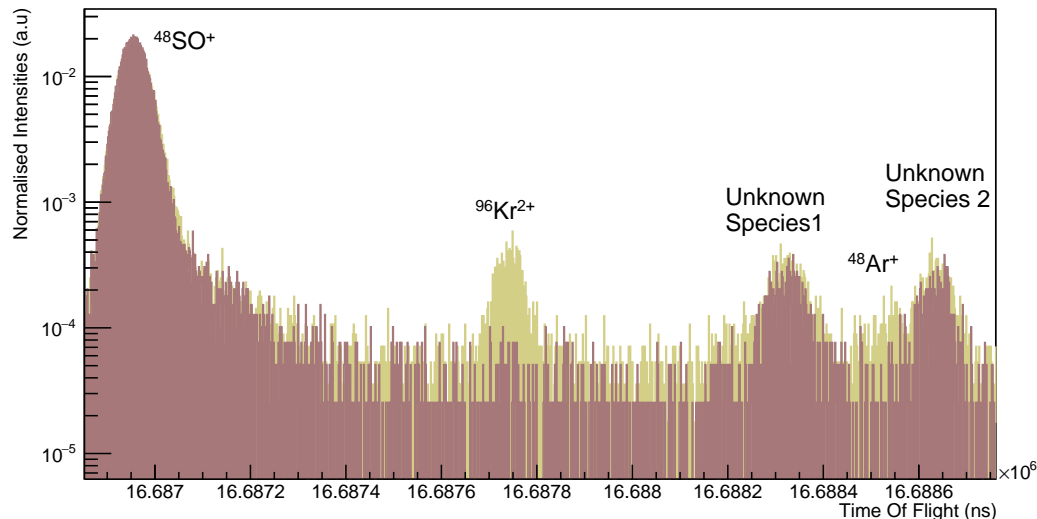


Figure 2.13: $A=48$ time-of-flight spectrum after 1000 revolutions inside the MRToF-MS. The spectrum recorded with protons on target results from the sum of 13 consecutive files and is represented in yellow. The spectrum in red represents a background measurement performed while the protons were off and is the sum of 21 consecutive files. Each spectrum is thus normalised to the total number of counts in the spectrum and stacked on top of each other to ease comparison.

quickly decreasing with increased buncher cooling time, similar to what is expected from a noble gas. The associated decay half-life was extracted from Figure 2.14 assuming a simple exponential decay function. The choice of this simple fit function is mostly dictated by the very low number of data points available to infer the decay constant. Nonetheless, since the charge exchange half-life for $^{38}\text{Ar}^+$ was measured to be 50 ms \pm 13 ms and the recommended half-life of $^{48}\text{Ar}^+$ is 415 ms \pm 15ms [A⁺17c] it seems fair to assume that only one decay mechanism is responsible for the loss of ions in the buncher within the range of cooling times considered. The yielded decay half-life is 25 ms \pm 5 ms. This result lies within 1.5 combined standard deviation from the charge exchange half-life observed with the cold traps for $^{38}\text{Ar}^+$.

Since the observed peak is consistent with the expected time-of-flight of $^{48}\text{Ar}^+$ and its behaviour inside the ISOLTRAP buncher seems to be consistent with that of a noble gas we assumed for the rest of the beam time that we are indeed dealing with an elusive $^{48}\text{Ar}^+$ peak. Nonetheless, the observed count rate was so low and the amount of contamination so high that this measurement constitutes by far the most challenging MRToF-MS measurement performed at ISOLTRAP. In total, 8 MRToF-MS spectra were used for the mass estimation. Each of these spectra results from the sum of 8 to 20 individual files recorded consecutively which were added together. Within the set of 8 spectra, as few as 30 and as much as 170 ion counts of $^{48}\text{Ar}^+$ were recorded. All in all, about 700 $^{48}\text{Ar}^+$ counts were observed.

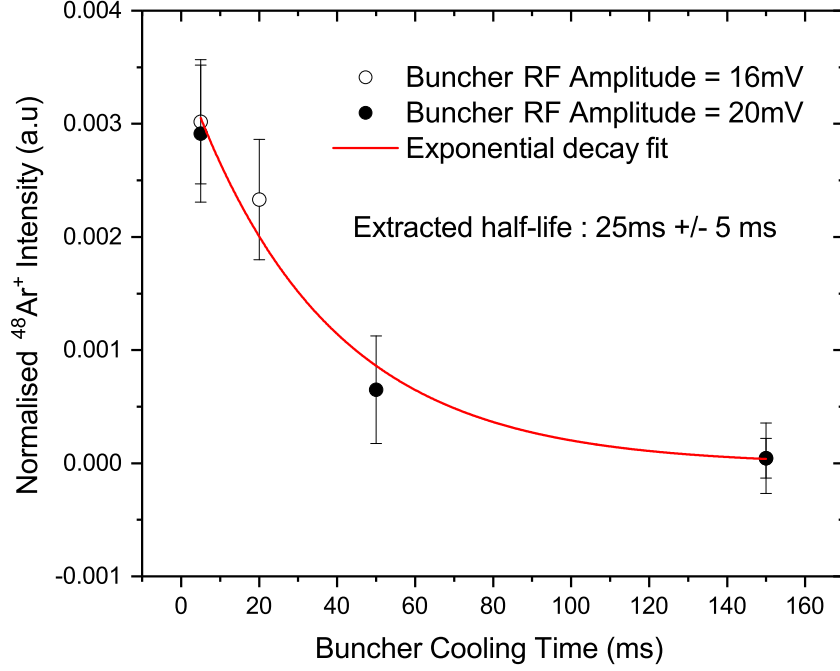


Figure 2.14: Intensity of the $^{48}\text{Ar}^+$ signal as a function of the buncher cooling time for a buncher RF amplitude of 16 mV and 20 mV. All other experimental parameters were kept constant. Each point was extracted from a spectrum resulting from the sum of 3 to 4 consecutive files. Hence, the intensity of the $^{48}\text{Ar}^+$ signal was normalised to the total number of ions obtained after summing.

Table 2.2: Summary of the production, preparation and measurement conditions for the isotopes $^{46-48}\text{Ar}$. In all cases, the MRToF trapping and the total preparation trap cycle are rounded. For the ToF-ICR data, the exact quadrupole excitation time applied in the measurement Penning trap is given. For the Ramsey type ToF-ICR resonances, the total quadrupole excitation time is decomposed as $\tau_{on}^{RF} - \tau_{off}^{RF} - \tau_{on}^{RF}$. See text for details.

Production					Preparation/Measurement				
Date	Target/Line	Source	Sep.	Energy	Ion	MRToF-MS	Prep. Trap	Meas. Trap	Method
July 2015	UC_x/Ta	VD7	HRS	30 kV	$^{46}\text{Ar}^+$	16.3 ms	104 ms	200 ms	$2 \times \text{ToF-ICR}$
					$^{47}\text{Ar}^+$	19.8 ms	104 ms	100 ms	$2 \times \text{ToF-ICR}$
								200 ms	$1 \times \text{ToF-ICR}$
Aug. 2017	UC_x/Ta	VD7	HRS	50 kV	$^{48}\text{Ar}^+$	16.7 ms		10-80-10 ms	$2 \times \text{Ramsey ToF-ICR}$
									$95 \times 1000\text{revs MRToF}$

Analysis of the data and mass determination

The previous chapter presented an overview of the experimental techniques used to produce, prepare, purify and measure the neutron-rich chromium and argon ions of interest for this work. The Penning trap mass spectrometry technique, which relies on the measurement of the free cyclotron frequency of an ion inside the trap's magnetic field, and the MRToF mass spectrometry technique, which relies on a time-of-flight measurement, were emphasized. While the content of both datasets were detailed, nothing was said regarding the data-analysis procedure. This chapter will present the general procedure used to extract a mass value from ToF-ICR resonances as well as its associated systematic errors and uncertainties. An MRToF-MS evaluation procedure based on binned maximum Likelihood estimation will be presented. A detailed review of the systematic errors of ISOLTRAP's MRToF-MS is missing from the literature. Hence, care will be taken to highlight the different sources of systematic errors considered for the analysis of the MRToF-MS data. Finally, specifics of the analysis of each dataset will be presented before providing a short comparison with existing datasets.

3.1 Generalities

3.1.1 ToF-ICR analysis

From Frequency ratio to mass

As we saw in the previous chapter, Penning-trap mass spectrometry relies on the determination of the free cyclotron frequency $\nu_c = \frac{qB}{2\pi m}$ of an ion of interest in the confining magnetic field of the trap. One can straightforwardly inverse the latter relation to express the mass-over-charge ratio of an ion as function of ν_c and the magnitude of the confining magnetic field B , which needs to be calibrated. In practice this is achieved by measuring the free cyclotron frequency of an ion of well-known mass (i.e whose mass is known to the $\sim 10^{-10}$ level) using the ToF-ICR technique presented in Chapter 2. Reference ions are most often provided by ISOLTRAP's offline ion source which delivers singly charged alkali ions of ^{39}K , ^{85}Rb , ^{133}Cs . Assuming that the ion of interest is also singly charged, which is the case for most ions delivered by the ISOLDE facility, its atomic mass m can be expressed as function of its mass cyclotron frequency ν_c , the mass of the

reference ion m_{ref} and the reference ion cyclotron ν_{ref} :

$$m = \frac{\nu_{c,ref}}{\nu_c}(m_{ref} - m_e) + m_e = r(m_{ref} - m_e) + m_e, \quad (3.1)$$

where m_e is the electron mass and r represents the frequency ratio :

$$r = \frac{\nu_{c,ref}}{\nu_c} = \frac{m^{ion}}{m_{ref}^{ion}}. \quad (3.2)$$

Expressing m as a function of the frequency ratio r not only eliminates the explicit B field dependence of the equation but also has a practical advantage since it allows for an easy re-determination of the mass of the ion of interest should the mass of the reference species be updated. Since the mass of the reference ions is well known, the statistical uncertainty of the mass to be determined is mostly influenced by the uncertainty on each of the frequency measurements.

Statistical uncertainty

The cyclotron frequency value and its associated statistical error are extracted using the EVA6 software which is very commonly used among the Penning trap mass spectrometry community [SR18]. This software performs a least-squares adjustment of the theoretical line shape to the experimental data points. Four free parameters and their associated errors are estimated : the cyclotron frequency, the overall time-of-flight offset, the magnetron radius inside the trap and a parameter ranging from 0 to 1 estimating the degree of completeness of the quadrupole conversion process.

The relative statistical uncertainty of a cyclotron frequency measurement with ISOLTRAP can be expressed using the following empirical formula [Bol01, K⁺03]:

$$\left(\frac{\delta\nu_c}{\nu_c}\right)_{stat} = \frac{c}{\nu_c \sqrt{N_{Tot} T_{RF}}} \propto \frac{1}{R \sqrt{N_{Tot}}}, \quad (3.3)$$

where N_{Tot} is the total number of recorded ions and c is dimensionless parameter close to 0.9 and which is mostly independent of the number of ions and T_{RF} . However, it varies slightly with the quality of the data. Hence, relation 3.3 brings forward the different factors which have an influence on the statistical uncertainty of the measured frequencies. We already touched upon how, in the context of the mass measurement of short-lived radioactive species, both the amount of data acquired and the excitation time can be limiting factors to the attainable resolving power of the ToF-ICR technique. These limitations also directly translate to the relative statistical uncertainty of a cyclotron frequency measurement. First, since the overall width of the ToF-ICR resonance is inversely proportional to the quadrupole excitation time, a long excitation time (~ 1 s) results in a narrow overall width (~ 1 Hz) of the resonance. In turns, this translates to an increased constrain on the center frequency estimation. In addition, the mean and width of the ToF distribution in each frequency step are the actual experimental quantities entering in the least-squares adjustment procedure used to yield the cyclotron frequency. Hence, it is easy to understand how the amount of statistics acquired in each step can directly influence the uncertainty of the extracted cyclotron frequency. Another factor which is found to influence the uncertainty of the measurement is related to the quality of the collected data. Indeed, several effects are known to cause the individual data points to scatter more or less around the

theoretical line shape. The most obvious such effects are directly related to how well the preparation of the ion ensemble and the excitation scheme inside the Precision Penning trap were setup (i.e timings, amplitude...). Additionally, we saw in the previous chapter that the presence of contaminants in high quantity can have detrimental effects on the measurement as it can induce shifts in the measured cyclotron frequency. Since their time-of-flight response to the excitation is different than that of the ions of interest, contaminants, even when present in low quantities, effectively add additional noise which can spoil the estimation of the mean time-of-flight at each frequency step. Such contaminants can obviously be isobaric but not only. Indeed, when working with short lived species, decay radiation can ionise the rest gas. Moreover, certain species are particularly prone to undergo charge-exchange reaction (e.g noble gases) or to chemically react with the impurities within our gas-filled traps.

Since the reference ions are stable species delivered by ISOLTRAP's offline ion source, the reference measurements are always pure high-statistics ($N_{Tot} \geq 1000$) resonances which are performed with a long excitation time (at most exclusively $T_{RF} = 1200$ ms). Hence, the statistical uncertainty of the frequency-ratio determination is mainly influenced by the precision with which the cyclotron frequency of the ion of interest is determined while the reference ions contribute only marginally.

Systematic errors

Since the different factors influencing the statistical uncertainty of a cyclotron-frequency measurement were briefly discussed in the previous paragraph, we have now to turn our focus towards the different sources of systematic errors. The latter were extensively studied for the ISOLTRAP mass spectrometer in [K⁺03].

The most problematic source of systematic error is that related to the presence of contaminant ions. We touched upon the influence of the presence of more than one ion in the trap and of contaminant ions on the measured cyclotron frequency in 2.3.3. This source of systematic error depends on the specific conditions faced during the experiment and as such, has to be treated on a case by case basis. Nonetheless, during data taking, the count rate is limited so that not more than 1-5 ions are on average detected [B⁺92]. This can also be performed during the analysis by considering only event where not more than 5 ion counts were detected. Coulomb interaction effects can be further studied during the analysis by performing a so-called "z-class" analysis. The latter consists in dividing the full data set into several subsets corresponding to different numbers of detected ions (or "z-classes"). The measured cyclotron frequency is then estimated for each "z-class" and the cyclotron frequency is then extrapolated to a number of detection event equivalent to the detection efficiency of the MCP system (usually around 20-30 %). This extrapolated frequency is then used, together with its associated error, to compute the frequency ratio [K⁺03].

One of the main sources of systematic error is related to the drift in the magnitude of the B -field with time. This means that at the time of the measurement of the cyclotron frequency of the ion of interest the trap's B -field will be slightly different from that at the time of the recording of the reference cyclotron frequency. The B -field drift has two main components. The first can be attributed to the decay of the current flowing through the superconducting magnet and results in a linear drift. The non-linear part of the magnetic field drift is related to fluctuations in ambient parameters such as a change in the helium pressure inside the trap's

cryostat or temperature fluctuations in the experimental area [K⁺03]. In order to correct for the linear B -field drift, reference measurements are performed shortly before and shortly after a measurement of the cyclotron frequency of the ion of interest. The cyclotron frequency of the reference ion is then linearly interpolated at the time at which the ion-of-interest's cyclotron frequency was recorded. The time stamp attributed for each cyclotron frequency is taken midway between the beginning and the end of the measurement. Because of the non-linear part of the B -field fluctuation the latter method does not perfectly correct bilisation for the B -field drifts. Since no pressure and temperature stabilisation systems are currently in place at ISOLTRAP the magnitude of the remaining part of the systematic error has been determined to be [K⁺03] :

$$\left(\frac{\delta\nu_c}{\nu_c}\right)_B = 6.35 \times 10^{-11} \Delta T / \text{min}, \quad (3.4)$$

where ΔT represents the elapsed time between the two reference measurements.

Another source of systematic error is related to the imperfection in the trap's electrostatic field. Such imperfections can arise from a deviation of the trap's electrostatic field from a pure quadrupole field, from misalignment between the trap electrodes or a mismatch between the symmetry axis of the E - and B -fields [B⁺90, Bla06]. These cause the measured frequency ratio r to deviate from the real values by an amount which is proportional to the mass difference between the ion of interest and the reference species. The magnitude of this so-called "mass dependent shift" was estimated using carbon clusters spanning the whole mass range [K⁺03]:

$$\left(\frac{\delta r}{r}\right)_m = 1.6 \times 10^{-10} (m - m_{ref}) / u. \quad (3.5)$$

In addition to the mass dependent and magnetic field drift, it was found that the measured frequency ratios still scatter around their true value to a degree which indicates the presence of residual systematic error (reduced χ^2 much greater than one) [K⁺03]. This magnitude of this systematic error was estimated to be :

$$\left(\frac{\delta r}{r}\right)_{res} = 8 \times 10^{-9}. \quad (3.6)$$

Mean frequency ratio and associated error

A frequency-ratio measurement consists of three cyclotron-frequency measurements. Two reference measurements, one taken right before and one right after the measurement of the cyclotron frequency of the ion of interest. The cyclotron frequency is estimated using the software EVA. The value of the reference cyclotron frequency is linearly interpolated to the time at which the ion of interest was recorded. This yields the frequency ratio r and its associated statistical error $(\delta r^i)_{stat}$. Since the magnetic field drift systematic error depends on the time elapsed between the two reference measurements, the magnetic-field drift error $(\delta r^i)_B$ is calculated at this stage and is added in quadrature to the statistical uncertainty to yield the uncertainty :

$$\delta r^i = \sqrt{(\delta r^i)_{stat}^2 + (\delta r^i)_B^2}. \quad (3.7)$$

This series of cyclotron frequency measurements is repeated a total of N times ($N = 2, 3, \dots$). The weighted mean of the frequency ratio is calculated to yield the

mean frequency ratio \bar{r} :

$$\bar{r} = \frac{\sum_i r^i / (\delta r^i)^2}{\sum_i 1 / (\delta r^i)^2}, \quad (3.8)$$

whose associated error is :

$$\delta \bar{r} = \sqrt{\frac{1}{\sum_i 1 / (\delta r^i)^2}}. \quad (3.9)$$

The scattering of the individual frequency ratio around \bar{r} is evaluated by calculating the reduced χ^2 and $\delta \bar{r}$ is eventually increased by a factor equal to the square root of reduced χ^2 if an over dispersion of the data is observed. The mean frequency ratio is then corrected for the mass dependent shift. A conservative approach is used whereby the magnitude of the mass dependent shift is also added in quadrature to $\delta \bar{r}$. The residual systematic is finally added in quadrature yielding the final absolute uncertainty [K⁺03]:

$$\delta \bar{r}_{final} = \sqrt{(\delta \bar{r})^2 + (\delta r)_m^2 + (\delta r)_{res}^2}. \quad (3.10)$$

The measured average frequency ratio is subsequently translated into a mass value and its associated error using equation 3.1.

3.1.2 MRToF-MS analysis

From time-of-flight spectra to mass values

First, let us recall equation 2.15 which links the mass m of an ion and its measured time-of-flight t after ISOLTRAP MRToF-MS :

$$t_i = a \sqrt{\frac{m_i}{q_i}} + b, \quad (3.11)$$

where a and b are calibrations parameters that need to be determined. To measure these parameters, the time-of-flight $t_{1,2}$ of two reference species of well known masses $m_{1,2}$ are used. If substituting (a, b) as a function of $t_{1,2}$ and $m_{1,2}$ in equation 3.11 and inverting it is perfectly possible the latter procedure would not allow for an easy re-evaluation of the mass-value should the mass of the reference species be updated at a later stage. Hence, the mass m of the ion of interest is rather expressed directly as function of the $t_{1,2}$ and $m_{1,2}$ as :

$$\sqrt{m} = C_{ToF} \Delta_{ref} + \Sigma_{ref} / 2, \quad (3.12)$$

where $\Delta_{ref} = \sqrt{m_1} - \sqrt{m_2}$, $\Sigma_{ref} = \sqrt{m_1} + \sqrt{m_2}$ while the coefficient C_{ToF} depends only on the measured time-of-flights and is expressed as :

$$C_{ToF} = \frac{2t - t_1 - t_2}{2(t_1 - t_2)}. \quad (3.13)$$

Several options are available regarding the choice of references. Of course these species can both be taken from ISOLTRAP's off-line ion source and in this case will be referred to as "offline" references. However, if contaminant species are present inside the ISOLDE beam and are close enough in mass such that they appear on the same number of turns as the ion of interest in the spectrum, they can also be used as references. These are the called "on-line" references. Most often, a stable

atomic or molecular ion contaminant, i.e a species of well known mass, falls into this category and therefore provides a perfect reference species. Using "online" references is always to be preferred over the choice of "offline" references since the former travel inside the MRToF device following a path similar to that of the ion of interest, thus cancelling out part of the systematics. In the following, the first species to be chosen as reference was an "offline" reference i.e ^{39}K , ^{85}Rb or ^{133}Cs ions provided by ISOLTRAP's offline ion source. The second reference was always chosen to be an "online" reference corresponding to a stable atomic or molecular ion.

Statistical uncertainty

The time-of-flight spectra used for the analysis are built by one of two commercial multi-channel analysers (model P7887 or MCS6A) manufactured by the company FAST ComTec GmbH [Com18]. These are being fed the direct output of the MRToF-MS time-of-flight detectors. The two multi-channel analysers differ mostly by their intrinsic resolution: 250 ps for the P7887 MCA and 100 ps for the MCS6A. The devices offer the possibility to process the input and build histograms, the binning of which is set as an integer multiple of the intrinsic resolution of the card. Hence, in the case of the P7887 MCA used for the chromium experiment time-of-flight spectra with a binning of 1 ns (i.e $4 * 250$ ps) were used. During the 2017 Argon experiment the MCS6A MCA was used to produce histograms with a binning of 0.8 ns ($8 * 100$ ps).

Let us assume there are N total number of bins in the histogram and define $n_{i=1,\dots,N}$ as the observed number of counts in bin i as well as $f_i(\theta)$ as the function describing the expected number of counts in bin i . The probability $p_i(\theta)$ of observing n_i counts in bin i when the expected number of counts in this bin is $f_i(\theta)$ follows a Poisson distribution : $p_i(\theta) = \frac{f_i(\theta)^{n_i} e^{-f_i(\theta)}}{n_i!}$ [Bar13]. Assuming that n_i is large (i.e $n_i \gg 5$ [Lyo86]) the Poisson probability distribution can be fairly well approximated by a Gaussian distribution of mean and variance $f_i(\theta)$. For practical reasons the variance of $p_i(\theta)$ is often replaced by the variance of the observed number of counts n_i [Lyo86]. Under these approximations the estimation of the set of parameters can be performed by minimising the quantity :

$$\chi^2 = \sum_{i=1}^N \left[\frac{n_i - f_i(\theta)}{n_i} \right]^2, \quad (3.14)$$

with respect to the set of parameters θ . This was the common method used for the analysis of MRToF spectrum. In the case of a high statistics time-of-flight distribution (e.g a reference peak) this method is straightforward and offer fast computing time. However, it suffers serious limitations when the statistics is low as is very often the case for a peak corresponding to an exotic species. In particular, problems arise if there are bins that have less than 5 counts since in this case the approximation that $p_i(\theta)$ is following a Gaussian distribution breaks down. In addition, in a least squares fit of an histogram, bins with zero counts are omitted since they lead to an estimated variance of zero. This result in biased fit results, which is detrimental for the accuracy of the analysis [BM13]. The problem of zero bins is especially problematic in our case. Indeed, assuming a flight time on the order of 20 ms (i.e for an ion of mass 80, after 1000 revolutions) and a resolving power R_{FWHM} of 100000, the full width at half maximum of an MRToF peak can be estimated to be on the order of 100 ns. This means that typically an MRToF

peak is around 200 ns wide in the spectrum i.e, it covers ~ 200 bins. Hence, at the very least $5 \times 200 = 1000$ ion events must be gathered in total if one wants at least $n_i = 5$. Hence, in most practical application the number of empty bins will be substantial. Grouping adjacent bins could be a solution to go around this problem. However, the number of empty bins often propagates in such a way that critical distortion of the peak shape are observed.

Hence, this method was not applied in this work and instead a binned maximum Likelihood fit was used. In this approach one considers that $p_i(\theta)$ is explicitly Poisson distributed and the probability of observing our histogram given the set of parameters θ is given by the so-called Likelihood function :

$$L(\theta) = \prod_{i=1}^N p_i(\theta) = \prod_{i=1}^N \frac{f_i(\theta)^{n_i} e^{-f_i(\theta)}}{n_i!}. \quad (3.15)$$

The set of parameters θ is obtained as the one maximising the value of L or, as most often used due to practical reasons, minimises the quantity $-\ln(L)$ [BM13]. The variance of a particular parameter θ_j is then given by the inverse of the second derivative of the log-likelihood function i.e : $\hat{V}(\theta_j) = \left(\frac{d^2 \ln(L)}{d\theta_j^2} \right)^{-1}$.

The mean of the time-of-flight distribution was estimated using the presented binned maximum likelihood method for the peaks corresponding to the two references and the ion-of-interest and used to compute the C_{ToF} coefficient. The latter method was built into a python data-analysis code written using the ROOFIT data-analysis toolkit which extends the native capabilities of the ROOT data analysis framework [WD05, BR97]. The statistical error of the CToF distribution follows from the propagation of the errors of the individual time-of-flight σ_{t,t_1,t_2} :

$$\sigma_{C_{ToF},stat} = \sqrt{\left(\frac{\partial C_{ToF}}{\partial t} \right)^2 \sigma_t^2 + \left(\frac{\partial C_{ToF}}{\partial t_1} \right)^2 \sigma_{t_1}^2 + \left(\frac{\partial C_{ToF}}{\partial t_2} \right)^2 \sigma_{t_2}^2} \quad (3.16)$$

Systematic Errors

The main source of systematic error is due to the individual fluctuations in the time-of-flight of species making the C_{ToF} coefficient. Time-of-flight fluctuations are mainly attributed to the variation in the voltage supplied to each mirrors. Because it is the closest to the reflection point, mirror 5 was shown to have the biggest influence on the mean time-of-flight of the peak as clearly visible in Figure 3.1 [W⁺12b]. The influence of mirror 5 is such that a ~ 0.1 part per million (i.e a few hundred μV of the applied ~ 2.5 keV) fluctuation in the applied voltage results in a ~ 1 ns mean time-flight-shift over a trajectory of 20 ms. This effect can be kept to an acceptable level by the use of high stability power supply. However, the question is, if such a shift does occur, how does it translate to a change in value of C_{ToF} ?

The partial derivatives of the C_{ToF} coefficient with respect to the time-of-flight of each of the species involved are important quantities to consider when examining how time-of-flight fluctuations impact the C_{ToF} value as well as to understand the "weight" of each species in the C_{ToF} uncertainty (and by extension to the mass

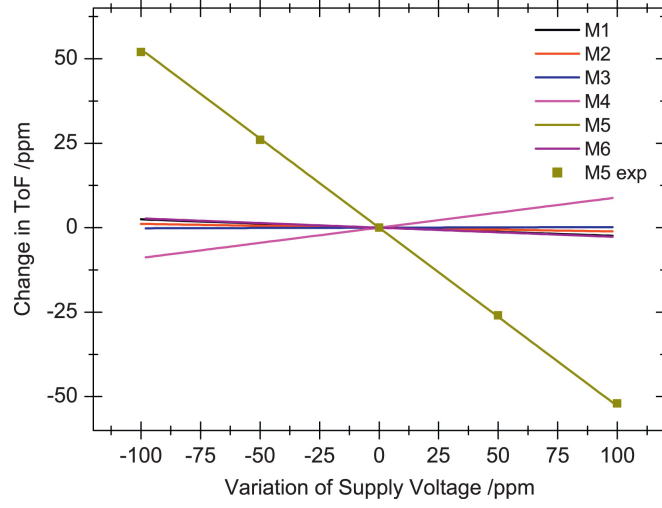


Figure 3.1: Time-of-flight deviation from the nominal value as function of the mirror-electrode voltages extracted from simulations (solid lines) and from experimental data (square points). Figure taken from [W⁺12b].

uncertainty). The partial derivative of C_{ToF} can be expressed as :

$$A = \frac{\partial C_{ToF}}{\partial t} = \frac{1}{t_1 - t_2}, \quad (3.17)$$

$$B = \frac{\partial C_{ToF}}{\partial t_1} = \frac{t_2 - t}{(t_1 - t_2)^2}, \quad (3.18)$$

$$C = \frac{\partial C_{ToF}}{\partial t_2} = \frac{t - t_1}{(t_1 - t_2)^2}. \quad (3.19)$$

Let t and t_1 be respectively the time of flight of the ion-of-interest and the online reference (i.e t and t_1 are contained within the same spectrum and are at most a few μs apart) while t_2 refers to the time of flight of the offline reference (e.g $^{85}\text{Rb}^+$, which for the two analysis presented is a few ms later than the online spectrum). One can already draw significant qualitative conclusions regarding the impact of time-of-flight drift on the C_{ToF} coefficient. Both A and B of 3.17 and 3.18 are on the same order of magnitude (i.e $\sim \left| \frac{1}{t_1 - t_2} \right|$) and of opposite sign meaning that a ToF drift affecting both the online reference and the ion-of-interest will cancel out. This give grounds to the claim which was made at the beginning of this section regarding the importance of choosing one reference among the stable contaminants within the same spectrum as the ion of interest. It is also apparent that, regardless of its sign, the factor C is a factor $\left| \frac{t - t_1}{t_1 - t_2} \right|$ smaller than the magnitude of both A and B demonstrating that a fluctuation impacting only the offline reference results in a change of C_{ToF} orders of magnitude lower. The absolute change in C_{ToF} can then be obtained by multiplying A, B or C by the corresponding ToF drift (and eventually by adding all these shifts in quadrature).

Figure 3.2 presents the relative impact of a shift in t, t_1 or t_2 on the value of the CToF coefficient. The CToF coefficient of Figure 3.2 is the one evaluated using $^{63}\text{Cr}^+$ and the isobaric $^{44}\text{Ca}^{19}\text{F}^+$ as the ion of interest and online reference (tof ~ 19 ms at 1000 revolutions while the two species are $\sim 1 \mu\text{s}$ apart) and $^{85}\text{Rb}^+$ as the offline reference (tof ~ 22 ms at 1000 revolution).

Another source of systematic uncertainty resides in the fact that there is no analytical formula that describes the peak shape of an MRToF device. Nothing yet

was said on the choice of function (or probability density function) f_i of 3.14 and 3.15. As can be seen in the bottom panel of Figure 2.10, the peaks present a clear asymmetry, leaning towards later time-of-flight values and making the time-of-flight estimation sensitive to the choice of "fit function". This tail is understood to originate from the ejection of the ion cloud from the ISOLTRAP buncher. Usually, in such experiments it is assumed that the peak shape is fairly well described by a Gaussian distribution. Since low-statistics peaks are fairly well approximated by a Gaussian peak shape and in order to keep consistency throughout the evaluation of the data a Gaussian peak shape was always assumed even for high statistic peaks presenting a tail.

In order to assess the influence of asymmetric probability density functions (pdfs) on the estimation of the mean time-of-flight two such pdfs were built using the ROOFIT package. Complex asymmetric pdfs incorporating up to 14 free parameters were purposely developed for the analysis of MRToF data [P⁺17]. However, since in our case the degree of asymmetry is somewhat low simpler asymmetric pdfs were considered. The "Single Exponential Gaussian" pdf results from the convolution of a precursor Gaussian and a precursor Exponential decay pdf while the "Double Exponential Gaussian" results from the convolution of two exponential decay pdfs of same decay constant (one on each side of the peak) and a central Gaussian. The latter pdfs thus require 3 parameters to be estimated : a mean, a standard deviation and a decay constant. These two pdfs have however several limitations. First, numerical instabilities when evaluating the convolution product can occur rendering the convergence of the parameter estimation very sensitive to its starting conditions. Secondly, strong correlations do exist between all three parameters rendering once more the convergence of the fit unstable while at the same time being potentially problematic for the estimation of the parameter confidence intervals since it may give rise to asymmetric errors. This becomes apparent when inspecting the profile likelihood functions (see [Dem13] for more information

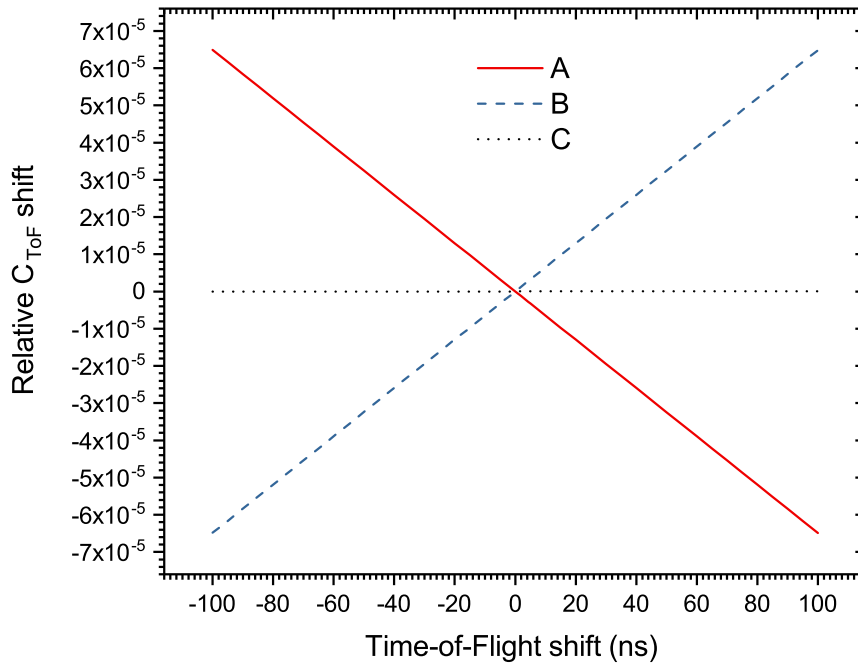


Figure 3.2: Relative change in the CToF coefficient as a function of the time-of-flight shift. The slopes of these curves are given by the coefficients A , B and C (see text for details).

of profile likelihoods). Hence, the choice was made to build a third asymmetric pdf, the "Exponential Gaussian Hybrid" (EGH) pdf, which uses an approximation of the exact SEG pdf presented in [L⁺01]. In the EGH pdf, the peak profile is parametrised as follows :

$$f_{egh}(t) = \begin{cases} H \exp(\frac{-(t-t_x)^2}{2\sigma^2 + \tau(t-t_x)}) & , 2\sigma^2 + \tau(t-t_x) > 0 \\ 0 & , 2\sigma^2 + \tau(t-t_x) < 0 \end{cases} \quad (3.20)$$

, where H and t_x are the coordinates of the peak maximum, σ is the standard deviation of the precursor Gaussian and τ is the time constant of the precursor exponential.

The EGH pdf has the advantage to reduce very significantly the correlation between the estimated parameters rendering the fit much more stable. It was thus used to study the influence of the fit result as function of the choice of the fitting pdf. Since the asymmetry is more or less pronounced from file to file the choice was made to evaluate the average time-of-flight difference between Gaussian and EGH peaks over many files. For each peak, the corresponding time-of-flight difference is subsequently translated into an uncertainty in the C_{ToF} value by multiplying the individual shifts by the corresponding coefficient of 3.17, 3.18 and 3.19.

As we saw in the previous Chapter, one of the limitations of MRToF devices is related to the Coulomb interaction between the ion species which causes the so-called "peak coalescence" phenomenon whereby the bunches corresponding to different species counter-intuitively tend to stick together rather than separate. This effect is obviously not only detrimental to the separation capabilities of the device but can also induce shifts of one species with respect to the other. The issue of Coulomb interaction inside the MRToF device is handled in the same fashion as the Penning trap. That is, the count rate is kept below a certain threshold in order to prevent significant impact on the measured mass. With the accumulated experience using the MRToF it has been observed that above a threshold of 7-8 ions detected per cycle this effect can start to play a significant role especially if the intensity ratio between species inside the device is unbalanced. One symptom is a systematic change in the difference between the time of arrival of two species within the same spectrum as a function of the beam gate. If the data is recorded so as to allow for an histogram to be saved cycle after cycle, one can perform a "z-class" analysis by splitting the total spectrum into subsets of different ion rate. The evolution of the measured C_{ToF} coefficient is thus monitored as a function of the ion rate. This procedure can only be performed in the case of high statistics and needs to be treated on a case by case basis.

Finally, besides online references the other species present in the dataset can be used to estimate the presence of a residual uncertainty after properly accounting for the aforementioned systematic errors. To this end, a C_{ToF} coefficient for these species is calculated using the same references as that used for the mass estimation of the ion of interest. In addition, a theoretical C_{ToF}^{AME} is calculated using the masses tabulated in the latest version of the atomic mass evaluation [W⁺17a]. The absolute residual systematic uncertainty is obtained by assuming it is evenly distributed over all the measurements and by imposing that the sum of squares deviation must be equal to its expectation value ν ; i.e numerically solving for $\sigma_{C_{ToF}}^{syst}$ in:

$$\sum_i \frac{(C_{ToF}^{AME} - C_{ToF}^{meas})_i^2}{(\sigma_{C_{ToF}}^{meas})_i^2 + (\sigma_{C_{ToF}}^{AME})_i^2 + (\sigma_{C_{ToF}}^{syst})^2} = \nu, \quad (3.21)$$

where the sum runs over all the species and ν corresponds to the total number of species taken into consideration.

Mean C_{ToF} error and associated error

In summary, the measurement of a C_{ToF} coefficient consists of the acquisition of a series of online spectra together with a series of offline references of $^{39}\text{K}^+$, $^{85}\text{Rb}^+$ and $^{133}\text{Cs}^+$ short before and/or after the online spectra. The mean time of flight of each peak, and its associated error is evaluated, using the binned maximum likelihood method assuming that the peaks follow a Gaussian distribution. This process is repeated for each online spectra at our disposal yielding N ($N = 2, 3, \dots$) individual C_{ToF} coefficients. Similarly to what is done for the measurement of frequency ratios, the weighted average $\overline{C_{ToF}}$ (and its corresponding statistical error $\sigma_{\overline{C_{ToF}},stat}$) of these N measurement is computed. The sum-of-square deviation between $\overline{C_{ToF}}$ and the individual data C_{ToF} is computed. In case a too large dispersion of the individual C_{ToF} is observed the $\sigma_{\overline{C_{ToF}},stat}$ is multiplied by the common square root of χ^2 factor. The systematic uncertainties related to the choice of fit function are evaluated. The influence of space charge related shifts is studied and its magnitude is pinned down. Finally, the absolute statistical uncertainty is computed and all sources of errors are added in quadrature to yield the final C_{ToF} uncertainty :

$$\sigma_{C_{ToF},total} = \sqrt{(\sigma_{\overline{C_{ToF}},stat})^2 + (\sigma_{C_{ToF},pdf})^2 + (\sigma_{C_{ToF},z-class})^2 + (\sigma_{C_{ToF},syst})^2}. \quad (3.22)$$

3.2 Neutron-rich argon isotopes

After briefly highlighting the analysis procedure for both ToF-ICR resonances and MRToF spectra. The following two sections will present the specifics of the analysis of the neutron-rich chromium and argon isotopes.

3.2.1 Analysis of the $^{46-47}\text{Ar}$ ToF-ICR resonances

^{46}Ar Analysis

As highlighted in Chapter 3, the acquisition of the ToF-ICR resonances for $^{46}\text{Ar}^+$ were particularly difficult because of the presence of the stable contaminant $^{34}\text{S}^{12}\text{C}^+$ requiring $m/\Delta m = 200\,000$ resolving power for the argon isotopes. Of course, this directly impacts the quality of the two ToF-ICR resonances that were recorded. In the end the outgasing of the stable contaminant meant that nearly clean resonances of $^{46}\text{Ar}^+$ were recorded and extra care was taken to assess the influence of this contaminant species. The presence of counts at a time-of-flight significantly lower than the base line close to the frequency of the contaminant (see dashed red vertical line in Figure 2.12) suggests that excited contaminant ions were observed.

Figure 3.3 represents the number of events as a function of the total number of ions recorded within the same event for one of the two resonances. One sees that a large majority of ejection resulted in no ions detected. As a result, on average only 0.2 ions per ejection were recorded. Hence, the probability of having more than one ion present inside the Penning trap at the same time is low. Hence, a strong influence of Coulomb effects is to be excluded. However, as described in the first section of the present chapter, these counts effectively add an additional

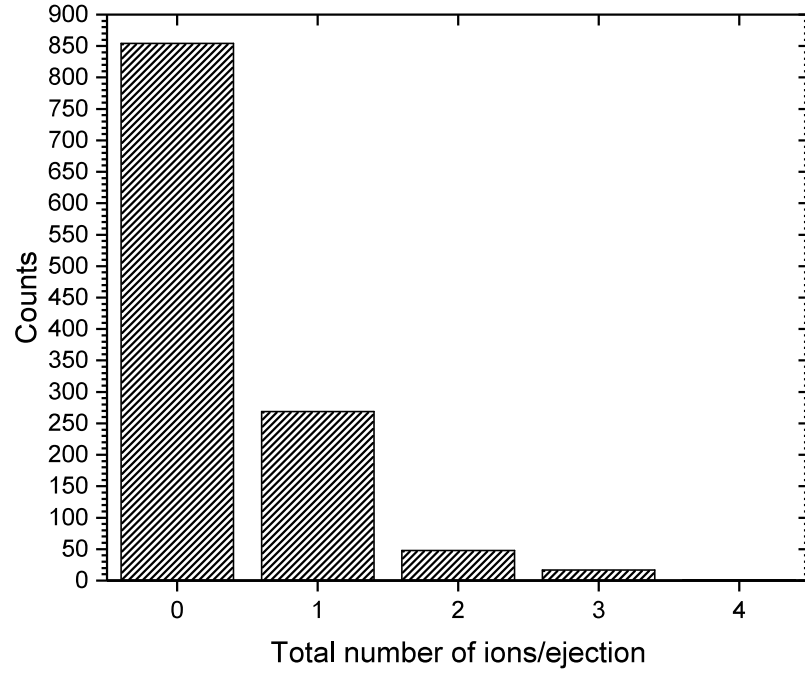


Figure 3.3: Histogram representing the number of detected ion for different total number of ions detected in one ejection. See text for details.

source of experimental noise which can influence the results of the fit. What Figure 3.3 shows is that among the events where ions were actually detected nearly 250 events correspond to one ion detected while this number drops by a factor 5 for 2 detected ions. For the "z-classes" where 2 or more are detected, the statistics is too low to allow for a proper estimation of the cyclotron frequency and a textbook "z-class" analysis as described in [K⁺03] is not possible.

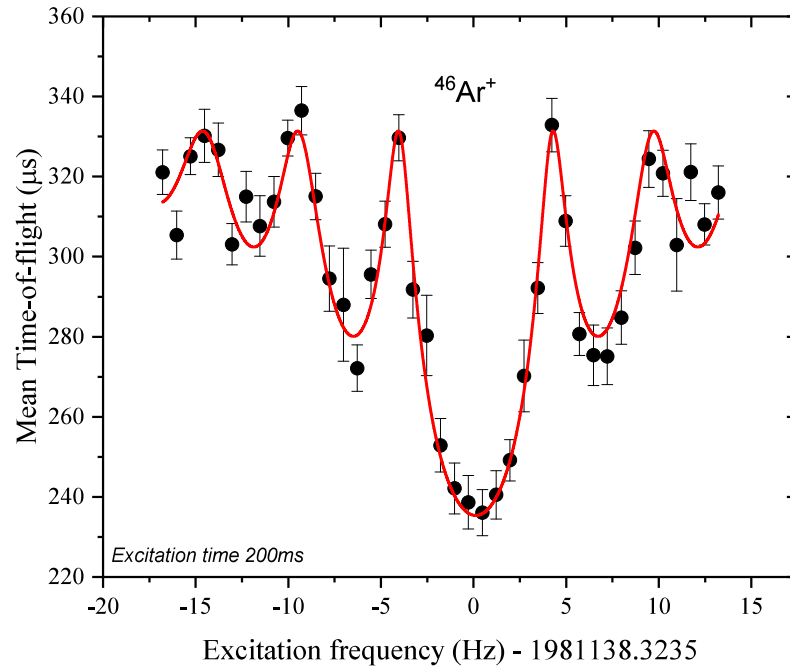


Figure 3.4: A $^{46}\text{Ar}^+$ resonance when only events where 1 detected ion per ejection are selected. The solid red line represents the result of the least-squares adjustment to the theoretical line-shape.

This situation being the same for both resonances, the frequency estimation was performed using only events where one ion count was recorded. An example of such a ToF-ICR resonance is shown on Figure 3.4 together with the associated adjusted line shape. As one can see the presence of the excited contaminant counts do not appear to significantly drag the estimated mean-of-flight towards lower values in the region close to the cyclotron frequency of $^{34}\text{S}^{12}\text{C}^+$ (~ 7.5 Hz to the right of the $^{46}\text{Ar}^+$ frequency). Nonetheless, the cyclotron frequency was also estimated using a line shape describing a double-resonance. However, within the statistical precision of the analysis no significant difference has been observed.

$^{39}\text{K}^+$ ions were used to provide the reference measurements yielding the mean frequency ratio corrected for the mass dependent shift of $R_{^{39}\text{K}^+}^{^{46}\text{Ar}^+} = 1.1797680972 \pm 6.4 \times 10^{-8}$. Hence, a relative precision of $\sim 5 \times 10^{-8}$ was reached for this measurement.

^{47}Ar Analysis

Fortunately, as described in the previous chapter the situation for mass $A=47$ was far different since it was possible to transport a clean $^{47}\text{Ar}^+$ beam to the precision Penning trap. Figure 2.11 attests of the purity and quality of the data obtained for this isotope which made the analysis on this mass straightforward. Once again $^{39}\text{K}^+$ ion were used as reference. The average frequency ratio resonance corrected for the mass dependent shift is thus : $R_{^{39}\text{K}^+}^{^{47}\text{Ar}^+} = 1.2055547092 \pm 3.4 \times 10^{-8}$ (relative uncertainty of $\sim 3 \times 10^{-8}$).

3.2.2 Analysis of ^{48}Ar MRToF spectra

In order to extract the mean time-of-flight of the ion distribution we identified as $^{48}\text{Ar}^+$, a specific probability density function was implemented. This pdf is composed of a sum of two components. The signal component used to describe the $^{48}\text{Ar}^+$ peak was chosen as a simple Gaussian pdf while the background is described by two Gaussians (one for each of the two background peaks). Besides the two Gaussians the background component also incorporates a uniform distribution in order to account for the seemingly uniform background covering the spectrum. The respective fractions of the two Gaussians were allowed to vary freely. Finally, in order to estimate the absolute strength of the background and signal components n_{bkg} and n_{sig} , the maximum-likelihood method was used in its extended form (c.f Extended Maximum Likelihood method in [BM13]). Hence, in total 8 free parameters were used in the adjustment. Figure 3.5 features an example of this fitting pdf. The individual components of the pdf are also represented.

This pdf was used to extract the time of flight information in 8 independant spectra. The stable $^{48}\text{SO}^+$ contaminant was used as online reference (relative AME-mass uncertainty $\sim \times 10^{-11}$). As the standard procedure dictates, the chemical nature of this contaminant was unambiguously identified by measuring its cyclotron frequency inside ISOLTRAP's measurement Penning trap. An offline beam of $^{85}\text{Rb}^+$ was used to provide the remaining reference. The scattering of the individual C_{ToF} values around their estimated average value was assessed yielding a reduced χ^2 value 1.05. Hence, as featured on Figure 3.6 no over or under-dispersion of the individual C_{ToF} values beyond statistical expectation was observed.

The data was recorded so as to maintain an unambiguous correlation between a start event (i.e buncher ejection trigger) and the stop events (ion detection signals)

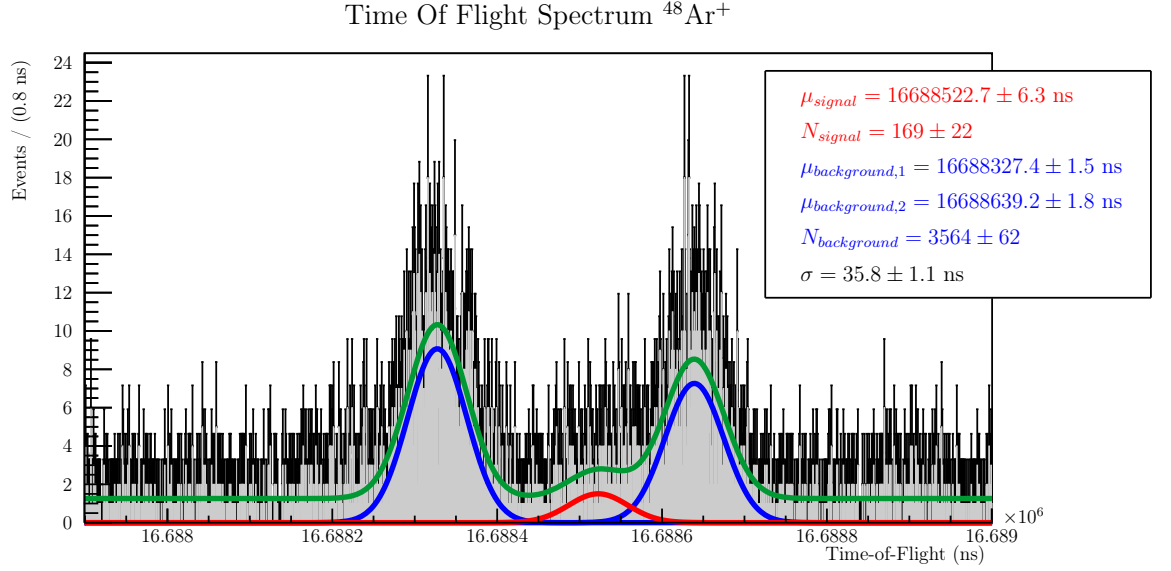


Figure 3.5: The model pdf used to extract the time of flight of $^{48}\text{Ar}^+$. The full pdf is represented using the solid green line while the solid blue and red lines represent respectively the background (two Gaussians) and signal (one Gaussian). The background component is used to constrain the width of the signal component. The reference $^{48}\text{SO}^+$ peak is outside the represented time of flight window.

recorded by the MCA. Hence, it is in theory possible to study the influence of the count rate on the fit result by performing a procedure very similar to a "z-class" analysis. What is especially important is that the time of flight difference between the online reference and ion of interest peak remain constant even at high count rate. However, similar to the situation encountered in the ToF-ICR

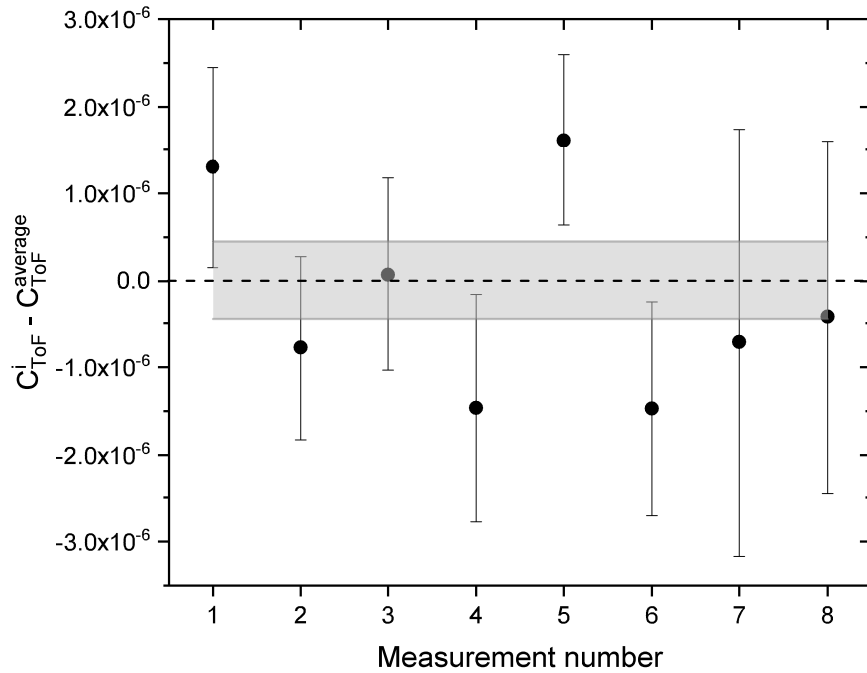
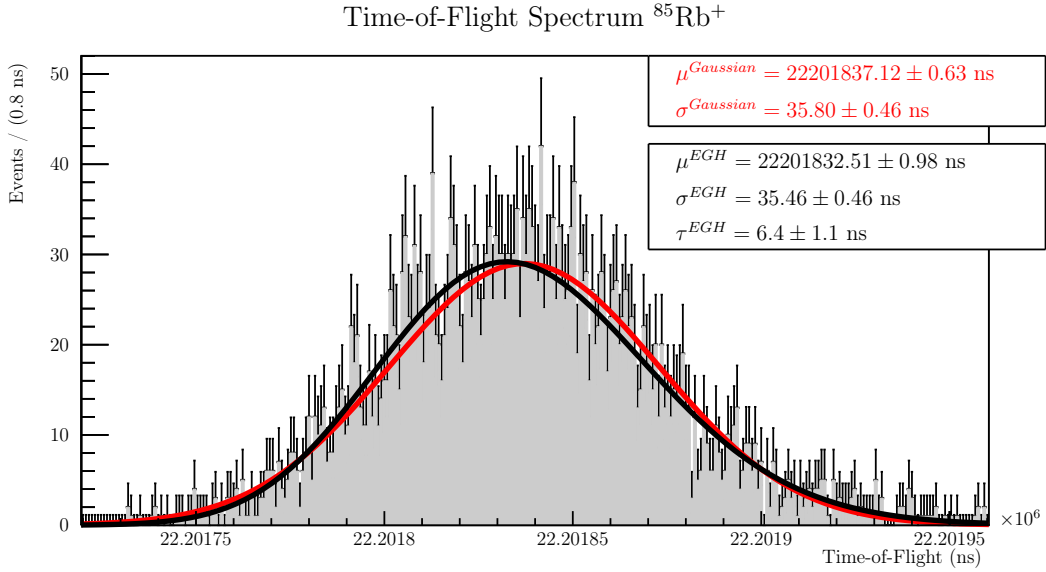


Figure 3.6: Scattering of the individual C_{ToF} coefficients around the average C_{ToF} value for $^{48}\text{Ar}^+$. The light-grey band represents the statistical 1σ band of the average C_{ToF} . The reduced χ^2 value is 1.05.

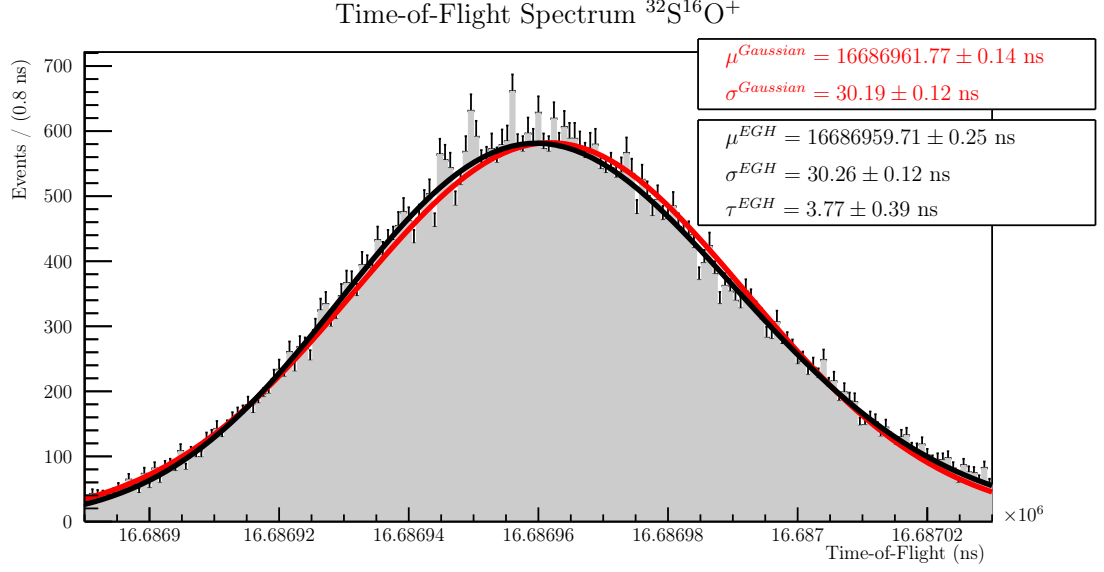
analysis of $^{46}\text{Ar}^+$, the total count rate was such that putting restrictions on the maximum number of ion events per start event ultimately results in a dramatic loss of statistics in the $^{48}\text{Ar}^+$ peak. Nonetheless, even if the beam gate was allowed to open for a various amount of time (between 10 to 40 ms) the overall count rate was always kept in a safe range (i.e below ~ 8 ions/event). Figure 3.6 is also further indication that, if present at all, the magnitude of the systematic uncertainty due to the Coulomb effect is below the statistical accuracy of the measurement.

Figure 3.7: Typical time-of-flight distribution of the $^{85}\text{Rb}^+$ offline reference. The peak distributions obtained after a fit to the data using a Gaussian pdf and the Exponentially Modified Gaussian pdf of [L⁺01] are represented in red and black respectively.



As far as fitting-procedure-related uncertainties are concerned, the robustness of the fit result with increasing binning was studied within the time of flight window of Figure 3.5. To this end, all spectra were fit using successively a bin width of 0.8 ns (corresponding to the binning with which the data were recorded), 1.6 ns (grouping 2 adjacent bins together), 3.2 ns (grouping of 4) and finally 4.8 ns (grouping 6 bins together). Up to binning 6 no difference in the extracted time of flight of $^{48}\text{Ar}^+$ and the neighboring unknown species could be observed beyond the statistical accuracy of the measurement.

Another source of systematic error to consider is the one related to the shape of the time of flight peak. Figure 3.7 and 3.8 show the fit results obtained using a Gaussian (in red) and the Exponentially Modified Gaussian pdf of [L⁺01] (in black) for the $^{85}\text{Rb}^+$ offline reference and $^{32}\text{S}^{16}\text{O}^+$ online reference. For all eight $^{85}\text{Rb}^+$ peaks used in this analysis, the difference in the estimated mean using both pdfs has been estimated to be of $5.0 \text{ ns} \pm 1.2 \text{ ns}$. The same average computed for the online $^{32}\text{S}^{16}\text{O}^+$ yields a difference of $1.3 \text{ ns} \pm 0.3 \text{ ns}$. Since in both cases the difference is not fully covered by the statistical uncertainty, the absolute value of the average time of flight difference was taken as a systematic uncertainty. In order to translate these shifts into a C_{ToF} variation, the coefficients of Equation 3.17-19 were computed (see discussion in 3.1.2). For $^{32}\text{S}^{16}\text{O}^+$, this procedure yields an absolute systematic error of the C_{ToF} coefficient of 2.35×10^{-7} while for $^{85}\text{Rb}^+$

Figure 3.8: Same as Figure 3.7 but for the online reference $^{32}\text{S}^{16}\text{O}^+$.

it is only 2.6×10^{-10} . Since the amount of statistics did not allow the same study concerning the $^{48}\text{Ar}^+$ time of flight distribution, the same systematic uncertainty as for the $^{32}\text{S}^{16}\text{O}^+$ peak was assumed.

The average C_{ToF} value, $C_{^{32}\text{S}^{16}\text{O}^+, ^{85}\text{Rb}^+}^{^{48}\text{Ar}^+} = 0.499715668 \pm (450)^{\text{stat}} \pm (332)^{\text{syst}}$. Adding the systematic and statistical uncertainties in quadrature yields a total uncertainty of 5.60×10^{-7} on the average C_{ToF} value.

3.2.3 Results

Table 3.1 summarizes the experimental results from this analysis. The newly obtained atomic mass excesses computed using $R_{^{39}\text{K}^+}^{^{46}\text{Ar}^+}$, $R_{^{39}\text{K}^+}^{^{47}\text{Ar}^+}$ and $C_{^{32}\text{S}^{16}\text{O}^+, ^{85}\text{Rb}^+}^{^{48}\text{Ar}^+}$ are presented. For comparison the recommended values from the most recent Atomic Mass Evaluation (AME2016) are also presented (values from the AME2012 are given for the sake of completeness) [W⁺17a, A⁺12]. The proximity between the AME2016 mass excess and the one reported in this work is explained by the fact that very preliminary values for $R_{^{39}\text{K}^+}^{^{46}\text{Ar}^+}$ and $R_{^{39}\text{K}^+}^{^{47}\text{Ar}^+}$ were privately communicated to the AME evaluators prior to the publication of the AME2016 [W⁺17a].

The mass excess of ^{46}Ar was primarily determined through two Q -value measurements : one in 1974 using the $^{48}\text{Ca}(^6\text{Li}, ^8\text{B})^{46}\text{Ar}$ reaction [J⁺74] and in 1980 using the $^{48}\text{Ca}(^{14}\text{C}, ^{16}\text{O})^{46}\text{Ar}$ reaction [M⁺80]. These measurements were complemented by a direct measurement performed using the Isochronous Mass Spectrometry technique at FSR-ESR storage ring (GSI, Germany) [Mat04] in 2004. All together these three measurements yielded a AME2012 [A⁺12] value for the ^{46}Ar atomic mass excess of $\text{ME}(^{46}\text{Ar})^{2012} = -29730 \pm 40 \text{ keV}$. Hence, our new measurement deviates by 41.3 keV (i.e just about 1 combined sigma deviation) from the value reported in the AME2012 and brings a factor 40 improvement in precision. The increase in precision is such that, as Table 3.1 shows, our Penning-trap measurement now carries the most weight in the determination of the AME2016 ^{46}Ar mass excess value.

Indeed the AME2012 atomic mass excess for this isotope was mainly influenced

Table 3.1: Frequency ratios ($r = \nu_{c,ref}/\nu_c$), time of flight ratios (C_{ToF}) and mass excesses of the argon isotopes measured in this work. Values of the mass excesses from the Atomic-Mass Evaluation 2016 (AME2016) [W⁺17a] are given for comparison. Values from AME2012 are also given [A⁺12] (# designates AME2012 extrapolated value). The masses of the reference ions were also taken from AME2016. Experimental half-lives are taken from the NUBASE2016 evaluation [A⁺17c].

Species	Half-life	Reference	ratio R or C_{ToF}	Mass Excess (keV)		
				New	AME2016	AME2012
⁴⁶ Ar	8.4(0.8) s	³⁹ K	$r = 1.1797680972(640)$	-29 771.3(2.3)	-29 772.9(1.1)	-29 730(40)
⁴⁷ Ar	1.23(0.03) s	³⁹ K	$r = 1.2055547092(340)$	-25 367.3(1.2)	-25 366.3(1.1)	-25 210(90)
⁴⁸ Ar	415(15) ms	³² S ¹⁶ O/ ⁸⁵ Rb	$C_{ToF} = 0.499715668(560)$	-22 354.8(16.5)	-22 280(310)	-22 440# (300)#

by the measurement of the Q -value of the reaction ⁴⁶Ar(d,p)⁴⁷Ar [G⁺06b]. In this study the authors reported a 700-keV deviation to a previous measurement obtained from the reaction ⁴⁸Ca(¹⁴C,¹⁵O)⁴⁷Ar [B⁺85]. In addition, the AME2012 also includes two direct time-of-flight measurements of ⁴⁷Ar [T⁺90, S⁺00] which due to their large uncertainty bore no significant weight in the estimation. Together these measurements yielded an AME2012 atomic mass excess of : $ME(^{47}\text{Ar})^{2012} = -25210 \pm 90$ keV. In addition to these measurements, the AME2016 also includes one more time of flight measurement performed at GANIL [G⁺12] as well as the preliminary value of the reported Penning-trap measurement of the ⁴⁷Ar mass excess. This time around, our measurement brings a factor 90 improvement in precision over the AME2012 mass excess while at the same time deviating by 157.3 keV from the latter. Once again, Table 3.1 shows that our preliminary Penning-trap value (and by extension the final reported in this work) carries all the weight of the estimation of the ⁴⁷Ar mass excess.

The B ρ -tof measurements performed at the NSCL [M⁺15a] were the first to report on a mass-excess value for the ⁴⁸Ar isotope. As a result this measurement is the only source on which the AME2016 ⁴⁸Ar mass excess is based and as a result : $ME(^{48}\text{Ar})^{NSCL} = ME(^{48}\text{Ar})^{AME2016} = -22280 \pm 310$ keV. An independent direct time of flight was recently performed at RIKEN, as a by-product of a measurement campaign focused on very exotic calcium isotopes, yielding a mass excess value of : $ME(^{48}\text{Ar})^{RIKEN} = -22330 \pm 120$ keV [Mo18]. This measurement, in agreement with that of NSCL, brought a factor 2.5 improvement in precision. In contrast, our measurement of the ⁴⁸Ar mass excess shows a factor ~ 19 improvement in precision while deviating from 74.8 keV from the AME2016 value. When compared to the RIKEN measurement our measurement still brings a factor ~ 7 improvement in precision and deviates from the RIKEN measurement by ~ 25 keV which is well within one combined sigma. Figure 3.9 shows the deviation of the atomic mass excess of ⁴⁶–⁴⁸Ar obtained in this work with respect to the AME2012 values (for ⁴⁸Ar the AME2012 extrapolation is replaced by the result from [M⁺15a]).

3.3 Neutron-rich chromium isotopes

3.3.1 Analysis of the ^{58–62}Cr⁺ ToF-ICR resonances

As described in the previous chapter the neutron-rich chromium dataset is considerably larger than the neutron-rich argon dataset but the experimental conditions were much more favourable. The use of the element-selective ISOLDE RILIS not only brought a significant ionisation efficiency improvement over the surface-

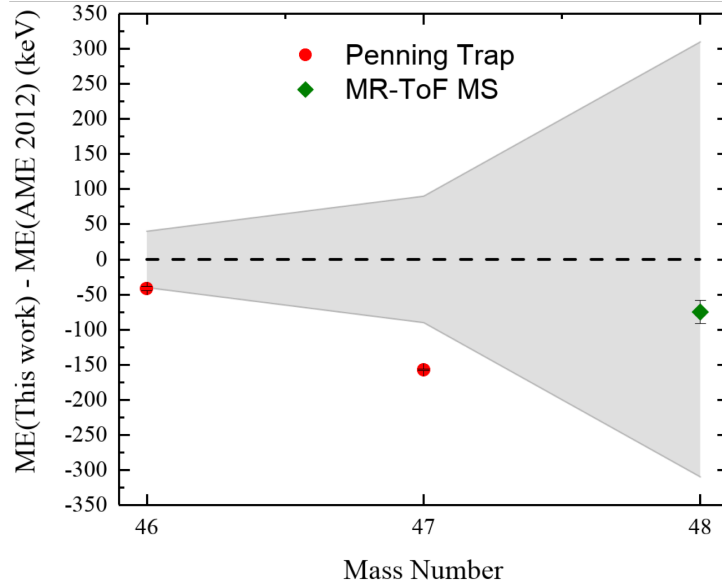


Figure 3.9: Deviation of the atomic mass excess of $^{46-47}\text{Ar}$ obtained in this work with respect to the AME2012 values. For ^{48}Ar our result is compared with that of [M⁺15a]. The grey shaded area represent the 1- σ uncertainty band. The filled red circles represent the values obtained from the Penning trap measurement while the green diamonds represent the MRToF-MS measurements.

ionised chromium ion beam but also it made for a very straightforward identification of the chromium species inside the MRToF. In the case of the isotopes $^{58-62}\text{Cr}$, the resolving power required to fully separate chromium from the surface ionised isobaric contaminants was such that the MRToF-MS was by far sufficient to clean away all contaminants thus providing a clean chromium-ion beam to the measurement Penning trap. An example of such an MRToF-MS spectrum obtained for $A = 59$ is shown in Figure 3.10. Such clean experimental conditions directly translated into a straightforward analysis of the ToF-ICR data. In all cases $^{85}\text{Rb}^+$ reference ions were used. For each species the obtained frequency ratio and the corresponding atomic mass excesses are reported in Table 3.2. Special care was taken regarding the final uncertainty of the $R_{^{85}\text{Rb}^+}^{^{58}\text{Cr}^+}$ frequency ratio. Indeed, after the filling of the measurement Penning trap's cryostat with liquid nitrogen, reference measurements performed using the pair of stable ions ($^{55}\text{Mn}^+$, $^{85}\text{Rb}^+$) showed a relative deviation of 5.26×10^{-8} for a total relative uncertainty of 1.00×10^{-8} . Since, in the AME the mass of the $^{55}\text{Mn}^+$ is determined consistently from five different routes [A⁺12] it was decided to include the relative frequency ratio deviation as a systematic uncertainty on the $R_{^{85}\text{Rb}^+}^{^{58}\text{Cr}^+}$ frequency ratio measurement. This procedure yields an additional 3.76×10^{-8} absolute uncertainty on the measured frequency ratio which is to be added in quadrature to the 1.12×10^{-8} absolute uncertainty obtained for the $R_{^{85}\text{Rb}^+}^{^{58}\text{Cr}^+}$ frequency ratio measurement.

3.3.2 Analysis of the $^{59-63}\text{Cr}^+$ MRToF-MS spectra

The neutron-rich chromium data set not only includes Penning-trap measurements for the isotopes $^{59-62}\text{Cr}$ but also allows for the determination of the atomic mass excess of the same isotopes using the MRToF-MS mass spectrometer. This constitutes a perfect opportunity to compare the results of both techniques. An example of the MRToF spectra used for this analysis is shown in Figure 3.10 for $A = 59$ and

corresponds to 1000 revolutions inside the MRToF-MS. In contrast to the $^{59-62}\text{Cr}$ isotopes, the yield of ^{63}Cr (estimated to be around 30 ions/s) was such that its transport to the precision Penning trap was not possible and only MRToF data are available for this isotope (a typical spectrum for this isotope is represented in Figure 2.10). For each isotope, a CaF^+ isobaric molecular ion was present in the spectrum and provided a perfect online reference. For the offline reference, $^{85}\text{Rb}^+$ ions from the ISOLTRAP offline ion source were used. The data analysis was performed using the binned Likelihood method described above. For each of the Cr isotopes considered, the C_{ToF} value was computed. This work being performed at an earlier stage of the thesis meant that the peak shape was handled differently than the method described in the argon section. There is no denying that the peak shape we encountered in this analysis is not Gaussian. However, since in addition to a Gaussian-like part the peaks also have a tail which becomes visible when the ion signal has dropped by about an order of magnitude with respect to its maximum. For example, in Figure 2.10 the ^{63}Cr peak appears more Gaussian than the CaF or TiO peak. When assuming a time-of-flight distribution described by the EGH pdf, imposing the shape parameters derived from peaks with higher statistics on the ^{63}Cr peak lead to numerical instability in the fit. Hence, for consistency reasons the analysis was performed using only a Gaussian peak shape. For this analysis, the peak shape uncertainty was taken into account on a case-by-case basis by evaluating how, for each peak, the choice of fit range influences the fit result.

In the whole data set, nine isobaric contaminants of well-known masses were identified : $^{59}\text{Mn}^+$, $^{59}\text{Fe}^+$, $^{60}\text{Ni}^+$, $^{61}\text{Fe}^+$, $^{61}\text{Mn}^+$, $^{61}\text{Ni}^+$, $^{45}\text{Sc}^{16}\text{O}^+$, $^{46}\text{Sc}^{16}\text{O}^+$, $^{124}\text{Sn}^{2+}$. For each of them, a coefficient $C_{\text{ToF}}^{\text{meas}}$ was evaluated. Similarly, a coefficient $C_{\text{ToF}}^{\text{AME}}$ was computed using the mass values as found in AME2012 [A⁺12]. The absolute systematic uncertainty on the C_{ToF} coefficients was evaluated by numerically solving the equation $\sum_{i=1}^9 \frac{(C_{\text{ToF}}^{\text{AME}} - C_{\text{ToF}}^{\text{meas}})_i^2}{(\sigma_{C_{\text{ToF}}}^{\text{meas}})_i^2 + (\sigma_{C_{\text{ToF}}}^{\text{AME}})^2 + (\sigma_{C_{\text{ToF}}}^{\text{sys}})^2} = 9$. This procedure yielded $C_{\text{ToF}}^{\text{sys}} = 0.87 \times 10^{-6}$ which was added in quadrature to the statistical uncertainty.

Finally, for this data set Coulomb interaction was only considered for ^{63}Cr . Indeed, for this isotope the production was so low that the beam gate was significantly increased during the recording of the data. As a result, an average of 30 ions per detection event was recorded in each of the seven spectra used for the analysis. Since at the time the data was recorded in a way which did not allow to perform a "z-class" analysis the question remained on how to assess the magnitude of the possible systematic uncertainty. Hence, the choice was made to rely on the 2014 data set. In the 2014 data set, the mass excess of ^{58}Cr could also be evaluated using MRToF spectra and the isobaric ^{58}Fe contaminant as online reference. In this case the average number of ions detected per event was similar to that of ^{63}Cr and the mass of ^{58}Cr evaluated in this way presented a 110 keV deviation to our Penning trap measurement. In the $A = 58$ spectrum the observed time of flight difference between the chromium and iron peak was ~ 1700 ns. For $A = 63$ the time of flight difference between the calcium fluorine peak and the chromium peak was around 1100 ns. Hence, the mass excess shift observed from the $A = 58$ spectrum for 1700 ns was scaled linearly to a shift of 1100ns. This yields an additional absolute systematic uncertainty of 3.74×10^{-6} to consider for ^{63}Cr .

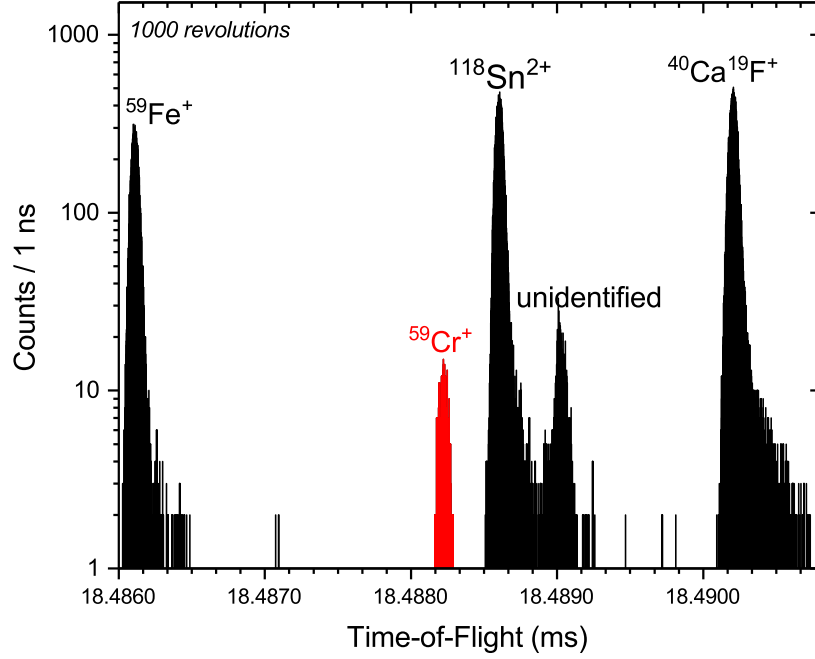


Figure 3.10: Typical MRToF spectrum for $A = 59$ at 1000 revolutions. The time of flight distribution corresponding to $^{59}\text{Cr}^+$ is represented in red.

3.3.3 Results

Table 3.2 also presents the atomic for $^{58-63}\text{Cr}$ mass excesses calculated using the frequency ratios as well as the C_{ToF} coefficients measured. At this stage it is already worth noticing that the atomic mass excesses obtained for $^{59-62}\text{Cr}$ from the Penning trap and MRToF-MS measurement do agree within their uncertainties. In this table, the new mass values are compared to the latest version of the AME [W⁺17a]. However, the mass excess obtained in this work for ^{58}Cr is already included in the AME2016 as private communication and as a result we will be discussing in the following the comparison of our results with the values of the AME2012 [A⁺12] before discussing the recent $B\rho$ -tof measurements of $^{59-64}\text{Cr}$ performed with the S800 spectrometer at the NSCL [M⁺16].

As far as the isotopes $^{58-60}\text{Cr}$ are concerned, the AME2012 atomic excess results from three independent measurement performed at the time of flight isochronous (TOFI) recoil spectrometer at Los Alamos [T⁺90, S⁺94a, B⁺98]. Compared to the AME2012 value the $\text{ME}(^{58}\text{Cr})^{2012} = -51830 \pm 200$ keV our Penning trap measurement provides a ~ 230 fold improvement in the uncertainty. At the same time, the new mass excess deviates by ~ 162 keV. Similarly, our Penning trap measurement of ^{59}Cr brings a factor ~ 360 improvement over the AME2012 mass excess. For this isotope, a 226 keV deviation from the AME2012 mass excess is obtained with $\text{ME}(^{59}\text{Cr})^{2012} = -47890 \pm 240$ keV. The most significant deviation from our newly obtained mass values to the AME2012 is obtained for ^{60}Cr ($\text{ME}(^{60}\text{Cr})^{2012} = -46500 \pm 210$ keV). Our Penning trap measurement deviates by ~ 408 keV from the AME value (nearly a $2\text{-}\sigma$ deviation) and brings a factor 190 fold improvement in the uncertainty.

For $^{61,62}\text{Cr}$ the results from [T⁺90, S⁺94a, B⁺98] are complemented by the Isochronous Mass Spectrometry measurement from [Mat04]. On the one hand, our newly obtained Penning trap mass value for ^{61}Cr deviates from the AME2012 one by ~ 36 keV and the uncertainty is brought down by a factor 70 from 130 keV

to 1.8 keV. On the other hand, our ^{62}Cr value deviates from the AME2012 value by ~ -42 keV and the uncertainty is brought down by a factor ~ 40 from 148 keV to 3.5 keV.

Finally, for ^{63}Cr the AME2012 mass excess is linked by two direct measurements : one from [Mat04] and a $B\rho$ -tof measurements performed at the NSCL [E⁺11]. Our MRToF measurement deviates by about 455 keV from the AME2012. The roughly 70 keV uncertainty of our MRToF-MS measurement is obviously large but is still a factor 6 smaller than that of the AME2012. Figure 3.11 shows the deviation of the atomic mass excess of $^{58-63}\text{Cr}$ obtained in this work with respect to the AME2012 values.

If only one of the newly measured mass excesses deviates from the AME2012 by more than one combined standard deviation, it should be stated that the many-fold uncertainty improvement brought by our new measurement of $^{58-62}\text{Cr}$ and the MRToF-MS measurement of ^{63}Cr will carry all the weight of the AME value for these isotopes. Indeed, very few new measurement were added in the 2016 version of the AME. The work from [X⁺15] performed at the CSRe in Langzhou reported on a IMS mass measurement of ^{61}Cr while $^{59-64}\text{Cr}$ were measured at the NSCL by Meisel and collaborators [M⁺16]. The latter measurements explain why the AME2016 mass excesses reported in Table 3.2 appear to be closer to our new results than what was observed for the AME2012. Indeed, apart from ^{62}Cr , all the mass-excess values from this work are lower (i.e the isotopes are found to be more bound) than in the AME2012 compilation. For $^{59,60,61}\text{Cr}$, [M⁺16] reports mass values which are between 420 and 580 keV more bound than found in this work. For ^{62}Cr both studies report a nucleus which is less bound by 42 keV and 37 keV for our study and theirs respectively, while ^{63}Cr appears more bound in both studies but our measurement indicate a nucleus ~ 200 keV more bound than found in [M⁺16]. As it is the case with all the previous measurements, the precision of the measurements of [M⁺16] is never below 400 keV making any reliable nuclear physics discussion difficult. Hence, we are confident that our newly obtained measurements can shine new light on the development of ground-state collectivity in the chromium isotopic chain.

Table 3.2: Frequency ratios ($r = \nu_{c,ref}/\nu_c$), time of flight ratios (C_{ToF}) and mass excesses of the chromium isotopes measured in this work. Values of the mass excesses from the Atomic Mass Evaluation 2016 (AME2016) [W⁺17a] are given for comparison. Values from AME2012 are also given [A⁺12]. The masses of the reference ions were also taken from AME2016. Experimental half-lives are taken from the NUBASE2016 evaluation [A⁺17c]. The yields correspond to the number of chromium ions per second delivered by the ISOLDE facility. The total transport efficiency of the experiment was estimated to be 0.5% behind the MR-ToF MS. The average proton current on target was 1.8 μA .

Species	Yield (ions/s)	Half-life	Reference	ratio R or C_{ToF}	Mass Excess (keV)		
					New	AME2016	AME2012
^{58}Cr	Not determined	7.0(0.3) s	^{85}Rb	$r = 0.6824024142(376)$	-51 991.8(3.0)	-51 991.8(1.5)	-51 830(200)
^{59}Cr	3×10^5	1050(90) ms	^{85}Rb	$r = 0.6942284208(85)$	-48 115.9(0.7)	-48 090(220)	-47 890(240)
			$^{40}\text{Ca}^{19}\text{F}/^{85}\text{Rb}$	$C_{ToF} = 0.500536923(887)$	-48 132(20)		
^{60}Cr	2×10^4	490(10) ms	^{85}Rb	$r = 0.7060206906(138)$	-46 908.5(1.1)	-46 670(190)	-46 500(210)
			$^{41}\text{Ca}^{19}\text{F}/^{85}\text{Rb}$	$C_{ToF} = 0.500484920(886)$	-46 917(19)		
^{61}Cr	2×10^3	243(9) ms	^{85}Rb	$r = 0.7178534753(230)$	-42 496.5(1.8)	-42 480(100)	-42 460(130)
			$^{42}\text{Ca}^{19}\text{F}/^{85}\text{Rb}$	$C_{ToF} = 0.500120578(976)$	-42 503(20)		
^{62}Cr	3×10^2	206(12) ms	^{85}Rb	$r = 0.7296512630(440)$	-40 852.6(3.5)	-40 890(150)	-40 890(150)
			$^{43}\text{Ca}^{19}\text{F}/^{85}\text{Rb}$	$C_{ToF} = 0.500047948(921)$	-40 841(18)		
^{63}Cr	3×10^1	129(2) ms	$^{44}\text{Ca}^{19}\text{F}/^{85}\text{Rb}$	$C_{ToF} = 0.49964187(386)$	-36 178(73)	-36 010(360)	-35 720(460)

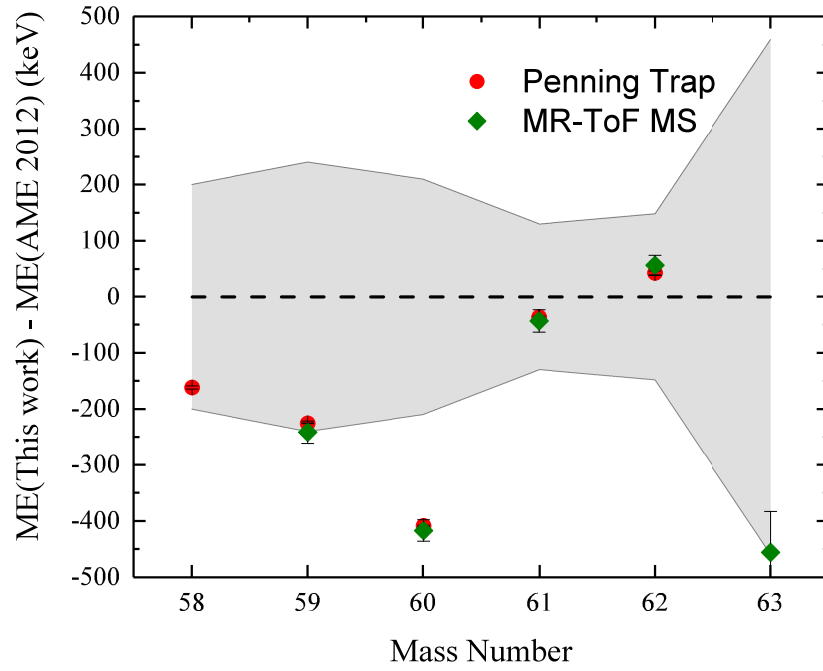


Figure 3.11: Deviation of the atomic mass excess of $^{58-63}\text{Cr}$ obtained in this work with respect to the AME2012 values. The grey shaded area represent the AME2012 uncertainty band. The filled red circles represent the values obtained from the Penning trap measurement while the green diamonds represent the MRToF-MS measurements.

Theoretical approaches to the nuclear many-body problem

Before focusing on the implication of the newly obtained mass values (c.f Chapter 3) on nuclear structure, we shall give in the following Chapter a brief introduction to the relevant theoretical approaches. The first section will present generalities concerning the nuclear many-body problem. We will see that while the nuclear many-body problem can be posed in a quite straightforward manner, its resolution faces strong conceptual and technical difficulties. In the following sections the concepts pertaining to the most prominent modern theoretical approaches to nuclear structure, namely the interacting shell-model and the nuclear density-functional theory, will be described. For each approach, a computer code implementing the resolution of the nuclear many-body problem and corresponding test calculations will be presented. Finally, the last section will focus on a fast developing *ab-initio* approach to nuclear structure rooted within the framework of the In-Medium Similarity-Renormalization-Group.

4.1 The nuclear many-body problem

4.1.1 Formulation of the problem

Historically, one of the first attempts to describe nuclear properties, which were predominantly binding energies, has been to consider that the nucleus behaves like a charged liquid drop. This Liquid Drop Model was at the foundation of several nuclear physics theoretical milestones such as the empirical mass formula of Bethe and Weizsäcker [Wei35, B⁺36], the description of nuclear fission [MF39] or, allowing the liquid drop to assume a deformed shape, the famous collective Bohr Hamiltonian [Boh52]. Even if a rigorous quantization of the Bohr Hamiltonian (see Chapter 1 of [RS80]) allows for a satisfactory description of vibrational and rotational states, the aforementioned approaches are in essence based on a macroscopic picture of the nucleus.

The aim of the following section is to lay the early groundwork for a fully microscopic description of the nucleus and its properties (binding energies, spins, parities, electromagnetic moments) of ground and excited states. We will also try to justify some of the adopted starting hypothesis. To this end, a discussion (inspired by that of Chapter 7 of [HJ⁺17]) on typical energy scales relevant to our problem is quite insightful. The typical energy of any nuclear process is situated

in the MeV range. Atoms, on the contrary, involve processes the typical energy of which are more than three orders of magnitude smaller (up to around 100 keV for the most energetic X-ray in heavy nuclei). At an energy scale of a few GeV, one enters the realm of quarks and gluons whose interaction through the strong force is governed by Quantum Chromo-Dynamics (QCD). Thus, if the atomic nucleus marks the intermediate scale between atoms and elementary particles, such as quarks and gluons, it seems only logical that a satisfying description of the nucleus must be fully rooted within the framework of quantum mechanics.

That being said, we still have to define what are the degrees of freedom of our problem and how the latter interact. It is observed experimentally, that mainly protons and neutrons are emitted during reaction experiments carried out with a characteristic momentum transfer of a few MeV/c. Hence, it seems natural, at that energy scale, to choose to describe the nucleus as a system of nucleons (protons and neutrons) in interaction. One can additionally make the observation that the mass of a nucleon (~ 1 GeV) is about three orders of magnitude larger than most nuclear processes thus justifying a non-relativistic treatment of our problem.

Unlike electrons, protons and neutrons are not elementary, their fundamental degrees of freedom being the quarks and the gluons interacting via the strong force. Because of the self-coupling of gluons which mediate the strong force, the interaction between colored objects, is weak at short distances. At distances of ~ 1 fm, however, it is strong thus explaining the confinements of quarks into colorless objects, the hadrons, of which protons and neutrons are the most famous representatives. As a consequence, at the scale of the nucleus the interaction between nucleons is the long distance residue of the strong interaction acting between colorless objects. This recalls the Van der Waals effective interaction between neutral molecules. One drastic difference lies in the fact that in this energy regime, QCD is highly non-perturbative thus complicating greatly the modelisation of the inter-nucleon interaction from first principles.

In order to make calculation feasible, the dynamics of A-nucleons in interaction is governed by the following Hamiltonian :

$$H = T + V = \sum_{i=1}^A \frac{\mathbf{p}_i^2}{2m_i} + \sum_{i<j}^A V_{ij} + \sum_{i<j<k}^A V_{ijk} + \dots, \quad (4.1)$$

where \mathbf{p}_i and m_i denote respectively the momentum and mass of the i-th nucleon while V_{ij} represents the N - N -interaction, V_{ijk} the N - N - N -interaction and the ellipsis represents the other many-body interactions which are very often neglected in most practical applications. Three and many-nucleon forces arise because formulating the problem in terms of a static potential with nucleons as degrees of freedom implies a momentum scale in which virtual processes (such as the excitation of the internal degrees of freedom of a nucleon by one scattering process, followed by a second scattering process with a different nucleon), are not resolved and appear as effective three-body interactions.

Our problem is expressed by the following many-body Schrödinger equation :

$$H |\psi_n\rangle = E_n |\psi_n\rangle, \quad (4.2)$$

where E_n and $|\psi_n\rangle$ are the eigenenergies and eigenstates of 4.1. The resolution of 4.2 thus requires two ingredients:

1. the specification of the inter-nucleon interaction to be used;

2. a many-body technique which implement the resolution of the secular problem.

4.1.2 Nuclear forces

Before attempting any resolution of the nuclear many-body problem one has to first specify the form of the inter-nucleon interaction. Historically, the difficulty of deriving the interaction between nucleons from first principles was overcome using phenomenological parametrization of the interaction.

Guided by symmetry considerations the non-relativistic two-body inter-nucleon interaction can be expressed as a sum of operators acting on the momentum, spin and isospin degrees of freedom. The radial dependence of the potential is often modeled using Yukawa-type meson-exchange potentials [Yuk35, VM01]. Once a general form of the two-body potential energy operator is obtained, the remaining coupling parameters are adjusted to reproduce the N - N scattering data (realistic interactions) [S⁺94b]. In recent years several high-precision phenomenological interactions have been derived in such a way reproducing N - N scattering data with a reduced $\frac{\chi^2}{d.o.f} \approx 1$. Famous examples of such interactions are the Argonne V₁₈ [W⁺95] and CD-Bonn2000 [Mac01] potentials. The typical behaviour of several high-precision potentials as a function of the inter-nucleon distance is represented on Figure 4.1. The long-range part of the interaction (Region I of Figure 4.1) is derived through the exchange of one virtual pion between nucleons. First modelled in the Yukawa theory [Yuk35] this term is now understood within the context of spontaneous symmetry breaking of chiral symmetry [E⁺09]. The intermediate range (Region II) of the interaction has the net attractive effect while the short range part shows a strong repulsion ("hard-core"). Beyond two-body, the inclusion of three-body interaction was shown to improve greatly the description of nuclear properties when the "high-precision" potentials are to be used for the calculation of the structure of light nuclei [C⁺83, P⁺01b]. Unfortunately, due to the limited amount of experimental data available, the structure of the "ad-hoc" inclusion of three-body contributions to the potentials suffers from strong model dependence. The inconsistent treatment of many-body contribution beyond two-body constitute one of the main limitations of the phenomenological derivation of the inter-nucleon potential.

If the high-precision phenomenological potentials met great success and are presently at the heart of many nuclear structure calculations, progress has been made over the last 30 years towards the resolution of the long lasting problem of deriving an inter-nucleon interaction from first principles. Weinberg laid the foundation for the application of the concept of Effective Field Theory (EFT) to low-energy QCD in relation with the derivation of the nuclear force [Wei79, Wei90]. One has first to identify the degrees of freedom relevant at the energy scale of nuclear physics : the pions and nucleons seem to be a natural choice. The next steps in the EFT program is to build the most general Lagrangian compatible with the spontaneous breaking of chiral symmetry (the underlying symmetry of low-energy QCD). The obtained effective Lagrangian contains an unlimited number of terms. An important notion pertaining to effective field theories is that of the hierarchy of scales. Indeed, if an infinity of Feynman diagrams can be computed from the effective Lagrangian, these diagrams do not have the same degree of importance. The organisation scheme according which the level of importance of each contribution is classified is called chiral perturbation theory (chPT). In this

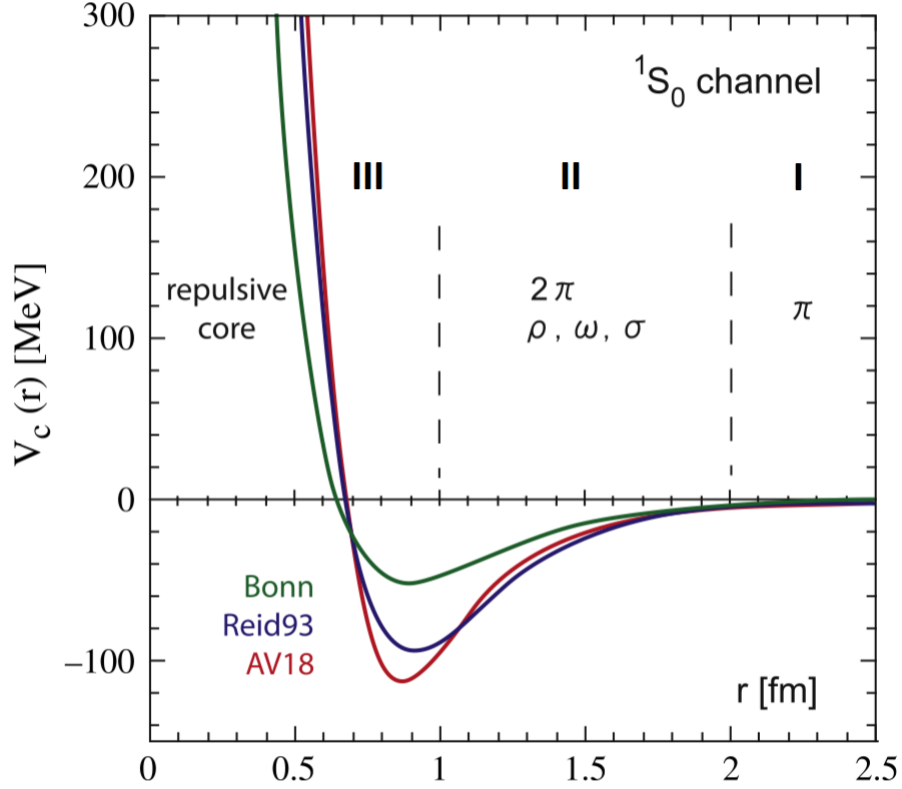


Figure 4.1: Evolution of several phenomenological N - N -interactions in the 1S_0 channel as a function of the inter-nucleon distance r . The picture was taken from ref. [AHI08]. I, II, III correspond to the long, intermediate and short range of the interaction (see text for details).

scheme, the diagrams are ranked in terms of powers, ν , of the quantity $\frac{Q}{\Lambda_x}$, where Q stands for a generic momentum or a pion mass and $\Lambda_x \sim 1$ GeV is the so-called chiral symmetry breaking scale. Once the diagrams are organised, they can be evaluated at any given order of chPT depending on the required precision. The reader is referred to Ref. [ME11, E⁺09] for more details of the derivation of the effective Lagrangian and the implementation of the chPT scheme.

In this theoretical framework the effective inter-nucleon interaction generated is not only consistent with the symmetries of QCD but also the different many-body contributions to the interaction are generated in a consistent fashion within the same framework. For instance, three-nucleon forces start appearing naturally at the NNLO, next-to-next-to-leading-order, corresponding to $\nu = 3$ in the chiral expansion, see Figure 1 of [ME11] and details therein. It is also worth mentioning that not all the parameters of the effective Lagrangian obtained from chiral-EFT are fixed from first principles. Indeed, at the energy scale of interest for nuclear physics, part of the high-energy contributions, equivalent to the exchange of mesons heavier than the pions in the conventional meson-exchange models, are included into the effective theory via low-energy coupling constants (LECs). These LECs are associated with contact terms in the effective Lagrangian and their values have to be obtained through a fit to the experimental π - N and N - N scattering data.

4.2 The nuclear shell-model

In this section, and the following ones, we will introduce some of the most prominent microscopic approaches aiming to provide a description of the nucleus. Through the presentation of the shell-model code ANTOINE [Cau89, C⁺99] and the HFB solver HFBTHO [S⁺13], some of practicalities of these approaches will also be briefly introduced. Additionally, the result of test calculations will be presented.

4.2.1 The independent particle model

As already mentioned, in the early days of nuclear physics, the nucleus was modelled by a charged liquid drop. However, based on new experimental observations (magic numbers, spin and parity systematics) the idea emerged that, similar to electrons in an atom, nucleons in the nucleus organise themselves in shells separated by energy gaps. Pertaining to the shell model picture of the nucleus is the existence of an average nuclear one-body potential in which the nucleons behave as independent particle. A satisfactory prescription for the expression of such a one-body nuclear mean-field was famously proposed by Mayer, Haxel and Jensen [May49, H⁺49]. The proposed single-body potential took the form of a simple isotropic harmonic oscillator modified with a centrifugal l^2 term and a spin-orbit $l \cdot s$ term :

$$U(r) = \frac{1}{2}\hbar\omega r + D l^2 + C l \cdot s. \quad (4.3)$$

The ground-state wave function of the nucleus is build by progressively filling the single particle orbits, from the bottom of the potential well, ensuring that the Pauli principle is respected. The total wave function of the system is thus the product of two Slater determinants, one for protons and one for neutrons. Hence, not without recalling the noble gases of chemistry, the nuclear magic numbers observed for stable nuclei correspond to closed proton or neutron shell configurations and are well reproduced within this model. The ordering of the single particle orbits obtained with the independent-particle potential of 4.3 is shown in Figure 4.2.

At the basis of the independent particle model (IPM) is the assumption that the main effect of the N - N -interaction is to generate a spherical mean field. However, it quickly became necessary to complete this "naive" shell model picture by including contributions from the thus far neglected "residual" interaction.

4.2.2 The interacting shell model

Configuration mixing

A way to visualize the interacting shell model is to imagine a decomposition of the general Hamiltonian 4.1 (restricted to its two-body contributions) as :

$$H = \sum_{i=1}^A [T_i + U_i] + \frac{1}{2} \sum_{i,j=1}^A \overbrace{[V_{ij} - U_i]}^{W_{ij}} = \sum_{i=1}^A h_i + H_{res} = H_0 + H_{res}, \quad (4.4)$$

where H_0 is a one-body Hamiltonian which governs the independent motion of the nucleons in an average potential generated by all other nucleons. H_{res} incorporates the contribution of the nucleon-nucleon interaction; in practice the latter is restricted to its two-body contribution only. Additionally, the success of the

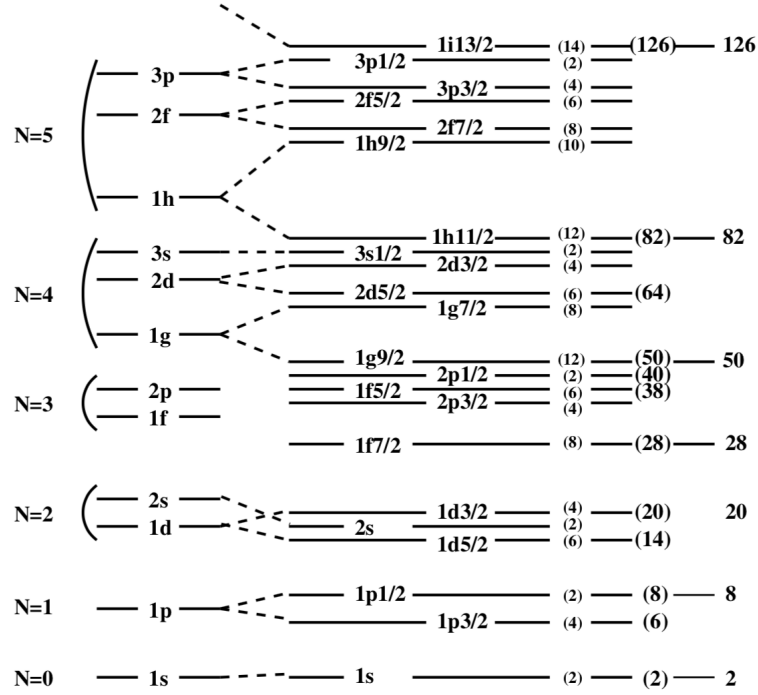


Figure 4.2: The structure of the "naive" shell model. Picture taken from ref. [PN01].

independent particle model suggests that with a suitable choice of U_i , for example eq. 4.3, H_{res} will be small enough so as to treat its effect perturbatively.

From the single particle orbits of H_0 , one can build all A-particle Slater determinants ϕ_i also called configurations (i runs on all the possible configurations). The shell model approach to the many-body problem thus proposes to express the Hamiltonian operator in the basis formed by all the ϕ_i . The problem 4.2 is thus one of diagonalising the matrix $\langle \phi_i | H | \phi_j \rangle$. The eigenstates $|\psi\rangle$ resulting from this diagonalisation can be expressed as :

$$|\psi\rangle = \sum_i c_i |\phi_i\rangle \quad (4.5)$$

The wavefunction ψ is thus a *mix* of the different configuration ϕ_i with the associated probability amplitude given by the coefficients c_i .

Restriction of the Hilbert-space

In practice, the dimension of the matrix $\langle \phi_i | H | \phi_j \rangle$ is such that the problem is most often untractable. A way around this issue is to restrict the number of active nucleons to a certain number of single particle orbits (valence orbits) outside of a core considered inert. The Hilbert space is thus divided in the following way [PN01, Hey94]:

1. Inert core : these orbits are forced to be always full. The core often correspond to a doubly-magic nucleus.
2. Valence space : the orbits in which nucleons are active.
3. External space : these orbits are considered always empty.

Following the decomposition of eq. 4.4, the two main ingredients to construct the Hamiltonian matrix are the eigenvalues of H_0 , the so-called single particle energies (SPEs), and the two-body matrix elements (TBMEs) $\langle j_a j_b; J | W | j_c j_d; J \rangle$ where $|j_c j_d; J\rangle$ is the two nucleon state resulting from the coupling of the two single-particle states j_c and j_d to the total angular momentum J .

As the full Hilbert space is restricted to only a few shells outside an inert core, the many-body Schrödinger equation 4.2 becomes an effective one $H_{eff} |\psi_{eff}\rangle = E |\psi_{eff}\rangle$. In practice, one needs to devise a scheme in order to connect all operators (including the Hamiltonian) to effective operators acting in the chosen space. One of the most commonly used procedures to connect the "bare" nucleon-nucleon interaction with a valence space potential is the well-established Brueckner G -matrix [B⁺54, RS80]. The first evaluation of the G -matrix for sd and pf shell nuclei was performed by Kuo and Brown in the second part of the 1960s [K⁺66, K⁺68] and marked one of the milestones in shell model calculations. Nonetheless, phenomenological readjustment of the two-body matrix elements is common practice in order to incorporate in an phenomenological way the neglected three-body contributions [C⁺05]. In recent years, techniques based on the V_{low-K} approach (decoupling of high and low momentum component of the interaction) or the similarity renormalization group, SRG, have been employed to adapt interactions obtained in the framework of chiral- EFT to a given valence space [BFS10, H⁺16b] (see section 4.4 for more details). Moreover, as shown on Figure 4.1, typical "realistic" interactions used to compute the TBMEs exhibit strong repulsion ("hard-core") at short inter-nucleon distances making them difficult to use in practical calculations. An added benefit of using interactions resulting from such renormalization procedures is they are better behaved at short distances.

Structure of the nuclear Hamiltonian

If the decomposition of the nuclear Hamiltonian as in eq. 4.4 is a common practice in many-body theories, Dufour and Zuker [D⁺96] showed that any sufficiently smooth Hamiltonian can be decomposed as : $H = H_m + H_M$. The so-called monopole Hamiltonian H_m is responsible for the saturation properties and the single-particle behaviour (evolution of spherical shell gaps) while the multipole Hamiltonian H_M contains all the other correlations. A study of the dominant components of the multipole Hamiltonian reveals that the latter are of two types [C⁺05]. On the one hand, the short-range pairing correlations (*particle-particle* correlations) favour the coupling of nucleons into pairs coupled to a total angular momentum 0 [May50]. Hence, the far reaching consequence of the pairing correlations is to drive the nucleus to sphericity. On the other hand, the long-range part of the multipole Hamiltonian is responsible for correlations of the *particle-hole* type, which in turn can be ordered in terms of quadrupole-quadrupole, octupole-octupole ... components, the net effects of which drive the nucleus towards deformation. Hence, such a decomposition allows studying the subtle interplay between the shell formation mechanism (through the monopole Hamiltonian) and correlations (through the multipole part) ultimately responsible for the evolution of nuclear properties far from stability. Additionally, the balance between *particle-hole* and *particle-particle* correlations will influence the evolution of the nucleus towards deformation.

4.2.3 The ANTOINE shell-model code

In this thesis, the shell-model code ANTOINE was used to estimate nuclear mass filters in the argon isotopic chain. Details related to ANTOINE, such as m -scheme formalism or the Lanczos diagonalisation method can be found in Refs. [Cau89, C⁺99]. The code and several worked tutorials are available [Cau10]. The reader is referred to [RS80, Hey94, NP09] for more details on the concepts and technicalities pertaining to the nuclear shell-model theory.

The calculations were performed using the *SDPF-U* shell-model interaction [NP09]. For this interaction, the neutron valence space spans the whole *sd-pf* shells for neutrons while the protons are restricted to the *sd* shells only. An added constraint is that particle excitations between the *sd* and *pf* shells are forbidden (so-called $0\hbar\omega$ calculation). Hence, if the nucleus playing the role of the inert core is ^{16}O , in practice the calculations are based on an implicit ^{28}O core.

In order to make sure that the restriction to a $0\hbar\omega$ model space was correctly implemented in the code's input file, each state of each nuclei ios listed in Table I of ref. [NP09] were computed. Our calculations show the same ordering of the states (same J^π , same excitation energy) as listed in the previously mentioned table.

For the even-even argon isotopes, the first $0^+, 2^+, 4^+$ states were computed while for the odd-even isotopes we chose to output the first $\frac{1}{2}^-, \frac{3}{2}^-, \frac{5}{2}^-$ and $\frac{7}{2}^-$ states. The obtained ground state energies were then used to evaluate the desired mass filters (c.f section 5.3). No further study was carried out with the code as a detailed analysis of the $N \sim 28$ neutron-rich nuclei using ANTOINE and the *SDPF-U* shell-model interaction was performed in [Gau10].

4.3 Self-consistent mean-field calculations

4.3.1 The Hartree-Fock-Bogolibov method

As we saw, the fact that a phenomenologically introduced mean-field bears qualitative resemblance to reality suggests that a mean-field extracted from the two-body nuclear interaction can provide an adequate approximation to the exact solution of the nuclear many-body problem. The Hartree-Fock method (HF) [RS80, B⁺03a] and its extensions rely on the variational principle and provide a scheme to derive a single-particle potential from a two-body interaction. In this subsection we will briefly introduce some of the most important results from the formalism. The following discussion is based on Chapters 5 and 6 of [RS80] and the reader is referred to these Chapters for more details.

The variational principle

At the heart of the mean-field method is the equivalence between the many-body Schrödinger equation and the condition that the expectation value of the energy is stationary with respect to infinitesimal variation of the wave function (a proof can be found in section 5.2 of [RS80]). In mathematical form this reads :

$$\delta E[\psi] = 0 \iff H|\psi\rangle = E|\psi\rangle, \quad (4.6)$$

where $E[\psi] = \frac{\langle\psi|H|\psi\rangle}{\langle\psi|\psi\rangle}$. In practice, the trial wave functions are chosen so as to have simple mathematical form and the variational principle is used to obtain an

approximation of the exact wave function of the system. Additionally, a fundamental property of the variational principle is that, if E_0 is the exact ground state energy of the system, one can show [RS80] that for any trial wave function $|\psi\rangle$ we have : $E[\psi] \geq E_0$.

A common way to express the nuclear many-body Hamiltonian of 4.1 is to pass from a coordinate-space representation to an occupation number representation built on the eigenstates of a single-particle operator (see appendix C of [RS80]). Most commonly, the choice is to use the eigenstates of the harmonic oscillator (HO). The associated Fock states represent a complete basis of the many-body wave functions. The added benefit of such a representation is that we can profit from the powerful tools of second quantization. Hence, if we give ourselves a single-particle basis, the second-quantized form of the Hamiltonian 4.1 reads :

$$H = \sum_{i,j} T_{ij} c_i^\dagger c_j + \frac{1}{4} \sum_{i,j,k,l} \bar{V}_{ijkl} c_i^\dagger c_j^\dagger c_l c_k, \quad (4.7)$$

where $T_{ij} = \langle i | T | j \rangle$ and $\bar{V}_{ijkl} = \langle ij | V | kl \rangle - \langle ij | V | lk \rangle$ are the matrix elements of the kinetic-energy operator and the antisymmetrised two-body matrix elements of the inter-nucleon interaction. c_i^\dagger and c_i represent the creation and annihilation operators for the state i of the chosen single-particle basis. The latter obey the Pauli principle through the anti-commutation relation : $\{c_i, c_j^\dagger\} = \delta_{ij}$. Within this formalism, a Slater determinant built on A arbitrary yet orthogonal single-particle wave functions ϕ_i can be expressed as :

$$|\phi\rangle = \prod_{i=1}^A c_i^\dagger |0\rangle, \quad (4.8)$$

where the c_i^\dagger are the creation operators associated to the states ϕ_i and $|0\rangle$ is the zero-particle vacuum.

The Hartree-Fock field

The expectation value of eq.4.7 can be expressed as a functional of the nuclear density ρ [RS80]. Hence, defining $\rho_{ij} = \langle \phi | c_j^\dagger c_i | \phi \rangle$ as the one-body density matrix we have :

$$E[\rho] = \sum_{i,j} t_{ij} \rho_{ji} + \frac{1}{2} \sum_{i,j,k,l} \rho_{ki} \bar{v}_{ijkl} \rho_{lj} = \langle \phi | H | \phi \rangle. \quad (4.9)$$

The energy minimisation is performed within the set of all A -body Slater determinants ϕ . Because of the one to one correspondence between a Slater determinant and it's associated one-body density matrix (see Appendix D of [RS80]) one can perform the energy minimization with respect to ρ instead of ϕ . One added constrain in this case is that for a Slater determinant, ρ must obey the relation : $\rho^2 = \rho$.

Thus, one can show that the product state ϕ obeys the variational principle if its density matrix obeys the commutation relation $[h, \rho] = 0$; with h defined as (see 5.3.3 of [RS80]):

$$h_{ij} = t_{ij} + \Gamma_{ij} = t_{ij} + \sum_{kl} \bar{v}_{iljk} \rho_{kl}. \quad (4.10)$$

Γ is the called Hartree-Fock field. This suggests that there exists a basis, the so-called *canonical*-basis, where both h and ρ are diagonal. In this basis the

Hartree-Fock equations can be expressed as an eigenvalue problem. Thus, if we call D the transformation matrix between our starting single-particle basis and the Hartree-Fock basis, the Hartree-Fock equations become :

$$\sum_j h_{ij} D_{jk} = \epsilon_k D_{ik}, \quad (4.11)$$

One can express the density matrix in terms of the matrix D as $\rho_{ij} = \sum_k D_{ik} D_{jk}^*$. Plugging this expression into 4.11, one can see we are faced with a *self-consistent* problem as h depends on the matrix D , which is the solution of the problem. This non-linear problem has to be solved iteratively. One can sketch the typical procedure used to solve the *self-consistent* problem in the following way:

1. Start with an initial guess for $D_{ik}^{(0)}$ from which one can build $\rho_{lk}^{(0)}$ and $h_{ij}^{(0)}$.
2. Diagonalize $h_{ij}^{(0)}$ and use its eigenvectors to construct $D_{ik}^{(1)}$ and the corresponding $\rho_{lk}^{(1)}$ and $h_{ij}^{(1)}$.
3. Repeat this procedure for (n) iterations until a predefined convergence criterion is reached. The resulting *Hartree-Fock* field Γ is the variationally optimised one-body approximation of the given interaction V_{ij} .

As we saw, the self-consistent field Γ depends not only on the original Hamiltonian but also on the density matrix solution of the Hartree-Fock equations. Hence, Γ does not necessarily exhibit the same symmetries as the Hamiltonian. Of course, the exact ground state wave function should retain the symmetries of the Hamiltonian. However, the convenience of symmetry breaking solutions is that it offers the possibility of approximating the effect of many-body correlations while still maintaining an independent particle picture. For instance, the breaking of rotational symmetry allows taking into account long-range correlations. We will see in what follows that allowing for the breaking of particle number conservation allows to treat the pairing correlations between like particles while allowing for the description of nuclear phenomena in a independent "particle" picture.

Pairing correlation

As was previously mentioned the interplay between *particle-particle* and *particle-hole* correlations is an essential ingredient to the evolution of nuclear structure in nuclei far from stability. So far, within the Hartree-Fock method, only the *particle-hole* correlations (via the long-range part of the Hartree-Fock field Γ) are taken into account. It seems rather intuitive to relate nuclear-pairing to the concept of Cooper pairs from condensed matter physics. The BCS formalism in the context of theoretical nuclear physics is detailed in Chapter 6 of [RS80]. Being a generalisation of the BCS theory, the Hartree-Fock Bogolyubov (HFB) method proposes to treat *particle-particle* and *particle-hole* correlations and their interdependence on the same footing through a series of self-consistent equations.

At the basis of the HFB formalism is the concept of Bogolyubov quasi-particles. The latter are defined through the so-called Bogolyubov transformation [RS80] :

$$\beta_k^\dagger = \sum_i U_{ik} c_i^\dagger + V_{ik} c_i. \quad (4.12)$$

The ground state of the even-even many-body system acts as the quasi-particle vacuum :

$$|\phi\rangle = \prod_k \beta_k |0\rangle, \quad (4.13)$$

and one can see that such a $|\phi\rangle$ obeys the relation : $\beta_k |\phi\rangle = 0$.

Additionally, the Bogolyubov transformation eq. 4.12 mixes particle creation and annihilation operators. As a consequence, the HFB vacuum is not an eigenstate of the particle number operator and as such $|\phi\rangle$ does not have a definite number of particles. Similar to the HF formalism, the coefficients U_{ik} and V_{ik} are to be variationally optimised. However, this variation has to be performed while still ensuring that the expectation value of the particle number operator had the desired value N . In practice, this is achieved by imposing a constraint on the average particle number through the use of a Lagrange multiplier; the so-called chemical potential.

Hence, considering the constraint on the average particle number, the HFB equations can be expressed as [RS80, S⁺10a] :

$$\mathcal{H} \begin{pmatrix} U_k \\ V_k \end{pmatrix} = \begin{pmatrix} h - \lambda & \Delta \\ -\Delta^* & -h^* + \lambda \end{pmatrix} \begin{pmatrix} U_k \\ V_k \end{pmatrix} = \begin{pmatrix} U_k \\ V_k \end{pmatrix} E_k, \quad (4.14)$$

where h is the Hamiltonian of Eq. 4.10 and λ is the so-called chemical potential. We see that, besides the Hartree-Fock field Γ another field, another field Δ enters in the expression of the HFB equations. This field is called the pairing field and is expressed as : $\Delta_{ij} = \frac{1}{2} \sum_{k,l} \bar{v}_{ijkl} \kappa_{kl}$, where κ is the so-called pairing tensor defined

as : $\kappa_{kl} = \langle \phi | c_l c_k | \phi \rangle$. Each eigenvector of empty quasi-particle state $\begin{pmatrix} U_k \\ V_k \end{pmatrix}$ is associated with the quasi-particle energy E_k and there is an eigenvector $\begin{pmatrix} V_k^* \\ U_k^* \end{pmatrix}$ of energy $-E_k$.

Two fields enter in the expression of the HFB equations. On the one hand, the more familiar Hartree-Fock field incorporates the *particle-hole* correlations ($c_i^\dagger c_j$) responsible for the development of nuclear deformation. On the other hand, the pairing field Δ encodes the *particle-particle* correlations ($c_i c_j$). Hence, we see that through the HFB equations both types of correlations are indeed treated simultaneously and on an equal footing. Once more, the HFB equations constitute a set of non-linear equations to be solved using a self-consistent loop similar to that presented in the case of the HF formalism. In this case both the single particle-hole (Γ) and particle-particle (Δ) mean-fields have to be computed (from ρ and κ) and then the quasi-particle Hamiltonian matrix \mathcal{H} can be diagonalised and the resulting eigenvectors are used as inputs for the subsequent iteration. The calculation of ρ and κ require that a choice be made relative to the occupation of the quasiparticle states. If in the HF case the lowest energy states were chosen to be filled according to the Pauli principle, in the HFB case there is *a priori* no prescription that can ensure the minimization of the energy (nor the convergence of the algorithm). Nonetheless, it is a common practice to choose to occupy the quasi-particles of negative energy [B⁺09b].

We saw that in the HFB formalism one needs to constraint the expectation value of the particle number single-particle operator to the number of nucleons of the even-even nucleus that we want to describe. However, searching for a wave

function which minimises the total energy under the constrain that the expectation value of some chosen single-particle operator, Q , is fixed to a given value is of more general interest. Indeed, one can impose such constraints through the use of a Lagrange multiplier (λ) such that the energy minimization is carried out on the quantity : $\langle \phi | H' | \phi \rangle = \langle \phi | H | \phi \rangle - \lambda \langle \phi | Q | \phi \rangle$. This formalism is commonly used within HFB framework in order to impose constraints on the nuclear multipole moments (most commonly the axial-quadrupole moment).

Our last remark will concern the restoration of the broken symmetries. The exact ground state of the system must exhibit the same symmetries as the initial nuclear Hamiltonian. Moreover, the restoration of the symmetries broken (translational symmetry, particle number, rotational symmetry) at the mean-field level is required for the description of excited states [Phy]. Additionally, the symmetry-restoration procedure brings along additional correlation energy with respect to that already incorporated at the mean field level. Of particular importance for an improved description of nuclear binding energies are the contributions brought from the restoration of rotational symmetry through the projection on a good angular momentum $J=0$. The subsequent mixing of mean-field configurations through, for example the Generate Coordinate Method (GCM) formalism [RS80, B⁺06], was also shown to bring a less significant yet still pronounced improvement of the description of nuclear binding energies for both mid-shell nuclei and those close to doubly-closed shell nuclei [B⁺06, BBH08]. However, the relative contribution to the total binding energy of correlation energy brought by the symmetry restoration procedure (dynamical correlations) and that already present at the field level (static correlations) differ quite drastically between nuclei where $A \geq 60$ and the lighter isotopes. Indeed, statistical correlations are significantly more pronounced in heavier nuclei than in the lighter ones. Hence, the impact of the symmetry restoration procedure on the binding energy predictions of the former is far less pronounced (this is only emphasized considering mass filters). On the contrary, dynamical correlations dominate only in lighter systems [B⁺06]. The mixing of nuclear wave functions over a large range of deformed mean-field configurations was also shown to significantly improve the description of other observables, such as the charge radii.

4.3.2 Nuclear energy-density functionals

Up to now, little was said regarding the type of interactions used within the generalised mean-field approach. Most commonly, two types of interaction are in use within the community : the zero-range Skyrme- and the finite-range Gogny-type [RS80]. The parameters of these interactions are usually adjusted on nuclear observables such as binding energies, and mean-square charge radii. Often (pseudo-observables) such as parameter related to infinite nuclear matter (compressibility, saturation...) or fission barrier are also included in the optimization procedure [K⁺10]. The standard parametrizations of each type of interaction, that is the Skyrme Sly4 parametrization [C⁺98] and the Gogny D1S [BGG91], are adjusted in this fashion.

If the effective interaction is responsible for the *particle-hole* component of the interaction, it does not incorporate the pairing correlations which are of *particle-particle* type. A common choice for the pairing interaction between like particles is the so-called density-dependent delta interaction [B⁺03a]. The latter can be

expressed as :

$$V_{pair}^{n,p} = V_0^{n,p} \left(1 - \alpha \frac{\rho(\mathbf{r})}{\rho_c}\right) \delta(\mathbf{r} - \mathbf{r}'). \quad (4.15)$$

In the above expression, $V_0^{n,p}$ is the pairing strength between like particles (which can be different between protons and neutrons), $\rho_c = 0.16 \text{ fm}^{-3}$ is the usual nuclear saturation density and α is a parameter the value of which defines the way the pairing interaction is distributed within the nucleus. For $\alpha = 0$ the density dependence of the pairing interaction vanishes and as a consequence the pairing is distributed in the volume of the nucleus. For $\alpha = 1$ the pairing is only active at the nuclear surface since in the nuclear interior the density is approximately equal to the saturation density. The intermediate value of $\alpha = 0.5$ is often used to give a mixed surface-volume character to the pairing interaction. As we can see, the pairing force is an "ad-hoc" addition to the nuclear effective interaction and as such its strength is not fixed. Most often, V_0 is adjusted to reproduce the odd-even staggering of binding energies along semimagic isotopic or isotonic chains.

Until recently, very few interactions were adjusted on other observables. The choice of adjusting the interaction's parameter on nuclear matter properties and data pertaining to spherical nuclei was mainly dictated by practical considerations. Hence, with the ever growing increase in computing power, new optimization strategies are starting to be developed. As a result, such initiatives as the UNEDF project started about a decade ago. One of the goal of this ambitious project is to provide updated parametrisation of the Skyrme energy density-functional as well as more consistent adjustment strategies on a wide range of nuclear data. Notably, nuclear data of deformed nuclei were taken into account. In total, for this new generation of functionals, 13 free parameters need to be adjusted to experimental data. Additionally, the neutron and proton pairing strengths are also adjusted together with the 13 parameters of the *particle-hole* channel. Hence, the the ambiguity in the choice of $V_0^{n,p}$ is eliminated. More details on the parametrisation and optimization strategies adopted for the UNEDF family of functionals can be found in [K⁺10]. As a result, when confronted to the experimentally measured binding energies (for a set of 520 even-even nuclei across the nuclear chart) the so-called UNEDF0 functional presents a root-mean-square deviation (RMS) of 1.45 MeV while the more commonly used Sly4 functional shows a RMSD of 4.8 MeV. Significant improvement over the regular Sly4 parametrization is also found when considering the residuals of the two-neutron separation energy.

4.3.3 The HFBTHO code

For the purpose of this thesis, self-consistent HFB calculations were carried out using the HFB solver HFBTHO v2.00d [S⁺13] and the functional UNEDF0. To run the code, jobs were submitted on CERN's batch service which at the time was using IBM's Platform LSF workload management program. The aim of the calculation was twofold, first as the literature often tabulates only results obtained for the even-even isotopes we would like to complete the results available for the chromium isotopes by computing the odd-A chromium isotopes within the HFB formalism. In a second stage we would like to study the development of ground-state collectivity in the even-even chromium isotopes towards and beyond $N=40$. To this end, we would like to compute potential energy surfaces by performing a series of quadrupole-constrained HFB calculations.

This code implements the resolution of the HFB equation enforcing axial symmetry. However, the code can allow for the breaking of reflection symmetry. HFBTHO also gives the possibility to perform HFB calculation while imposing constraints on the expectation value of axial multipole moments (multipolarity up to 8). The code expands the HFB equations on a (eventually deformed) harmonic oscillator basis. Approximate particle number restoration was performed using the so-called Lipkin-Nogami prescription as described in [S⁺12]. For the *particle-hole* channel of the interaction the user has the freedom to choose among several energy-density functionals of the Skyrme-type. The pairing correlations are taken into consideration through a zero-range pairing interaction of the form 4.15. By default the code uses recommended values for the parameters of the pairing interaction. The possibility remains for the user to input custom values. The zero-range nature of the pairing force imposes that a cut-off be applied in the quasi-particle space. A value of 60 MeV is typically used for this cutoff [S⁺13, D⁺01].

A prominent feature of HFBTHO is the possibility to compute odd-even or odd-odd nuclei using the so-called quasi-particle blocking. Within the HFB formalism the ground-state of an odd-A nucleus is built as a one quasi-particle excitation of the quasi-particle vacuum corresponding to a neighbouring even-even nucleus $|\phi\rangle$. A one quasi-particle state $|\phi_k\rangle = \beta_k^\dagger |\phi\rangle$ is in practice created by replacing column k of the matrices U and V (i.e a quasi-particle state of energy E_k) by the corresponding column in the matrices V^* and U^* (i.e the quasi-particle state of energy $-E_k$) [B⁺74, D⁺09]. A consequence of such a procedure is that the occupation number of a single-particle state becomes always equal to one while the corresponding time-reversal conjugate state is always empty. As such, the latter state does not contribute to pairing anymore; it is "blocked" [RS80, B⁺09b]. In practical calculations, one needs to be able to identify the index k of the quasi-particle state to block at each iteration. In that matter, HFBTHO follows a similar prescription as HFODD (allowing for symmetry unrestricted calculations) and details can be found in [S⁺10a, D⁺09].

Unfortunately, there is no guarantee that blocking the quasi-particle state with the lowest energy will effectively yield the solution of the lowest energy. Hence, several candidate quasi-particle states around the Fermi level must be tried. The one quasi-particle state representing the odd-A isotope to be described is chosen as the one yielding the lowest ground state energy. HFBTHO offers the possibility of computing all blocking candidates using quasi-particle states within a 2 MeV range around the Fermi-level [S⁺13]. A consequence of the computation of odd-A isotopes within the blocking formalism is thus that the computation time is increased significantly. Additionally, the *exact* blocking procedure explicitly breaks the time-reversal symmetry. Hence, in this case the time-odd components of the energy density functional have to be fully taken into account [S⁺10a]. In order to limit computation time required to compute odd-A nuclei, one can try to find an approximation to the "exact" blocking procedure which ensures the preservation of the time-reversal symmetry. For instance, one could consider that the unpaired nucleon sits half in a given orbital and the other half in the corresponding time-reversed partners thus preserving time-reversal symmetry; this is the so-called Equal-Filling Approximation (EFA) [PM⁺08]. As time-reversal symmetry is built into HFBTHO, the computation of odd-A isotopes relies on the EFA. The EFA was shown to yield results similar to that obtained with the full blocking procedure in the case where contributions from time-odd fields are switched off. In the same contribution the time-odd fields were shown to be on average 50 keV

only, validating the EFA as a suitable approximation for most nuclear structure applications [S⁺10a]. With HFBTHO the HFB problem is expressed in the par-

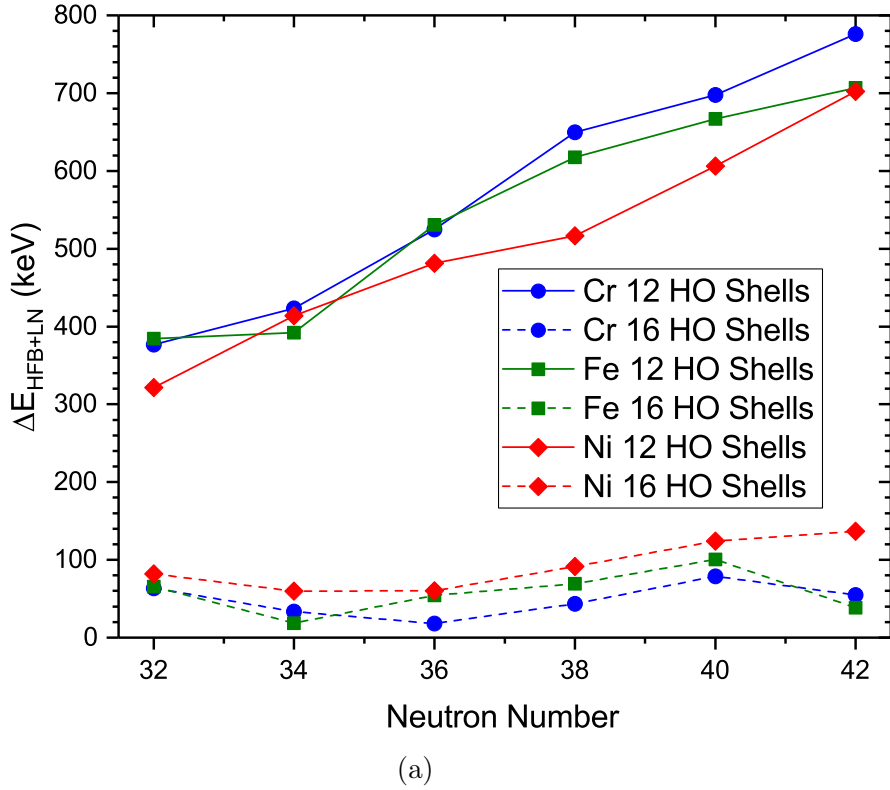


Figure 4.3: Difference between the HFB+Lipkin Nogami corrections energy computed using $N_{shells}=12$ (plain lines) and $N_{shells}=16$ (dashed lines) compared to that computed using $N_{shells}=20$. The difference is plotted against neutron number in the range $N=32-42$ for even-even nickel (red-diamonds), iron (green-squares) and chromium isotopes (blue-circles)

tile number representation built on a basis of the Hilbert space constituted of harmonic oscillator wave functions. As previously mentioned, in practice the HO basis on which the wave function is expanded has a finite size, which introduces truncation errors. In an attempt to predict the location of driplines on the proton and neutron rich-side Erler *et al.*, [E⁺12] calculated nuclei from $Z=2$ to $Z=120$. Erler *et al.* [E⁺12] used $N_{shells} = 20$ major shells in their study. First, unconstrained calculations for even-even nickel, iron and chromium (between $N=30-42$) were performed using $N_{shells} = 20$. Additionally, IBM Platform LSF clusters offer the possibility through their so-called *Job arrays* to submit a group of jobs sharing a common executable and common resources but vary only by their input file. This feature seemed particularly well suited for our purpose. Hence, this first set of calculations was also used to create and test bash scripts enabling to automatically create HFBTHO input files ready to be submitted as LSF *Job arrays* on CERN's computing clusters. Each script is purposely made to create inputs for given different scenario : computing a whole isotopic chain (odd and even A), only even-even isotopes of a given chain, only odd-A isotopes or potential energy surfaces of one isotope.

As was mentioned in [S⁺09], the strength of HFBTHO is its speed as the calculation of a nucleus using $N_{shells}=20$ typically takes 3 min on a standard laptop. Using $N_{shells}=20$ is exaggerated for the nuclei we want to study. We would like to

compare our calculations to tabulated values (for the even-even cases) while still minimising the computing time. Hence to test the influence of the choice of N_{shells} on the calculated absolute binding energy and two-neutron separation energy, two subsequent series of calculations were performed using $N_{shells}=12$ and $N_{shells}=16$. The results are compared to the one obtained using $N_{shells}=20$ and the result is shown in Figure 4.3 for the HFB+Lipkin Nogami correction energy. From Figure 4.3, one sees that, in our region of interest, the $N_{shells}=12$ calculations predict nuclei which are systematically underbound with respect to the $N_{shells}=20$. The discrepancy is linearly increasing with neutron number and reaches nearly 800 keV for ^{66}Cr . On the contrary, the $N_{shells}=16$ result shows significantly improved convergence as the predicted binding energy is always contained within 150 keV of the $N_{shells}=20$.

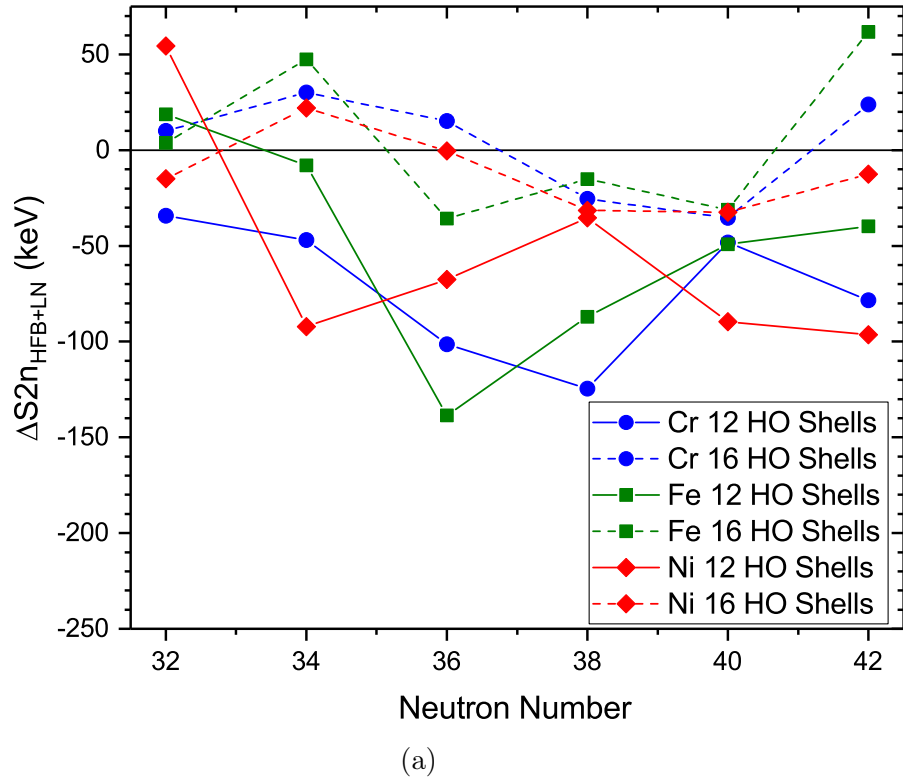


Figure 4.4: Difference between S_{2n} values computed using $N_{shells}=12$ (plain lines) and $N_{shells}=16$ (dashed lines) compared to that computed using $N_{shells}=20$. The difference is plotted against neutron number in the range $N=32-42$ for even-even nickel (red-diamonds), iron (green-squares) and chromium isotopes (blue-circles).

In general, the increase in the basis size always lowers the binding energy. This is especially true in very neutron-rich system as more and more states close to the continuum need to be described. The convergence of the absolute binding energy with N_{shells} is thus in general rather slow. The two-neutron separation energy, being essentially a difference in binding energies converges much faster. This can be seen in Figure 4.4a. Hence, for all three computed chains, the extracted S_{2n} values seem well converged already using $N_{shells}=12$. Piecing all this information together, we chose to use $N_{shells}=16$ for the rest of the study. This choice offers, both good convergence for both the two-neutron separation energy and the binding energy and the computation time is a factor 2 lower than for $N_{shells}=20$.

4.4 The In-Medium Similarity Renormalization Group

Over the last three decades, the development of *ab-initio* many-body methods to solve the nuclear many-body problem have gone hand in hand with that of chiral-effective interactions. Indeed, the consistent order-by-order organisation of nuclear forces obtained within the chPT framework allows for the rigorous inclusion of many-body terms up to the desired accuracy while keeping the theoretical error under control. Of course, *ab-initio* many-body methods are very complex and for some time their applicability was restricted to light $A \leq 12$ nuclei and for heavier systems was limited to closed-shell nuclei. However, since the beginning of the decade, tremendous progress has been made towards the application of such techniques to open-shell systems. One such method is the so-called, valence space formulation of the In-Medium Similarity Renormalization Group technique.

We have already touched upon the use of Renormalization group techniques and their use to decouple low and high momentum scales to "pre-process" bare inter-nucleon interactions. The Similarity Normalization Group (SRG) uses a continuous unitary transformation in order to smoothly tailor a given free-space Hamiltonian to assume a chosen structure in momentum space [F.]. Inspired by the free-space SRG, the idea emerged that one could use SRG-like method in order to decouple physics at different excitation energy scale in a many-body system such as the nucleus. This is the In-Medium Similarity Renormalization Group [H⁺13]. Reviews of the application of the IM-SRG method in nuclear physics are found in [H17, H⁺16b] (and references therein) and we will outline here only its basic concepts.

In such an approach, one aims at incorporating as many many-body correlations as possible into a so-called reference state on top of which a basis of the many-body Hilbert space is built. This reference state can be chosen as a Slater-determinant obtained from an HF calculation; this is the Single-Reference IM-SRG method whose applicability is restricted to the ground-state of closed-shell nuclei. The extension to open-shell nuclei is done through the use of a correlated reference state (e.g resulting of an HFB calculation). In this case, the many-body basis includes up to A-quasi-particle/quasi-hole excitations. This is the so called Multi-Reference IMSRG method which is in practice so-far only limited to ground-state even-even nuclei. Irrespective of the IM-SRG method used, the free-space intrinsic nuclear Hamiltonian is Normal Ordered with respect to the reference state. The Normal Ordering with respect to the reference state has for consequence that the zero-, one- and two-body parts of the Normal Ordered Hamiltonian now incorporate contributions from the free three-body nuclear interaction. Hence, even if the Normal-Ordered Hamiltonian is restricted only to its two-body contributions, the latter do contain the *in-medium* effect from higher order many-body contributions; this is the normal-ordered two-body approximation. The ground state of the system is then decoupled from the other A- (quasi)-particle/(quasi)-excitation following an SRG-like decoupling procedure. A summary of results obtained with these methods is available in [H17, H⁺16b].

To add to the versatility of the IM-SRG method, one can also use this procedure to construct non-empirical shell-model Hamiltonians. This allows to systematically study how common interacting shell model phenomenology emerges from first principles (through the use of a chiral-effective free-space interaction for example). The advantage of such a method is that, as we have seen, the interacting shell model allows straightforward access to the calculation of many nuclear

observables for both ground and excited states.

In the shell-model picture, the inert core can be viewed as vacuum state for the valence configurations. The inert core can thus be considered as the reference state (in practice it is obtained through an HF calculation of the core nucleus) for the IM-SRG procedure. The IM-SRG evolution is then performed so as to decouple the valence-space configurations from states involving core excitations as well as states which are outside the valence-space. The obtained TBMEs can then be used in a standard nuclear shell model code. This method has gained a lot of momentum in very recent years due to its success in reproducing excitation spectra as well as binding energies [S⁺16b, S⁺17b, L⁺18, I⁺18] and has now reached the tin region [M⁺18a].

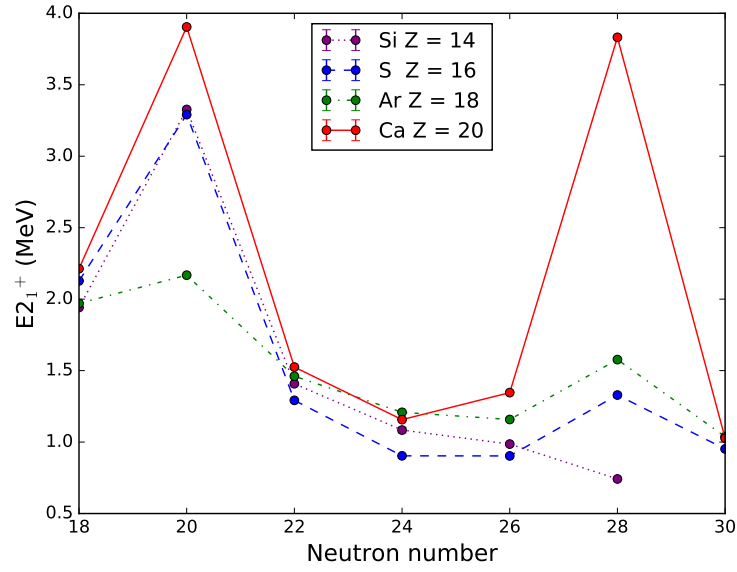
Interpretation

5.1 The $N = 28$ and $N = 40$ "Islands of Inversion"

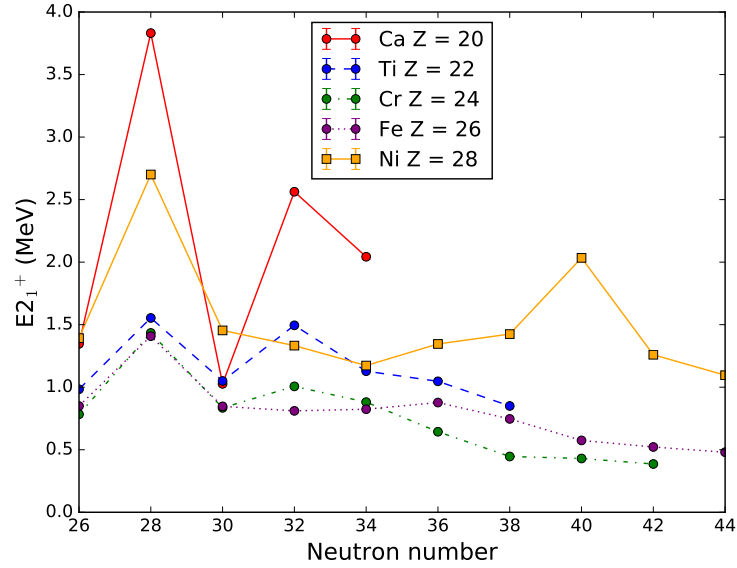
Evidence for the erosion or appearance of shell closures are often obtained through spectroscopic studies which measure the energy of the first excited states (hereafter noted $E2_1^+$) and quadrupole transition probabilities, i.e $B(E2: 2_1^+ \rightarrow 0_1^+)$. The correlated increase of $E2_1^+$ and decrease in $B(E2)$ is one of the usual signatures for closed shells while the inverse correlated variation often marks the collapse of a shell gap since it reflects an increased propensity for neutrons to be excited across the shell gap. An illustration of the progressive collapse of the $N = 28$ shell gap is given in Figure 5.1a, which presents the systematics of the $E2_1^+$ energies in the silicon, sulfur, argon and calcium isotopic chains. If a strong $N = 28$ shell gap is present in ^{48}Ca , its demise in the silicon isotopic chain has been established through various spectroscopic studies [B⁺07, C⁺06, T⁺12a, S⁺14c]. The sulfur chain is found to be transitional with signatures of shape-coexistence at and in the direct vicinity of ^{44}S [G⁺97, GAB⁺09, G⁺09b, F⁺10b, SG⁺11]; a phenomenon often encountered at the border of the IoI [N⁺16].

As far as the argon isotopic chain is concerned, the systematics of the $E2_1^+$ energies suggest a weakened yet present $N = 28$ gap [GAB⁺09, B⁺08a] (see Figure 5.1a). Similar conclusions are drawn from complementary work including the study of ^{45}Ar via the β -decay of ^{45}Cl [G⁺03b] and investigations of the neutron single-particle properties of neutron-rich argon species via knockout [G⁺05a] and nucleon transfer reactions [G⁺06b, G⁺08]. However, the study of $B(E2: 2_1^+ \rightarrow 0_1^+)$ gives conflicting results as three independent studies yield a rather low $B(E2)$ [S⁺96, G⁺03a, C⁺14a, W⁺12a] compatible with the persistence of the $N = 28$ gap in this chain, while a recent life-time measurement [M⁺10] suggests the opposite.

The $N=40$ shell gap, which arises naturally using a harmonic oscillator potential, is washed away by the inclusion of the spin-orbit term in the nuclear mean-field. Nonetheless, as seen in Figure 5.1b, experimental evidence such as a high lying $E2_1^+$ energy at ^{68}Ni is in support of the magic-like character of this sub-shell gap [B⁺82]. Similar to what was observed inside the $N=20$ island of inversion, the properties of excited states ($E2_1^+$, $B(E2)$) along the $N=40$ isotones suggest a rapid development of collectivity from ^{68}Ni to a transitional ^{66}Fe [L⁺10b] and finally a strongly deformed ^{64}Cr [G⁺10, B⁺15, B⁺12, C⁺13]. In addition, dominant collective behavior appears to persist past $N=40$ as observed in [S⁺15]. One of the most striking differences between the preceding example and the development of nuclear collectivity south of ^{68}Ni is the suddenness with which the onset of col-



(a) $E2_1^+$ for the silicon, sulphur, argon and calcium isotopic chains (MeV).



(b) $E2_1^+$ for the calcium, titanium, chromium, iron and nickel isotopic chains (MeV).

Figure 5.1: Evolution of the energy of the first excited 2^+ state in even-even isotopes for isotopic chains from $Z = 14$ to 28. Source ENSDF database 2017 [ens17].

lectivity kicks in. Indeed, the removal of only two protons from ^{68}Ni is already sufficient to drive ^{66}Fe towards deformation.

If the Islands of Inversion often emerge from spectroscopic results, recent developments have revealed the importance of a more comprehensive approach to the study of nuclear structure. In that regard, the example of ^{52}Ca , is telling. While the relatively large $E(2_1^+)$ [G⁺06a] and large empirical shell gap [W⁺13a] seem to highlight the doubly magic character of this isotope, recent high-resolution measurements of its electromagnetic moments and mean-squared charge radius [GR⁺16] do not seem to fit with the picture of a doubly closed-shell nucleus. It is this rather peculiar combination of nuclear observables which makes this nucleus a real challenge for theory.

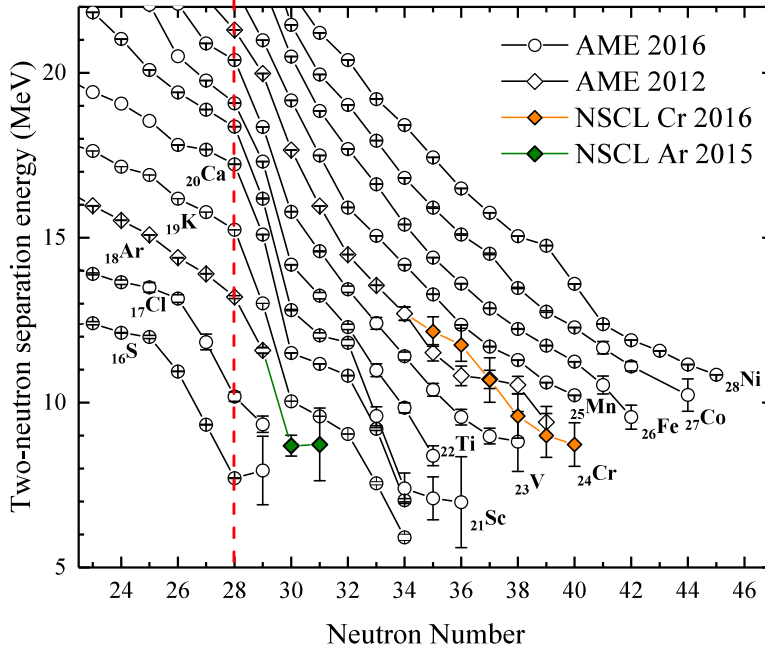


Figure 5.2: S_{2n} trends for the isotopic chains ranging from $Z = 16$ to 28 [W⁺17a]. The trends for the argon and chromium isotopic chains are decomposed into the contribution from the AME2012 [A⁺12] and recent time-of-flight measurements performed with the S800 spectrometer at the NSCL [M⁺15a, M⁺16].

In the $N=28$ region, time-of-flight mass measurements performed at GANIL with the SPEG spectrometer have reached down to $Z = 16$ (S) [S⁺00] hinting at the possible erosion of the $N=28$ shell closure in the sulfur and chlorine isotopic chains. In addition, recent time-of-flight measurements performed using the S800 spectrometer at the NSCL suggested the presence of a strong shell $N = 28$ in the argon isotopic chain [M⁺15a]. The corresponding S_{2n} trends are presented in Figure 5.2. The systematics of the changes in mean-square nuclear charge radii (with respect to $N = 38$) along the argon isotopic chain are also compatible with a pronounced shell effect at $N = 28$ in this chain [KBG⁺96, B⁺08b]. Results of the new ISOLTRAP measurements concerning the persistence of $N=28$ will be discussed in section 5.3.

In the $N=40$ Island of Inversion, mass spectrometry studies have reached down in Z to the chromium isotopic chain, while laser-spectroscopy information is only available for the manganese isotopes [N⁺12, F⁺10a, H⁺16c, H⁺15b, B⁺16]. Previous time-of-flight mass measurement results from AME12 [T⁺90, S⁺94a, B⁺98, Mat04, E⁺11, X⁺15, M⁺16] suggest a sudden onset of deformation towards $N=40$

in the chromium chain. Indeed the S_{2n} trend follows a steady decrease out to $N = 34$. Entering a region of strong deformation, the associated gain in binding energy due to an increase in correlations is such that an upward kink becomes visible in the S_{2n} trend. In the AME2012 [A⁺12] chromium trend, such a kink is observed at $N=36$. However, the recent NSCL measurements suggest a significantly different trend with a kink present at $N = 34$. The calibration process of such time-of-flight mass spectrometers can be a complex endeavor [M⁺13] often casting doubts of the reliability of such measurements, especially regarding the large error bars associated with such measurements.

The close link between the evolution of shell structure and the underlying nuclear interaction makes such regions perfect testing grounds for many theoretical approaches. The region between the magic proton numbers 20 and 28, in which the chromium chain is located, is the perfect playground to benchmark rapidly developing *ab-initio* approaches to nuclear structure, which have now reached $Z=50/N=82$ [M⁺18a]. Significantly, however, this region marks the frontier of what is accessible to these methods [L⁺18] as well as large-scale shell-model calculations [H⁺05, L⁺10a]. Extensive studies of $N=28$ region of deformation have been carried out using large-scale shell model calculations [NP09, Gau10, C⁺14b]. These predictions will be compared to the new ISOLTRAP results in the following section.

5.2 Development of ground-state collectivity towards $N=40$ in the chromium chain

5.2.1 Phenomenological discussion of the S_{2n} trend

The S_{2n} trend obtained from the newly measured chromium masses is presented in Figure 5.3. If the AME2012 trend shows a kink at $N=38$, the new S_{2n} trend shows a markedly different behavior. It appears to be very smooth, gradually curving up approaching $N=40$. This suggests that a gradual onset of deformation is visible in the ground-state of neutron-rich chromium isotopes. It is important to emphasize that while the old results are compatible with the new ones, their error bars prevent any meaningful conclusion. A parallel has often been drawn between the ^{64}Cr isotope, for which maximum quadrupole deformation seems to be reached for this whole region, and ^{32}Mg in the $N = 20$ IoI [G⁺10, L⁺10a]. The S_{2n} trend obtained for the ^{12}Mg chain is shown, from $N = 14$ to 20, in the top panel of Figure 5.7. The qualitative similarities between the new chromium S_{2n} trend and that of magnesium is striking.

Before further discussing the trend of S_{2n} , let us consider the following quantity : $\delta_{2n}(N, Z) = S_{2n}(N, Z) - S_{2n}(N + 2, Z)$. $\delta_{2n}(N, Z)$ is the so-called two-neutron empirical shell gap [L⁺03], often used to quantify the magnitude of the drop in S_{2n} at the crossing of a magic number. In order to exactly match a change in S_{2n} to a change in $\delta_{2n}(N, Z)$, we define the quantity $\delta_{2n}^*(N, Z) = S_{2n}(N - 2, Z) - S_{2n}(N, Z)$. $\delta_{2n}^*(N, Z)$ can be viewed as a finite-difference derivative of the S_{2n} curve. Hence, a drop in the S_{2n} trend is associated to a sudden increase in $\delta_{2n}^*(N, Z)$. On the contrary, a reduction in $\delta_{2n}^*(N, Z)$ signals a flattening of the S_{2n} ; a phenomenon often interpreted as a signature of nuclear collectivity due to a gain in binding energy through correlations [C⁺10].

The trend of $\delta_{2n}^*(N, Z)$ for the ground and 2_1^+ state of the chromium and iron chains are represented in the bottom panel of Figure 5.3. After $N = 36$ the values of

δ_{2n}^* for both the ground state and the 2_1^+ state are smaller than the one obtained for the iron chain. As a result, the flattening of both S_{2n} trends for chromium appears stronger than in the Fe chain. Consequently, the gain in correlation-energy in the chromium isotopic chain appears faster than in the iron chain. In addition, for both chains, the δ_{2n}^* value for the two states are relatively close. Nonetheless, at the onset of collectivity observed in $E2_1^+$ trends, i.e at $N = 38$ for Fe and $N=36$ for Cr [S⁺15], the ground state δ_{2n}^* is higher, illustrating a slightly more pronounced gain in binding-energy per added nucleon in the 2_1^+ .

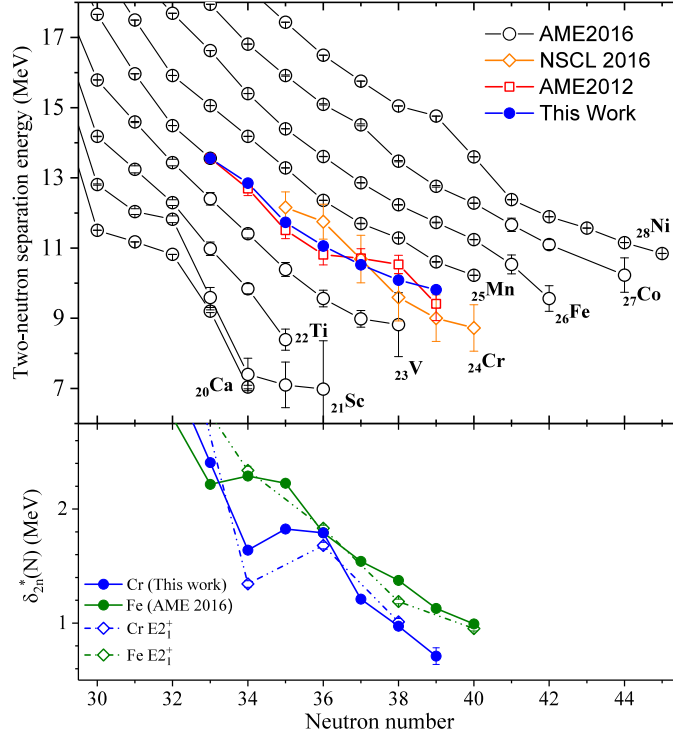


Figure 5.3: *Top*: S_{2n} trend obtained from the newly measured chromium masses. *Bottom*: δ_{2n}^* for the ground and excited 2_1^+ state in the chromium and iron isotopic chains [G⁺10, S⁺15].

5.2.2 Development of quadrupole collectivity : the mean-field point of view

In order to confront the newly obtained experimental S_{2n} with the theoretical predictions, self-consistent mean field calculations were performed using the HF-BTHO code [S⁺13] and the UNEDF0 functional [K⁺10]. Details of the code and the present calculations are presented in Chapter 4. The resulting S_{2n} trend is presented in the lower panel of 5.7. For $N > 33$ the UNEDF0 predictions are in very good quantitative agreement with our new results.

In order to push our investigations further, quadrupole-constrained HFB calculations were subsequently performed for the even- N isotopes. The evolution of the total energy as a function of the axial deformation parameter β_2 is displayed in Figure 5.4 for $^{54-68}\text{Cr}$. It appears that $^{54-66}\text{Cr}$ are all predicted to be spherical. Starting with ^{62}Cr a shoulder at a prolate deformation of $\beta_2 \sim 0.2$ starts to develop. Static deformation sets in at ^{68}Cr where the ground state is predicted with $\beta_2 \sim 0.2$. The gradual onset of deformation thought to be responsible for the S_{2n} behaviour (Figure 5.3) is beautifully illustrated.

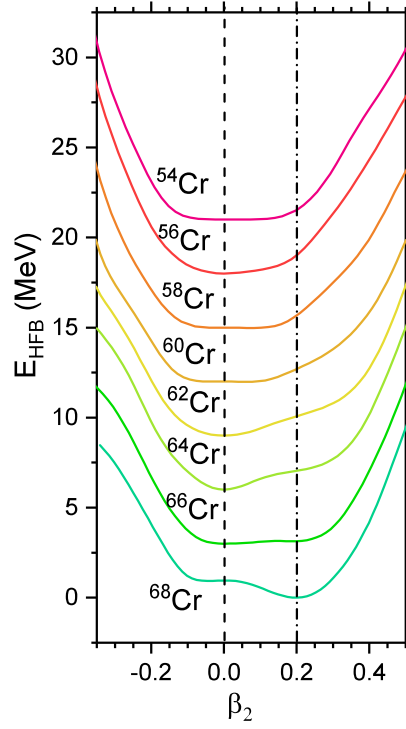


Figure 5.4: Potential energy curves as a function of the quadrupole deformation-parameter β_2 for the $Z = 24$ isotopes. For each the absolute minimum value of the potential energy curve is taken as the energy reference. In addition, each curve is arbitrarily shifted by 3 MeV in order to ease comparison. Dashed and dash-dotted vertical lines indicate β_2 values of 0 and 0.2 respectively.

Figure 5.5 presents the proton and neutron canonical single-particle energies in a range of ± 5 MeV around the Fermi surface (represented as a thick red line) for ^{64}Cr . For $\beta_2 = 0$ spherical single-particle orbits with well defined (n, l, j) quantum numbers are obtained. These orbits are $2j + 1$ degenerate. At non-zero deformation this degeneracy is lifted and Nilsson-like orbits are obtained [RS80]. Often, the minimas observed in the potential energy surfaces can be tracked to the development of sizable gaps in the single particle spectrum. Hence the spherical minimum observed for this isotope, can be explained by the fact the neutron Fermi energy crosses the gap between the $1f_{5/2}$ and $1g_{9/2}$ orbits. Around $\beta_2 \sim 0.2$, the level density is low but the spectrum does not show the opening of a significant gap.

The observation of a spherical ground state for ^{64}Cr is consistent with previous predictions using the Gogny D1S functional [G⁺09a, R⁺16b], where the importance of beyond-mean-field approaches to adequately describe collectivity in the chromium chain was highlighted.

5.2.3 Large-scale shell-model calculations and VS-IMSRG

Figure 5.7 shows the comparison of our experimental S_{2n} trend to that predicted using various shell-model approaches. A marked discrepancy is observed between experimental and the GXPF1A phenomenological interaction [H⁺05]. This deficiency of the GXPF1A phenomenological interaction to correctly reproduce the onset of quadrupole collectivity around $N = 40$ is commonly understood by the fact that the valence space (see Figure 5.6) used for this interaction does not

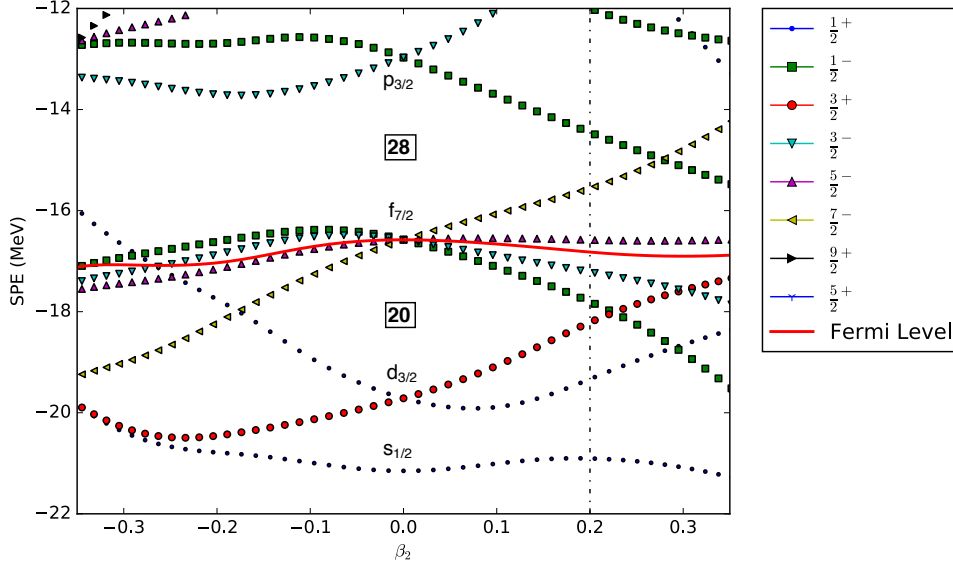
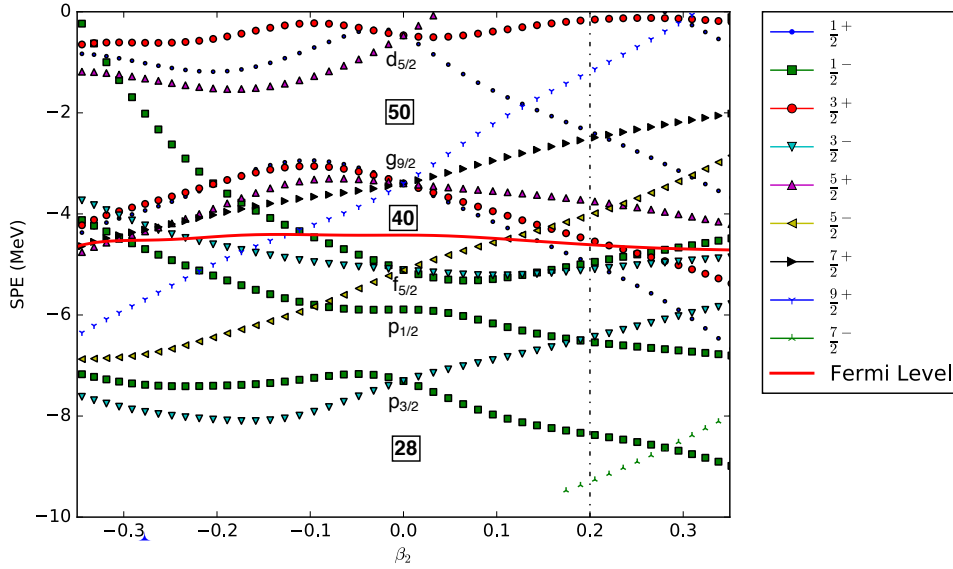
(a) Canonical proton single particle energies for ^{64}Cr .(b) Canonical neutron single particle energies for ^{64}Cr .

Figure 5.5: Proton and neutron single-particle energies for ^{64}Cr calculated for the UNDEF0 functional. The thick red line indicates the position of the fermi level.

include the $2d_{5/2}$ and $1g_{9/2}$ orbits.

The LNPS shell-model interaction was purposely developed to describe nuclei in the collective region around $N = 40$ and its valence space encompasses the full pf -shell for protons and the $pf d_{5/2} g_{9/2}$ orbitals for neutrons (c.f Figure 5.6). The inclusion of the $2d_{5/2}$ and $1g_{9/2}$ orbitals are crucial to the development of

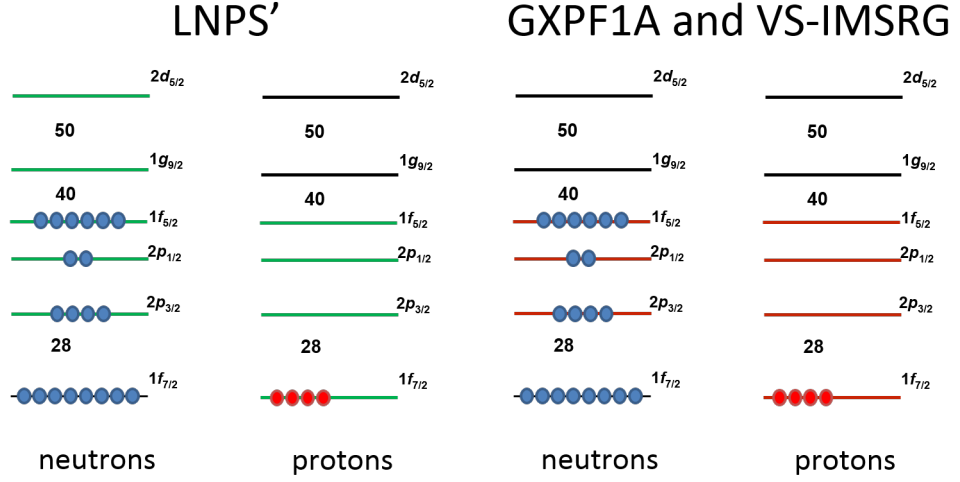


Figure 5.6: Schematic representation of the valence spaces used for the LNPS', GXPF1A and VS-IMSRG calculations.

quadrupole collectivity since they form (together with $3s_{1/2}$ which is excluded from the LNPS valence space) a quasi- $SU(3)$ block, a subspace consisting of the lowest $\Delta j = 2$ orbitals of a major shell (see [L⁺10a] and reference therein). Figure 5.7 shows the S_{2n} trend predicted from a modified version (dubbed LNPS') of the original LNPS devised to better reproduce the results from [M⁺16]. The agreement with experiment is able to qualitatively capture the tendencies of the S_{2n} curve. However, the LNPS' trend shows a systematic overestimation of the S_{2n} values reaching almost 1 MeV compared to the experimental results.

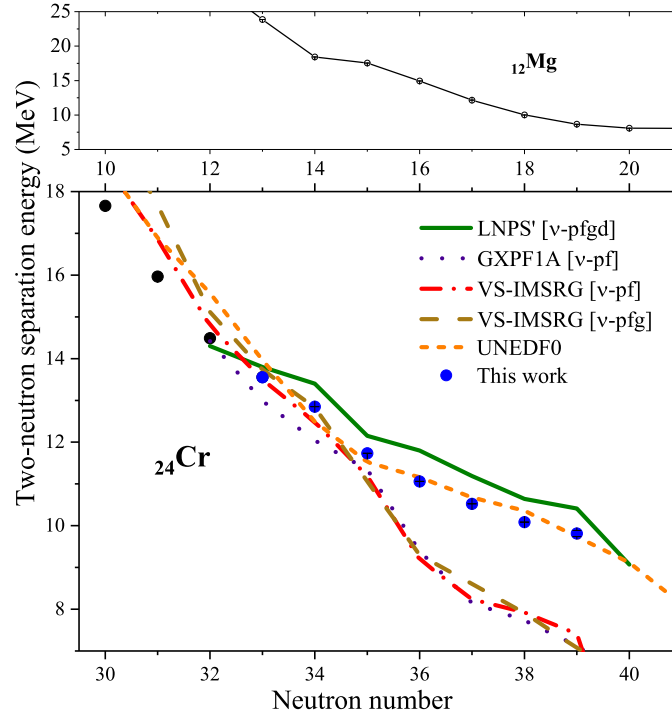


Figure 5.7: *Top*: Two-neutron separation energy of the Mg chain [W⁺17a]. *Bottom*: Comparison between the experimental S_{2n} trends predicted by various theoretical approaches.

Finally, the S_{2n} trend is compared to state-of-the-art shell-model calculations

performed using the *ab-initio* Valence-space formulation of the In-Medium Similarity Renormalization group (VS-IMSRG). This method allows to test nuclear forces derived *ab-initio* in fully-open shell systems [$T^{+12}b$, $B^{+14}a$, $S^{+16}b$, $S^{+17}b$, $S^{+17}a$]. Indeed, with four protons outside the nearest closed shell the chromium isotopes are currently beyond the reach of other large-space *ab-initio* methods. The interaction used are those described in [$S^{+17}a$] and have been proven to well reproduce ground-state properties of nuclei throughout the *sd* and *pf* regions [$S^{+16}a$, $H^{+16}a$, GR^{+16} , $S^{+17}a$]. The Magnus formulation of the IMSRG [$M^{+15}b$, $H^{+16}b$] was used to decouple the ^{40}Ca core as well as a *pf*-shell valence space Hamiltonian. With the ensemble-normal ordering introduced in [$S^{+17}b$], effects of 3N forces between valence nucleons are included, such that a different valence space Hamiltonian is constructed specifically for each nucleus. The final diagonalization was performed using the NuShellX@MSU shell-model code [$B^{+14}b$].

Figure 5.7 shows that starting at $N = 35$, the VS-IMSRG trend reaches a level of discrepancy equivalent to that observed with the GXPF1A interaction. The proximity between the two trends hints towards the fact the VS-IMSRG interaction is missing the same degrees of freedom for describing the physics in the region. The inclusion of the $g_{9/2}$ orbital into the valence-space (attempted for the first time), also shown in Figure 5.7, does not significantly improve the calculations. Further increasing the size of the valence space by including the $d_{5/2}$ orbital leads to untractable calculations beyond $^{60}\text{Cr}_{36}$. For this isotope, the improvement in S_{2n} was only around 100 keV with the occupancy of the $d_{5/2}$ around 2 %. Taking these two points into consideration, it seems unlikely that the absence of the $d_{5/2}$ can solely be responsible for the lack of agreement to the experimental data. This constitutes a severe test of the VS-IMSRG approach.

5.3 Strength of the $N=28$ shell closure in neutron-rich Argon isotopes

5.3.1 Phenomenological discussion of the binding energy trends

We shall now examine the impact of the newly measured argon masses on the strength of the $N = 28$ shell closure. From Figure 5.8 it is quite apparent that the deviations observed in the mass values do not translate into significant deviations of the new S_{2n} trend with respect to the one obtained from the combination of the AME2012 [A^{+12}] and the recent time-of-flight measurements of Meisel *et al.* [$M^{+15}a$]. This observation can be explained by the fact that all three argon masses measured in this work were found to be more bound than previously thought. As a result, the S_{2n} value for ^{48}Ar is increased by only 33 keV. The high-precision data thus firmly confirm the conclusion of [$M^{+15}a$] of the persistence of a strong $N = 28$ shell-gap in the argon isotopic chain. However, the mass uncertainty of ^{49}Ar reported in [$M^{+15}a$] is so large that no further conclusion can be drawn past $N = 28$.

Figure 5.9 shows the evolution of Δ_{3n} as function of the neutron number N for the sulfur, argon and calcium isotopic chains. The enhanced staggering observed at the $N = 28$ neutron number in the argon chains also indicates the presence of a sizable shell gap. Within the large uncertainties, the lack of staggering in the sulfur chain indicates the weak nature of the $N=28$ shell gap in this chain. The strength of the $N=28$ gap can be straightforwardly estimated since it corresponds to the

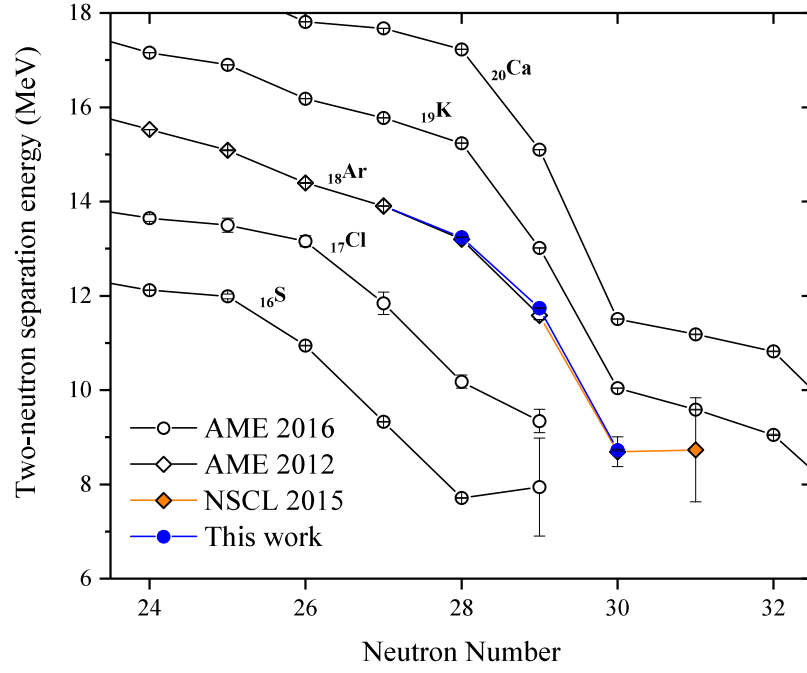


Figure 5.8: Trends of S_{2n} in the $N=28$ region for isotopic chains ranging from sulfur to calcium.

drop in the values of the one-neutron separation energy at the crossing of this specific neutron number. Hence, the value of the one-neutron empirical shell-gap at $N = 28$ is simply twice the value of the three-point estimator of the odd-even staggering $\Delta_{3n}(28, 18) : \Delta_{1n}(28, 18) = S_n(28, 18) - S_n(29, 18) = 2 * \Delta_{3n}(28, 18) = 4.405 \text{ MeV} \pm 0.004 \text{ MeV}$. This value is in agreement with that extracted from the study of the $^{46}\text{Ar}(d,p)^{47}\text{Ar}$ reaction [G⁺06b] : $4.470 \text{ MeV} \pm 0.090 \text{ MeV}$. As a result, even if all the masses measured are found to be more bound than in the AME2012

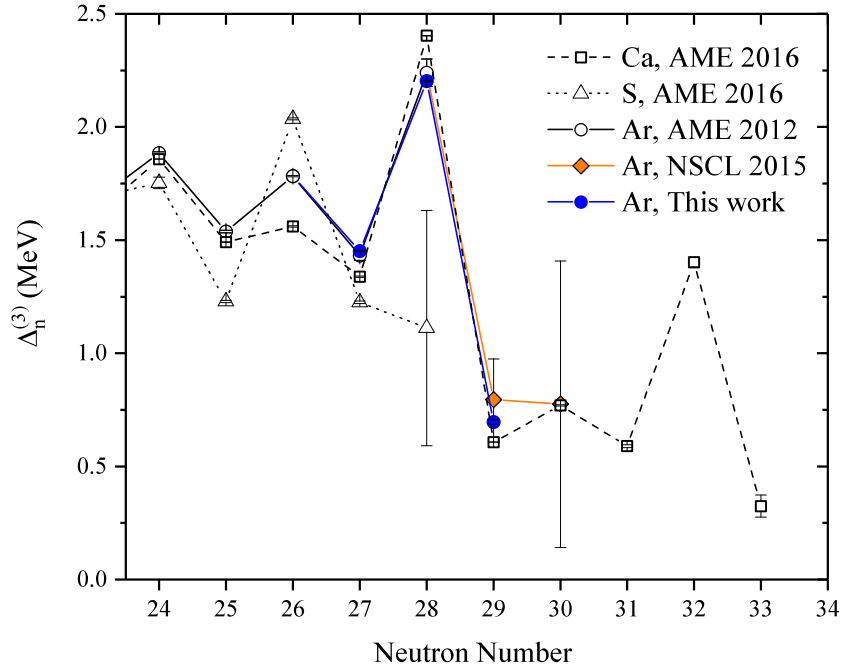


Figure 5.9: Three points estimator of the odd-staggering for the calcium, argon and sulfur isotopic chains.

values, they contribute to a reduction of the one-neutron empirical shell-gap by 73 keV. In addition, compared to ^{48}Ca , ^{46}Ar exhibits a $N = 28$ shell gap which is 402 keV ($\pm 4\text{keV}$) smaller. Given ^{48}Ca is doubly magic, we find the $N = 28$ shell to be quite robust.

5.3.2 Comparison to various theoretical approaches

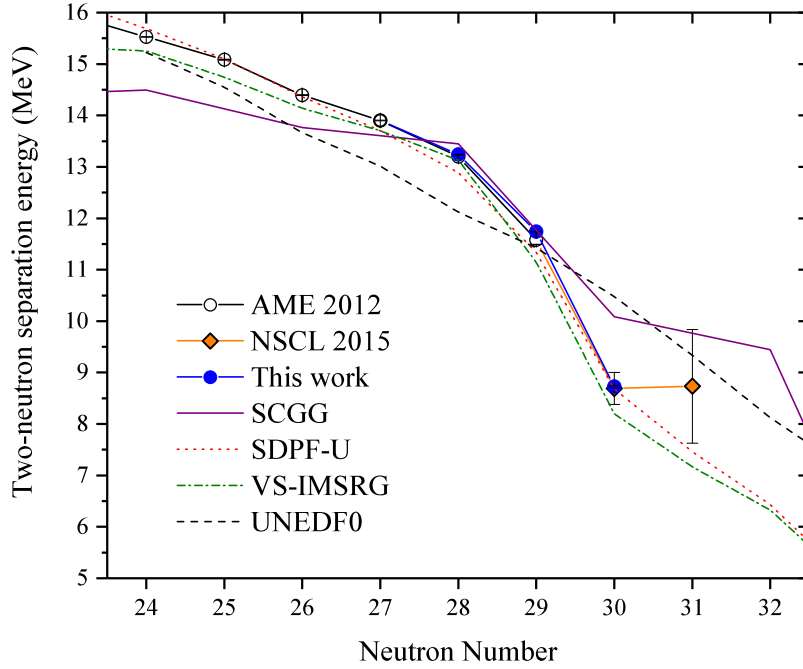


Figure 5.10: Comparison between the S_{2n} trend obtained from this work and the ones predicted from various theoretical approaches. See text for details.

Mass filters for Ar isotopes trends predicted from various theoretical approaches are presented in Figure 5.10 and 5.11. Mean-field calculations of even-even and odd-even argon isotopes were performed using the universal nuclear energy-density functional (UNEDF0) [K⁺10]. Details of the calculation procedure are given in Chapter 4. The corresponding S_{2n} trend (see 5.10) shows a steady decrease that misses the experimentally observed drop at $N = 28$. Moreover, Figure 5.11 the three-point mass difference shows none of the features associated with the presence of a shell closure at $N = 28$. Figure 5.11 also shows that the overall scale of the predicted Δ_{3n} is underestimated. This could point to fact that the adjusted UNEDF0 pairing strength is too weak to correctly describe this region.

In addition to self-consistent mean-field calculations, shell-model calculations were performed following the procedure described in the previous chapter. The calculated ground state of the neutron-rich argon isotopes up to $N = 35$ was calculated. The predicted S_{2n} and Δ_{3n} trends are presented in Figures 5.10 and 5.11, respectively. For these shell-model calculations using the SDPF-U [NP09] phenomenological interaction, the agreement for both mass-filters is excellent pointing to an adequate description of the ground-state of the neutron-rich argon isotopes in this region.

In continuation of the work presented in [RAA⁺15, W⁺13a], the experimental trend was confronted with predictions from state-of-the-art *ab-initio* calculations making use of the Self-Consistent Green-Gorkov (SCGG) functions formalism

[S⁺14b]. These calculations are yet to be published and extend the work presented in [S⁺14b] towards $N = 40$ [Som]. As a result, details of the calculations are similar to that in [RAA⁺15]. Overall, the SCGG description of the S_{2n} trend, presented in Figure 5.10, is of good quality. It is quite remarkable that the $N = 28$ shell closure emerges from these *ab-initio* calculations, they underestimate the strength of the $N = 28$ shell closure.

Similar to the neutron-rich chromium case, *ab-initio* VS-IMSRG were performed for the Ar isotopic chains. Details of the calculations are similar to those described for the chromium isotopic chain. The chosen valence space is however different since in the present case the calculations are performed on a ^{28}O core. As a result, the proton valence space spans the whole *sd*-shell while the neutrons span the whole *pf*-shell [S⁺17a]. The agreement between the predicted trends of both S_{2n} as well as Δ_{3n} and the experiment is excellent. As a result, we extended the calculations to the Ca and S isotopic chains. A comparison between the predicted and experimental trends (see Figure 5.12) reveals that not only is the persistence of the $N=28$ shell gap for argon very well described within this approach, but it also reproduces just as well the demise of the $N=28$ shell gap in the neutron-rich sulfur isotopic chain. A precise determination of the mass of ^{45}S is mandatory to provide additional constraints on this model.

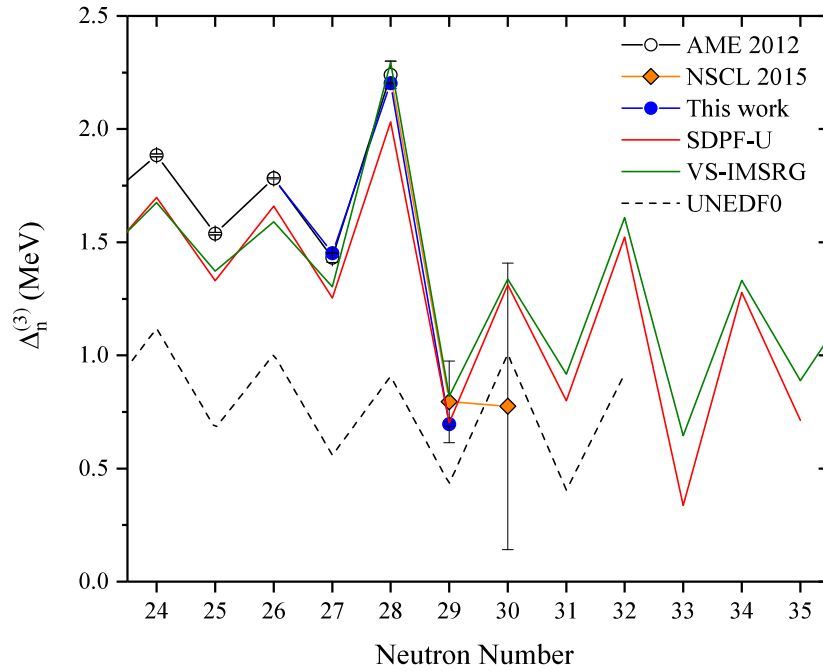


Figure 5.11: Comparison between the pairing gap trend obtained from this work and the ones predicted from various theoretical approaches. See text for details.

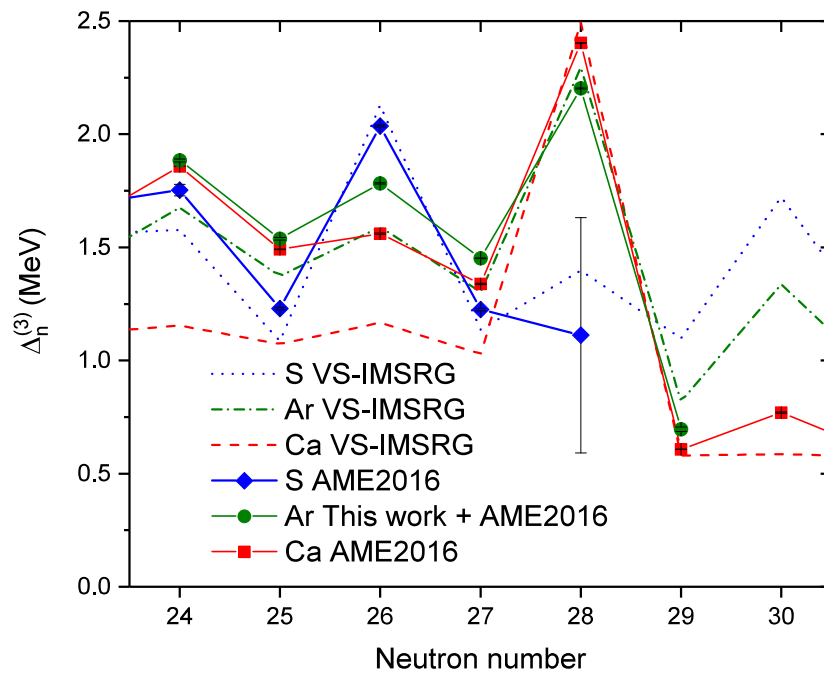


Figure 5.12: Comparison between the empirically determined pairing-gap trend and the one obtained by the valence-space IMSRG calculations. See text for details.

Conclusion and Outlook

In this work, the masses of the neutron-rich $^{46-48}\text{Ar}$ and $^{58-63}\text{Cr}$ isotopes were measured. The beams of interest were produced at the radioactive ion beam facility ISOLDE located at CERN [C⁺17]. The measurements were performed using the online Penning trap mass-spectrometer ISOLTRAP [M⁺08]. Two measurement techniques were used. $^{46-47}\text{Ar}$ and $^{58-62}\text{Cr}$ were measured using the Time-of-Flight Ion-Cyclotron technique, the working principle of which was presented [M⁺08]. ^{48}Ar and ^{63}Cr were measured using ISOLTRAP's MRToF-MS [W⁺13b] due to their low production yield. In addition to the Penning trap data measurements of $^{59-62}\text{Cr}$ were also performed with the MRToF-MS.

The details of the analysis procedure for the Penning-trap data were presented. A data-analysis procedure based on binned maximum Likelihood estimation was presented for the MRToF data evaluation. The source and magnitude of the systematic uncertainties of each measurement method and analysis procedure were detailed. One of the main sources of systematic uncertainty of the MRToF measurement is related to the choice of fitting model. This problem is recurrent in the fast developing field of MRToF mass spectrometry. Nonetheless, we decided to adopt a more pragmatic approach to that developed in [P⁺17] and address this issue by systematically evaluating the influence of various choices of fit function on the extracted time-of-flight. Since $^{59-62}\text{Cr}$ were measured using both techniques, these isotopes offered a rare chance to compare the MRToF-MS and Penning trap results. No statistically significant deviations with respect to the Penning trap mass values was observed.

The mass values obtained in this work are a up to a factor 90, for argon, and 300, for chromium, more precise than in the current literature. On the one hand, the new argon mass values firmly confirm the persistence of the $N = 28$ shell closure in this chain. Even if all of the measured argon masses are found to be more bound, they contribute to a net reduction of the one-neutron shell gap by 73 keV. Nonetheless, when compared to the doubly-magic ^{48}Ca the empirical gap is only reduced by 400 keV. This leads us to conclude that the $N = 28$ shell closure is not significantly quenched in the argon chain. On the other hand, the chromium mass results illustrate the development of ground state collectivity towards $N = 40$. The precise data reveal changes in the S_{2n} trend which suggests a gradual development of ground-state collectivity. This conclusion is at odds with all previous measurements. The gain of correlation-energy per-added-nucleon is found to be more pronounced in the chromium chain than the iron chain. The new data also allowed to compare the behavior of the ground and 2_1^+ states. We found that if their behaviors are similar well within the region of deformation, at the transition

point the correlation-energy per-added-nucleon is more pronounced in the excited state.

The experimental trends were compared to various theoretical models. HFB calculations were performed using the UNEDF0 function and the mean-field solver HFBTHO. In both chains, the odd-even isotopes were computed using quasi-particle blocking within the Equal Filling Approximation. The S_{2n} is quantitatively well reproduced by the mean-field predictions in the chromium chain. However, at odds with spectroscopic results, quadrupole moment-constrained HFB calculations show a development of static deformation starting only at ^{68}Cr . This result is understood by the presence of a sizable $N = 40$ gap in the neutron single particle spectrum while the level density at prolate deformation remains high, preventing gaps to open.

When compared to both experimental S_{2n} trends, predictions obtained from large-scale shell-model calculations reach a satisfactory level of agreement indicating that the physics in the region is well described by the current phenomenological interactions.

The experimental data were also compared to a fast developing *ab-initio* method based on a valence-space approach to the In-Medium Similarity Renormalization Group. For the argon isotopic chain, we found the agreement to the experimental data quite remarkable. Extending the VS-IMSRG calculations to the calcium and sulfur chains, it appears that they reproduce quite remarkably the demise of the $N = 28$ shell closure as it appears in the systematics of the empirical pairing gap. *pf*-shell calculations performed for the fully open-shell chromium isotopes reveal a strong disagreement with experiments similar to that obtained with phenomenological interactions, which are known to lack the relevant degrees of freedom to describe the physics in this region. Extension to a $\nu - pfg$ valence space show no improvement and further developments are ongoing regarding the extension to a $\nu - pfgd$ valence space. Hence, the newly measured data provide important guidance for the improvement of such *ab-initio* approaches.

The study of ground state collectivity towards $N = 40$ through high-precision mass measurements must be extended further. Indeed, the measurements presented in this work do not reach ^{64}Cr which is a pivotal nuclide in this region in regards to the recent experimental and theoretical studies reporting the persistence of the deformation past ^{64}Cr and ^{66}Fe [S^{+15} , N^{+16}]. Furthermore, measurements of mean-square charge radii and electromagnetic moments are yet to reach the chromium isotopic chain and are crucial for the establishment of a robust understanding of the nuclear phenomena at play in the region. With CERN's second long-shutdown period around the corner, discussions to develop a mass measurement program dedicated to neutron-rich iron and chromium with the TITAN group at TRIUMF (Vancouver, Canada) are currently ongoing.

Below the argon isotopic chain, our knowledge of the mass surface does not extend further than $N = 29$ in the Cl and S chains while no experimental data is currently available chains past $N = 28$ in the phosphorus chain. As far as the silicon chain is concerned, the mass excess of ^{42}Si has yet to be determined. In addition, most isotopes in this region had their mass determined by low precision time-of-flight measurements. The chemical nature of the Si, S, P and Cl elements is such that ISOL facilities are not the best suited for their production. However, the advancement of the next generation of RIB facilities should allow Penning trap mass spectrometers such as LEBIT to tackle this region in the near future. As far as the argon chain alone is concerned, an extension of the mass measurement

program towards $^{50}\text{Ar}_{32}$ is also of importance to assess the extent of the $N = 32$ shell closure south of the ^{52}Ca and ^{51}K [W⁺13a, RAA⁺15].

Appendices

Publications related to this thesis work

- A. de Roubin, D. Atanasov, K. Blaum, S. George, F. Herfurth, D. Kisler, M. Kowalska, S. Kreim, D. Lunney, V. Manea, E. Minaya Ramirez, M. Mougeot, D. Neidherr, M. Rosenbusch, L. Schweikhard, A. Welker, F. Wienholtz, R. N. Wolf and K. Zuber, "Nuclear deformation in the $A \approx 100$ region: Comparison between new masses and mean-field predictions", *Phys. Rev. C* **96**, 014310 (2017)
- A. Welker, N. A. S. Althubiti, D. Atanasov, K. Blaum, T. E. Cocolios, F. Herfurth, S. Kreim, D. Lunney, V. Manea, M. Mougeot, D. Neidherr, F. Nowacki, A. Poves, M. Rosenbusch, L. Schweikhard, F. Wienholtz, R. N. Wolf and K. Zuber, "Binding Energy of ^{79}Cu : Probing the Structure of the Doubly Magic ^{78}Ni from Only One Proton Away", *Phys. Rev. Lett.* **119**, 192502 (2017)
- M. Mougeot, D. Atanasov, K. Blaum, K. Chrysalidis, T. Day Goodacre, D. Fedorov, V. Fedosseev, S. George, F. Herfurth, J. D. Holt, D. Lunney, V. Manea, B. Marsh, D. Neidherr, M. Rosenbusch, S. Rothe, L. Schweikhard, A. Schwenk, C. Seiffert, J. Simonis, S. R. Stroberg, A. Welker, F. Wienholtz, R. N. Wolf and K. Zuber, "Precision Mass Measurements of $^{58-63}\text{Cr}$: Nuclear Collectivity Towards the $N=40$ Island of Inversion", *Phys. Rev. Lett.* **120**, 232501 (2018)

Appendix **B**

Precision Mass Measurements of $^{58-63}\text{Cr}$: Nuclear Collectivity Towards the $N = 40$ Island of Inversions

Precision Mass Measurements of $^{58-63}\text{Cr}$: Nuclear Collectivity Towards the $N = 40$ Island of Inversion

M. Mougeot,^{1,*} D. Atanasov,^{2,†} K. Blaum,² K. Chrysalidis,^{3,12} T. Day Goodacre,^{3,13,‡} D. Fedorov,⁴
V. Fedosseev,³ S. George,^{2,§} F. Herfurth,⁵ J. D. Holt,⁶ D. Lunney,¹ V. Manea,³ B. Marsh,³ D. Neidherr,⁵
M. Rosenbusch,^{7,||} S. Rothe,³ L. Schweikhard,⁷ A. Schwenk,^{8,9,2} C. Seiffert,³ J. Simonis,^{10,8,9} S. R. Stroberg,⁶
A. Welker,^{11,¶} F. Wienholtz,^{7,¶} R. N. Wolf,^{2,**} and K. Zuber¹¹

¹CSNSM-IN2P3-CNRS, Université Paris-Sud, Orsay 91405, France

²Max-Planck-Institut für Kernphysik, Saupfercheckweg 1, Heidelberg 69117, Germany

³CERN, Geneva 1211, Switzerland

⁴Petersburg Nuclear Physics Institute, Gatchina 188300, Russia

⁵GSI Helmholtzzentrum für Schwerionenforschung GmbH, Darmstadt 64291, Germany

⁶TRIUMF, 4004 Wesbrook Mall, Vancouver, British Columbia V6T 2A3, Canada

⁷Universität Greifswald, Institut für Physik, Greifswald 17487, Germany

⁸Institut für Kernphysik, Technische Universität Darmstadt, Darmstadt 64289, Germany

⁹ExtreMe Matter Institute EMMI, GSI Helmholtzzentrum für Schwerionenforschung GmbH, Darmstadt 64291, Germany

¹⁰Institut für Kernphysik and PRISMA Cluster of Excellence, Johannes Gutenberg-Universität, Mainz 55099, Germany

¹¹Institut für Kern- und Teilchenphysik, Technische Universität Dresden, Dresden 01069, Germany

¹²Institut für Physik, Johannes Gutenberg-Universität, D-55099 Mainz, Germany

¹³School of Physics Astronomy, The University of Manchester, Manchester M13 9PL, United Kingdom



(Received 22 November 2017; revised manuscript received 6 March 2018; published 6 June 2018)

The neutron-rich isotopes $^{58-63}\text{Cr}$ were produced for the first time at the ISOLDE facility and their masses were measured with the ISOLTRAP spectrometer. The new values are up to 300 times more precise than those in the literature and indicate significantly different nuclear structure from the new mass-surface trend. A gradual onset of deformation is found in this proton and neutron midshell region, which is a gateway to the second island of inversion around $N = 40$. In addition to comparisons with density-functional theory and large-scale shell-model calculations, we present predictions from the valence-space formulation of the *ab initio* in-medium similarity renormalization group, the first such results for open-shell chromium isotopes.

DOI: 10.1103/PhysRevLett.120.232501

Over the past few decades, the stability of proton and neutron “magic” numbers has been a major focus of experimental nuclear physics. Early momentum came from the vanishing of the $N = 20$ shell closure near ^{32}Mg in mass measurements [1] from which arose the idea of the “island of inversion.”

Extensive effort has followed to examine the classical signatures for magicity in exotic nuclei (e.g., empirical shell gap or the energy of the first excited 2_1^+ state). More than three decades later, the robustness of all major shell closures has been assessed [2]. Along the way, a number of subshells (e.g., $N = 40$ in ^{68}Ni [3] or $N = 32, 34$ in $^{52,54}\text{Ca}$ [4,5]) have even been shown to exhibit localized magic behavior.

Recent developments have revealed the importance of a more comprehensive approach to the study of nuclear structure. The example of ^{52}Ca is telling: While the relatively large $E(2_1^+)$ [6] and large empirical shell gap [5] indicate doubly magic character, recent high-resolution measurements of the electromagnetic moments and the mean-squared charge radius [7] do not. However, the question of declaring ^{52}Ca “magic” or not is less important than the rather peculiar combination of ground state properties which makes this nucleus a real challenge for theory.

With hints of a shell closure in ^{68}Ni and $^{52,54}\text{Ca}$ and a variety of phenomena in between, this region between the magic proton numbers 20 and 28 is the perfect playground to benchmark rapidly developing *ab initio* approaches, which have now reached $Z = 50$ [8]. More significantly, this region marks the frontier of what is straightforwardly accessible to these methods [9] and large-scale shell-model calculations [10,11].

Published by the American Physical Society under the terms of the Creative Commons Attribution 4.0 International license. Further distribution of this work must maintain attribution to the author(s) and the published article's title, journal citation, and DOI.

Unfortunately, the majority of observables currently available in the region are limited to excited states and transition probabilities, especially for the chromium isotopic chain which lies right in the middle. Similar to the $N = 20$ island of inversion, the properties of excited states along the $N = 40$ isotones suggest a rapid development of collectivity from a doubly magic ^{68}Ni [3] to a transitional ^{66}Fe [12] and finally a strongly deformed ^{64}Cr [13–16]. Additionally, dominant collective behavior appears to persist past $N = 40$ [17], possibly merging the $N = 40$ island of inversion with a region of deformation in the vicinity of ^{78}Ni [18].

Below ^{68}Ni , high-precision mass spectrometry studies have reached down as far as the manganese chain [19,20], while laser-spectroscopy information is available only for the manganese isotopes [21–23]. Time-of-flight mass measurement results in the atomic mass evaluation 2016 [24] suggest a sudden onset of deformation towards $N = 40$ in the chromium chain. However, the data are not precise enough to draw reliable nuclear-structure conclusions.

The need for accurate and precise mass values of neutron-rich chromium isotopes is also of interest in the field of astrophysics. Neutron-rich chromium masses can play an important role in the cooling and heating of the crust of accreted neutron stars, possibly impacting the associated astrophysical observables. Indeed, the electron-capture sequence $^{64}\text{Cr} \rightarrow ^{64}\text{V} \rightarrow ^{64}\text{Ti}$ was shown to be the main heating source in the lower layers of the outer crust [25,26]. Additionally, nuclides in regions of strong deformation, such as ^{59}Cr and ^{63}Cr , were shown [27] to allow for strong Urca cooling [28] cycles.

In this Letter, we report the first precision measurements of the ground-state binding energies of short-lived neutron-rich chromium isotopes. Our results are compared to all major families of nuclear models, including density-functional theory and large-scale shell model as well as *ab initio* calculations from the recently developed nucleus-dependent valence-space formulation of the in-medium similarity renormalization group (VS-IMSRG) [29].

The chromium isotopes measured in this work were produced at the ISOLDE [30] radioactive ion beam facility at CERN as fission products from the interaction of a 1.4-GeV proton beam impinging on a thick UC_x target. The target was heated to approximately 1900°C to enable the species of interest to diffuse into a dedicated ionization region. For the first time at an ISOL facility, chromium-ion beams were produced using a resonance ionization laser ion source (RILIS) [31]. A three-step scheme was developed, the details of which can be found in Ref. [32]. The chromium ions were transported to the ISOLTRAP setup [33,34], at a kinetic energy of 30 keV, via the high-resolution separator magnets of the ISOLDE facility. Ions were accumulated in a linear radio-frequency quadrupole cooler and buncher for 10 ms [35]. The resulting ion bunches were subsequently decelerated by a pulsed drift

cavity to an energy of 3.2 keV before being injected into a multireflection time-of-flight mass separator (MR-TOF MS) [36]. Inside the MR-TOF MS, the ion bunch underwent typically 1000 revolutions between two electrostatic mirrors separating the isobaric constituents of the bunch. In this work, the molecular contaminants CaF^+ and TiO^+ were predominant in the ISOLDE beam. To provide the subsequent Penning traps with purified beams, the ejection timing of the MR-TOF MS was optimized to suppress contamination [37]. After cooling inside a preparation Penning trap [38], the chromium ions were delivered to ISOLTRAP's precision Penning trap, where the mass measurements were carried out.

The mass determination relies on the measurement of the cyclotron frequency $\nu_c = qB/(2\pi m)$ of an ion with mass m and charge q in a magnetic field of strength B . Before and after each measurement of chromium ions, the cyclotron frequency of a reference ion was determined. In this experiment, $^{85}\text{Rb}^+$ ions provided by ISOLTRAP's offline ion source were used. The masses of $^{58-62}\text{Cr}$ were measured using the TOF ion cyclotron resonance (ICR) technique, in both the one-pulse excitation [39] and the two-pulse Ramsey excitation schemes [40] (upper panel in Fig. 1).

In the case of ^{63}Cr , the production yield was so low that the mass determination could be performed only by using ISOLTRAP's MR-TOF MS as a mass spectrometer. The

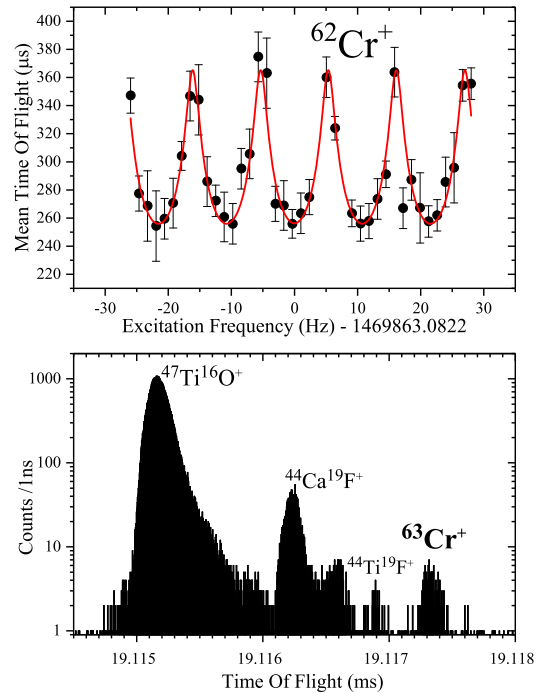


FIG. 1. Top: A typical TOF ICR resonance of $^{62}\text{Cr}^+$ ions using a Ramsey-type excitation scheme (10-80-10 ms [40]). The line represents a fit to the data points. Bottom: Number of events as a function of the flight time after 1000 revolutions of the $A = 63$ ISOLDE beam inside the MR-TOF MS.

ions' time of flight was recorded with an electron multiplier placed behind the MR-TOF MS. The relationship between a singly charged ion's flight time t and its mass m is given by $t = a(m)^{1/2} + b$. The parameters a and b can be determined by measuring the flight times $t_{1,2}$ of reference ions with well-known masses $m_{1,2}$ following the same number of laps in the MR-TOF MS as the ion of interest. The mass of the ion of interest is then determined as [5] $\sqrt{m} = C_{\text{TOF}}(\sqrt{m_1} - \sqrt{m_2}) + 0.5(\sqrt{m_1} + \sqrt{m_2})$, where $C_{\text{TOF}} = (2t - t_1 - t_2)/[2(t_1 - t_2)]$. In the present work, the masses of $^{59-63}\text{Cr}$ were determined in this fashion. Each time-of-flight spectrum was calibrated using the isobaric CaF^+ ions and offline $^{85}\text{Rb}^+$ ions, which were measured after the same number of revolutions inside the MR-TOF device. An example of a time-of-flight spectrum is presented in the bottom panel in Fig. 1.

Because of the low statistics encountered in some spectra, the analysis was performed in all cases using the binned maximum likelihood method assuming a Gaussian peak shape. In total, ~ 2000 ^{63}Cr ions were recorded over seven spectra, some containing as few as 90 counts. Typically, 1000 revolutions inside the MR-TOF MS were used but with some variations (900–1200). The chromium-ion peak was identified unambiguously by blocking the first step of the RILIS scheme. Isobaric references were identified by the measurement of their cyclotron frequencies in the precision Penning trap. In all cases, the contribution associated with the offline species to the statistical uncertainty was evaluated to be more than 3 orders of magnitude smaller than that associated with the online species. As a result, effects related to relative time-of-flight fluctuations between offline and online species are by far below the current statistical precision of the

measurements. Nonetheless, to keep these effects under control, an offline-reference spectrum was measured shortly before the acquisition of every online spectrum. The asymmetries of the peak were taken into account on a case-by-case basis by evaluating the influence of the range on the fit results. Systematic contributions to the C_{TOF} uncertainty were evaluated from online data to be 0.87×10^{-6} . An additional systematic uncertainty accounting for possible time-of-flight drifts arising from Coulomb interaction between reference species and ions of interest was found to only play a significant role for ^{63}Cr , for which an additional C_{TOF} uncertainty of 3.74×10^{-6} was added in quadrature. The final frequency and/or time-of-flight ratios, as well as their associated uncertainties corresponding to one standard deviation, are listed in Table I. The mass excesses of $^{59-62}\text{Cr}$ determined with the MR-TOF MS agree within their uncertainties with the values from the well-established TOF ICR technique.

Figure 2 shows the two-neutron separation energies, defined as $S_{2n}(N, Z) = ME(N-2, Z) - ME(N, Z) + 2M_n$, for the region of interest where $ME(N, Z)$ represents the mass excess of an isotope with N neutrons and Z protons and M_n is the neutron mass excess. The AME2012 [42] suggests the presence of a kink at $N = 38$ in the S_{2n} trend. The trend obtained in this work shows a markedly different behavior. It appears very smooth with an upward curvature when approaching $N = 40$, suggesting that a gradual onset of collectivity is visible in the ground state of neutron-rich Cr isotopes. The trend of S_{2n} observed closely resembles that of Mg in the original island of inversion from $N = 14$ to 20, shown in the upper panel in Fig. 3.

To quantify the S_{2n} trend, the lower panel in Fig. 2 shows the quantity $\delta_{2n}^*(N, Z) = S_{2n}(N-2, Z) - S_{2n}(N, Z)$. A

TABLE I. Frequency ratios ($r = \nu_{c,\text{ref}}/\nu_c$), time-of-flight ratios (C_{TOF}), and mass excesses of the chromium isotopes measured in this work. Values of the mass excesses from the Atomic-Mass Evaluation 2016 (AME2016) [24] are given for comparison. The masses of the reference ions were also taken from AME2016. Experimental half-lives are from Ref. [41]. The yields correspond to the number of chromium ions per second delivered by the ISOLDE facility. The total transport efficiency of the experiment was estimated to be 0.5% behind the MR-TOF MS. The average proton current on target was $1.8 \mu\text{A}$.

Ion	Yield (ions/s)	Half-life	Reference	Ratio r or C_{TOF}	Mass excess (keV)	
					New	AME16
^{58}Cr ^a	Not determined	7.0(0.3) s	^{85}Rb	$r = 0.6824024142(376)$	-51991.8(3.0)	-51991.8(1.5)
^{59}Cr	3×10^5	1050(90) ms	^{85}Rb	$r = 0.6942284208(85)$	-48115.9(0.7)	-48090(220)
			$^{40}\text{Ca}^{19}\text{F}/^{85}\text{Rb}$	$C_{\text{TOF}} = 0.500536923(887)$	-48132(20)	
^{60}Cr	2×10^4	490(10) ms	^{85}Rb	$r = 0.7060206906(138)$	-46908.5(1.1)	-46670(190)
			$^{41}\text{Ca}^{19}\text{F}/^{85}\text{Rb}$	$C_{\text{TOF}} = 0.500484920(886)$	-46917(19)	
^{61}Cr	2×10^3	243(9) ms	^{85}Rb	$r = 0.7178534753(230)$	-42496.5(1.8)	-42480(100)
			$^{42}\text{Ca}^{19}\text{F}/^{85}\text{Rb}$	$C_{\text{TOF}} = 0.500120578(956)$	-42503(20)	
^{62}Cr	3×10^2	206(12) ms	^{85}Rb	$r = 0.7296512630(440)$	-40852.6(3.5)	-40890(150)
			$^{43}\text{Ca}^{19}\text{F}/^{85}\text{Rb}$	$C_{\text{TOF}} = 0.500047948(922)$	-40841(18)	
^{63}Cr	3×10^1	129(2) ms	$^{44}\text{Ca}^{19}\text{F}/^{85}\text{Rb}$	$C_{\text{TOF}} = 0.49964187(386)$	-36178(73)	-36010(360)

^aMass value included in the 2016 mass evaluation as a private communication.

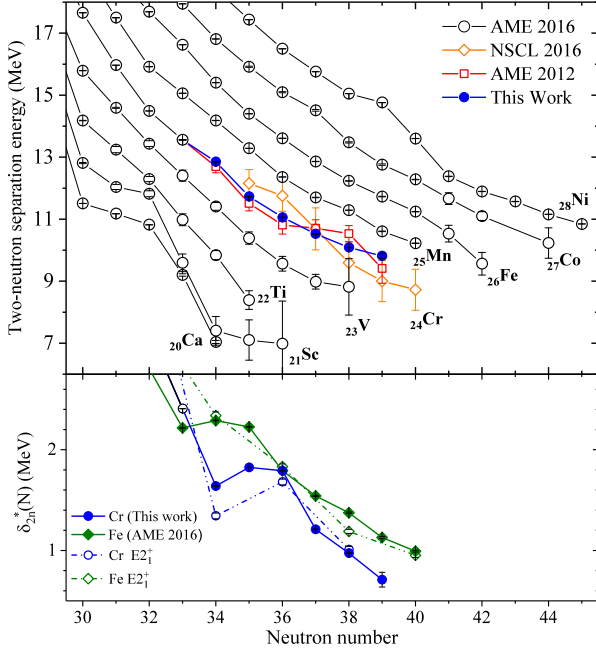


FIG. 2. Top: The S_{2n} trend for Cr from AME2016 [24] is decomposed between the results compiled in the 2012 mass evaluation [42] and recent results from the S800 spectrometer at the NSCL [25]. Bottom: The trend of $\delta_{2n}^*(N, Z)$ for the ground and 2_1^+ excited states [13,17] in the Cr and Fe chains.

low value of δ_{2n}^* marks a flattening of S_{2n} , so the reduction of δ_{2n}^* is usually associated with an increase of collectivity by a gain in the correlation energy [43]. The δ_{2n}^* is plotted for both ground and 2_1^+ states of the Fe and Cr isotopes. One notices that for $N > 36$ the δ_{2n}^* values of Cr (both ground and 2_1^+ state) are smaller than the ones of Fe isotopes, meaning a stronger flattening of S_{2n} and a faster correlation-energy gain. The values of the ground and 2_1^+ states for each isotopic chain are relatively close, but at the onset of collectivity observed in the $E2_1^+$ trends ($N = 36$ for Cr and $N = 38$ for Fe [13]), the ground-state δ_{2n}^* is higher, illustrating a slower gain in the correlation energy.

S_{2n} trends obtained from different theoretical approaches are presented in the lower panel in Fig. 3. Mean-field calculations of even-even and odd-even chromium isotopes were performed using the universal nuclear energy-density functional (UNEDF0) [44]. The HFBTHO code, which solves the Hartree-Fock-Bogolyubov (HFB) equations enforcing axial symmetry [45], was used. The odd- N isotopes were computed performing quasiparticle blocking within the so-called equal-filling approximation [46]. The Lipkin-Nogami prescription was used for approximate particle-number restoration. The UNEDF0 predictions are in very good quantitative agreement for $N > 33$. Additionally, quadrupole moment-constrained HFB calculations were performed for the even- N chromium isotopes. Our calculations predict a spherical ground state for ^{64}Cr and show the development of static deformation starting

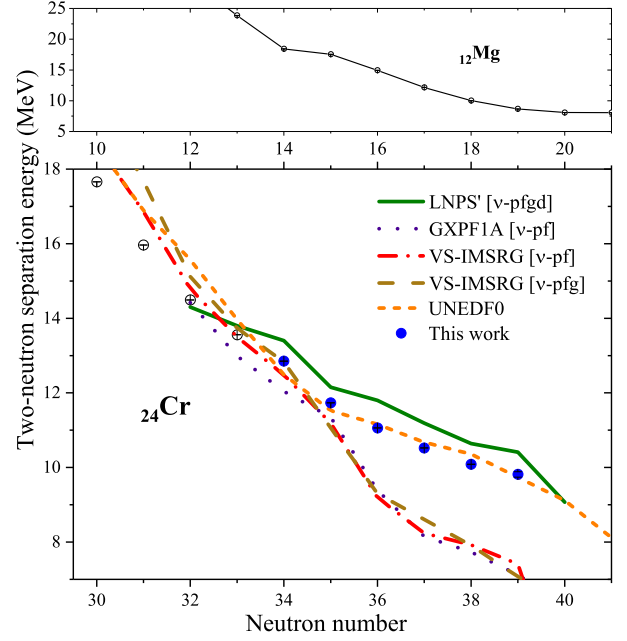


FIG. 3. Top: Two neutron-separation energies of the Mg chain [24]. Bottom: Comparison between the experimental S_{2n} values for the chromium isotopes and predictions from various nuclear models. For shell-model Hamiltonians, the corresponding neutron valence space is indicated in brackets.

only at ^{68}Cr ($\beta \approx 0.2$). This is consistent with previous predictions using the Gogny D1S functional [47,48], where the importance of beyond-mean-field approaches to adequately describe collectivity in the chromium chain was highlighted.

The traditional approach of the nuclear configuration interaction treats the dynamics of valence particles outside an inert core using a phenomenological Hamiltonian optimized to a specific valence space. This approach can access many observables and is applicable far from closed shells, provided the diagonalization remains computationally tractable. In the phenomenological shell model, the interplay between the central field and the tensor component of the nuclear interaction was proposed to be responsible for the shell-evolution phenomenon [49–51]. A reduction of the associated spherical shell gaps may give rise to a deformed ground state provided that correlations are sufficient to energetically favor an intruder state. The marked discrepancy between the S_{2n} trend obtained in this work and the one predicted using the GXPF1A phenomenological interaction [10] highlights the need to include the $d_{5/2}$ and $g_{9/2}$ orbitals in the valence space in order to reach agreement between theory and experiment. The LNPS' interaction [11] was derived specifically to correct for this deficiency. The valence space adopted is therefore based on a ^{48}Ca core and includes the full pf shell for protons and the neutron $pf_{5/2}g_{9/2}d_{5/2}$ orbitals [11]. LNPS' is a version in which the global monopole term was made

30 keV more attractive in order to reproduce the S_{2n} trend obtained in Ref. [25]. Nonetheless, the LNPS' trend shows a systematic overestimation of the S_{2n} values of almost 1 MeV compared to the present work.

We have also performed *ab initio* calculations using the VS-IMSRG [29,52–55], which allow us to test nuclear forces in fully open-shell systems. With four protons outside the nearest closed shell, the chromium isotopes are currently beyond the reach of other large-space *ab initio* methods. We start from the 1.8/2.0 (EM) $NN + 3N$ interactions developed in Refs. [55,56], which reproduce well ground-state properties of nuclei throughout the *sd* and *pf* regions [7,55,57,58]. Unless specified, details of the calculations are the same as those given in Ref. [55]. We then use the Magnus formulation of the IMSRG [59,60] to decouple the ^{40}Ca core as well as a *pf*-shell valence-space Hamiltonian. With the ensemble-normal ordering introduced in Ref. [29], we include effects of $3N$ forces between valence nucleons, such that a different valence-space Hamiltonian is constructed specifically for each nucleus. The final diagonalization was performed using the NuShellX@MSU shell-model code [61]. The lower panel in Fig. 3 shows the S_{2n} derived within this framework.

A marked discrepancy between the theoretical and experimental trends obtained in this work is observed starting at $N \geq 35$. It is worth noting that the VS-IMSRG trend closely resembles that obtained with the phenomenological GXPf1A interaction, hinting that the VS-IMSRG interaction is missing the same degrees of freedom for describing the physics in the region. To investigate this possibility, we have extended the VS-IMSRG for the first time to allow for mixed-parity valence spaces. As in the LNPS interaction, by excluding the neutron $f_{7/2}$ orbital, we are then able to include the neutron $g_{9/2}$ orbital in the valence space. Unfortunately, we see that the addition of the $g_{9/2}$ orbital does not significantly improve the calculations. An attempt to include the neutron $d_{5/2}$ orbital was made. However, the dramatic increase in dimension is such that above ^{60}Cr the calculation becomes intractable. Nonetheless, the calculation for ^{60}Cr shows that the additional neutron $d_{5/2}$ orbital is occupied at $\sim 2\%$, a value similar to the one obtained for the LNPS interaction and in Gogny D1S calculations [62]. The improvement of S_{2n} was only of around 100 keV, insufficient to correct the discrepancy observed in Fig. 3. Consequently, the absence of the $d_{5/2}$ orbital cannot alone be responsible for the observed discrepancy at and beyond $A = 60$. The difficulty in capturing deformation in the VS-IMSRG calculations is only now being explored but likely originates in neglected three- or higher-body operators, the physics of which is not built into the valence-space Hamiltonian [63]. Work in this direction is currently in progress.

In conclusion, benefiting from the laser-ionized chromium ion beam developed at the ISOLDE facility for this experiment, the masses of the neutron-rich isotopes $^{58-63}\text{Cr}$

were measured using precision mass-spectrometry techniques. The present mass values are a factor of up to 300 times more precise than the ones in the literature, thus greatly refining our knowledge of the mass surface in the vicinity of $N = 40$. We exclude a sudden onset of deformation showing rather a gradual enhancement of ground-state collectivity in the chromium chain. We illustrate that, in the region of enhanced collectivity, the gain in binding energy per added neutron is more significant in the Cr chain than in the Fe chain and slightly more pronounced in the excited 2^+ states. The evolution of the S_{2n} trend is well reproduced by both the UNEDF0 density functional and the LNPS' phenomenological shell-model interaction. For the first time, we apply the *ab initio* VS-IMSRG to open-shell chromium isotopes, exploring extensions to mixed-parity valence spaces. The precise data thus provide important constraints to guide the ongoing development of *ab initio* approaches to nuclear structure.

We thank K. Sieja for stimulating discussions. M. M. thanks A. Pastore for his help with the mean-field calculations presented in this work. We thank the ISOLDE technical group and the ISOLDE Collaboration for their support. A. W. acknowledges support from the Wolfgang-Gentner program. We acknowledge support by the French Institut National de Physique Nucléaire et de Physique des Particules (IN2P3), the Bundesministerium für Bildung und Forschung (05P12HGC11, 05P12HGFNE, 05P15HGCIA, 05P15RDFN1, 05P15ODCIA), the European Research Council Grant No. 307986 STRONGINT, the Max-Planck Society, and the National Research Council and Natural Sciences and Engineering Research Council of Canada. Computations were performed with an allocation of computing resources at the Jülich Supercomputing Center (JURECA) and at the Max-Planck-Institute for Nuclear Physics. This work was supported in part by the Deutsche Forschungsgemeinschaft through the Cluster of Excellence Precision Physics, Fundamental Interactions and Structure of Matter (PRISMA). This project has received funding through the European Union's Seventh Framework Programme for Research and Technological Development under Grant Agreements: 267194 (COFUND), and 289191 (LA3NET). This project has received funding from the European Union's Horizon 2020 research and innovation programme under Grant Agreement No. 654002. This project has also received funding from the European Union's Seventh framework through European Nuclear Science and Applications Research under Grant Agreement No. 262010.

*Corresponding author.

maxime.mougeot@csnsm.in2p3.fr

†Present address: Technische Universität Dresden, 01069 Dresden, Germany.

- [‡]Present address: TRIUMF, 4004 Wesbrook Mall, Vancouver, BC V6T 2A3, Canada.
- [§]Present address: Ernst-Moritz-Arndt-Universität, Institut für Physik, Greifswald 17487, Germany.
- ^{||}Present address: RIKEN Nishina Center for Accelerator-Based Science, Wako, Saitama 351-0198, Japan.
- [¶]Present address: CERN, 1211 Geneva, Switzerland.
- ^{**}Present address: ARC Centre of Excellence for Engineered Quantum Systems, The University of Sydney, NSW 2006, Australia.
- [1] C. Thibault, R. Klapisch, C. Rigaud, A. M. Poskanzer, R. Prieels, L. Lessard, and W. Reisdorf, Direct measurement of the masses of ^7Li and $^{26-32}\text{Na}$ with an on-line mass spectrometer, *Phys. Rev. C* **12**, 644 (1975).
- [2] O. Sorlin and M.-G. Porquet, Nuclear magic numbers: New features far from stability, *Prog. Part. Nucl. Phys.* **61**, 602 (2008).
- [3] M. Bernas, P. Dessagne, M. Langevin, J. Payet, F. Pougheon, and P. Roussel, Magic features of ^{68}Ni , *Phys. Lett. B* **113**, 279 (1982).
- [4] D. Steppenbeck *et al.*, Evidence for a new nuclear ‘magic number’ from the level structure of ^{54}Ca , *Nature (London)* **502**, 207 (2013).
- [5] F. Wienholtz *et al.*, Masses of exotic calcium isotopes pin down nuclear forces, *Nature (London)* **498**, 346 (2013).
- [6] A. Gade *et al.*, Cross-shell excitation in two-proton knockout: Structure of ^{52}Ca , *Phys. Rev. C* **74**, 021302 (2006).
- [7] R. F. Garcia Ruiz *et al.*, Unexpectedly large charge radii of neutron-rich calcium isotopes, *Nat. Phys.* **12**, 594 (2016).
- [8] T. D. Morris, J. Simonis, S. R. Stroberg, C. Stumpf, G. Hagen, J. D. Holt, G. R. Jansen, T. Papenbrock, R. Roth, and A. Schwenk, Structure of the Lightest Tin Isotope, *Phys. Rev. Lett.* **120**, 152503 (2018).
- [9] E. Leistenschneider *et al.*, Dawning of the $N = 32$ Shell Closure Seen through Precision Mass Measurements of Neutron-Rich Titanium Isotopes, *Phys. Rev. Lett.* **120**, 062503 (2018).
- [10] M. Honma, T. Otsuka, B. A. Brown, and T. Mizusaki, Shell-model description of neutron-rich pf-shell nuclei with a new effective interaction GXPF 1, *Eur. Phys. J. A* **25**, 499 (2005).
- [11] S. M. Lenzi, F. Nowacki, A. Poves, and K. Sieja, Island of inversion around ^{64}Cr , *Phys. Rev. C* **82**, 054301 (2010).
- [12] J. Ljungvall *et al.*, Onset of collectivity in neutron-rich Fe isotopes: Toward a new island of inversion?, *Phys. Rev. C* **81**, 061301 (2010).
- [13] A. Gade *et al.*, Collectivity at $N = 40$ in neutron-rich ^{64}Cr , *Phys. Rev. C* **81**, 051304 (2010).
- [14] T. Braunroth *et al.*, Reduced transition strengths of low-lying yrast states in chromium isotopes in the vicinity of $N = 40$, *Phys. Rev. C* **92**, 034306 (2015).
- [15] T. Baugher *et al.*, Intermediate-energy Coulomb excitation of $^{58,60,62}\text{Cr}$: The onset of collectivity toward $N = 40$, *Phys. Rev. C* **86**, 011305 (2012).
- [16] H. L. Crawford *et al.*, Quadrupole Collectivity in Neutron-Rich Fe and Cr Isotopes, *Phys. Rev. Lett.* **110**, 242701 (2013).
- [17] C. Santamaria *et al.*, Extension of the $N = 40$ Island of Inversion towards $N = 50$: Spectroscopy of ^{66}Cr , $^{70,72}\text{Fe}$, *Phys. Rev. Lett.* **115**, 192501 (2015).
- [18] F. Nowacki, A. Poves, E. Caurier, and B. Bounthong, Shape Coexistence in ^{78}Ni as the Portal to the Fifth Island of Inversion, *Phys. Rev. Lett.* **117**, 272501 (2016).
- [19] S. Naimi *et al.*, Surveying the $N = 40$ island of inversion with new manganese masses, *Phys. Rev. C* **86**, 014325 (2012).
- [20] R. Ferrer *et al.*, Penning trap mass spectrometry of neutron-rich Fe and Co isotopes around $N = 40$ with the LEBIT mass spectrometer, *Phys. Rev. C* **81**, 044318 (2010).
- [21] H. Heylen *et al.*, Changes in nuclear structure along the Mn isotopic chain studied via charge radii, *Phys. Rev. C* **94**, 054321 (2016).
- [22] H. Heylen *et al.*, Spins and magnetic moments of $^{58,60,62,64}\text{Mn}$ ground states and isomers, *Phys. Rev. C* **92**, 044311 (2015).
- [23] C. Babcock *et al.*, Quadrupole moments of odd-A $^{53-63}\text{Mn}$: Onset of collectivity towards $N = 40$, *Phys. Lett. B* **760**, 387 (2016).
- [24] M. Wang, G. Audi, F. G. Kondev, W. J. Huang, S. Naimi, and X. Xu, The AME2016 atomic mass evaluation (II). Tables, graphs and references, *Chin. Phys. C* **41**, 030003 (2017).
- [25] Z. Meisel *et al.*, Time-of-flight mass measurements of neutron-rich chromium isotopes up to $N = 40$ and implications for the accreted neutron star crust, *Phys. Rev. C* **93**, 035805 (2016).
- [26] S. Gupta, E. F. Brown, H. Schatz, P. Moller, and K.-L. Kratz, Heating in the accreted neutron star ocean: Implications for superburst ignition, *Astrophys. J.* **662**, 1188 (2007).
- [27] H. Schatz *et al.*, Strong neutrino cooling by cycles of electron capture and β -decay in neutron star crusts, *Nature (London)* **505**, 62 (2014).
- [28] G. Gamow and M. Schoenberg, Neutrino theory of stellar collapse, *Phys. Rev.* **59**, 539 (1941).
- [29] S. R. Stroberg, A. Calci, H. Hergert, J. D. Holt, S. K. Bogner, R. Roth, and A. Schwenk, Nucleus-Dependent Valence-Space Approach to Nuclear Structure, *Phys. Rev. Lett.* **118**, 032502 (2017).
- [30] R. Catherall *et al.*, The ISOLDE facility, *J. Phys. G* **44**, 094002 (2017).
- [31] V. I. Mishin, V. N. Fedoseyev, H.-J. Kluge, V. S. Letokhov, H. L. Ravn, F. Scheerer, Y. Shirakabe, S. Sundell, and O. Tengblad, Chemically selective laser ion-source for the CERN-ISOLDE on-line mass separator facility, *Nucl. Instrum. Methods Phys. Res., Sect. B* **73**, 550 (1993).
- [32] T. Day Goodacre, K. Chrysalidis, D. V. Fedorov, V. N. Fedosseev, B. A. Marsh, P. L. Molkanov, R. E. Rossel, S. Rothe, and C. Seiffert, The identification of autoionizing states of atomic chromium for the resonance ionization laser ion source of the ISOLDE radioactive ion beam facility, *Spectrochim. Acta B Atom. Spectros.* **129**, 58 (2017).
- [33] M. Mukherjee *et al.*, ISOLTRAP: An on-line Penning trap for mass spectrometry on short-lived nuclides, *Eur. Phys. J. A* **35**, 1 (2008).
- [34] S. Kreim *et al.*, Recent exploits of the ISOLTRAP mass spectrometer, *Nucl. Instrum. Methods Phys. Res., Sect. B* **317**, 492 (2013).
- [35] F. Herfurth *et al.*, A linear radiofrequency ion trap for accumulation, bunching, and emittance improvement of

- radioactive ion beams, *Nucl. Instrum. Methods Phys. Res., Sect. A* **469**, 254 (2001).
- [36] R. Wolf *et al.*, On-line separation of short-lived nuclei by a multi-reflection time-of-flight device, *Nucl. Instrum. Methods Phys. Res., Sect. A* **686**, 82 (2012).
- [37] F. Wienholtz, S. Kreim, M. Rosenbusch, L. Schweikhard, and R. N. Wolf, Mass-selective ion ejection from multi-reflection time-of-flight devices via a pulsed in-trap lift, *Int. J. Mass Spectrom.* **421**, 285 (2017).
- [38] G. Savard, S. Becker, G. Bollen, H.-J. Kluge, R. B. Moore, T. Otto, L. Schweikhard, H. Stolzenberg, and U. Wiess, A new cooling technique for heavy ions in a Penning trap, *Phys. Lett. A* **158**, 247 (1991).
- [39] M. König, G. Bollen, H.-J. Kluge, T. Otto, and J. Szerypo, Quadrupole excitation of stored ion motion at the true cyclotron frequency, *Int. J. Mass Spectrom.* **142**, 95 (1995).
- [40] S. George, K. Blaum, F. Herfurth, A. Herlert, M. Kretzschmar, S. Nagy, S. Schwarz, L. Schweikhard, and C. Yazidjian, The Ramsey method in high-precision mass spectrometry with Penning traps: Experimental results, *Int. J. Mass Spectrom.* **264**, 110 (2007).
- [41] G. Audi, F. G. Kondev, M. Wang, W. J. Huang, and S. Naimi, The NUBASE2016 evaluation of nuclear properties, *Chin. Phys. C* **41**, 030001 (2017).
- [42] G. Audi, M. Wang, A. H. Wapstra, F. G. Kondev, M. MacCormick, X. Xu, and B. Pfeiffer, The Ame2012 atomic mass evaluation, *Chin. Phys. C* **36**, 1287 (2012).
- [43] R. B. Cakirli, R. F. Casten, and K. Blaum, Correlations of experimental isotope shifts with spectroscopic and mass observables, *Phys. Rev. C* **82**, 061306 (2010).
- [44] M. Kortelainen, T. Lesinski, J. More, W. Nazarewicz, J. Sarich, N. Schunck, M. V. Stoitsov, and S. Wild, Nuclear energy density optimization, *Phys. Rev. C* **82**, 024313 (2010).
- [45] M. V. Stoitsov, N. Schunck, M. Kortelainen, N. Michel, H. Nam, E. Olsen, J. Sarich, and S. Wild, Axially deformed solution of the Skyrme-Hartree-Fock-Bogoliubov equations using the transformed harmonic oscillator basis (II) hfbtho v2.00d: A new version of the program, *Comput. Phys. Commun.* **184**, 1592 (2013).
- [46] S. Perez-Martin and L. M. Robledo, Microscopic justification of the equal filling approximation, *Phys. Rev. C* **78**, 014304 (2008).
- [47] L. Gaudefroy, A. Obertelli, S. Peru, N. Pillet, S. Hilaire, J. P. Delaroche, M. Girod, and J. Libert, Collective structure of the $N = 40$ isotones, *Phys. Rev. C* **80**, 064313 (2009).
- [48] T. R. Rodríguez, A. Poves, and F. Nowacki, Occupation numbers of spherical orbits in self-consistent beyond-mean-field methods, *Phys. Rev. C* **93**, 054316 (2016).
- [49] T. Otsuka, R. Fujimoto, Y. Utsuno, B. A. Brown, M. Honma, and T. Mizusaki, Magic Numbers in Exotic Nuclei and Spin-Isospin Properties of the NN Interaction, *Phys. Rev. Lett.* **87**, 082502 (2001).
- [50] T. Otsuka, T. Suzuki, R. Fujimoto, H. Grawe, and Y. Akaishi, Evolution of Nuclear Shells due to the Tensor Force, *Phys. Rev. Lett.* **95**, 232502 (2005).
- [51] N. A. Smirnova, B. Bally, K. Heyde, F. Nowacki, and K. Sieja, Shell evolution and nuclear forces, *Phys. Lett. B* **686**, 109 (2010).
- [52] K. Tsukiyama, S. K. Bogner, and A. Schwenk, In-medium similarity renormalization group for open-shell nuclei, *Phys. Rev. C* **85**, 061304(R) (2012).
- [53] S. K. Bogner, H. Hergert, J. D. Holt, A. Schwenk, S. Binder, A. Calci, J. Langhammer, and R. Roth, Nonperturbative Shell-Model Interactions from the In-Medium Similarity Renormalization Group, *Phys. Rev. Lett.* **113**, 142501 (2014).
- [54] S. R. Stroberg, H. Hergert, J. D. Holt, S. K. Bogner, and A. Schwenk, Ground and excited states of doubly open-shell nuclei from ab initio valence-space Hamiltonians, *Phys. Rev. C* **93**, 051301(R) (2016).
- [55] J. Simonis, S. R. Stroberg, K. Hebeler, J. D. Holt, and A. Schwenk, Saturation with chiral interactions and consequences for finite nuclei, *Phys. Rev. C* **96**, 014303 (2017).
- [56] K. Hebeler, S. K. Bogner, R. J. Furnstahl, A. Nogga, and A. Schwenk, Improved nuclear matter calculations from chiral low-momentum interactions, *Phys. Rev. C* **83**, 031301(R) (2011).
- [57] J. Simonis, K. Hebeler, J. D. Holt, J. Menendez, and A. Schwenk, Exploring sd-shell nuclei from two- and three-nucleon interactions with realistic saturation properties, *Phys. Rev. C* **93**, 011302(R) (2016).
- [58] G. Hagen *et al.*, Neutron and weak-charge distributions of the ^{48}Ca nucleus, *Nat. Phys.* **12**, 186 (2016).
- [59] T. D. Morris, N. M. Parzuchowski, and S. K. Bogner, Magnus expansion and in-medium similarity renormalization group, *Phys. Rev. C* **92**, 034331 (2015).
- [60] H. Hergert, S. K. Bogner, T. D. Morris, A. Schwenk, and K. Tsukiyama, The In-Medium Similarity Renormalization Group: A novel ab initio method for nuclei, *Phys. Rep.* **621**, 165 (2016).
- [61] B. A. Brown, and W. D. M. Rae, The Shell-Model Code NuSHELLX@MSU, *Nucl. Data Sheets* **120**, 115 (2014).
- [62] J. M. Dugas *et al.*, β -decay measurements for $N > 40$ Mn nuclei and inference of collectivity for neutron-rich Fe isotopes, *Phys. Rev. C* **83**, 054312 (2011).
- [63] J. Henderson *et al.*, Testing microscopically derived descriptions of nuclear collectivity: Coulomb excitation of ^{22}Mg , [arXiv:1709.03948](https://arxiv.org/abs/1709.03948).

Appendix C

High-precision measurement of the ^{18}Ne
superaligned β -decay Q -value

EUROPEAN ORGANIZATION FOR NUCLEAR RESEARCH

Proposal for the ISOLDE and Neutron Time-of-Flight Committee

High-precision measurement of the ^{18}Ne superallowed β -decay Q -value

January 10, 2018

D. Atanasov¹, K. Blaum², M. Eibach³, S. George², K. Gulyuz^{4,5}, F. Herfurth⁶, W. Huang⁷,
A. Herlert⁸, J. Karthein², D. Lunney⁷, V. Manea¹⁰, M. Mougeot⁷, D. Neidherr⁶, M.
Redshaw^{4,5}, M. Rosenbusch¹¹, R. Sandler⁴, L. Schweikhard³, C. Sumithrarachchi⁵, A.
Welker¹⁰, F. Wienholtz¹⁰, R. N. Wolf¹² and K. Zuber¹

¹Technische Universität Dresden, 01069 Dresden, Germany

²Max-Planck-Institut für Kernphysik, Saupfercheckweg 1, 69117 Heidelberg, Germany

³Ernst-Moritz-Arndt-Universität, Institut für Physik, 17487 Greifswald, Germany

⁴Department of Physics, Central Michigan University, Mount Pleasant, MI, 48879, USA

⁵National Superconducting Cyclotron Laboratory, East Lansing, MI, 48824, USA

⁶GSI Helmholtzzentrum für Schwerionenforschung GmbH, 64291 Darmstadt, Germany

⁷CSNSM-IN2P3-CNRS, Université Paris-Sud, 91406 Orsay, France

⁸FAIR GmbH, 64291 Darmstadt, Germany

¹⁰CERN, 1211 Geneva, Switzerland

¹¹RIKEN Nishima Center for accelerator-based science, Wako, 351-098 Saitama

¹²ARC Centre of Excellence for Engineered Quantum Systems, School of Physics, The University of Sydney, NSW 2006, Australia

Spokesperson(s): **M. Eibach** (eibach@nscl.msu.edu)

M. Mougeot (maxime.mougeot@csnsm.in2p3.fr)

Local contact: **M. Mougeot** (maxime.mougeot@csnsm.in2p3.fr)

Abstract

We propose to perform a high-precision measurement of the ^{18}Ne superallowed β -decay Q_{EC} -value using the Penning-trap mass spectrometer ISOLTRAP. The result will be used in the determination of the ^{18}Ne corrected $\mathcal{F}t$ -value. Despite showing the biggest deviation to the world average the ^{18}Ne corrected $\mathcal{F}t$ -value is among the least precisely known. We propose to measure the Q -value of the ground-state transition to a precision of 20 eV. The contribution of the Q_{EC} -value uncertainty to the uncertainty in $\mathcal{F}t$ -value would then be pushed below the contribution of the half-life, which was recently measured at TRIUMF. Thus, the precision and accuracy of the $\mathcal{F}t$ -value would be entirely limited by the contribution from the branching ratio measurement, and the Q_{EC} -value, so far a combination of a Penning-trap mass and one resulting from reaction measurements, would be set on solid ground. These data provide a test of the conserved vector current hypothesis and of the unitarity of the Cabibbo-Kobayashi-Maskawa (CKM) quark mixing matrix.

Requested shifts: 8

1. General Motivation

Superaligned Fermi β -decays occur between nuclear analog states with spin $J^\pi = 0^+$ and isospin $T = 1$, and depend uniquely on the vector part of the weak interaction. Precise experimental determinations of ft -values for these β -decays, along with small, theoretically calculated corrections, can provide a test of the conserved vector current (CVC) hypothesis, set limits on the existence of possible scalar currents, and contribute to the most demanding available test of the unitarity of the Cabibbo-Kobayashi-Maskawa (CKM) quark mixing matrix. The ft -value is calculated from three experimentally determined quantities: the decay transition energy, Q_{EC} ; the half-life of the parent state, $t_{1/2}$; and the branching ratio of the transition of interest, R . The ft -value is usually combined with theoretical corrections to yield a “corrected” $\mathcal{F}t$ -value [1]:

$$\mathcal{F}t = ft(1 + \delta'_R)(1 + \delta_{NS} - \delta_C) = \frac{K}{2G_V^2(1 + \Delta_R^V)}. \quad (1)$$

The terms that modify ft are δ'_R and δ_{NS} , which comprise the transition dependent part of the radiative correction, and δ_C , the isospin-symmetry-breaking correction. The term Δ_R^V is the transition independent part of the radiative correction, K is a constant, $K/(\hbar c)^6 = 8120.2776(9) \times 10^{-10} \text{ GeV}^{-4}\cdot\text{s}$, and G_V is the vector coupling constant. According to the CVC hypothesis, G_V , and hence $\mathcal{F}t$, should be the same for all superallowed β -decays.

In the most recent critical survey of all experimental and theoretical superallowed β -decay data [1], 14 transitions, with $\mathcal{F}t$ -value uncertainties of less than $\pm 0.4\%$, were used to determine the world-average $\overline{\mathcal{F}t}$ -value. Entering to the fifth power in the calculation of the $\mathcal{F}t$ -value, precise and accurate Q_{EC} -values are extremely important for the determination of $\mathcal{F}t$. Over the last decades, Penning traps have proven themselves as the tool of choice for performing such measurements. The improved precision and accuracy they have provided compared to nuclear reaction data revealed that in some cases previously accepted values [2] were incorrect by as much as 6σ [3–5]. Following the recent determination of the Q_{EC} -value for ^{14}O [6] with the LEBIT Penning-trap at the NSCL, all 14 of the high-precision superallowed transitions have now Q_{EC} -values determined with a Penning trap.

In the 2015 survey of Ref. [1], 4 additional transitions (in ^{18}Ne , ^{26}Si , ^{30}S , and ^{42}Ti) with complete experimental data sets—measured values for Q_{EC} , $t_{1/2}$ and R —were evaluated, but were not precise enough to be included in the mean $\mathcal{F}t$ -value calculation ($\overline{\mathcal{F}t}$). Since then, the experimental data has been improved for ^{42}Ti , and obtained for ^{46}Cr , ^{50}Fe , and ^{54}Ni for the first time [7,8]. Nonetheless, the precision reached for the latter transitions is not yet high

enough to contribute to $\overline{\mathcal{F}t}$. Hence, there are now 21 transitions with complete data sets. Of the 7 less precise $\mathcal{F}t$ -values, ^{18}Ne shows the largest deviation from $\overline{\mathcal{F}t}$ (see Figure 1). The uncertainty in $\mathcal{F}t$ for ^{18}Ne is dominated by the 2.7% fractional uncertainty in the branching ratio, from a single measurement made in 1975 [9]. A new but unpublished measurement was recently performed at SPIRAL, GANIL with a 0.7% fractional uncertainty [10] with further improvement being in reach at ISOLDE/CERN [11]. In addition, the ^{18}Ne half-life was recently measured to be $t_{1/2} = 1.66400^{+0.00057}_{-0.00048}$ s [12], approximately two times more precise than the previously accepted value [13]. Therefore, an improved determination of the ^{18}Ne Q_{EC} -value of the superallowed transition to the daughter 0^+ state in ^{18}F is required with the aim to push the uncertainty to the same level as the most precise theoretical correction. The ground-state transition Q -value is obtained from a Penning-trap measurement at ISOLTRAP for ^{18}Ne (see inset of Fig. 2) [14] and nuclear reaction data for the daughter, ^{18}F [15,16]. The uncertainty on the ground-state transition Q -value is currently 589 eV [17] whereas the excitation energy of the daughter 0^+ state is known to a precision of 80 eV [1]. Hence, more than a factor 3.5-fold improvement on the ground-state Q -value is needed to bring down the contribution to the ^{18}Ne $\mathcal{F}t$ -value uncertainty due to the superallowed Q_{EC} -value to at least the same level as that due to $t_{1/2}$. Additionally, the data from the two reactions determining the AME mass of ^{18}F [15,16] both deviate from the adjusted AME input by more than 1.5 standard deviations [17]. In order to avoid systematic errors on the Q_{EC} -value it would be necessary to use the Penning-trap technique, which has been time and time again proven to yield not only precise but also accurate results.

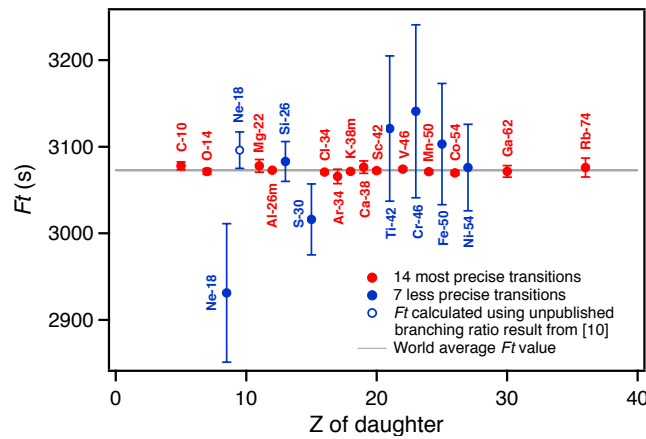


Figure 1: $\mathcal{F}t$ -values vs. Z of the daughter nucleus for the 14 most precisely determined transitions (in red) used to determine the world average $\mathcal{F}t$ -value, and for 7 less precisely determined transitions (in blue). The open blue circle shows the ^{18}Ne $\mathcal{F}t$ -value calculated using the unpublished branching ratio measurement of Ref. [10].

2. Experimental techniques

The proposed measurement of the ^{18}Ne superallowed β -decay Q_{EC} -value will be performed using the ISOLTRAP [18] apparatus at ISOLDE/CERN. The current ISOLTRAP setup combines three different ion trapping techniques for ion beam cooling, bunching and purification for high-precision mass measurement. With this sequence of beam preparation stages, it has been possible to perform high-precision mass measurements even with contaminants three or four orders of magnitude more abundant than the ion of interest.

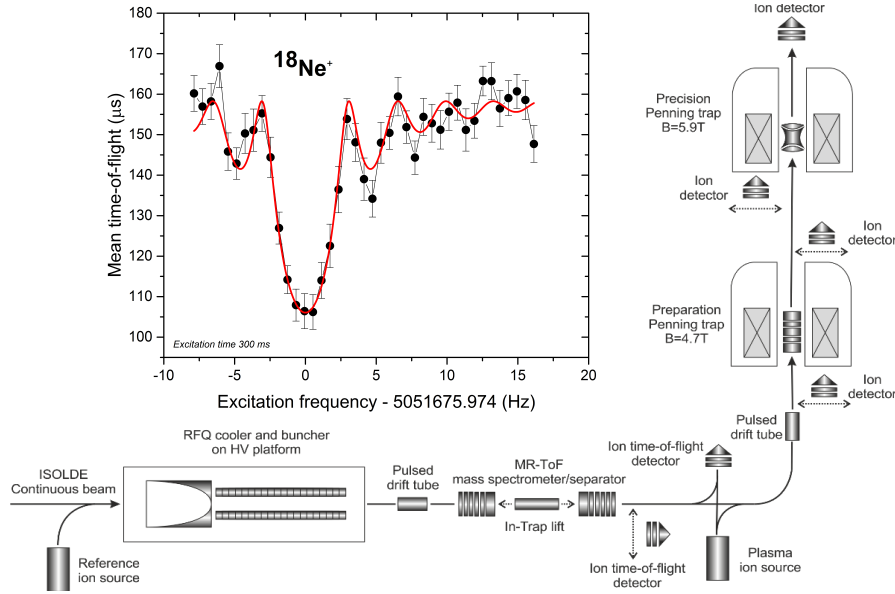


Figure 2: Schematic overview of the current ISOLTRAP setup. Inset: Example of a $^{18}\text{Ne}^+$ ToF-ICR resonance obtained at ISOLTRAP for an excitation time of 300 ms [14].

A schematic view of the ISOLTRAP mass spectrometer is presented in Figure 2. The Q_{EC} -value determination will be performed using the precision Penning trap and the well-established Ramsey-type time-of-flight ion-cyclotron-resonance (ToF-ICR) technique [19], or the recently implemented Phase-Imaging Ion-Cyclotron-Resonance (PI-ICR) technique [20].

The Q_{EC} -value is defined as the energy equivalent of the mass difference between parent and daughter atoms

$$Q_{EC} = (M_p - M_d)c^2 = \left(\frac{f_c^d}{f_c^p} - 1 \right) (M_d - M_e)c^2 = (R - 1)(M_d - M_e)c^2, \quad (2)$$

where the indices p and d refer to the parent and daughter respectively, R is the ratio of the cyclotron frequencies between daughter and parent and M_e is the electron mass. The aim of

the proposed experiment is to measure the ground-state transition Q_{EC} -value of the isobaric pair $^{18}\text{Ne}/^{18}\text{F}$ to a precision of about 20 eV thus improving the current uncertainty by a factor 30. Hence, the contribution of the ground-state masses in the uncertainty of the superallowed Q_{EC} -value would become significantly smaller than the contribution from the uncertainty in the excitation energy of the daughter 0^+ state in ^{18}F . Very recently, the mass differences of the pairs $^{21}\text{Na}/^{21}\text{Ne}$ and $^{23}\text{Mg}/^{23}\text{Na}$ were determined by ISOLTRAP using the Ramsey type ToF-ICR technique to a precision better than 20 eV and 30 eV respectively, thus demonstrating the spectrometer's ability to determine Q -values with a relative precision of a few 10^{-6} [21]. In the present case, to reach an uncertainty on the Q_{EC} -value on the order of 20 eV the cyclotron frequency ratio between daughter and mother nuclides has to be determined to a relative precision of about 10^{-9} . The statistical uncertainty in f_c obtained using the single excitation-pulse ToF-ICR technique is approximately given by

$$\frac{\delta f_c}{f_c} = \frac{1}{f_c T_{rf} \sqrt{N}}, (3)$$

where T_{rf} is the measurement time for the ion inside the trap and N is the total number of ions collected during a measurement of the cyclotron frequency. Hence, for $T_{rf} = 600$ ms and $N \sim 1000$, the frequency of each species of interest could be determined in a single measurement to a relative precision of 10^{-8} yielding a statistical uncertainty of 250 eV on the value of the ground-state Q_{EC} -value. With a Ramsey-type excitation scheme [19] one can gain a factor 3 in precision. Hence, the desired precision can be reached in about 20 measurements of R .

In order to reduce the systematic errors to a minimum and to achieve the target precision, it is necessary to measure the cyclotron frequencies of the parent and daughter isobars in the same run, meaning in the same experimental conditions. Furthermore, to determine the Q_{EC} -value with a precision of 20 eV, the beam sent to ISOLTRAP's measurement Penning trap should be purely composed of the species under study. Table 1 presents the mass resolving power required to separate ^{18}Ne from ^{18}F as well as from the two most probable stable contaminants we should be facing, namely ^{18}O and H_2O . The MR-ToF isobar separator, which can routinely achieve a mass resolving power on the order of 10^5 , is in itself by far sufficient to separate the pair of interest and the stable contamination. Finally, to minimize charge-exchange losses in the ISOLTRAP buncher, the buffer-gas inlet will be cooled with liquid nitrogen and the bunching time will be optimized [14] which requires additional time for optimization. We note that studying the trapping, cooling and bunching of positive fluorine

ions within an RFQ cooler and buncher is also of high interest for the INTC-I-171 LOI [22].

3. Beam time request

Element	Half-life	Mass Excess [keV]	unc. [keV]	Mass resolving power to ^{18}Ne	Yield [ions/ μC]
^{18}Ne	1.6 s	5317.6	0.4	-	$2 \cdot 10^5$
^{18}F	109.7 min	873.1	0.5	3 800	$1 \cdot 10^6$
^{18}O	stable	-782.8156	0.0007	2 800	stable
H_2O	stable	9840.9398	0.0002	3 700	stable

Table 1: Half-life, Mass Excess [17] and Mass resolving power for ^{18}Ne and ^{18}F as well as the stable contaminant ^{18}O and H_2O . The expected yields for ^{18}Ne and ^{18}F using SiC/VD5 unit are also presented [23].

We propose to use a SiC target coupled to a VADIS hot transfer line ion source (VD5) to ease the effusion of atomic F towards the ionisation region. The yield of ^{18}F was measured to be 1.8×10^7 ions/ μC at the ISOLDE-SC. More recent measurements of $^{27}\text{Al}^{18}\text{F}^+$ with an intensity of 1.7×10^7 ions/ μC were reported from the offline separator. Assuming a factor 10 loss with respect to the molecular sideband, one would thus expect a yield of 1×10^6 ions/ μC of atomic ^{18}F [23]. For ^{18}Ne , ISOLDE-SC yields are reported using a SiC-MK5 target/ion source combination. The enhancement factor brought by the use of the more recent VD5 ion source over the MK5 plasma ion source would put the expected yield of ^{18}Ne at the level of about 2×10^5 ions/ μC [23]. Hence, it seems feasible to extract both species from the same target and ion source unit. We note that neon masses down to ^{17}Ne have already been measured with ISOLTRAP [24].

If the measurement is performed with an average of one ion per measurement cycle in the trap (to minimize possible frequency shifts due to the Coulomb interaction), and assuming a total cycle time of 1 s, then a resonance could be obtained in less than 50 mins. In order to obtain a fully uncorrelated data set, each measurement of the frequency ratio R necessitates the measurement of three ToF-ICR resonances (^{18}F - ^{18}Ne - ^{18}F). Hence, 50 hours or equivalently 6 shifts are necessary to reach the aimed uncertainty of 20 eV. Additionally, 1 shift is required to tune the transport from ISOLDE into ISOLTRAP, study the charge exchange phenomenon, and optimise the transport towards the precision Penning trap. Finally, we request one additional shift to verify the robustness of the result to systematic detuning of the setup. For systematic cross-checks a few PI-ICR resonances will also be taken.

Summary of requested shifts : We request 6 shifts for measurements, 1 shift for tuning and 1 shift for systematic investigations.

References

- [1] J.C. Hardy, and I.S. Towner, Phys. Rev. C 91, 025501 (2015).
- [2] H. Vonach, *et al.*, Nucl. Phys. A 278, 189 (1977).
- [3] G. Savard, *et al.*, Phys. Rev. Lett. 95, 102501 (2005).
- [4] T. Eronen, *et al.*, Phys. Rev. Lett. 97, 232501 (2006).
- [5] T. Eronen, *et al.*, Phys. Rev. Lett. 100, 132502 (2008).
- [6] A.A. Valverde, *et al.*, Phys. Rev. Lett. 114, 232502 (2015).
- [7] P. Zhang, *et al.*, Phys. Lett. B 767, 20 (2017).
- [8] I.S. Towner, and J.C. Hardy, Phys. Rev. C 92, 055505 (2015).
- [9] J.C. Hardy, *et al.*, Nucl. Phys. A 246, 61 (1975).
- [10] H. Bouzomita-Zran, Ph.D. Thesis, Universite de Caen Normandie (2015).
- [11] M. Aouadi, *et al.*, Proposal to the ISOLDE and Neutron Time-of-Flight Committee, CERN-INTC-2016-051/INTC-P-481 (2016).
- [12] A.T. Laffoley, *et al.*, Phys. Rev. C 92, 025502 (2015).
- [13] G.F. Grinyer, *et al.*, Phys. Rev. C 87, 045502 (2013).
- [14] K. Blaum, *et al.*, Nuc. Phys. A 764, 305c (2004).
- [15] R.O. Bondelid and J.W. Bulter, Nuc. Phys. 53, 618 (1964).
- [16] C. Rolfs, *et al.*, Nuc. Phys. A 240, 221 (1975).
- [17] M. Wang, *et al.*, Chinese Phys. C 41, No. 3 (2017).
- [18] M. Mukherjee, *et al.*, Eur. Phys. A 35, 1 (2008).
- [19] S. George, *et al.*, Int. Jour. Mass Spec. 264, 110-201 (2007).
- [20] S. Eliseev, *et al.*, Appl. Phys. B 114, 107 (2014).
- [21] J.Karthein, *et al.*, Article in preparation.
- [22] R.F Garcia Ruiz, *et al.*, CERN-INTC-2016-037 / INTC-I-171.
- [23] ISOLDE target group, Private Communication.
- [24] W. Geithner, *et al.*, Phys. Rev. Lett. 101, 252502 (2008).

Appendix

DESCRIPTION OF THE PROPOSED EXPERIMENT

The experimental setup comprises: ISOLDE central beam line and ISOLTRAP setup. The ISOLTRAP setup has safety clearance, the memorandum document 1242456 ver.1 “Safety clearance for the operation of the ISOLTRAP experiment” by HSE Unit is released and can be found via the following link: <https://edms.cern.ch/document/1242456/1>.

Part of the	Availability	Design and manufacturing
ISOLTRAP setup	<input checked="" type="checkbox"/> Existing	<input checked="" type="checkbox"/> To be used without modification

HAZARDS GENERATED BY THE EXPERIMENT (if using fixed installation:) Hazards named in the document relevant for the fixed ISOLTRAP installation.

Résumé en langue française

Avant-propos

Cette partie du présent manuscrit a pour but de présenter en langue française un condensé des travaux effectués et des résultats obtenus dans le cadre de ce travail de thèse. Priorité est donnée aux résultats et à l'interprétation physique de ces derniers. Le lecteur étant intéressé par des détails d'ordres plus techniques est cordialement invité à suivre les références renvoyant au texte original en langue anglaise.

Résumé des travaux de thèse

Cette thèse a pour objet l'étude de l'évolution de la structure nucléaire dans deux régions clés de la carte des noyaux. D'une part, la question de la persistance de la fermeture de couche à $N=28$ dans les isotopes d'argon $^{46-48}\text{Ar}$, riches en neutrons, est étudiée. D'autre part, le développement de phénomènes collectifs dans l'état fondamental des isotopes $^{58-63}\text{Cr}$ à l'approche de l'îlot d'inversion à $N=40$ est également abordé. Ces deux phénomènes ont été longuement étudiés dans la littérature (c.f section 5.1 et les références qui y sont citées) principalement à travers des études de spectroscopie nucléaire. Ces études semblent établir l'affaiblissement de la fermeture de couche à $N=28$ dans la chaîne isotopique de l'argon ainsi que l'émergence d'une région de forte déformation dans la chaîne des chromes (culminant à l'isotope ^{64}Cr et persistant au delà).

Puisqu'il convient d'apporter une approche nouvelle pour étudier ces phénomènes, ces deux questions sont donc abordées du point de vue expérimental à travers des mesures de masse de précision en exploitant le lien naturel qui existe entre le défaut de masse d'un système lié est son énergie de liaison (c.f Chap. 1). Si des mesures de masses pré-existent les mesures effectuées dans le cadre de cette thèse, ces dernières sont relativement imprécises et il convient de confronter les résultats existants à des mesures de haute précision. Les faisceaux radioactifs étudiés ont été produits à ISOLDE (CERN). Les mesures ont été effectuées en utilisant le spectromètre de masse ISOLTRAP (c.f section 2.2) lors de trois périodes expérimentales d'une semaine environ: une en Juillet 2015 pour $^{46-47}\text{Ar}$, une en Avril 2016 pour $^{58-63}\text{Cr}$ et enfin la dernière en Aout 2017 pour ^{48}Ar . ISOLTRAP se base sur la mesure de la fréquence cyclotron libre ($\nu_c \propto \frac{1}{m}$) d'ions radioactifs confinés dans un piège de Penning. A proprement parler, la mesure s'effectue en utilisant une technique longuement éprouvée : la résonance cyclotronique ionique en temps de vol (ToF-

ICR) dont les détails techniques sont donnés au chapitre 3. Toujours à la recherche d'un gain en pouvoir de résolution en masse et en sensibilité, ISOLTRAP a été pionnier dans l'utilisation des séparateurs de masse et spectromètres en temps de vol à réflexions multiples (MRToF-MS). Dans cet appareil la mesure de masse est basée sur la mesure du temps de vol t d'un ion de masse m selon la relation : $t = a\sqrt{m} + b$, où a et b sont des constantes de calibration à déterminer expérimentalement (c.f 2.3.2). Pour des raisons évidentes de simplicité, il apparaît naturel de choisir comme espèce de calibration un contaminant provenant du même spectre en temps de vol que l'ion d'intérêt. Puisque il n'est pas toujours possible de trouver deux espèces de calibration dans le même spectre que l'ion d'intérêt, la deuxième calibrant provient d'une source d'ions alcalins propre à ISOLTRAP. Cette technique permet bien souvent de mesurer des espèces plus exotiques que la technique ToF-ICR qui est fortement limité par la demi-vie des espèces à étudier. Ainsi les isotopes $^{46-47}\text{Ar}$ et $^{58-62}\text{Cr}$ ont été mesurés en utilisant cette dernière tandis que ^{48}Ar et ^{63}Cr n'ont pu être mesurés qu'avec le MRToF-MS. $^{58-62}\text{Cr}$ ont également été mesurés avec le MRToF-MS offrant ainsi la possibilité de comparer les résultats des deux méthodes.

Un rappel des sources d'erreurs systématiques de la technique ToF-ICR est présenté en 3.1.1. Une attention toute particulière a été apportée à l'étude des erreurs systématiques de la technique MRToF-MS. Pour limiter l'effet des biais d'analyse en raison d'une faible statistique, une méthode d'analyse basée sur le principe de maximisation de la vraisemblance est tout d'abord mise en place pour l'analyse des données MRToF-MS (c.f 3.1.2). Il est ensuite montré que si une espèce contaminante ainsi qu'une espèce provenant de la source d'ions hors ligne d'ISOLTRAP sont choisis pour la calibration de l'appareil MRToF-MS, alors l'influence sur le résultat final des fluctuations en temps de vols de l'espèce hors ligne est négligeable en comparaison de celles affectant la mesure du temps de vol des espèces en ligne. Puisque le calibrant en ligne suit le même chemin à travers l'appareil il paraît logique qu'au premier ordre les fluctuations affectant ces deux espèces se compensent; ceci est également démontré de manière quantitative. Ainsi, seules les fluctuations affectant la différence en temps de vol entre le calibrant en ligne et l'ion d'intérêt sont à considérer comme potentiellement problématiques. L'ambiguïté dans le choix de la densité de probabilité utilisée lors de l'analyse des spectres et l'interaction Coulombienne entre les espèces présentes dans le MRToF-MS apparaissent comme les principales sources de ce type d'erreurs. Pour chaque jeux de données mesuré avec le MRToF-MS la magnitude de ces effets est étudié (c.f 3.1.2).

Table D.1: Rapport de fréquences ($r = \nu_{c,ref}/\nu_c$), rapports de temps de vol (C_{ToF}) et excès de masse atomique pour les isotopes d'argon mesurés dans le cadre cette thèse. Les excès de masse atomique extrait de l'AME 2016 [W⁺17a] et de l'AME 2012 [A⁺12] sont donnés pour comparaison (# désigne des valeurs extrapolées dans l'AME2012). Les masses des ions de références sont extraites de l'AME 2016. Les demi-vie expérimentales proviennent de l'évaluation NUBASE2016 [A⁺17c].

Espèce	Demi-vie	Référence	Rapport R ou C_{ToF}	Excès de masse (keV)		
				Cette Thèse	AME2016	AME2012
^{46}Ar	8.4(0.8) s	^{39}K	$r = 1.1797680972(640)$	-29 771.3(2.3)	-29 772.9(1.1)	-29 730(40)
^{47}Ar	1.23(0.03) s	^{39}K	$r = 1.2055547092(340)$	-25 367.3(1.2)	-25 366.3(1.1)	-25 210(90)
^{48}Ar	415(15) ms	$^{32}\text{S}^{16}\text{O}/^{85}\text{Rb}$	$C_{ToF} = 0.499715668(560)$	-22 354.8(16.5)	-22 280(310)	-22 440# (300)#

Les excès de masses atomiques extraits des données (c.f section 3.2) sont présentés dans les Tables D.1 et D.2 respectivement pour $^{46-47}\text{Ar}$ et $^{58-63}\text{Cr}$. Il est im-

Table D.2: Rapport de fréquences ($r = \nu_{c,ref}/\nu_c$), rapports de temps de vol (C_{ToF}) et excès de masse atomique pour les isotopes de chrome mesurés dans le cadre cette thèse. Les excès de masse atomique extrait de l'AME 2016 [W⁺17a] et de l'AME 2012 [A⁺12] sont donnés pour comparaison (# désigne des valeurs extrapolées de l'AME2012). Les masses des ions de références sont extraits de l'AME 2016. Les demi-vie expérimentales proviennent de l'évaluation NUBASE2016 [A⁺17c]. Les taux de productions correspondent au nombre d'ions de chrome par seconde produit lors de cette expérience. Au total, l'efficacité du transport des ions jusqu'au MRToF-MS était de 0.5 %. En moyenne, la cible a été irradiée avec un courant de protons de $1.8\mu\text{A}$.

Espèce	Taux (ions/s)	Demi-vie	Référence	Rapport R or C_{ToF}	Excès de masse (keV)		
					Cette Thèse	AME2016	AME2012
⁵⁸ Cr	Non déterminé	7.0(0.3) s	⁸⁵ Rb	$r = 0.6824024142(376)$	-51 991.8(3.0)	-51 991.8(1.5)	-51 830(200)
⁵⁹ Cr	3×10^5	1050(90) ms	⁸⁵ Rb	$r = 0.6942284208(85)$	-48 115.9(0.7)	-48 090(220)	-47 890(240)
			⁴⁰ Ca ¹⁹ F/ ⁸⁵ Rb	$C_{ToF} = 0.500536923(887)$	-48 132(20)		
⁶⁰ Cr	2×10^4	490(10) ms	⁸⁵ Rb	$r = 0.7060206906(138)$	-46 908.5(1.1)	-46 670(190)	-46 500(210)
			⁴¹ Ca ¹⁹ F/ ⁸⁵ Rb	$C_{ToF} = 0.500484920(886)$	-46 917(19)		
⁶¹ Cr	2×10^3	243(9) ms	⁸⁵ Rb	$r = 0.7178534753(230)$	-42 496.5(1.8)	-42 480(100)	-42 460(130)
			⁴² Ca ¹⁹ F/ ⁸⁵ Rb	$C_{ToF} = 0.500120578(976)$	-42 503(20)		
⁶² Cr	3×10^2	206(12) ms	⁸⁵ Rb	$r = 0.7296512630(440)$	-40 852.6(3.5)	-40 890(150)	-40 890(150)
			⁴³ Ca ¹⁹ F/ ⁸⁵ Rb	$C_{ToF} = 0.500047948(921)$	-40 841(18)		
⁶³ Cr	3×10^1	129(2) ms	⁴⁴ Ca ¹⁹ F/ ⁸⁵ Rb	$C_{ToF} = 0.49964187(386)$	-36 178(73)	-36 010(360)	-35 720(460)

portant de noter que par rapport aux résultats existants les masses obtenues sont jusqu'à 90 fois plus précises pour les isotopes de l'argon et jusqu'à 300 fois pour les chromes. Si tous les isotopes d'argon mesurés apparaissent plus liés, le gap-neutron empirique (courbe bleue en Figure D.1 est réduit de 73 keV. Toutefois, celui-ci n'est réduit que de 400 keV comparé à sa valeur pour le noyau ⁴⁸Ca qui est doublement magique. Ceci nous conduit à penser que la fermeture de couche à $N=28$ est bien présente dans la chaîne isotopique de l'argon.

Dans la chaîne isotopique des chromes, les systématiques de l'énergie de séparation à deux neutrons (c.f le panneau supérieur de la Figure D.2) suggère un développement graduel de la collectivité dans l'état fondamental des chromes à l'approche de $N=40$. En effet, cette dernière semble clairement s'aplanir à l'approche de $N=40$. Ce comportement est très proche de celui observé dans la chaîne du magnésium à l'approche de $N=20$ (représenté sur le panneau supérieur de la Figure D.4). Le gain en énergie de corrélation pour chaque neutrons ajouté au système apparaît plus prononcé dans la chaîne isotopique des chromes par rapport à la chaîne du fer, comme le montre le panneau inférieur de la Figure D.2. En effet la quantité $\delta_{2n}^*(N, Z) = S_{2n}(N-2, Z) - S_{2n}(N, Z)$ peut être interprété comme la dérivée de la courbe S_{2n} . Une diminution de $\delta_{2n}^*(N, Z)$ indique donc un aplatissement de la courbe $S_{2n}(N, Z)$. Ce phénomène est souvent due à un gain important en énergie de corrélation et est souvent interprété comme une signature du développement d'une région de collectivité nucléaire. Aussi ces mesures permettent de mettre en évidence pour la première fois un comportement différent entre l'état fondamental et le premier état excité pour les isotopes pairs-pairs de fer et de chrome. En effet, au point de transition vers la région de déformation (i.e à $N=36$ pour le chrome et $N=38$ pour le fer) le gain en énergie de corrélation pour chaque neutrons ajouté au système apparaît plus prononcé dans l'état excité que dans l'état fondamental.

En ce qui concerne la chaîne isotopique de l'argon, il apparaît sur la Figure D.3 que les prédictions théoriques obtenues en utilisant une méthode de type modèle en couches (c.f Chap. 4 pour une introduction générale ainsi que les détails des calculs effectués dans le cadre de cette thèse) et l'interaction phénoménologique

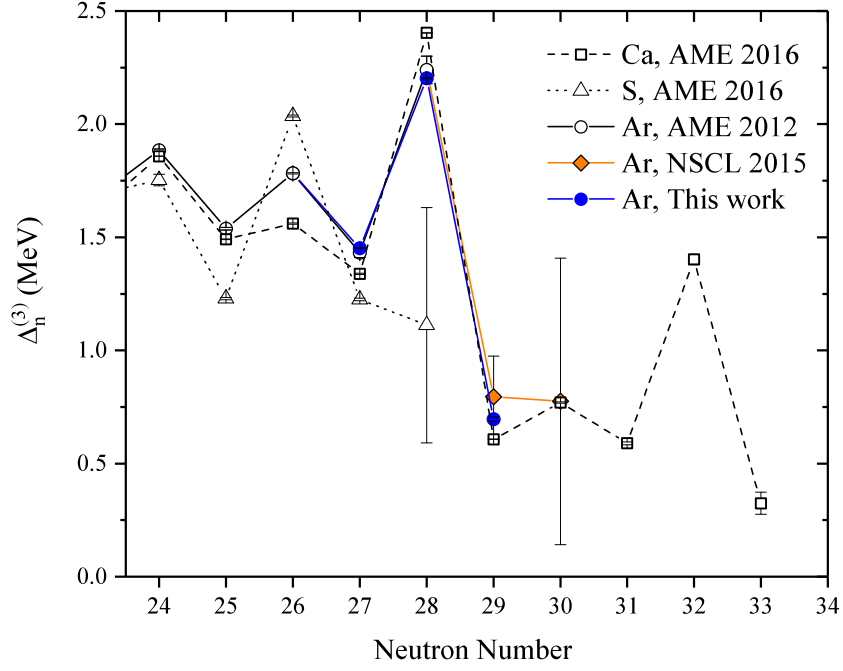


Figure D.1: Gap empirique d'appariement neutron pour les chaines isotopiques du calcium, de l'argon et du soufre. La courbe bleue est tirée des mesures expérimentales obtenues dans cette thèse. La courbe orange quant à elle est tirée de [M⁺15a].

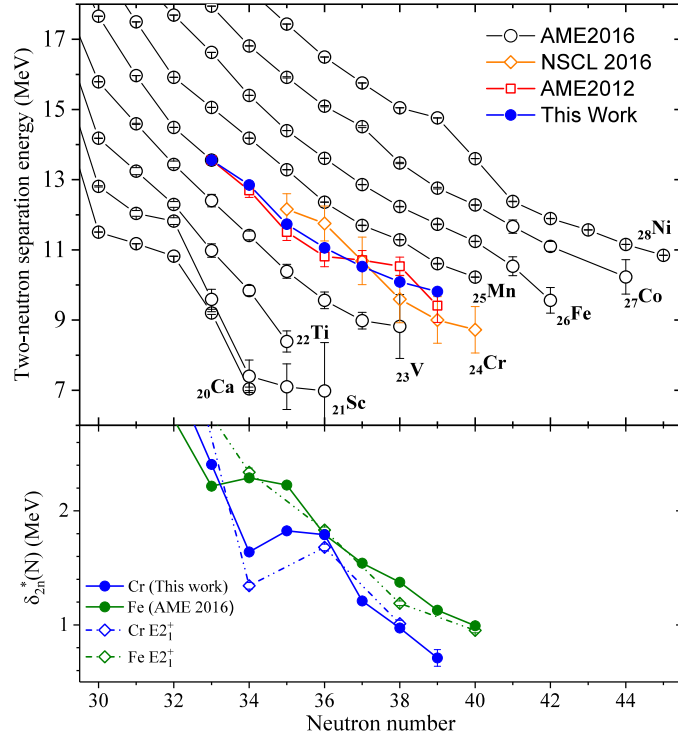


Figure D.2: *Top*: Energie de séparation à deux neutrons, S_{2n} , obtenue lors de cette thèse (courbe bleue). La courbe orange est obtenue d'après [M⁺16].

Bottom: δ_{2n}^* pour l'état fondamental et le premier état excité 2_1^+ pour les chaines isotopiques de chrome (courbe bleue) et de fer (en vert) [G⁺10, S⁺15].

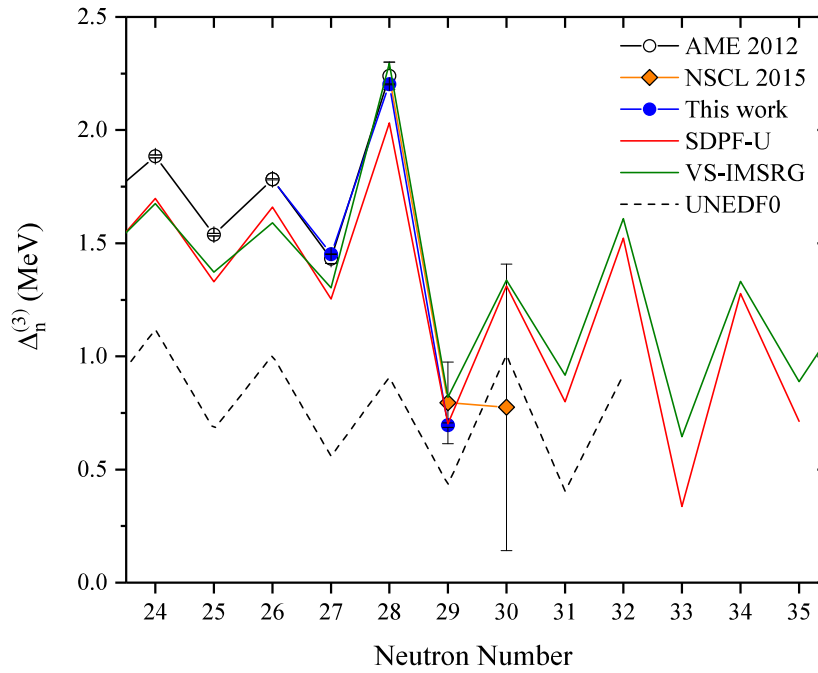


Figure D.3: Comparaison entre le gap empirique d'appariement neutron expérimental et diverses approches théoriques. Voir texte pour plus de détails. La courbe bleue est obtenue d'après les mesures rapportées dans cette thèse.

SDPFU [NP09] reproduisent de manière satisfaisante les résultats expérimentaux. Ces derniers ont aussi été comparés à des calculs de modèle en couches utilisant une interaction dérivée à partir d'une méthode *ab-initio* de type *VS-IMSRG* [T⁺12b, B⁺14a, S⁺16b, S⁺17b, S⁺17a]. Il apparaît que ces prédictions sont également à même de reproduire les données expérimentales.

Pour la chaîne des chromes, une comparaison (courbe orange pointillée sur la Figure D.4) à des prédictions du type champs moyen non-relativiste (calculs entrepris dans le cadre de ce travail de thèse c.f Chap. 4) montre une bonne adéquation avec les résultats expérimentaux. Toutefois lorsque, dans le cadre de cette approximation, les propriétés de déformation de l'état fondamental des isotopes du chrome sont exploré il apparaît que ces derniers sont prédits sphériques ce qui semble en contradiction avec les résultats tirés des études de spectroscopie. En comparant (voir Figure D.4) les résultats des calculs de modèles en couches utilisant les interactions phénoménologiques *GXPF1A* et *LNPS'* [H⁺05, L⁺10a, M⁺15a] ainsi que de la méthode *ab-initio* *VS-IMSRG*, il apparaît que seuls les calculs utilisant un espace de valence comprenant les niveaux ν -*pfgd* semblent à même de reproduire les données expérimentales. Lorsqu'une extension de la méthode *VS-IMSRG* d'un espace de valence ν -*pf* aux niveaux ν -*pfg* est entreprise aucune amélioration significative n'est observée. Une extension supplémentaire incluant le niveau ν - $d_{5/2}$ n'est pour le moment pas envisageable bien que des travaux soient en cours à ce sujet.

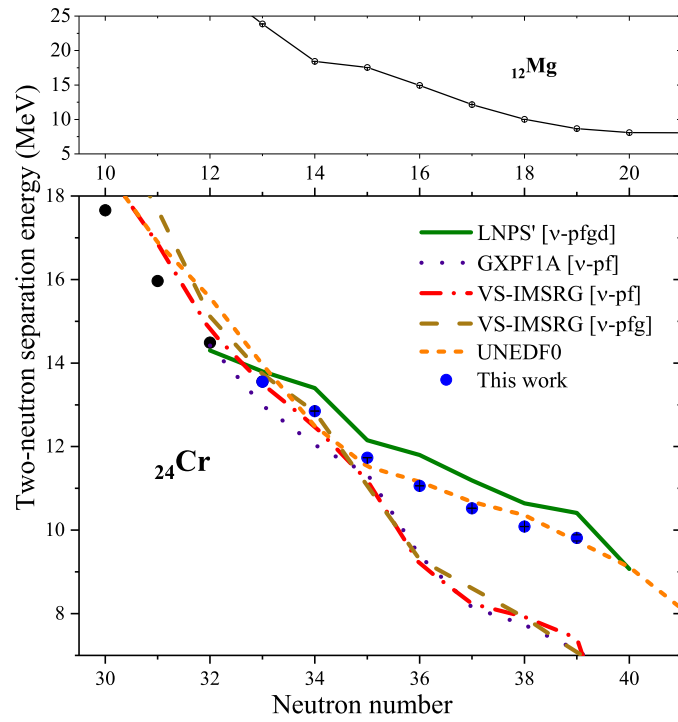


Figure D.4: *Top*: Énergie de séparation à deux neutrons de la chaîne du magnésium Mg [W⁺17a].

Bottom: Comparaison entre l'énergie de séparation à deux neutrons expérimentale et diverses approches théoriques. La courbe bleue est obtenue d'après nos mesures expérimentales.

Bibliography

Bibliography

- [A⁺12] G. Audi et al. The atomic mass evaluation. *Chinese Phys. C*, 36:1287, 2012.
- [A⁺17a] B. P. Abbott et al. Multi-messenger Observations of a Binary Neutron Star Merger. *The Astrophys. Jour. Lett.*, 848(2):L12, oct 2017.
- [A⁺17b] B.P. Abbott et al. GW170817: Observation of Gravitational Waves from a Binary Neutron Star Inspiral. *Phys. Rev. Lett.*, 119(16):161101, oct 2017.
- [A⁺17c] G. Audi et al. The NUBASE2016 evaluation of nuclear properties. *Chinese Phys. C*, 41(3):030001, 2017.
- [AHI08] S Aoki, T Hatsuda, and N Ishii. The nuclear force from Monte Carlo simulations of lattice quantum chromodynamics. *Comp. Sci. and Disc.*, 1(1):015009, 2008.
- [Ast19a] F. W. Aston. The Constitution of the Elements. *Nature*, 104(2616):393–393, dec 1919.
- [Ast19b] F.W. Aston. Lxxiv. a positive ray spectrograph. *The London, Edinburgh, and Dublin Philosophical Magazine and Journal of Science*, 38(228):707–714, 1919.
- [Ast20] F.W. Aston. LIX. The mass-spectra of chemical elements. *The London, Edinburgh, and Dublin Philosophical Magazine and Journal of Science*, 39(233):611–625, 1920.
- [Ast27] F. W. Aston. Atoms and their Packing Fractions. *Nature*, 120(3035):956–959, dec 1927.
- [B⁺36] H. A. Bethe et al. Nuclear Physics A. Stationary States of Nuclei. *Rev. Mod. Phys.*, 8:82–229, Apr 1936.
- [B⁺54] K. A. Brueckner et al. Two-Body Forces and Nuclear Saturation. I. Central Forces. *Phys. Rev.*, 95:217–228, 1954.
- [B⁺74] B. Banerjee et al. On the character of the Hartree-Fock-Bogoliubov solutions in a rotating frame. *Nucl. Phys. A*, 221(3):564 – 572, 1974.
- [B⁺82] M. Bernas et al. Magic features of ⁶⁸Ni. *Phys. Lett. B*, 113(4):279 – 282, 1982.

- [B⁺85] W. Benenson et al. The masses of ^{51}Ca and ^{47}Ar . *Phys. Lett. B*, 162(1):87 – 91, 1985.
- [B⁺87] G. Bollen et al. First absolute mass measurements of short-lived isotopes. *Hyperfine Interactions*, 38(1):793–802, Dec 1987.
- [B⁺90] G. Bollen et al. The accuracy of heavy-ion mass measurements using time of flight-ion cyclotron resonance in a Penning trap. *Journal of Applied Physics*, 68(9):4355–4374, 1990.
- [B⁺92] G. Bollen et al. Resolution of nuclear ground and isomeric states by a Penning trap mass spectrometer. *Phys. Rev. C*, 46:R2140–R2143, Dec 1992.
- [B⁺98] Y. Bai et al. Mass measurement in the fp-shell using the TOFI spectrometer. *AIP Conf. Proc.*, 455(1):90–93, 1998.
- [B⁺03a] Michael Bender et al. Self-consistent mean-field models for nuclear structure. *Rev. Mod. Phys.*, 75:121–180, 2003.
- [B⁺03b] K. Blaum et al. Masses of ^{32}Ar and ^{33}Ar for Fundamental Tests. *Phys. Rev. Lett.*, 91:260801, Dec 2003.
- [B⁺03c] K Blaum et al. Recent developments at ISOLTRAP: towards a relative mass accuracy of exotic nuclei below 10^{-8} . *Journal of Physics B: Atomic, Molecular and Optical Physics*, 36(5):921, 2003.
- [B⁺06] M. Bender et al. Global study of quadrupole correlation effects. *Phys. Rev. C*, 73:034322, 2006.
- [B⁺07] B. Bastin et al. Collapse of the $N = 28$ Shell Closure in ^{42}Si . *Physical Review Letters*, 99(2):022503, jul 2007.
- [B⁺08a] S. Bhattacharyya et al. Structure of Neutron-Rich Ar Isotopes Beyond $N = 28$. *Phys. Rev. Lett.*, 101(3):032501, jul 2008.
- [B⁺08b] K. Blaum et al. Nuclear moments and charge radii of argon isotopes between the neutron-shell closures $N=20$ and $N=28$. *Nucl. Physics A*, 799(1):30 – 45, 2008.
- [B⁺09a] D. Beck et al. Electric and magnetic field optimization procedure for Penning trap mass spectrometers. *Nucl. Instr. and Meth. A*, 598(2):635 – 641, 2009.
- [B⁺09b] George Bertsch et al. Hartree-Fock-Bogoliubov theory of polarized Fermi systems. *Phys. Rev. A*, 79:043602, 2009.
- [B⁺12] T. Baugher et al. Intermediate-energy Coulomb excitation of $^{58,60,62}\text{Cr}$: The onset of collectivity toward $N = 40$. *Phys. Rev. C*, 86:011305, Jul 2012.
- [B⁺13] Y Blumenfeld et al. Facilities and methods for radioactive ion beam production. *Phys. Scr.*, 2013(T152):014023, 2013.

- [B⁺14a] S. K. Bogner et al. Nonperturbative shell-model interactions from the in-medium similarity renormalization group. *Phys. Rev. Lett.*, 113:142501, 2014.
- [B⁺14b] B.A. Brown et al. The Shell-Model Code NuShellX@MSU. *Nucl. Data Sheets*, 120:115 – 118, 2014.
- [B⁺15] T. Braunroth et al. Reduced transition strengths of low-lying yrast states in chromium isotopes in the vicinity of $N = 40$. *Phys. Rev. C*, 92:034306, Sep 2015.
- [B⁺16] C. Babcock et al. Quadrupole moments of odd-A $^{53-63}\text{Mn}$: Onset of collectivity towards $N = 40$. *Phys. Lett. B*, 760:387 – 392, 2016.
- [Bar13] R. Barlow. *Data Analysis in High Energy Physics*, chapter 1, pages 1–26. Wiley-Blackwell, 2013.
- [BBH08] M. Bender, G. F. Bertsch, and P.-H. Heenen. Collectivity-induced quenching of signatures for shell closures. *Phys. Rev. C*, 78:054312, 2008.
- [BFS10] S.K. Bogner, R.J. Furnstahl, and A. Schwenk. From low-momentum interactions to nuclear structure. *Prog. Part. Nucl. Phys.*, 65(1):94 – 147, 2010.
- [BG86] L. S. Brown and G. Gabrielse. Geonium theory: Physics of a single electron or ion in a Penning trap. *Rev. Mod. Phys.*, 58:233–311, 1986.
- [BGG91] J.F. Berger, M. Girod, and D. Gogny. Time-dependent quantum collective dynamics applied to nuclear fission. *Comp. Phys. Comm.*, 63(1):365 – 374, 1991.
- [Bla06] Klaus Blaum. High-accuracy mass spectrometry with stored ions. *Phys. Rep.*, 425(1):1 – 78, 2006.
- [BM13] O. Behnke and L. Moneta. *Data Analysis in High Energy Physics*, chapter 2, pages 27–73. Wiley-Blackwell, 2013.
- [Boh52] A. Bohr. *Mat. Fys. Medd. K Dan. Vidensk. Selsk.*, 26(14), 1952.
- [Bol01] G. Bollen. Mass measurements of short-lived nuclides with ion traps. *Nucl. Phys. A*, 693(1):3 – 18, 2001.
- [BR97] R. Brun and F. Rademakers. ROOT — An object oriented data analysis framework. *Nucl. Instr. and Meth. A.*, 389(1):81 – 86, 1997.
- [C⁺83] J. Carlson et al. Three-nucleon interaction in 3-, 4- and ∞ -body systems. *Nucl. Phys. A*, 401(1):59 – 85, 1983.
- [C⁺98] E. Chabanat et al. A Skyrme parametrization from subnuclear to neutron star densities Part II. Nuclei far from stabilities. *Nucl. Phys. A*, 635(1):231 – 256, 1998.
- [C⁺99] E. Caurier et al. *Acta Phys. Pol. B*, 30:705, 1999.

- [C⁺05] E. Caurier et al. The shell model as a unified view of nuclear structure. *Rev. Mod. Phys.*, 77:427–488, 2005.
- [C⁺06] C. M. Campbell et al. Measurement of Excited States in Si 40 and Evidence for Weakening of the N = 28 Shell Gap. *Phys. Rev. Lett.*, 97(11):112501, sep 2006.
- [C⁺10] R. B. Cakirli et al. Correlations of experimental isotope shifts with spectroscopic and mass observables. *Phys. Rev. C*, 82:061306, Dec 2010.
- [C⁺13] H. L. Crawford et al. Quadrupole Collectivity in Neutron-Rich Fe and Cr Isotopes. *Phys. Rev. Lett.*, 110:242701, Jun 2013.
- [C⁺14a] S Calinescu et al. Study of the neutron-rich isotope 46 Ar through intermediate coulomb excitation. 45:200, 2014.
- [C⁺14b] E. Caurier et al. Merging of the islands of inversion at N = 20 and N = 28. *Phys. Rev. C*, 90(1):014302, jul 2014.
- [C⁺17] R Catherall et al. The ISOLDE facility. *J. of Phys. G*, 44(9):094002, 2017.
- [Cau89] E. Caurier. Antoine code, 1989.
- [Cau10] E. Caurier. Shell model code antoine, 2010.
- [Com18] FAST ComTec. FAST ComTec MCS6A documentation. <https://www.fastcomtec.com/products/product-lines/ufm/multiscaler-tof-mcs6a/>, 2018.
- [D⁺68] H. G. Dehmelt et al. "Bolometric" Technique for the rf Spectroscopy of Stored Ions. *Phys. Rev. Lett.*, 21:127–131, 1968.
- [D⁺96] M. Dufour et al. Realistic collective nuclear Hamiltonian. *Phys. Rev. C*, 54:1641–1660, 1996.
- [D⁺01] J. Dobaczewski et al. Pairing interaction and self-consistent densities in neutron-rich nuclei. *Nucl. Phys. A*, 693(1):361 – 373, 2001.
- [D⁺09] J. Dobaczewski et al. Solution of the Skyrme–Hartree–Fock–Bogolyubov equations in the Cartesian deformed harmonic-oscillator basis.: (VI) hfodd (v2.40h): A new version of the program. *Comp. Phys. Comm.*, 180(11):2361 – 2391, 2009.
- [D⁺13] P. Doornenbal et al. In-Beam γ -Ray Spectroscopy of Mg 34 , 36 , 38 : Merging the N = 20 and N = 28 Shell Quenching. *Phys. Rev. Lett.*, 111(21):212502, nov 2013.
- [D⁺17] T. Day Goodacre et al. The identification of autoionizing states of atomic chromium for the resonance ionization laser ion source of the ISOLDE radioactive ion beam facility. *Spect. Acta B*, 129:58 – 63, 2017.

- [DAK04] P. Delahaye, F. Ames, and A. Kellerbauer. Study of the charge exchange process at low energy with REXTRAP. *Nucl. Phys. A*, 746:604 – 607, 2004. Proceedings of the Sixth International Conference on Radioactive Nuclear Beams (RNB6).
- [Deh90] H. G. Dehmelt. Experiments with an isolated subatomic particle at rest. *Rev. Mod. Phys.*, 62:525–530, 1990.
- [Dem13] L. Demortier. *Data Analysis in High Energy Physics*, chapter 4, pages 107–151. Wiley-Blackwell, 2013.
- [E⁺09] E. Epelbaum et al. Modern theory of nuclear forces. *Rev. Mod. Phys.*, 81:1773–1825, Dec 2009.
- [E⁺11] A. Estradé et al. Time-of-Flight Mass Measurements for Nuclear Processes in Neutron Star Crusts. *Phys. Rev. Lett.*, 107:172503, Oct 2011.
- [E⁺12] Jochen Erler et al. The limits of the nuclear landscape. *Nature*, 486(7404):509–512, 06 2012.
- [E⁺14] S. Eliseev et al. A phase-imaging technique for cyclotron-frequency measurements. *App. Phys. B*, 114(1):107–128, Jan 2014.
- [Edd20] A. S. Eddington. The Internal Constitution of the Stars. *Nature*, 106(2653):14–20, sep 1920.
- [ens17] Evaluated nuclear structure data file database, 2017.
- [F.] Wegner F. Flow-equations for hamiltonians. *Annalen der Physik*, 506(2):77–91.
- [F⁺10a] R. Ferrer et al. Penning trap mass spectrometry of neutron-rich Fe and Co isotopes around $N = 40$ with the LEBIT mass spectrometer. *Phys. Rev. C*, 81:044318, Apr 2010.
- [F⁺10b] C. Force et al. Prolate-Spherical Shape Coexistence at $N = 28$ in S 44. *Phys. Rev. Lett*, 105(10):102501, sep 2010.
- [F⁺13] R. Ferrer et al. In gas laser ionization and spectroscopy experiments at the Superconducting Separator Spectrometer (S3): Conceptual studies and preliminary design. *Nucl. Ins. Meth. Phys. B*, 317:570 – 581, 2013. XVIth International Conference on ElectroMagnetic Isotope Separators and Techniques Related to their Applications, December 2–7, 2012 at Matsue, Japan.
- [F⁺17] Valentin Fedosseev et al. Ion beam production and study of radioactive isotopes with the laser ion source at ISOLDE. *J. of Phys. G*, 44(8):084006, 2017.
- [G⁺80] G. Gräff et al. A direct determination of the proton electron mass ratio. *Zeit. für Phys. A*, 297(1):35–39, 1980.
- [G⁺97] T. Glasmacher et al. Collectivity in 44S. *Phys. Lett. B*, 395(3-4):163–168, mar 1997.

- [G⁺03a] A. Gade et al. Detailed experimental study on intermediate-energy Coulomb excitation of ⁴⁶Ar. *Phys. Rev. C*, 68(1):014302, jul 2003.
- [G⁺03b] S. Grévy et al. Beta-decay studies at the N=28 shell closure. *Nucl. Phys. A*, 722:C424–C428, jul 2003.
- [G⁺05a] A. Gade et al. Knockout from Ar 46 : $l = 3$ neutron removal and deviations from eikonal theory. *Phys. Rev. C*, 71(5):051301, may 2005.
- [G⁺05b] C Guénaut et al. Mass measurements of ⁵⁶Cr and the question of shell reincarnation at N = 32. *Jour. Phys. G*, 31(10):S1765, 2005.
- [G⁺06a] A. Gade et al. Cross-shell excitation in two-proton knockout: Structure of ⁵²Ca. *Phys. Rev. C*, 74:021302, Aug 2006.
- [G⁺06b] L. Gaudefroy et al. Reduction of the Spin-Orbit Splittings at the $N = 28$ Shell Closure. *Phys. Rev. Lett.*, 97:092501, Aug 2006.
- [G⁺07a] S. George et al. Ramsey Method of Separated Oscillatory Fields for High-Precision Penning Trap Mass Spectrometry. *Phys. Rev. Lett.*, 98:162501, 2007.
- [G⁺07b] S. George et al. The Ramsey method in high-precision mass spectrometry with Penning traps: Experimental results. *Int. J. Mass Spectrom.*, 264:110 – 121, 2007.
- [G⁺08] L. Gaudefroy et al. Structure of the $N = 27$ isotones derived from the Ar 44 (d , p) Ar 45 reaction. *Phys. Rev. C*, 78(3):034307, sep 2008.
- [G⁺09a] L. Gaudefroy et al. Collective structure of the $N = 40$ isotones. *Phys. Rev. C*, 80:064313, Dec 2009.
- [G⁺09b] L. Gaudefroy et al. Shell Erosion and Shape Coexistence in S 27 16 43. *Phys. Rev. Lett.*, 102(9):092501, mar 2009.
- [G⁺10] A. Gade et al. Collectivity at $N = 40$ in neutron-rich ⁶⁴Cr. *Phys. Rev. C*, 81:051304, May 2010.
- [G⁺12] L. Gaudefroy et al. Direct Mass Measurements of B 19 , C 22 , F 29 , Ne 31 , Na 34 and Other Light Exotic Nuclei. *Phys. Rev. Lett.*, 109(20):202503, nov 2012.
- [GAB⁺09] A. Gade, P. Adrich, D. Bazin, B. A. Brown, J. M. Cook, C. Aa. Diget, T. Glasmacher, S. McDaniel, A. Ratkiewicz, K. Siwek, and D. Weisshaar. In-Beam γ -Ray Spectroscopy of Very Neutron-Rich Nuclei: Excited States in S 46 and Ar 48. *Phys. Rev. Lett.*, 102(18):182502, may 2009.
- [Gam30] Mass defect curve and nuclear constitution. *Proc. Royal Soc. of London A*, 126(803):632–644, 1930.
- [Gau10] L. Gaudefroy. Shell model study of $N \simeq 28$ neutron-rich nuclei. *Phys. Rev. C*, 81:064329, 2010.
- [Got16] A. Gottberg. Target materials for exotic isol beams. *Nucl. Instr. Meth. B*, 376:8 – 15, 2016.

- [GR⁺16] R. F. Garcia Ruiz et al. Unexpectedly large charge radii of neutron-rich calcium isotopes. *Nature Phys.*, 12:594, 2016.
- [H⁺49] O. Haxel et al. On the "magic numbers" in nuclear structure. *Phys. Rev.*, 75:1766–1766, Jun 1949.
- [H⁺01] F Herfurth et al. A linear radiofrequency ion trap for accumulation, bunching, and emittance improvement of radioactive ion beams. *Nucl. Instr. Meth. A*, 469(2):254 – 275, 2001.
- [H⁺05] M. Honma et al. Shell-model description of neutron-rich pf-shell nuclei with a new effective interaction GXPF 1. *Eur. Phys. J. A*, 25(1):499–502, 2005.
- [H⁺11] Kris Heyde et al. Shape coexistence in atomic nuclei. *Rev. Mod. Phys.*, 83(4):1467–1521, nov 2011.
- [H⁺13] H. Hergert et al. In-medium similarity renormalization group with chiral two- plus three-nucleon interactions. *Phys. Rev. C*, 87:034307, 2013.
- [H⁺15a] J. C. Hardy et al. Superaligned $0^+ \rightarrow 0^+$ nuclear β decays: 2014 critical survey, with precise results for V_{ud} and CKM unitarity. *Phys. Rev. C*, 91:025501, Feb 2015.
- [H⁺15b] H. Heylen et al. Spins and magnetic moments of $^{58,60,62,64}\text{Mn}$ ground states and isomers. *Phys. Rev. C*, 92:044311, Oct 2015.
- [H⁺16a] G. Hagen et al. Neutron and weak-charge distributions of the ^{48}Ca nucleus. *Nature Phys.*, 12:186, 2016.
- [H⁺16b] H. Hergert et al. The in-medium similarity renormalization group: A novel ab initio method for nuclei. *Physics Reports*, 621:165 – 222, 2016. Memorial Volume in Honor of Gerald E. Brown.
- [H⁺16c] H. Heylen et al. Changes in nuclear structure along the Mn isotopic chain studied via charge radii. *Phys. Rev. C*, 94:054321, Nov 2016.
- [H17] Hergert H. In-medium similarity renormalization group for closed and open-shell nuclei. *Phys. Scr.*, 92(2):023002, 2017.
- [Hey94] K.L.G. Heyde. *The nuclear shell model*. Springer series in nuclear and particle physics. Springer-Verlag, 1994.
- [HJ⁺17] M. Hjorth-Jensen et al. *An Advanced Course in Computational Nuclear Physics: Bridging the Scales from Quarks to Neutron Stars*. Lecture Notes in Physics. Springer International Publishing, 2017.
- [I⁺18] C. Izzo et al. Precision mass measurements of neutron-rich Co isotopes beyond $N = 40$. *Phys. Rev. C*, 97:014309, 2018.
- [id18] ETP ion detect. ETP ion detect MAGNETOF detector documentation. <https://www.etp-ms.com/faqs/literature/MagneTOF:ANewClassofRobustSub-nanosecondTOFDetectorswithExceptionalDynamicRange>, 2018.

- [J⁺74] N. A. Jelley et al. Masses for ^{43}Ar and the new isotopes ^{45}Ar and ^{46}Ar . *Phys. Rev. C*, 9:2067–2070, May 1974.
- [K⁺66] T.T.S. Kuo et al. Structure of finite nuclei and the free nucleon-nucleon interaction: An application to ^{18}O and ^{18}F . *Nuclear Physics*, 85(1):40 – 86, 1966.
- [K⁺68] T.T.S. Kuo et al. Reaction matrix elements for the 0f-1p shell nuclei. *Nucl. Phys. A*, 114(2):241 – 279, 1968.
- [K⁺76] R. Kirchner et al. Investigation of gaseous discharge ion sources for isotope separation on-line. *Nucl. Instr. Meth.*, 133(2):187 – 204, 1976.
- [K⁺95] M. König et al. Quadrupole excitation of stored ion motion at the true cyclotron frequency. *Int. J. Mass Spectrom.*, 142(1–2):95 – 116, 1995.
- [K⁺03] Kellerbauer, A. et al. From direct to absolute mass measurements: A study of the accuracy of ISOLTRAP. *Eur. Phys. J. D*, 22(1):53–64, 2003.
- [K⁺10] M. Kortelainen et al. Nuclear energy density optimization. *Phys. Rev. C*, 82:024313, 2010.
- [K⁺13] S. Kreim et al. Recent exploits of the ISOLTRAP mass spectrometer. *Nucl. Instr. Meth. B*, 317(0):492 – 500, 2013.
- [K⁺16] M. Knoop et al. *Trapped Charged Particles*. Advanced Textbooks in Physics. World Scientific, 2016.
- [K⁺17] Daniel Kasen et al. Origin of the heavy elements in binary neutron-star mergers from a gravitational-wave event. *Nature*, 551(7678):80, oct 2017.
- [KBG⁺96] A. Klein, B.A. Brown, U. Georg, M. Keim, P. Lievens, R. Neugart, M. Neuroth, R.E. Silverans, L. Vermeeren, and ISOLDE Collaboration. Moments and mean square charge radii of short-lived argon isotopes. *Nuclear Physics A*, 607(1):1 – 22, 1996.
- [L⁺01] K. Lan et al. A hybrid of exponential and gaussian functions as a simple model of asymmetric chromatographic peaks. *Jour. of Chrom. A*, 915(1):1 – 13, 2001.
- [L⁺03] D. Lunney et al. Recent trends in the determination of nuclear masses. *Rev. Mod. Phys.*, 75:1021–1082, Aug 2003.
- [L⁺09] D Lunney et al. Masses of noble gases. Jan 2009.
- [L⁺10a] S. M. Lenzi et al. Island of inversion around ^{64}Cr . *Phys. Rev. C*, 82:054301, Nov 2010.
- [L⁺10b] J. Ljungvall et al. Onset of collectivity in neutron-rich Fe isotopes: Toward a new island of inversion? *Phys. Rev. C*, 81:061301, Jun 2010.
- [L⁺12] R. Luis et al. Optimization studies of the CERN-ISOLDE neutron converter and fission target system. *The Euro. Phys. Jour. A*, 48(6):90, Jun 2012.

- [L⁺18] E. Leistenschneider et al. Dawning of the $N = 32$ Shell Closure Seen through Precision Mass Measurements of Neutron-Rich Titanium Isotopes. *Phys. Rev. Lett.*, 120:062503, Feb 2018.
- [Lyo86] L. Lyons. *Statistics for Nuclear and Particle Physicists*, page 74–124. Cambridge University Press, 1986.
- [M⁺80] W. Mayer et al. Spectroscopy of neutron-rich nuclei produced in ^{14}C induced reactions on ^{48}Ca . *Phys. Rev. C*, 22:2449–2453, Dec 1980.
- [M⁺05] F.G. Major et al. *Charged Particle Traps: Physics and Techniques of Charged Particle Field Confinement*. Charged Particle Traps. Springer, 2005.
- [M⁺08] M. Mukherjee et al. ISOLTRAP: An on-line Penning trap for mass spectrometry on short-lived nuclides. *Euro. Phys. J. A*, 35(1):1–29, 2008.
- [M⁺10] D. Mengoni et al. Lifetime measurements of excited states in neutron-rich Ar 44 , 46 populated via a multinucleon transfer reaction. *Phys. Rev. C*, 82(2):024308, aug 2010.
- [M⁺13] Z. Meisel et al. Time-of-flight mass spectrometry of very exotic systems. *Int. Jour. of Mass Spectr.*, 349-350:145–150, sep 2013.
- [M⁺15a] Z. Meisel et al. Mass Measurements Demonstrate a Strong $N = 28$ Shell Gap in Argon. *Phys. Rev. Lett.*, 114(2):022501, jan 2015.
- [M⁺15b] T. D. Morris et al. Magnus expansion and in-medium similarity renormalization group. *Phys. Rev. C*, 92:034331, Sep 2015.
- [M⁺16] Z. Meisel et al. Time-of-flight mass measurements of neutron-rich chromium isotopes up to $N = 40$ and implications for the accreted neutron star crust. *Phys. Rev. C*, 93:035805, Mar 2016.
- [M⁺18a] T. D. Morris et al. Structure of the Lightest Tin Isotopes. *Phys. Rev. Lett.*, 120:152503, 2018.
- [M⁺18b] M. Mougeot et al. Precision Mass Measurements of $^{58-63}\text{Cr}$: Nuclear Collectivity Towards the $N = 40$ Island of Inversion. *Phys. Rev. Lett.*, 120:232501, 2018.
- [Mac01] R. Machleidt. High-precision, charge-dependent bonn nucleon-nucleon potential. *Phys. Rev. C*, 63:024001, 2001.
- [Mat04] M. Matos. *Isochronous mass measurements of short-lived neutron rich nuclides at the FRS-ESR facilities*. PhD thesis, 2004.
- [May49] M. G. Mayer. On closed shells in nuclei. ii. *Phys. Rev.*, 75:1969–1970, Jun 1949.
- [May50] M. G. Mayer. Nuclear Configurations in the Spin-Orbit Coupling Model. II. Theoretical Considerations. *Phys. Rev.*, 78:22–23, 1950.
- [ME11] R. Machleidt and D.R. Entem. Chiral effective field theory and nuclear forces. *Physics Reports*, 503(1):1 – 75, 2011.

- [MF39] L. Meitner and O. R. Frisch. Disintegration of Uranium by Neutrons: a New Type of Nuclear Reaction. *Nature*, 143(3615):239–240, feb 1939.
- [Mo18] S. Michimasa, , and otghers. Magic Nature of Neutrons in Ca 54 : First Mass Measurements of Ca 55 – 57. *Phys. Rev. Lett.*, 121(2):022506, jul 2018.
- [N⁺12] S. Naimi et al. Surveying the $N = 40$ island of inversion with new manganese masses. *Phys. Rev. C*, 86:014325, Jul 2012.
- [N⁺16] F. Nowacki et al. Shape Coexistence in ^{78}Ni as the Portal to the Fifth Island of Inversion. *Phys. Rev. Lett.*, 117:272501, 2016.
- [NP09] F. Nowacki and A. Poves. New effective interaction for $0\hbar\omega$ shell-model calculations in the $sd - pf$ valence space. *Phys. Rev. C*, 79:014310, 2009.
- [O⁺01] T. Otsuka et al. Magic numbers in exotic nuclei and spin-isospin properties of the NN interaction. *Phys. Rev. Lett.*, 87:082502, Aug 2001.
- [O⁺05] T. Otsuka et al. Evolution of Nuclear Shells due to the Tensor Force. *Phys. Rev. Lett.*, 95:232502, Nov 2005.
- [P⁺01a] H. B. Pedersen et al. Ion Motion Synchronization in an Ion-Trap Resonator. *Phys. Rev. Lett.*, 87:055001, 2001.
- [P⁺01b] S. C. Pieper et al. Quantum Monte Carlo Calculations Of Light Nuclei. *Annual Review of Nuclear and Particle Science*, 51(1):53–90, 2001.
- [P⁺10] L. Penescu et al. Development of high efficiency Versatile Arc Discharge Ion Source at CERN ISOLDE. *Review of Scientific Instruments*, 81(2):02A906, 2010.
- [P⁺17] S. Purushothaman et al. Hyper-EMG: A new probability distribution function composed of Exponentially Modified Gaussian distributions to analyze asymmetric peak shapes in high-resolution time-of-flight mass spectrometry", journal = "International Journal of Mass Spectrometry. 421:245 – 254, 2017.
- [Pau90] W. Paul. Electromagnetic traps for charged and neutral particles. *Rev. Mod. Phys.*, 62:531–540, 1990.
- [Phy] [structure of even-even nuclei using a mapped collective hamiltonian and the d1s gogny interaction.
- [PM⁺08] Sara Perez-Martin et al. Microscopic justification of the equal filling approximation. *Phys. Rev. C*, 78:014304, Jul 2008.
- [PN01] Alfredo Poves and Frederic Nowacki. *The nuclear shell model*, pages 70–101. Springer Berlin Heidelberg, Berlin, Heidelberg, 2001.
- [R⁺13a] Ryan Ringle et al. Penning trap mass spectrometry of rare isotopes produced via projectile fragmentation at the LEBIT facility. *Intern. Journ. of Mass Spectr.*, 349-350:87 – 93, 2013. 100 years of Mass Spectrometry.

- [R⁺13b] M. Rosenbusch et al. Towards systematic investigations of space-charge phenomena in multi-reflection ion traps. *AIP Conference Proceedings*, 1521(1):53–62, 2013.
- [R⁺16a] E. Minaya Ramirez et al. Conception of PIPERADE: A high-capacity Penning-trap mass separator for high isobaric contamination at DESIR. *Nucl. Instr. Meth. B*, 376:298 – 301, 2016. Proceedings of the XVIIth International Conference on Electromagnetic Isotope Separators and Related Topics (EMIS2015), Grand Rapids, MI, U.S.A., 11-15 May 2015.
- [R⁺16b] Tomás R. Rodríguez et al. Occupation numbers of spherical orbits in self-consistent beyond-mean-field methods. *Phys. Rev. C*, 93:054316, 2016.
- [RAA⁺15] M. Rosenbusch, P. Ascher, D. Atanasov, C. Barbieri, D. Beck, K. Blaum, Ch. Borgmann, M. Breitenfeldt, R. B. Cakirli, A. Cipollone, S. George, F. Herfurth, M. Kowalska, S. Kreim, D. Lunney, V. Manea, P. Navrátil, D. Neidherr, L. Schweikhard, V. Somà, J. Stanja, F. Wienholtz, R. N. Wolf, and K. Zuber. Probing the $N = 32$ Shell Closure below the Magic Proton Number $Z = 20$: Mass Measurements of the Exotic Isotopes $K\ 52$, 53 . *Physical Review Letters*, 114(20):202501, may 2015.
- [RH⁺97] H. Raimbault-Hartmann et al. A cylindrical Penning trap for capture, mass selective cooling, and bunching of radioactive ion beams. *Nucl. Instr. Meth. B*, 126(1):378 – 382, 1997. International Conference on Electromagnetic Isotope Separators and Techniques Related to Their Applications.
- [RS80] P. Ring and P. Schuck. *The nuclear many-body problem*. Springer-Verlag, 1980.
- [S⁺91] G. Savard et al. A new cooling technique for heavy ions in a Penning trap. *Phys. Lett. A*, 158(5):247 – 252, 1991.
- [S⁺94a] H. L. Seifert et al. Mass measurement of neutron-rich isotopes from ^{51}Ca to ^{72}Ni . *Zeit. für Phys. A*, 349(1):25–32, 1994.
- [S⁺94b] V. G. J. Stoks et al. Construction of high-quality NN potential models. *Phys. Rev. C*, 49:2950–2962, 1994.
- [S⁺96] H. Scheit et al. New Region of Deformation: The Neutron-Rich Sulfur Isotopes. *Phys. Rev. Lett.*, 77(19):3967–3970, nov 1996.
- [S⁺00] F. Sarazin et al. Shape Coexistence and the $N = 28$ Shell Closure Far from Stability. *Phys. Rev. Lett.*, 84:5062–5065, May 2000.
- [S⁺08] O. Sorlin et al. Nuclear magic numbers: New features far from stability. *Prog. Part. Nucl. Phys.*, 61(2):602 – 673, 2008.
- [S⁺09] M. Stoitsov et al. Large-scale mass table calculations. *Intern. Journ. of Mod. Phys. E*, 18(04):816–822, 2009.

- [S⁺10a] N. Schunck et al. One-quasiparticle states in the nuclear energy density functional theory. *Phys. Rev. C*, 81:024316, 2010.
- [S⁺10b] N.A. Smirnova et al. Shell evolution and nuclear forces. *Phys. Lett. B*, 686(2–3):109 – 113, 2010.
- [S⁺12] N. Schunck et al. Solution of the Skyrme–Hartree–Fock–Bogolyubov equations in the Cartesian deformed harmonic-oscillator basis.: (VII) hfodd (v2.49t): A new version of the program. *Comp. Phys. Comm.*, 183(1):166 – 192, 2012.
- [S⁺13] M.V. Stoitsov et al. Axially deformed solution of the Skyrme–Hartree–Fock–Bogolyubov equations using the transformed harmonic oscillator basis (II) hfbtho v2.00d: A new version of the program. *Comp. Phys. Com.*, 184(6):1592 – 1604, 2013.
- [S⁺14a] P. Schury et al. A high-resolution multi-reflection time-of-flight mass spectrograph for precision mass measurements at RIKEN/SLOWRI. *Nucl. Instr. Meth. B*, 335:39 – 53, 2014.
- [S⁺14b] V. Somà et al. Chiral two- and three-nucleon forces along medium-mass isotope chains. *Phys. Rev. C*, 89:061301, Jun 2014.
- [S⁺14c] S. R. Stroberg et al. Single-particle structure of silicon isotopes approaching Si 42. *Phys. Rev. C*, 90(3):034301, sep 2014.
- [S⁺15] C. Santamaria et al. Extension of the $N = 40$ Island of Inversion towards $N = 50$: Spectroscopy of ^{66}Cr , $^{70,72}\text{Fe}$. *Phys. Rev. Lett.*, 115:192501, Nov 2015.
- [S⁺16a] J. Simonis et al. Exploring sd -shell nuclei from two- and three-nucleon interactions with realistic saturation properties. *Phys. Rev. C*, 93(1):011302(R), 2016.
- [S⁺16b] S. R. Stroberg et al. Ground and excited states of doubly open-shell nuclei from ab initio valence-space Hamiltonians. *Phys. Rev. C*, 93(5):051301(R), 2016.
- [S⁺17a] J. Simonis et al. Saturation with chiral interactions and consequences for finite nuclei. *Phys. Rev. C*, 96:014303, 2017.
- [S⁺17b] S. R. Stroberg et al. Nucleus-dependent valence-space approach to nuclear structure. *Phys. Rev. Lett.*, 118:032502, 2017.
- [Sch06] Stefan Schwarz. IonCool—A versatile code to characterize gas-filled ion bunchers and coolers (not only) for nuclear physics applications. *Nucl. Instr. Meth. A*, 566(2):233 – 243, 2006.
- [SG⁺11] D. Santiago-Gonzalez et al. Triple configuration coexistence in S 44. *Phys. Rev. C*, 83(6):061305, jun 2011.
- [Som] V. Somá. Self-consistent green-gorkov calculations. private communication.
- [SR18] S. Schwartz and R. Ringle. Eva software and documentation. <https://groups.nsc1.msu.edu/lebit/downloads/index.html>, 2018.

- [T⁺75] C. Thibault et al. Direct measurement of the masses of ^{11}Li and $^{26-32}\text{Na}$ with an on-line mass spectrometer. *Phys. Rev. C*, 12:644–657, Aug 1975.
- [T⁺90] X. L. Tu et al. Direct mass measurements of the neutron-rich isotopes of chlorine through iron. *Zeit. für Phys. A*, 337(4):361–366, dec 1990.
- [T⁺97] R. C. Thompson et al. The motion of small numbers of ions in a Penning trap. *Zeit. für Phys. D*, 42(4):271–277, Dec 1997.
- [T⁺12a] S. Takeuchi et al. Well Developed Deformation in Si 42. *Physical Review Letters*, 109(18):182501, nov 2012.
- [T⁺12b] K. Tsukiyama et al. In-medium similarity renormalization group for open-shell nuclei. *Phys. Rev. C*, 85:061304(R), 2012.
- [Tho97] J. J. Thomson. XL. Cathode Rays. *The London, Edinburgh, and Dublin Philosophical Magazine and Journal of Science*, 44(269):293–316, oct 1897.
- [Tho99] J. J. Thomson. LVIII. On the masses of the ions in gases at low pressures. *The London, Edinburgh, and Dublin Philosophical Magazine and Journal of Science*, 48(295):547–567, dec 1899.
- [Tho07] J.J. Thomson. XLVII. On rays of positive electricity. *The London, Edinburgh, and Dublin Philosophical Magazine and Journal of Science*, 13(77):561–575, 1907.
- [Tho12] J.J. Thomson. XIX. Further experiments on positive rays. *The London, Edinburgh, and Dublin Philosophical Magazine and Journal of Science*, 24(140):209–253, 1912.
- [U. 02] U. Köster. Intense radioactive-ion beams produced with the ISOL method. *Eur. Phys. J. A*, 15(1):255–263, 2002.
- [Vla16] M. Vladimír. *BINDING ENERGY OF STRONGLY DEFORMED RADIONUCLIDES : penning-trap mass spectrometry and mean-field... theoretical studies*. SPRINGER, 2016.
- [VM01] R. Vinh Mau. *The theory of the nucleon-nucleon interaction*, pages 1–38. Springer Berlin Heidelberg, Berlin, Heidelberg, 2001.
- [W⁺95] R. B. Wiringa et al. Accurate nucleon-nucleon potential with charge-independence breaking. *Phys. Rev. C*, 51:38–51, 1995.
- [W⁺12a] R. Winkler et al. Quadrupole Collectivity beyond $N = 28$: Intermediate-Energy Coulomb Excitation of Ar 47, 48. *Phys. Rev. Lett.*, 108(18):182501, apr 2012.
- [W⁺12b] R.N. Wolf et al. On-line separation of short-lived nuclei by a multi-reflection time-of-flight device. *Nucl. Instr. Meth. A*, 686:82 – 90, 2012.
- [W⁺13a] F. Wienholtz et al. Masses of exotic calcium isotopes pin down nuclear forces. *Nature*, 498:346–349, 2013.

- [W⁺13b] R.N. Wolf et al. ISOLTRAP’s multi-reflection time-of-flight mass separator/spectrometer. *Intern. Journ. of Mass Spectr.*, 349-350:123 – 133, 2013. 100 years of Mass Spectrometry.
- [W⁺15] F Wienholtz et al. Towards ultrahigh-resolution multi-reflection time-of-flight mass spectrometry at ISOLTRAP. *Physica Scripta*, 2015(T166):014068, 2015.
- [W⁺17a] M. Wang et al. The AME2016 atomic mass evaluation (II). Tables, graphs and references. *Chinese Phys. C*, 41(3):030003, 2017.
- [W⁺17b] A. Welker et al. Binding Energy of ⁷⁹Cu: Probing the Structure of the Doubly Magic ⁷⁸Ni from Only One Proton Away. *Phys. Rev. Lett.*, 119:192502, Nov 2017.
- [W⁺17c] F. Wienholtz et al. Mass-selective ion ejection from multi-reflection time-of-flight devices via a pulsed in-trap lift. *Int. J. of Mass Spectrom.*, 421(Supplement C):285 – 293, 2017.
- [WD05] Verkerke W. and Kirkby D. The roofit toolkit for data modeling. *TheR00FITtoolkitfordatamodeling*. http://roofit.sourceforge.net/docs/roofit_phystat05.pdf, 2005.
- [Wei35] C. F. v. Weizsäcker. Zur theorie der kernmassen. *Zeit. für Phys.*, 96(7):431–458, 1935.
- [Wei79] Steven Weinberg. Phenomenological Lagrangians. *Physica A: Stat. Mech. and App.*, 96(1):327 – 340, 1979.
- [Wei90] S. Weinberg. Nuclear forces from chiral lagrangians. *Phys. Lett. B*, 251(2):288 – 292, 1990.
- [WGM09] G. Werth, V.N. Gheorghe, and F.G. Major. *Charged Particle Traps II: Applications*. Springer Series on Atomic, Optical, and Plasma Physics. Springer Berlin Heidelberg, 2009.
- [Wig37] E. Wigner. On the Consequences of the Symmetry of the Nuclear Hamiltonian on the Spectroscopy of Nuclei. *Phys. Rev.*, 51(2):106–119, jan 1937.
- [WMRS12] Robert N. Wolf, Gerrit Marx, Marco Rosenbusch, and Lutz Schweikhard. Static-mirror ion capture and time focusing for electrostatic ion-beam traps and multi-reflection time-of-flight mass analyzers by use of an in-trap potential lift. *Intern. Jour. Mass Spectr.*, 313:8 – 14, 2012.
- [WP90] H. Wollnik and M. Przewloka. Time-of-flight mass spectrometers with multiply reflected ion trajectories. *Intern. Journ. Mass Spectro. and Ion Proc.*, 96(3):267 – 274, 1990.
- [X⁺15] X. Xing et al. Direct mass measurements of neutron-rich ⁸⁶Kr projectile fragments and the persistence of neutron magic number N = 32 in Sc isotopes. *Chinese Phys. C*, 39(10):104001, 2015.
- [Yuk35] H. Yukawa. On the Interaction of Elementary Particles I. *Proc. Phys. Math. Soc. Jap.*, 17:48–57, 1935. [Prog. Theor. Phys. Suppl.1,1(1935)].

Titre : Etude des phénomènes nucléaires collectifs à travers des mesures de masse de précision d'isotopes riches en neutrons d'argon et de chrome

Mots clés : structure nucléaire, pièges à ions, spectrométrie de masse

Résumé : Le lien étroit existant entre la masse d'un noyau et son énergie de liaison fait de la masse un observable incontournable pour enrichir notre compréhension de l'évolution de la structure nucléaire dans des régions de la carte des noyaux éloignées de la vallée de la stabilité. Dans cette thèse deux régions présentant d'importants changements structuraux sont étudiés à travers des mesures de masses de haute précision effectuées à ISOLDE/CERN avec le spectromètre ISOLTRAP. De nombreux résultats de spectroscopie nucléaire indiquent que la chaîne isotopique du chrome présente les changements structuraux les plus importants dans toute la région de déformation nucléaire observée au sud du nickel 68. Cette thèse présente les premières mesures de haute précision des isotopes $^{58-63}\text{Cr}$ grâce à des techniques de spectrométrie de masse de pointe faisant appel à l'utilisation d'un piège de Penning ainsi qu'à un spectromètre en temps de vol de type MRTof-

MS. Les mesures ainsi obtenues sont jusqu'à 300 fois plus précises que celles disponibles dans la littérature actuelle. Au contraire des résultats précédents, ces nouvelles mesures suggèrent une évolution progressive de l'état fondamental des chromes vers la déformation aux abords de $N=40$. La question de la persistance de la fermeture de couche à $N=28$ dans la chaîne de l'argon est aussi abordée dans le cadre de cette thèse de doctorat à travers la mesure des isotopes 46-48 de l'argon. Les résultats d'une précision améliorée confirment la présence d'une forte fermeture de couche à $N=28$ dans l'argon. Pour chaque jeu de données la procédure d'analyse est détaillée. L'implication pour la physique nucléaire des résultats expérimentaux obtenus sont discutés de manière phénoménologique ainsi qu'à travers des modèles représentant l'état de l'art de la recherche en physique nucléaire théorique.

Title : Nuclear collectivity studied through high-precision mass measurements of neutron-rich argon and chromium isotopes

Keywords : nuclear structure, ion traps, mass spectrometry

Abstract : Due to their inherent relationship with the binding energy, nuclear masses are the fingerprint of all the interactions taking place within the nucleus. As such, precise and accurate mass values are an essential ingredient to the comprehensive understanding of nuclear phenomena in exotic regions of the chart of nuclides. In this thesis, two key regions exhibiting dramatic structural evolution are investigated by means of high precision mass measurements performed with the online mass spectrometer ISOLTRAP at ISOLDE/CERN. Numerous spectroscopy results indicate that the chromium isotopic chain exhibits the most dramatic structural changes within the region situated south of ^{68}Ni . This thesis reports on the first high-precision mass measurements of the neutron-rich $^{58-63}\text{Cr}$ isotopes using the well established Penning trap mass spectrometry technique as well as the MRTof-MS technique pioneered at ISOLTRAP in recent years. The obtained mass values are up to

300 times more precise than the ones currently available in the literature. At odds with previous results, the new mass values exclude a sudden onset of ground-state collectivity rather favouring a smooth transition towards deformation approaching $N=40$. The question of the persistence of the $N=28$ shell closure in the Argon chain is also studied in this PhD work through the measurement of the neutron-rich $^{46-48}\text{Ar}$ isotopes. The results of improved precision confirm the presence of a strong $N=28$ shell closure in the Argon chain. For both datasets, the detailed data analysis procedure will be presented. The implication of the obtained mass values for nuclear structure will be discussed through a phenomenological discussion of the binding energy trend. The results will also be discussed in the light of state of the art nuclear models including results from the promising valence-space formulation of the *ab-initio* IM-SRG formalism

